CHARACTERIZATION AND MODELING OF LONG-TERM BEHAVIOR OF FRP-TO-CONCRETE INTERFACE IN AGGRESSIVE ENVIRONMENTS

by

SHAHROOZ AMIDI

JIALAI WANG, COMMITTEE CHAIR
KENNETH J. FRIDLEY
MARK E. BARKEY
JAMES A. RICHARDSON
SRIRAM AALETI

A DISSERTATION

Submitted in partial fulfillment of the requirements
for the degree of Doctor of Philosophy
in the Department of Civil, Construction and Environmental Engineering
in the Graduate School of
The University of Alabama

TUSCALOOSA, ALABAMA

2015

Copyright Shahrooz Amidi 2015
ALL RIGHTS RESERVED

ABSTRACT

Fiber reinforced polymer (FRP) composites have emerged as one the foremost structural materials in retrofit/rehabilitation of concrete structural members in the last decades. The long-term durability of the FRP-to-concrete interface in aggressive environments places a critical role in the success of this technique. A comprehensive program using both the analytical and experimental approaches has been carried out in this study to examine the integrity and long-term durability of the FRP-to-concrete interface in presence of aggressive environments.

Novel analytical solutions based on three-parameter elastic/viscoelastic foundation models have been developed for adhesively bonded joints first in this study to gain better understanding of stress transfer through FRP-to-concrete interface. These models overcome drawbacks in existing models by satisfying all boundary conditions and producing different peel stress distributions along two adhesive-adherend interfaces, making it possible to accurately predict the location of debonding initiation. These models have been verified with finite element analysis and experimental observations.

Comprehensive experimental programs have been carried out to evaluate the deterioration of the FRP-to-concrete induced by moisture. In the first part, a novel environment-assisted subcritical debonding method using a wedge driving test has been proposed to examine the synergistic effect of the mechanical loads and environmental conditions on the deterioration of the FRP-to concrete interface. The deterioration of the interface induced by water has also been evaluated through measuring the residual fracture toughness of the FRP-to-concrete interface conditioned in water through two different ways. It has been found that conditioning method can

have significant effect on the testing results. A novel wedge-split test has been proposed and carried out to directly measure the traction-separation law of the epoxy-concrete interfaces under mode-I loading, which is not available in the literature. The potential of using silane coupling agent to improve the durability of the FRP-to-concrete interface has also been examined in the experimental program. Testing results confirm that the residual fracture toughness of the FRP-to-concrete interface attacked by moisture can be significantly increased by silane treatment.

DEDICATION

I dedicate this dissertation to my lovely family, to my eternal love, Toloo, without her this long journey would have been impossible. I dedicate it to my parents for giving me all the love and the sacrifice in their lives. I dedicate this work to my younger brother Roozbeh, who has always been my true friend. I also dedicate this dissertation to my father and mother in law, to my sister and brother in law, who have always believed in me and supported me unconditionally. I was fortunate in my life to have you all on my side.

LIST OF ABBREVIATIONS AND SYMBOLS

2PEF	Two-parameter elastic foundation
3PEF	Three-parameter elastic foundation
3PVF	Three-parameter viscoelastic foundation
a	Crack length
a_0	Distance between the wedge and the strain gauge
b	Width of the specimen
B_i	Shear stiffness of adherends
b_i	Width of adherends
c	Distance of the top surface to the neutral axis
C	Moisture concentration (Fick's second law)
CFRP	Carbon fiber reinforced polymer
C_i	Axial stiffness of adherends
CLS	Cracked-lap-shear
COD	Crack opening displacement
CZM	Cohesive zone model
D	Creep compliance (Schapery solution)
D	Bending stiffness
DAQ	Data acquisition
DCB	Double cantilever beam

D_i	Flexural stiffness of adherends
D^i_w	Moisture diffusivity (Fick's second law)
E	Relaxation modulus (Schapery solution)
e	Distance from the mass center to the vertical axial (wedge splitting test)
E_0	Longitudinal modulus of elasticity of the adhesive
E_a	Longitudinal modulus of elasticity of the adhesive
EASD	Environment-assisted subcritical debonding
EB	Externally bonded
E_i	Longitudinal modulus of elasticity of adherends
E_R	Constant (Schapery solution)
ERR	Energy release rate
FEA	Finite element analysis
FPZ	Fracture process zone
FRP	Fiber reinforced polymer
G	Fracture energy release rate
G_0	Initial shear modulus of the adhesive
G_∞	Ultimate shear modulus of the adhesive
G_a	Shear modulus of elasticity of the adhesive
G_c	Critical fracture energy release rate
GDP	Gross domestic product
G_i	Shear modulus of elasticity of adherends
G_I	Mode-I fracture energy release rate
G_{II}	Mode-II fracture energy release rate

G_{int}	Intrinsic fracture toughness energy
G-R	Goland and Reissner
G_{th}	Threshold fracture energy release rate
H	Relative humidity (Fick's second law)
h	Crack length (wedge splitting test)
h_0	Thickness of the adhesive
h_a	Thickness of the adhesive
h_i	Thickness of adherends
HODT	Higher order displacement theory
I_{RH}	Interface relative humidity
J	J-integral (Fernlund solution)
J_f	J-integral (Schapery solution)
k	Linear spring stiffness
K	Bulk modulus of the adhesive layer
k_1 *and* k_2	Stiffness coefficients of the Maxwell model
L	Total length of the bond
L_a	Nominal crack length
L_{eff}	Effective length
LEFM	Linear Elastic Fracture Mechanics
$m.g$	Weight (wedge splitting test)
M_3	Bending moment (Fernlund solution)
MC	Moisture concentration
M_c	Moisture content

M_{ci}	Interface moisture content
MD	Molecular dynamics
M_i(i=1,2)	Internal bending moment of adherends
M_i	Initial moisture content
M_m	Maximum moisture content
M_T	Resulting bending moment
MTS	Material Testing System
n	Outward unit normal vector (Fernlund solution)
$N_i(i=1,2)$	Internal axial force of adherends
NSM	Near-surface mounted
N_T	Resulting axial force
OPC	Ordinary Portland cement
P	Crack tip (Schapery solution)
P	Applied pulling force
P_3	Axial load (Fernlund solution)
P_{sp}	Horizontal applied force
P_v	Vertical applied force
$Q_i(i=1,2)$	Internal transverse shear force of adherends
Q_T	Resulting shear force
s	Slip of the debonded section
s_c	Maximum slip
SEM	Scanning electron microscope
SLS	Standard Linear Solid (Rheological model)

SLS	Single-lap-shear
T	Traction vector (Fernlund solution)
t	Thickness of the specimen (wedge splitting test)
t_0	Retardation time
T_g	Glass transition
TOM	Tsai, Oplinger, and Morton model
u	Displacement vector (Fernlund solution)
u_i	Axial displacement at the neutral axis of adherends
U_i	Displacement of adherends
$u^R{}_i$	Displacement vector (Schapery solution)
V_3	Shear load (Fernlund solution)
W	Energy density (Fernlund solution)
w	Crack opening at any point on the crack length (wedge splitting test)
w_a	Deflection of the adhesive
w_i	Deflection at the neutral axis of adherends
W_i	Deflection of adherends
WST	Wedge splitting test
α	Crack length (Schapery solution)
Γ_0	Intrinsic fracture energy
Γ_o	J-integral path (Fernlund solution)
γ_{xy}	Adhesive shear strain
Δ	Deflection at the end of the crack
δ	Crack opening distance at the crack mouth (wedge splitting test)

ε	Strain
ε_x	Adhesive longitudinal strain
ε_{yi}	Interfacial normal strain
η	Viscose damping coefficient
η	Friction constant (wedge splitting test)
κ	Shear coefficient
ξ	J-integral path (Schapery solution)
σ	Traction (wedge splitting test)
σ_i	Interfacial peel stress
σ_x	Adhesive longitudinal stress
τ	Adhesive shear stress
$\tau^R{}_i$	Interfacial stress (Schapery solution)
ϕ_i	Rotation angle at the neutral axis of adherends

ACKNOWLEDGEMENTS

I would like to express my deepest gratitude to all people helped make this dissertation possible. Without Dr. Jialai Wang, my advisor, and his guidance, support and encouragement, this dissertation never would have happened. I would like to thank my committee members, Dr. Kenneth Fridley, Dr. James Richardson, Dr. Mark Barkey, and Dr. Sriram Aaleti for not only their insights into my dissertation, helpful comments and suggestions, but for all that I have learned from them during my study at the University of Alabama. I would also like to thank Brandon Pritchett for his assistance with making the specimens and running the tests. Finally, I wish to thank my dear friends and my colleagues William Guin, Wei Pan, Xin Qian, and Fengjuan Liu for their enormous help and support throughout these years.

This work is partially supported by the National Science Foundation under grant No. 0927938.

CONTENTS

ABSTRACT……ii

DEDICATION……iv

LIST OF ABBREVIATIONS AND SYMBOLS……v

ACKNOWLEDGEMENTS…….....xi

LIST OF TABLES…….. xvii

LIST OF FIGURES…….....xviii

CHAPTER 1: INTRODUCTION……....1

1.1. Background and necessity of the research 1

1.2. Analytical studies on adhesively bonded joints 3

1.2.1. Interface stress analysis 3

1.2.1.1. Adhesively bonded single-lap joints 4

1.2.1.2. Adhesively bonded double-lap joints 7

1.2.2. Viscoelastic analysis 7

1.2.2.1. Viscoelastic stress analysis of adhesively bonded joints 7

1.3. Experimental studies on durability of FRP-to-concrete adhesively bonded joints 10

1.3.1. Subcritical debonding of the FRP-to-concrete interface 11

1.3.2. Critical debonding behaviors of the FRP-to-concrete interface 16

1.3.2.1. Previous experimental studies 16

1.3.2.2. Modeling degradation of the FRP-to-concrete interface in aggressive environments……....20

1.4. Research needs, tasks and dissertation organization 22

CHAPTER 2: THREE-PARAMETER ELASTIC FOUNDATION MODEL OF DOUBLE-LAP ADHESIVELY BONDED JOINTS…….....25

Abstract 25

2.1. Introduction 26

2.2. Three-parameter elastic foundation model of a double-lap joint 29

2.3. Results and verification 38

2.4. Conclusion 47

2.5. References 49

CHAPTER 3: THREE-PARAMETER VISCO-ELASTIC FOUNDATION MODEL OF ADHESIVELY BONDED JOINTS PART I: SINGLE-LAP JOINTS……....51

Abstract 51

3.1. Introduction 52

3.2. Three-parameter viscoelastic foundation model (3PVF) 54

3.2.1. Asymmetric single-lap joint 55

3.2.2. Symmetric single-lap joint 67

3.3. Verification and comparisons 71

3.3.1. Asymmetric single-lap joint 73

3.3.2. Symmetric single-lap joint 77

3.4. Conclusion 79

3.5. References 80

CHAPTER 4: THREE-PARAMETER VISCO-ELASTIC FOUNDATION MODEL OF ADHESIVELY BONDED JOINTS PART II: DOUBLE-LAP JOINTS…..……83

Abstract 83

4.1. Introduction 84

4.2. Three-parameter viscoelastic foundation model for double-lap joints 85

4.3. Verification and parametric studies 98

4.4. Conclusions 105

4.5. References 106

CHAPTER 5: SUBCRITICAL DEBONDING OF FRP-TO-CONCRETE BONDED INTERFACE UNDER SYNERGISTIC EFFECT OF LOAD, MOISTURE, AND TEMPERATURE 108

Abstract 108

5.1. Introduction 109

5.1.1. Environment-assisted subcritical debonding of the FRP-to-concrete interface 110

5.1.2. Enhance durability of the FRP-to-concrete interface using silane coupling agent 115

5.2. Materials and testing 117

5.2.1. Specimen manufacturing 117

5.2.2. Application of the silane coupling agent 120

5.2.3. Experiment setup 121

5.2.4. Testing plan 124

5.3. Testing results and discussions 125

5.3.1. EASD testing of the CFRP-to-concrete bonded interface at 23.9°C 125

5.3.2. EASD testing of the CFRP-to-concrete bonded interface at 32.2°C (90°F) 129

5.3.3. EASD of FRP-to- concrete interface at 43.3°C (110°F) 131

5.3.4. Fitting the EASD testing results 133

5.3.5. Discussions 135

5.3.5.1. Failure mode of EASD 135

5.3.5.2. Effect of silane treatment on the moisture resistance of the interface 137

5.3.5.3. Swelling of the epoxy 139

5.4. Conclusions 140

5.5. References 141

CHAPTER 6: CRITICAL DEBONDING OF FRP-TO-CONCRETE INTERFACE……145

Abstract 145

6.1. Introduction 146

6.2. Research scopes and organization 148

6.3. Materials and testing 148

6.3.1. Fracture toughness of the CFRP-to-concrete specimens conditioned in water 150

6.3.1.1. Experimental set-up 150

6.3.1.2. Wedge driving test 151

6.3.1.3. Pulling test 152

6.3.1.4. Moisture diffusion simulation 153

6.3.1.5. Testing plan 156

6.4. Testing results and discussion 157

6.4.1. Wedge driving and pulling tests 157

6.4.2. Moisture diffusion simulation 160

6.5. Conclusions 167

6.6. References 168

CHAPTER 7: DIRECT MEASUREMENT OF TRACTION-SEPARATION LAW OF CONCRETE/EPOXY INTERFACES SUBJECTED TO MOISTURE ATTACK UNDER MODE-I LOADING……173

Abstract 173

7.1. Introduction 174

7.2. Materials and testing 178

7.2.1. Wedge splitting test 178

7.2.2. Crack opening displacement (COD) measurement using DIC 181

7.2.3. Testing plan 182

7.2.4. Direct measurement of the traction-separation law and fracture toughness under mode-I loading 182
7.3. Conclusions 192
7.4. References 193
CHAPTER 8: INTRINSIC DEBONDING OF FRP-TO-CONCRETE INTERFACE……...197
Abstract 197
8.1. Introduction 198
8.2. Specimen design 200
8.3. Materials and testing method 204
8.4. Testing results and discussion 208
8.4.1. Wedge driving test 208
8.4.2. Interface relative humidity within the epoxy-concrete interface 212
8.5. Conclusions 218
8.6. References 219
CHAPTER 9: SUMMARY, CONCLUSIONS AND FUTURE WORKS…….222
9.1. Summary 222
9.2. Conclusions 225
9.3. Public impacts 226
9.4. Future works 226
REFERENCES……229

LIST OF TABLES

Table 2-1: Geometrical parameters of the double-lap joint 40

Table 2-2: Mechanical properties of the materials of the joint 40

Table 3-1: Geometrical parameters of the single-lap joint 72

Table 3-2: Mechanical properties of the single-lap joint 72

Table 4-1: Geometrical parameters of the double-lap joint 99

Table 4-2: Mechanical properties of the materials of the joint 99

Table 5-1: Mechanical properties of CFRP 119

Table 5-2: Mechanical properties of Epoxy.....119

Table 5-3: Data fitting parameters based on Eq. (6) 134

Table 6-1: Mechanical properties of CFRP 150

Table 6-2: Mechanical properties of Epoxy..... 150

Table 6-3: Experimental diffusivities of materials used in fracture toughness tests 162

Table 6-4: Parameters of the relationship between the fracture energy and the I_{RH} 167

Table 7-1: Tri-linear traction-separation law parameters 188

Table 8-1: Mechanical properties of CFRP 206

Table 8-2: Mechanical properties of the epoxy 206

Table 8-3: Parameters of the relationship between the fracture energy and the I_{RH} …..216

LIST OF FIGURES

Fig. 1-1: FRP plating techniques: (a) EB, (b) NSM 2

Fig. 1-2: Possible mechanisms of FRP-to-concrete bond failure 3

Fig. 1-3: Early single-lap bonded joint models a) Volkersen 1-D bar model b) G-R 1-D beam model 4

Fig. 1-4: Tsai, Oplinger, and Morton modified single-lap joint model: (a) modified 1-D bar model, (b) modified 1-D beam model 5

Fig. 1-5: The shear, peel and longitudinal normal stresses distributions using HODT: (a) middle surface of the adhesive layer, (b) adhesive-adherend interface..... 6

Fig. 1-6: Double-lap bonded joint models a) Volkersen/de Bruyne 1-D bar model b) Tsai, Oplinger, and Morton modified 1-D bar model 7

Fig. 1-7: Delale and Erdogan adhesive layer model and the Voigt- SLS rheological model..... 8

Fig. 1-8: Brinson symmetric lap shear specimen and the modified Bingham model. 9

Fig. 1-9: Mirman and Knecht Free body diagram of two-layered bonded beam 9

Fig. 1-10: Modified Maxwell SLS model..... 10

Fig. 1-11: Existing flexural testing techniques: (a) strength based testing method, (b) fracture based testing method 11

Fig. 1-12: CB specimen under peel force and crack growth rate vs. applied force for glass 12

Fig. 1-13: Schematic illustration of environment-assisted debond 13

Fig. 1-14: Tapered double cantilever aluminum/epoxy specimen and the environment-assisted subcritical debonding for different relative humidity levels 14

Fig. 1-15: Wedge driving test specimen and comparison between environment-assisted subcritical debonding in ambient condition and different aqueous conditions 15

Fig. 1-16: Actual debonding configuration and peel and shear specimens 18

Fig. 1-17: Peel and shear fracture toughness for specimens conditioned in water 18

Fig. 1-18: Comparison between fracture toughness of ingress and reversal specimens conditioned at room temperature: (a) peel test, (b) shear test 19

Fig. 1-19: Epoxy-concrete beam sandwich specimen and Interface fracture toughness variation with moisture content 19

Fig. 1-20: Relative humidity contour and interface region relative humidity at different transverse locations versus immersion time 21

Fig. 1-21: Empirical relationship between fracture toughness and interface moisture content: (a) peel fracture specimens, (b) shear fracture specimens 22

Fig. 2-1: Simply supported double-lap joint beam geometry 30

Fig. 2-2: Free body diagram of the assumed quadrant shown in Fig. 2-1(b) 31

Fig. 2-3: A three-parameter elastic foundation model 33

Fig. 2-4: Comparison of the present model with FEA, experimental and analytical (TOM) results obtained by Tsai and Morton 39

Fig. 2-5: FEA model of a simply supported double-lap joint under axial tension with a close illustration of the lower-left corner meshing 40

Fig. 2-6: Comparison the shear stress distribution obtained by the present solution and that by the FEA for different thicknesses of the adhesive layer. 41

Fig. 2-7: Comparison the peel stresses along two interfaces obtained by the present analytical model and that by the FEA for different thicknesses of the adhesive layer 42

Fig. 2-8: Shear stress distribution of the adhesive layer of double-lap joints with different thicknesses: (a) shear stress distribution along the whole adhesive layer, (b) shear stress at the very left end of the adhesive layer, (c) shear stress at the very right end of the adhesive layer 43

Fig. 2-9: Peel stress distribution along the inner interface of the double-lap joints: (a) peel stress distribution along the whole inner interface, (b) peel stress at the very left end the interface, (c) peel stress at the very right end of the interface 44

Fig. 2-10: Peel stress distribution along the outer interface of the double lap joints: (a) peel stress distribution along the whole interface, (b) peel stress at the very left end of the interface, (c) peel stress at the very right end of the interface 46

Fig. 2-11: Typical failure modes of a double-lap joint under tensile force: (a) shear failure, (b) tensile failure, (c) mixed tensile and shear failure for a unidirectional model ([0]16). 48

Fig. 3-1: A simply supported single-lap joint 55

Fig. 3-2: Free body diagram of the adhesively bonded single-lap joint 56

Fig. 3-3: Deformation model of the adhesive layer: (a) stress equilibrium of the adhesive layer, (b) deformation model of the adhesive layer 57

Fig. 3-4: Standard Linear Solid Model 59

Fig. 3-5: Finite element model of (a) simply supported single-lap joint under axial tension, (b) close illustration of the lower-left corner 72

Fig. 3-6: Comparison the 3PVF model with the FEA on shear stress distribution in an asymmetric single-lap joint 73

Fig. 3-7: Time-dependent shear stress distribution of the asymmetric single-lap joint in the adhesive layer: (a) shear stress distribution along the whole interface, (b) shear stress at the very left edge of the adhesive layer, (c) shear stress at the very right edge of the adhesive layer. 75

Fig. 3-8: Time-dependent peel stress distribution of the asymmetric single-lap joint along the top interface: (a) peel stress distribution along the whole interface, (b) peel stress at the very left edge of the interface, (c) peel stress at the very right edge of the interface 76

Fig. 3-9: Time-dependent peel stress distribution of the asymmetric single-lap joint along the bottom interface: (a) peel stress distribution along the whole interface, (b) peel stress at the very left edge of the interface, (c) peel stress at the very right edge of the interface 77

Fig. 3-10: Comparison between the 3PVF model and FEA on shear stress distribution within the adhesive layer of the symmetric single-lap joint 78

Fig. 3-11: Comparison between the 3PVF model and FEA on peel stress distribution along two adherend/adhesive interfaces of the symmetric single-lap joint 79

Fig. 4-1: A simply supported double-lap joint 86

Fig. 4-2: Free body diagram of the assumed quadrant shown in Fig. 4-1(b) 88

Fig. 4-3: Deformation model of the adhesive layer: (a) stress equilibrium of the adhesive layer, (b) deformation model of the adhesive layer 89

Fig. 4-4: Standard Linear Solid Model 91

Fig. 4-5: Finite element model of a simply supported double-lap joint under tension. 99

Fig. 4-6: Comparison of shear stress in the adhesive layer of the double-lap joint obtained by the present 3PVF model and FEA 100

Fig. 4-7: Comparison of the peel stresses in the double-lap joint obtained by the present model and the FEA. 101

Fig. 4-8: Time-dependent shear stress within the adhesive layer of the double-lap joint: (a) Shear stress distribution along the whole interface, (b) shear stress at the very left edge of the adhesive layer, (c) shear stress at the very right edge of the adhesive layer. 102

Fig. 4-9: Time-dependent peel stress along the inner surface of the double-lap joint: (a) Peel stress distribution along the whole inner interface, (b) peel stress at the very left edge of the interface, (c) peel stress at the very right edge of the interface 104

Fig. 4-10: Time-dependent normal stress distribution of the double-lap joint along the interface between outer adherend and adhesive layer a) Total normal stress distribution b) normal stress at the very left edge of the interface c) normal stress at the very right edge of the interface 105

Fig. 5-1 Reaction of water with a strained crack tip bond to propagate the crack at the driving forces below the critical fracture energy 112

Fig. 5-2: Crack growth velocity as a function the strain energy release rate. 112

Fig. 5-3: Schematic of covalent bonds and water attack at adhesive to concrete interface treated with silane coupling agent 117

Fig. 5-4: Testing specimen.....118

Fig. 5-5: Testing set-up 122

Fig. 5-6: Comparison of crack length determined by the indirect method using a strain gauge and the direct method using a digital microscope for a specimen without silane treatment tested in water at 23.9°C.....124

Fig. 5-7: Crack grows with time at 23.9°C: (a) in tap water and in air with different relative humidity levels, (b) Close-up of crack growing at different relative humidity levels.126

Fig. 5-8: Subcritical debonding of interface at 23.9°C: (a) in tap water and at different relative humidity levels, (b) in air with different relative humidity levels.....128

Fig. 5-9: Crack grows with time at different relative humidity levels at 32.2°C.....130

Fig. 5-10: Subcritical debonding of the FRP-to-concrete joints at 32.2°C.....130

Fig. 5-11: Crack length with time at 43.3°C: (a) Long-term results, (b) at the beginning of the test.....132

Fig. 5-12: Subcritical debonding of FRP-to-concrete joint at 43.3°C 133

Fig. 5-13: Fitting curves of subcritical debonding under synergistic effect of mechanical loads, moisture, and temperature 135

Fig. 5-14: Debonded epoxy side of the tested specimens 137

Fig. 5-15: water-induced damage in epoxy-concrete interface untreated with silane: (a) SEM image of interface crack induced by soaking in water for 7 days, (b) C mapping of the interface, (c) O mapping of the interface 138

Fig. 5-16: water-induced damage in epoxy-concrete interface treated with silane: (a) SEM image of interface crack induced by soaking in water for 7 days, (b) C mapping of the interface, (c) O mapping of the interface 139

Fig. 5-17: Swelling of the epoxy layer subjected to 43.3°C and RH of 65%: (a) before testing, (b) one hour after testing 140

Fig. 6-1: Wedge driving test specimen 149

Fig. 6-2: Pulling test specimen 150

Fig. 6-3: Experimental set-up for fracture toughness tests of CFRP-to-concrete specimens 151

Fig. 6-4: Specimens setup: (a) the wedge driving test setup, (b) the pulling test setup 152

Fig. 6-5: Calculation of the mode-II fracture energy release rate from the pulling test 153

Fig. 6-6: Schematic illustration of the water diffusion from the CFRP-to-concrete bond towards the epoxy-concrete interface 154

Fig. 6-7: Samples used in water absorption test: (a) epoxy sample, (b) CFRP sample, (c) Concrete sample 155

Fig. 6-8: Effect of water conditioning, duration and being wet or dry at the time of test, on mode-I fracture toughness of untreated or treated specimens with silane coupling agent 158

Fig. 6-9: Effect of water conditioning on mode-II fracture energy release rate for untreated or treated specimens with silane coupling agent 159

Fig. 6-10: Debonded epoxy side of the tested specimens under mode-I loading 160

Fig. 6-11: Experimental and Fickian absorption model for (a) CFRP, (b) Epoxy, (c) Concrete at room temperature (23°C) 161

Fig. 6-12: FEA model used for moisture diffusion along the epoxy-concrete interface 162

Fig. 6-13: Relative humidity contour versus immersion time: (a) 1-month transverse section, (b) 3-month transverse section, (c) 6-month transverse 164

Fig. 6-14: Relative humidity contour versus immersion: (a) 1-month longitudinal section, (b) 3-month longitudinal section, (c) 6-month longitudinal section 164

Fig. 6-15: Interface relative humidity along the epoxy-concrete interface: (a) Transverse section, (b) Longitudinal section 165

Fig. 6-16: The relationship between the fracture energy release rate and the average interface relative humidity along the epoxy-concrete interface: (a) Mode-I fracture, (b) Mode-II fracture 166

Fig. 7-1: Geometry of the wedge splitting test specimen 179

Fig. 7-2: Wedge splitting test: (a) Testing set-up, (b) Free-body diagram of the wedge.....180

Fig. 7-3: Pattern, displacements, and discrete functions used in DIC 182

Fig. 7-4: Free-body diagram of the half specimen.....185

Fig. 7-5: Splitting load versus COD measured at the crack mouth (δ) for a specimen conditioned in water for 16 weeks.....186

Fig. 7-6: Measured traction- separation law of the epoxy-concrete interface under mode-I for a specimen conditioned in water for 8 weeks.....187

Fig. 7-7: Tri-linear traction-separation model for the concrete/epoxy interface under mode-I loading 188

Fig. 7-8: Tri-linear traction-separation laws measured for concrete/epoxy interface after conditioning in water: (a) effect of conditioning in water on the traction-separation law, (b) effect of silane on the traction-separation law of the interface after conditioning in water, (c) effect of water conditioning on the stiffness of the concrete/epoxy interface.....190

Fig. 7-9: Effect of duration of water conditioning on the fracture energy of the concrete/epoxy interface with and without silane coupling agent.....191

Fig. 7-10: Debonded epoxy sides of wedge splitting test specimens 192

Fig. 8-1: FEA model (50.8 X 50.8 X 50.8 mm^3) for evaluation of water level on relative humidity along the epoxy-concrete interface: (a) Specimens size: 50.8 X 50.8 X 50.8 mm3, (b) Specimens size 50.8 X 50.8 X 25.4 mm^3 201

Fig. 8-2: Interface relative humidity along the epoxy-concrete interface exposed to different water levels: (a) after 1 week, (b) after 16 weeks.....203

Fig. 8-3: Interface relative humidity along the epoxy-concrete interface of the specimen with 25.4 mm thickness concrete block and exposed to 50% water level.....204

Fig. 8-4: Intrinsic debonding test specimen.....205

Fig. 8-5: Test set-up for intrinsic debonding tests 207

Fig. 8-6: Specimens for intrinsic debonding test 207

Fig. 8-7: Effect of water conditioning duration on intrinsic debonding fracture release rate for untreated or treated specimens with silane coupling agent. 210

Fig. 8-8: Debonded CFRP side of the intrinsic tested specimens: (a) control specimen, (b) 4 weeks in water (untreated), (c) 4 weeks in water (treated), (d) 8 weeks in water (untreated), (e) 8 weeks in water (treated), (f) 16 weeks in water (untreated), (g) 16 weeks in water (treated).....211

Fig. 8-9: FEA model used for moisture diffusion along the epoxy-concrete interface in an intrinsic debonding test.....212

Fig. 8-10 Relative humidity contour versus immersion time in an intrinsic debonding test: (a) 4-week longitudinal section, (b) 8-week longitudinal section, (c) 16-week longitudinal section.....213

Fig. 8-11: Relative humidity contour versus immersion time in an intrinsic debonding test: (a) 4-week longitudinal section, (b) 8-week longitudinal section, (c) 16-week longitudinal section.....213

Fig. 8-12: Interface relative humidity along the epoxy-concrete interface for an intrinsic test: (a) Transverse section, (b) Longitudinal section 1 214

Fig. 8-13: The relationship between the fracture energy release rate and the average I_{RH} along the epoxy-concrete interface for an intrinsic debonding test 1.....215

Fig. 8-14: Comparison between the intrinsic and extrinsic debonding fracture energy release rate versus I_{RH} along the epoxy-concrete interface: (a) at lower I_{RH}, (b) at higher I_{RH} 217

CHAPTER 1

INTRODUCTION

1.1. Background and necessity of the research

The need for safe, effective, and efficient methods to strengthen and upgrade our nation's infrastructure is clear. ASCE's 2013 Report Card for America's Infrastructure estimates that the U.S. would necessitate to spend $3.6 trillion on aging infrastructures by 2020[1]. Based on the Bureau of Transportation Statistics (2008), around 15,200 out of 600,000 bridges throughout the country are either structurally deficient or functionally obsolete (about 25%) [2]. Replacing all these bridges is a huge burden on the economy, therefore rehabilitation and retrofitting of damaged structural and non-structural members can be presumed as the most effective way in this matter.

Fiber reinforced polymer (FRP) composites have emerged as important structural materials in the last three decades. FRP composites are in different shapes, manufactured by various techniques and of diverse materials. Usually FRP composite are defined as a combination of fibers (unidirectional, woven, etc.) and a resin matrix. Resin matrices are generally made of organic adhesives and are used to protect fibers, align and distribute stresses among them [15]. Common fibers available in market are classified in three groups: glass, aramid and carbon. Among their many applications in civil infrastructure, retrofitting/rehabilitating reinforced concrete structures is most popular with many advantages of FRP such as high corrosion resistance, high strength-to-weight ratio, and easy of handling [3]–[14]. In this application, FRP plates/fabrics/strips are either externally bonded (EB), or near-

surface mounted (NSM) on concrete structures through structural adhesives to strengthen the existing structures (Fig. 1-1) [5]–[14], [16]–[21]. To improve the strengthening efficiency, prestress can be applied to FRP. This technique has evolved into one of primary techniques to address the deterioration of nation's infrastructure system due to natural extreme events, excessive use, and intentional attacks.

A FRP-to-concrete adhesively bonded joint is formed when FRP is externally bonded to the concrete, which consists of a FRP plate, a host concrete section, and a thin adhesive (mostly a type of epoxy). A large body of testing results show that debond along the FRP-to-concrete interface is one of the most common failure modes of the FRP-strengthened concrete structures. Here the FRP-to-concrete interface refers to a small interphase zone between FRP and concrete, including adhesive, a thin layer of concrete adjacent to adhesive and the adhesive/concrete interface. This interface plays a critical role in the integrity and durability of the structure. Any failure of this interface can result in pre-mature of the joint, leading to failure of the structure. So far, a large number of studies have been conducted on the short-term behavior of this FRP-to-concrete interface [23]. Very limited studies have been conducted on the long-term durability of this interface [24]–[30]. A number of critical questions regarding the long-term durability of the FRP-to-concrete interface still remain unaddressed, hampering the widespread usage of the FRP external bonding technique [31]–[33].

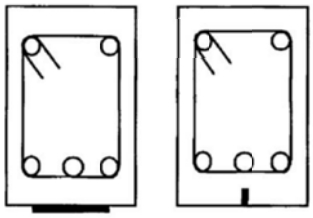

Fig. 1-1 FRP plating techniques a) EB b) NSM [21].

Five failure modes have been identified for the FRP-to-concrete interface in the literature. Debonding can occur either within the FRP, the epoxy, or the concrete, or along the interface between the epoxy and the FRP, or the one between the epoxy and concrete. [34] (Fig. 1-2).

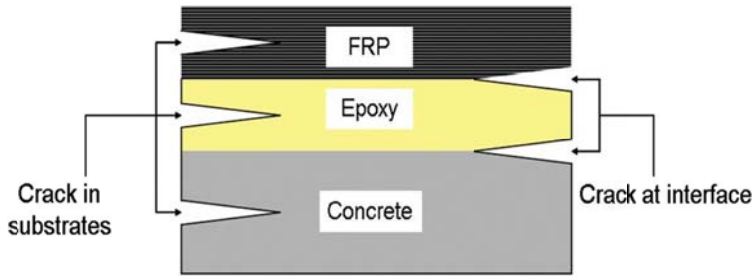

Fig. 1-2 Possible mechanisms of FRP-to-concrete bond failure [34].

1.2. Analytical studies on adhesively bonded joints

1.2.1. Interface stress analysis

FRP externally strengthened structures can be modeled as adhesively bonded joints, which have been largely used in different industrial fields such as automotive, aerospace, and construction. These joints connecting two structural adherends using a layer of adhesive provide a uniform connection between adherends and avoid stress concentrations due to techniques such as riveting [36]. In addition, adhesively bonded joints are less time-consuming, easy to execute and enjoy reliable corrosion resistance [15]; nevertheless, the pre-mature failure of the bond raises some doubts concerning its viability. Extensive studies have been carried out to analyze the stresses within the bond using numerical or analytical methods. Finite element analysis (FEA) techniques are the most widely used numerical method to analyze the adhesively bonded joints. Although the numerical method can predict stresses in the joints with high accuracy, it is time consuming and lacks of flexibility. In this sense, closed-form analytical solution is more desirable and therefore, attracts the attentions from many researchers.

1.2.1.1. Adhesively bonded single-lap joints

Volekrsen (1938) presented a simple model for a mechanical joint with a number of fasteners connecting rigid unidirectional bars (Fig. 1-3(a)) [37], which is unable to account for the flexural and the shear deformations of an adhesively bonded joints. In 1944, Goland and Reissner [38] proposed a new model (G-R) for adhesively bonded single-lap joints. It models the adhesive layer as a series of uniformly distributed shear and vertical springs. This model can take both the shear and flexural deformations into consideration. Since no interaction between the shear and the vertical springs is considered, the G-R model essentially models the adhesive layer as a two-parameter elastic foundation (2PEF) (Fig. 1-3(b)). Therefore, the G-R model is also referred to 2PEF model in this study, based on which, a number of new modified or refined models have been proposed to analyze the stresses in the adhesively bonded joints [39]–[49].

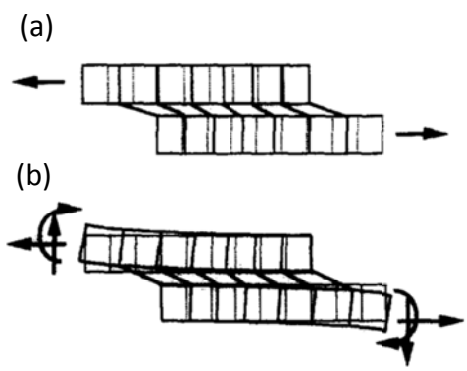

Fig. 1-3 Early single-lap bonded joint models: (a) Volkersen 1-D bar model, (b) G-R 1-D beam model [49].

Tsai, Oplinger, and Morton modified the G-R model by including the adherend shear deformations and assuming a linear distribution of shear stress through the thickness of the adherend. (TOM model, Fig. 1-4) [49]. Tong considered non-linear behavior of the adhesive to formulate the governing equation for a sing-lap joint [48].

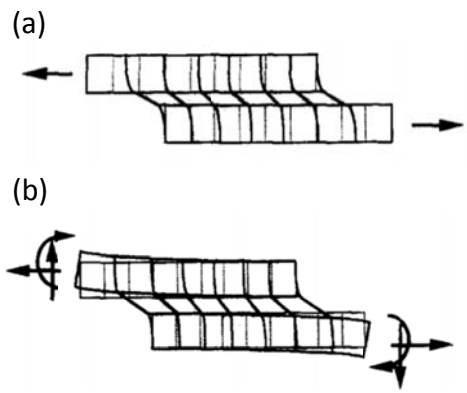

Fig. 1-4 Tsai, Oplinger, and Morton modified single-lap joint model: (a) modified 1-D bar model, (b) modified 1-D beam model [49].

Martensen and Thomsen also considered the inelastic and non-linear behaviors of the adhesive and proposed a non-linear formulation for single-lap joints with a modified von Mises criterion and a secant modulus approach for the effective stress–strain relationship of the adhesive [50].

Luo and Teng, in an effort to modify G-R model for thick adherends, proposed a model in which linear variation of the displacement components through the adhesive thickness is determined by using a higher order displacement theory (HODT) [40]. This model was able to predict shear, peel, and longitudinal stress distribution along the interface, particularly close to the ends. It was concluded that the adhesive longitudinal normal stress is considerably larger compared with the peel and shear stresses and should be included in the interface stress analysis in case of having a thick adhesive layer (Fig. 1-5).

Although most of the 2PEF models can successfully predict the stress distributions within the adhesively bonded joints with acceptable accuracy, they suffer from a few flaws. First, 2PEF model cannot satisfy zero-shear stress boundary condition at the free edge of the adhesive layer, as pointed out by Delale et al. [51] The 2PEF model predicts the maximum shear stresses at the free edges of the adhesive; while free edge boundary conditions requires this shear stress to be

zero. Second, the 2PEF model assumes that peel stress through the adhesive layer is a constant; while many studies showed that the peel stresses along the two interfaces between the adhesive and the adherends are different, particularly at the edges near the end of the interface [52].

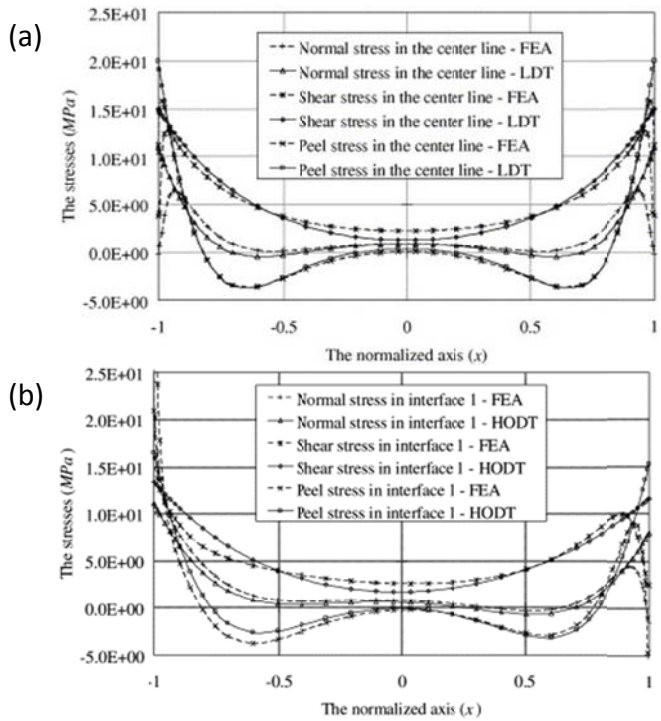

Fig. 1-5 The shear, peel and longitudinal normal stresses distributions using HODT: (a) middle surface of the adhesive layer, (b) adhesive-adherend interface [40].

To overcome the weaknesses of 2PEF models, many efforts have been made to model the adhesive layer as a continuum [53]–[59]. These models are able to satisfy the zero-shear stress boundary and capture two different peel stresses along two interfaces. However, lack of closed-from solutions made them relatively complicated and difficult to use [60].

To overcome these difficulties, Wang and Zhang proposed a three-parameter elastic foundation (3PEF) model for a single-lap joint considering two dissimilar normal stress functions for each interface. This model can satisfy all boundary conditions and the force equilibrium in the adhesive layer [61].

1.2.1.2. Adhesively bonded double-lap joints

Adhesively bonded double-lap joints, as shown in Fig. 1-6 are other popular lap joints. One advantage of these joints over the single-lap ones is that both connecting adherends are concentric. In other words, this joint can retain the geometric properties of the adherend before the connection and keep it unchanged after the joint. This is not true for the single-lap joints where the distance between two connecting adherends generates a local bending moment at the bond.

A number of analytical solutions have been proposed for the double-lap joint by modifying the 2PEF model for the single-lap joints, (Fig. 1-6) [39], [42], [43], [49], [62]–[66]. However, these existing solutions suffer from an inherent drawback that the existence of the peel stress along the adhesive layer is ignored.

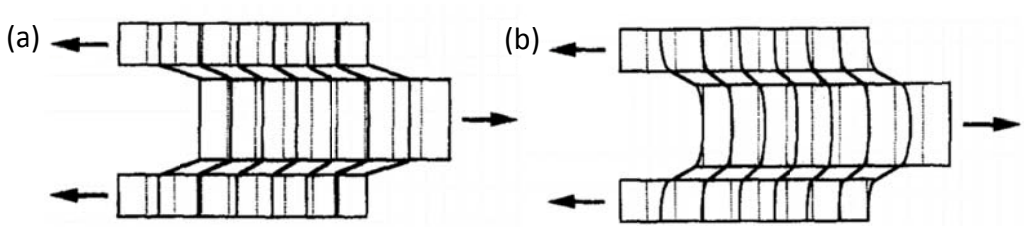

Fig. 1-6 Double-lap bonded joint models (a) Volkersen/de Bruyne 1-D bar model, (b) Tsai, Oplinger, and Morton modified 1-D bar model [49].

1.2.2. Viscoelastic analysis

1.2.2.1. Viscoelastic stress analysis of adhesively bonded joints

Epoxy adhesive is a viscoelastic material and its properties changes with time under loading. In fact, epoxy starts viscoelastic behavior just after curing, affecting the stress and strain distributions on the high stress concentration regions [67]–[72]. This phenomenon has been observed in a large number of studies conducted on adhesively bonded joints [73]–[90]. Various studies on the long-term behavior of the adhesively bonded joints have already proved that the maximum peel and shear stresses close to the edges can be significantly reduced and alleviated

due to viscoelastic behavior of the adhesive. Some of the researchers used quasi-static solution of bulk materials [91], but many others developed rheological solutions based on classic viscoelastic models such as Maxwell, Kelvin-Voigt and Burgers.

Maxwell and Kelvin-Voigt models are not suitable for the epoxy adhesives. Given that the Maxwell model uses the linear relation with time, it overestimates the long-term deformation. On the other hand, Kelvin model is unable to capture the instantaneous deformation [79]. Delale and Erodgan presented a closed-from viscoelastic solution for a symmetric single-lap joint [72] by modeling the adhesive layer as a three Voigt-Standard Linear Solid (SLS) model (Fig. 1-7). They considered a linear adhesive layer with two identical adherend. The adhesive strain tensor was decomposed into one hydrostatic component and one deviatoric component. Only the latter one was used in analysis based on the experimental studies. The final governing equation was given after solving some complicated differential equations and using Laplace transform technique. Although this analytical model can provide time-dependent solutions for the shear stress and an identical normal stress along the adhesive layer, it is unable to provide closed form solution for general joints.

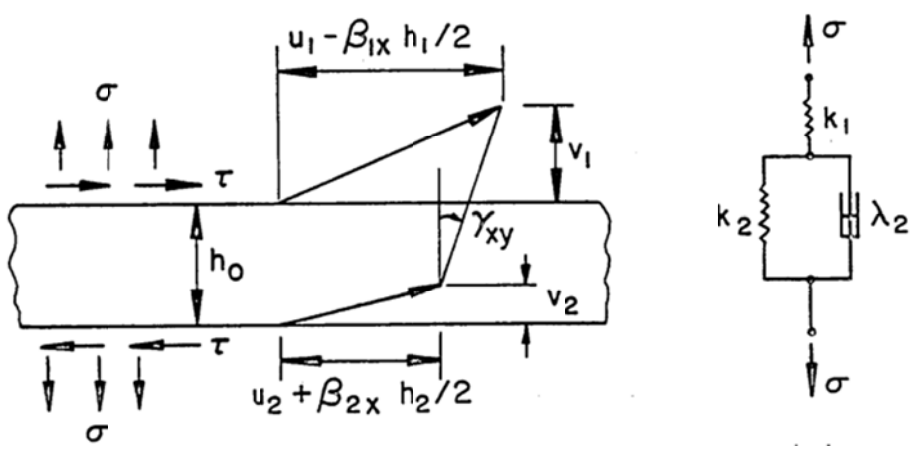

Fig. 1-7 Delale and Erdogan adhesive layer model and the Voigt- SLS rheological model [72].

Brinson adopted a modified Bingham model and used it to solve a linear-viscoelastic problem of a symmetric lap shear specimen (Fig. 1-8) [70]. The model correlated the long-term viscoelastic behavior of the joint to the bulk adhesive properties. Shishesaz and Reza employed the same rheological three-parameter model for a single-lap joint. However, the effect of bending of the joint is ignored and only the shear stress was obtained[89].

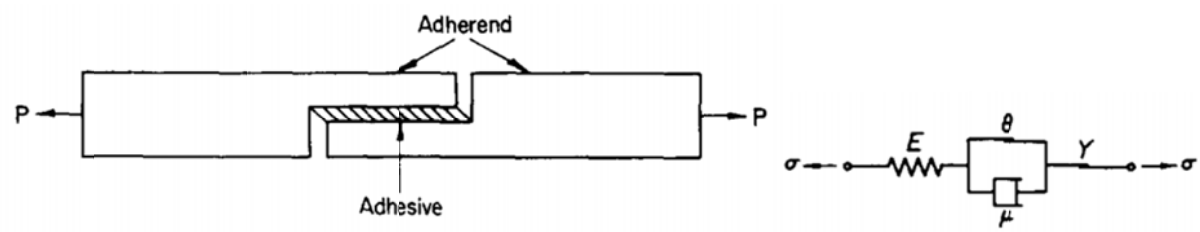

Fig. 1-8 Brinson symmetric lap shear specimen and the modified Bingham model [70].

Mirman and Knecht proposed an analytical solution using Maxwell's creep law for bi-material assembly, particularly for the electronic packaging applications [68]. Their results reached good agreement with the FEA; however, the adhesive deformation was ignored in the analysis and only the maximum peel stress was considered in calculations (Fig. 1-9).

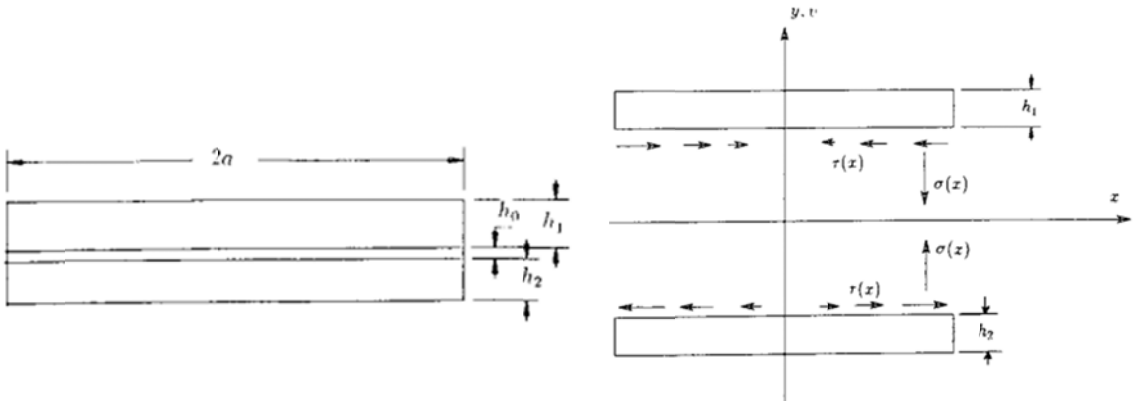

Fig. 1-9 Mirman and Knecht Free body diagram of two-layered bonded beam [68]

Meshgin et al. tested some FRP-to-concrete adhesively bonded joints under sustained shear stress for up to nine months to investigate the long-term behavior of the epoxy adhesive using a double-shear test setup [79]. Three primary parameters including the ratio of sustained shear stress to ultimate shear strength, the time-before-loading and the thickness of the epoxy

adhesive layer were considered. Based on the experimental observations, two rheological models (Findley and Maxwell SLS) were proposed for the creep behavior of the epoxy. They demonstrated that the modified Maxwell SLS (Fig. 1-10) can properly simulate the long-term creep behavior of the epoxy adhesive.

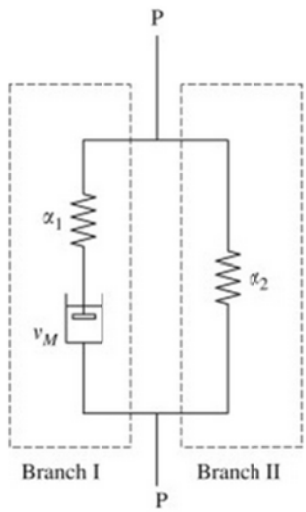

Fig. 1-10 Modified Maxwell SLS model [79]

Zhang and Wang employed the SLS model proposed by Meshgin et al. to develop a three-parameter foundation model to study the long-term characteristics of the FRP-to-concrete joints. A closed-form solution for interface stresses, resultant forces, the deflections and rotations were developed which showed a good agreement with numerical analysis.

1.3. Experimental studies on durability of FRP-to-concrete adhesively bonded joints

Numerous experimental studies have showed that the foremost cause for pre-mature failure of FRP strengthened structures is debonding of the FRP-to-concrete interface [35]. Two testing methods are available to evaluate the strength of the FRP-to-concrete interface: strength-based and fracture toughness–based methods [24], [27], [30], [116]–[120] (Fig. 1-11). In the former method, the maximum debonding load is recorded as the strength of the interface; while in the latter method, the fracture toughness G_c which is the energy release rate at catastrophic

failure of the interface, is obtained as the strength of the interface. Debond as defined by RILEM is “a gradual process where slow growth of cracks occurs at the interface”. This type of slow cracks, which grows at very slow rate and under much smaller energy than the critical energy release rate, only can occur and propagate if environmental conditions exist and assist the separation [121]. In fact, the catastrophic debonding at the critical energy release rate, is only the final stage of a long-term crack propagation process which has been started early because of the synergistic effect of debonding loads and environment conditions. So far, most studies have been focused on the short-term catastrophic failure of the interface. Few efforts have been made to investigate the long-time durability and very slow crack propagation within the FRP-to-concrete interface under aggressive environments.

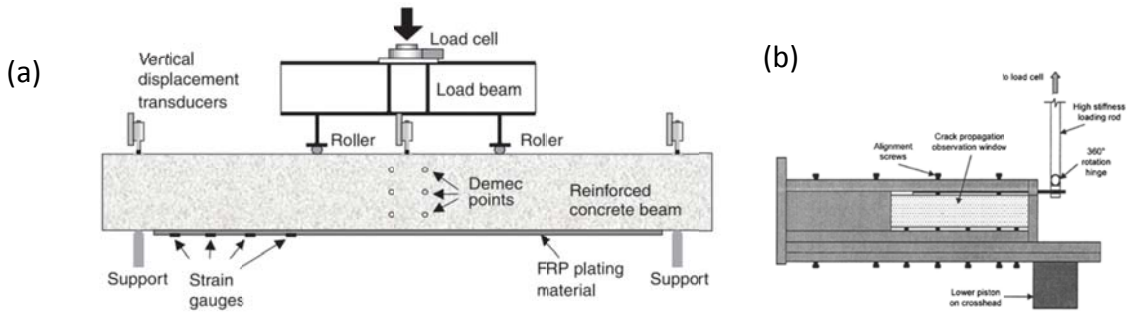

Fig. 1-11 Existing flexural testing techniques: (a) strength based testing method [118], (b) fracture based testing method [30].

1.3.1. Subcritical debonding of the FRP-to-concrete interface

In comparison with the critical debonding, the very slow crack propagation in presence of aggressive environment and under a load lower than the catastrophic failure load of the interface is called environment-assisted subcritical debonding (EASD) [122]–[128]. Existing works imply that the EASD can be defined as synergistic interaction between the chemical bonds between the adhesive and the adherend and the aggressive environment.

Wiederhorn et al., for the first time, termed subcritical crack growth after studying on bulk ceramic materials such as soda-lime-silica glass and sapphire [122]. They applied constant

force to the ends of the two arms of a cantilever beam specimen (DCB) under different environments (Fig. 1-12). Crack growth rate was measured as a function of applied load in gaseous nitrogen at 25°C and distilled water at temperatures of 2°C, 25°C, 43°C and 90°C. Results obtained from the subcritical test showed two stages in glass fracture: a prior stage with slow crack propagation and a catastrophic stage with rapid crack growth. Two distinct regions, region I exponentially dependent on the applied force and region II which is almost plateau, were obvious clear in the prior stage.

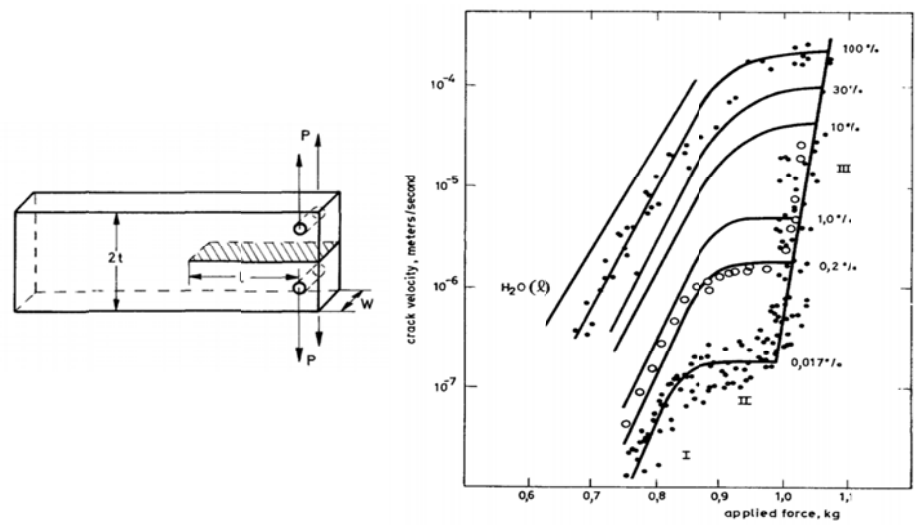

Fig. 1-12 DCB specimen under peel force and crack growth rate vs. applied force for glass [122].

As illustrated in Fig. 1-13, In Region I, the debond growth is so slow that the environmental species have enough time to transport to the crack tip to enable the environmental attack mechanism to occur readily. As a result, the debond growth rate is dependent on both the reaction rate and the mechanical load *G*. In Region II, the debond growth is faster so that the debond growth rate is controlled by the availability of the environmental species. As a result, the debond growth rate is almost independent of the mechanical load *G*.

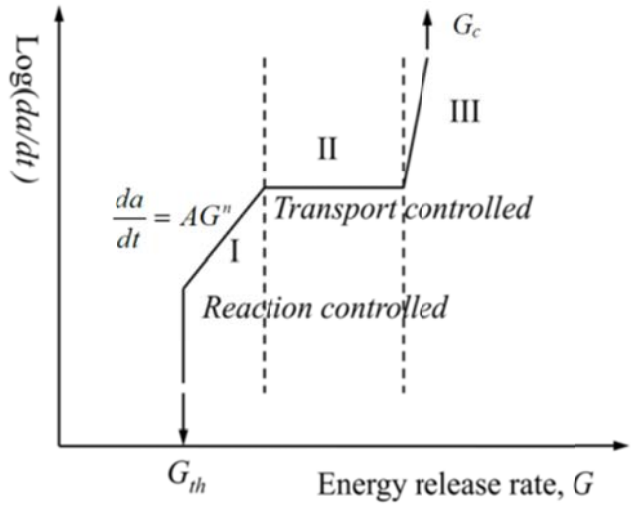

Fig. 1-13 Schematic illustration of environment-assisted debond [15].

Very few studies have been carried out to examine the EASD in adhesively bonded joints. Mostovoy and Ripling et al. experimentally investigated EASD of contoured double cantilever beam adhesive specimens (tapered aluminum/epoxy sandwich beam) under long-time static loading in liquid water or a humid atmosphere [129]–[131] (Fig. 1-14). They observed a threshold (G_{th}) much smaller than G_c which is dependent on the relative humidity and the type of the adhesive. They also found that the threshold value decreases when humidity level increases. However, this observation of having a specific threshold was questioned by Kinloch [132]. Kinloch and his team later conducted some studies on metallic joints, bonded with a rubber-toughened epoxy adhesive and under monotonic loads in different relative humidity levels and in water [133], [134]. In their studies, they distinguished three different regions, as given in Fig. 1-13, and concluded that different mechanisms can be observed under different environmental conditions.

Although very slow crack propagation at proportionally smaller loads has been observed in a few debonding tests of the FRP-to-concrete interfaces ; this subcritical debonding or delayed failure was attributed to the viscosity of adhesive, the creep or other unexpected reasons [75], [79], [135], [136]. Kinloch et al. recognized the EASD in their study on adhesively bonded joints

and suggested that the environmental conditions should be considered as an important factor and instead of focusing more on the adhesive layer[133]. Although metal adherend was used in their study, this suggestion is also applied to the FRP-to-concrete interface.

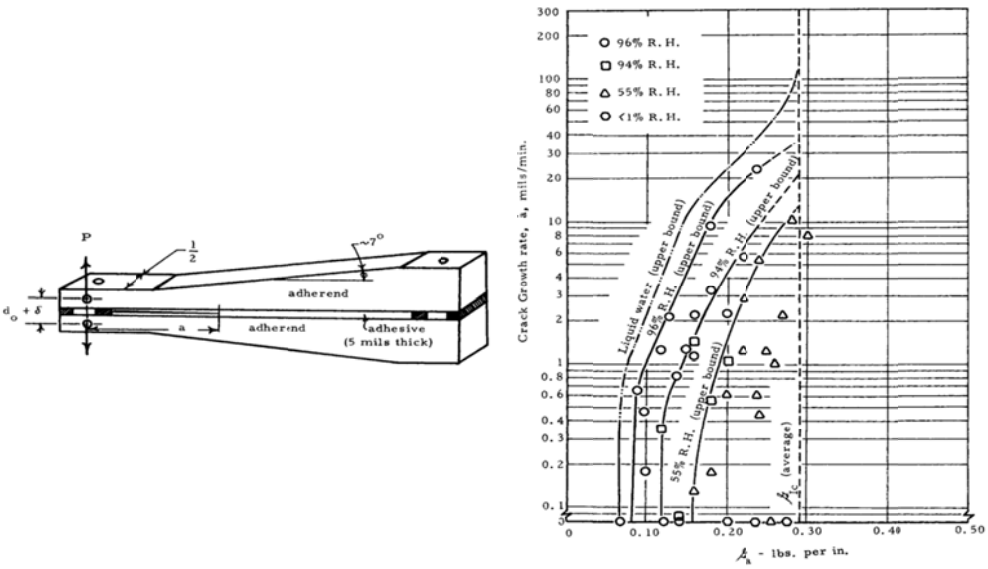

Fig. 1-14 Tapered double cantilever aluminum/epoxy specimen and the environment-assisted subcritical debonding for different relative humidity levels [129].

Water is one of the most dangerous environmental conditions that can deteriorate the adhesive bond [31]. Shimizu et al. suggested that water molecules can ingress through the interface between the epoxy and the concrete and eliminate the bond molecules [137]. In a recent research by Zhang et al, the EASD of the epoxy-concrete interface have been studied using a wedge-driving test for FRP-to-concrete interfaces in different aqueous solutions: ambient environment, tap water, deicing salt solution, and alkaline solutions [138]. The test specimen is made of two adherends bonded with an adhesive layer. While the specimen is maintained in a harsh environment, the steel wedge is gradually driven inside the bond leading to a peel force at the contact point. They found a remarkable difference between subcritical debonding in ambient condition and in aqueous conditions (Fig. 1-15). More importantly, they found the major debonding mode of EASD in aqueous conditions is adhesive, which is different from the

cohesive failure mode of the interface in critical debonding tested at ambient environments. They suggested that this shift in failure mode can be caused by two reasons: very slow loading rate, and the effect of environmental conditions.

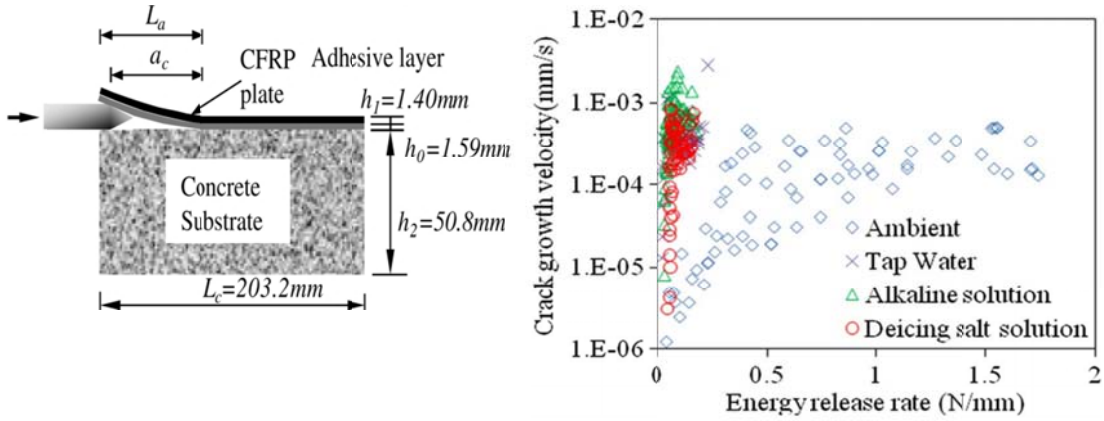

Fig. 1-15 Wedge driving test specimen and comparison between environment-assisted subcritical debonding in ambient condition and different aqueous conditions [138].

Most in-service failures of the adhesive-adherend bonds are caused by environmental degradation of the interface. In existing studies, the synergistic effect of relative humidity levels and temperature with mechanical subcritical loads in subcritical debonding of epoxy-concrete interfaces has not been studied yet.

Existing studies on the durability of FRP-to-concrete interface are limited only to evaluation of the deterioration of mechanical properties subject to different environments. No significant work has been dedicated to enhance the durability of the FRP-to-concrete interface in the literature. Some previous studies on metal-to-metal adhesively bonded joints demonstrated that using an organic primer, silane coupling agent, can improve the long-term durability of the interface.

Organofunctional silane coupling agents have been used for many years to facilitate the bond between organic materials such as epoxy adhesives and inorganic materials, mostly metal substrates [140] in which remarkable achievements have been made in improving the durability

and the strength of the bond [133], [134], [141]–[146]. Ye et al. tested two groups of specimens at ambient temperature and evaluated silane surface treatment effect on the bond strength and the fracture toughness of the FRP-to-concrete interface [147]. The first group consisted of specimens with smooth and untreated concrete surface; while in the second group concrete surfaces were sandblasted before applying the primer and the epoxy adhesive. As a result, the fracture energy of the smooth concrete surface was improved from 61 J /m^2 to 126 J /m^2, which was as much as the sandblasted specimen. However, the application of the silane coupling agent did not improve bond strength and fracture toughness of the sandblasted concrete specimen. They suggested that since debond of the sandblasted specimen is cohesive and controlled by the concrete, silane bounding agent does not have any benefits. No durability test was conducted by Ye et al and, therefore, it is unclear whether silane can improve the durability of FRP-to-concrete interface.

1.3.2. Critical debonding behaviors of the FRP-to-concrete interface

1.3.2.1. Previous experimental studies

Although critical debonding of the FRP-to-concrete interface have been extensively studied for many years, there are still a few unsolved issues on the long-term durability of this interface in presence of aggressive environments [31]–[33]. Studies conducted on dry specimens tested under ambient conditions showed that debond usually occurs with the concrete adjacent to the epoxy-concrete interface [35]. As a result, the strength and the durability of the interface will be controlled by the concrete. The long-term durability of the FRP-to-concrete interface under different environmental conditions has become the focus of a few recent studies [29], [30], [117], [148]–[152]. Karbhari and Engineer investigated the durability and the performance of the interface using small cement mortar beams strengthened with wet-layup composite plates [150]. Specimens were tested in a four-point bending test after exposure to ambient conditions and

environmental conditions including water, synthetic seawater, being frozen and freeze-thaw cycles. They showed that after first month of immersion, moisture uptake can decrease both strength and stiffness of the bond. They found out that the selection of the appropriate adhesive type is vastly important to prevent pre-mature failure due to environmental attacks. It was also shown that using carbon fiber reinforced polymer (CFRP) composites and epoxy adhesive with higher glass transition (T_g) can end up with a more durable retrofit.

Büyüköztürk et al. extensively studied the long-term debonding and extended both experimental and numerical approaches to examine the moisture affected debonding failure of the FRP-to-concrete interface in FRP-strengthened concrete structures [30]. They suggested that it is essential to separately study the peel and shear fracture and develop independent mode-I and mode-II specimens because the real debonding configuration is in mixed mode (

Fig. 1-16) due to the intermediate differential crack movement. Mode I and II specimens were mechanically tested after being subjected to the accelerated moisture conditions in different time intervals (2, 4 and 8 weeks) at both regular and high-temperature moistures (23°C and 50°C). Experimental results showed that for a certain moisture concentration (*MC*), the fracture toughness of the interface decreases by 60% in few weeks [30] (Fig. 1-17). In an important observation, it was understood that for all conditioned specimens, the fracture plane is placed along the epoxy-concrete interface, different from the control dry specimens, in which the failure mode is cohesive.

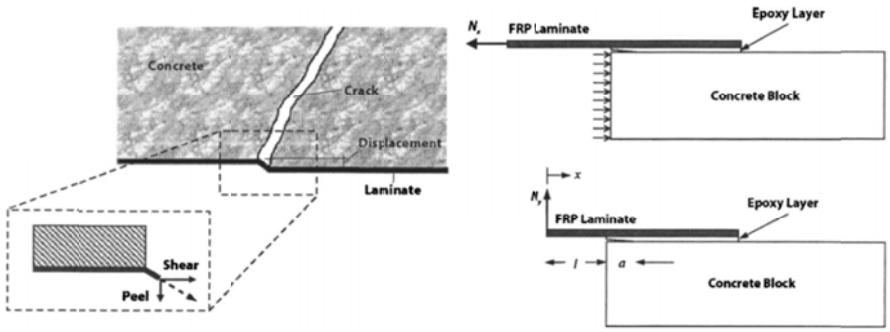

Fig. 1-16 Actual debonding configuration and peel and shear specimens [30].

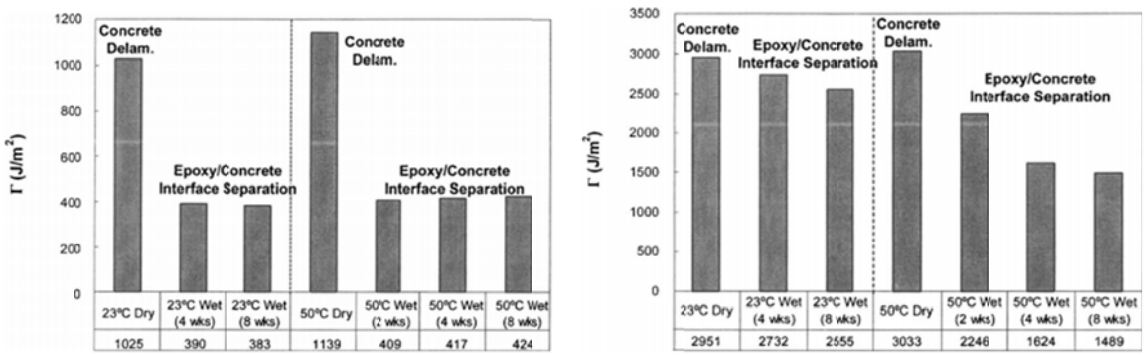

Fig. 1-17 Peel and shear fracture toughness for specimens conditioned in water [30].

In another study by Tuakta and Büyüköztürk the bond strength of FRP strengthened concrete structures were investigated [34]. The same peel and shear specimens as their previous study were tested after exposure to cyclic moisture conditions (periodic wetting/drying cycles), and then epoxy-concrete interfaces were characterized by fracture toughness. They developed a method to correlate the moisture content in the bond-line, which is known from the FEA using moisture diffusion technique with the residual of the fracture toughness of the interface. Some of the specimens after conditioning for couple of weeks at 23°C and 50°C were left to dry for four days, and their fracture toughness and Young's modulus of concrete were determined. Cyclic moisture tests showed that interface loses its initial strength even after a few weeks conditioning; while the concrete Young's modulus can retain its original value after drying. Although reversal specimens did not acquire their original strengths (in comparison to the ingress specimens), they

regained more fracture toughness of the interface (Fig. 1-18). In another study, similar results were found for sandwich beam specimens consisting of a layer of epoxy in the middle of two concrete blocks [153]. Experimental results for mode-I and mixed mode fracture, showed up to 50% loss of the initial fracture toughness in the epoxy-concrete interface after exposure to the moisture condition for several weeks (Fig. 1-19). Once again the authors observed shifting the debonding mode from the cohesive (concrete substrate) to the epoxy-concrete interface.

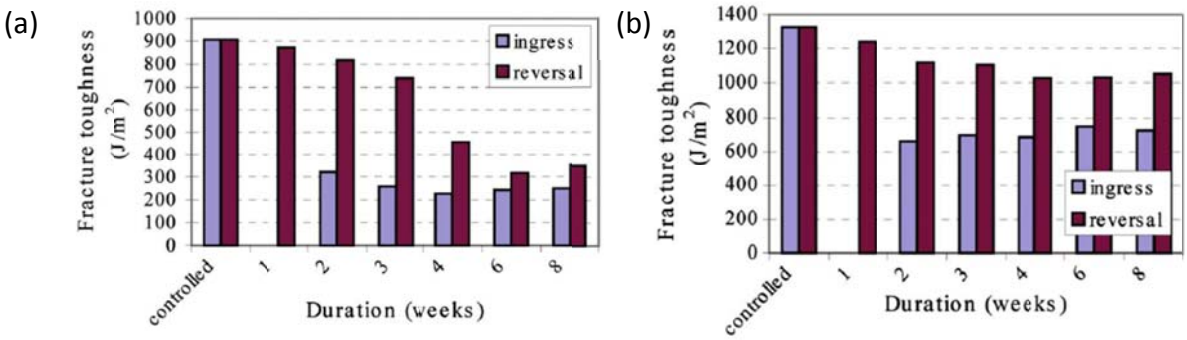

Fig. 1-18 Comparison between fracture toughness of ingress and reversal specimens conditioned at room temperature: (a) peel test, (b) shear test [34].

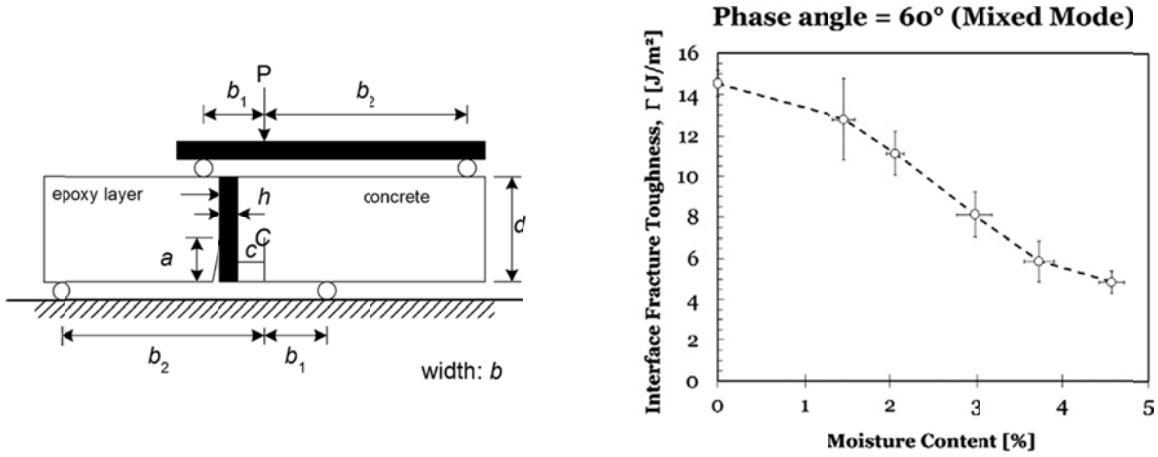

Fig. 1-19 Epoxy-concrete beam sandwich specimen and interface fracture toughness variation with moisture content [153].

1.3.2.2. Modeling degradation of the FRP-to-concrete interface in aggressive environments

Results obtained from different studies on the long-term degradation of the epoxy-concrete interface can be affected by many factors such as size and materials of the specimens, methods and durations of conditioning. All these factors play roles in the existing experimental studies on the long-term durability of the FRP-to-concrete interface. As a result, existing experimental tests are specimen-dependent and it is difficult to compare the testing results from different studies. To overcome this issue, one effort was made to correlate the residual strength (i.e. the fracture toughness) of the interface to the moisture content within the interface.

Ouyang and Wan modeled moisture transportation in a FRP strengthened concrete specimen using a finite element technique and considering the Fick's law of diffusion [154]. All moisture diffusivity coefficients for the FRP, the epoxy and the concrete were determined by the absorption and desorption tests (desorption method for the concrete and absorption test for the epoxy). They made two assumptions in their modeling: 1) only a two-dimensional model was considered in which no moisture flux was present along the longitudinal direction of the specimen, and 2) it was assumed that diffusivity is independent from the flux path. Thus, one-dimensional diffusivity parameters can be implemented in the model. 100% (saturated in water) and 78% boundary conditions were chosen for the FEA model. Numerical results for relative humidity contours with 100% relative humidity boundary condition showed that most of the interface moisture intake enters into the model in two ways: form the free edges of the bond and the sides of the concrete specimens. Overall, moisture diffusion in the model showed that even after 8 weeks, half-height of the concrete block was still dry. Also, the average numerical relative humidity along the interface, measured by a circular hygrometer probe, was in a good agreement with the experimental data. It was shown that the interface relative humidity value can be

increased with longer exposure to water. However, even after 8 weeks, the numerical results showed uneven moisture distribution along the interface (Fig. 1-20). This issue raises some doubts regarding the average moisture as the representative of the entire region. In other words, since the edges of the interface have more moisture content than the most inner parts, the obtained correlation between the bond strength and the moisture is not intrinsic and generic.

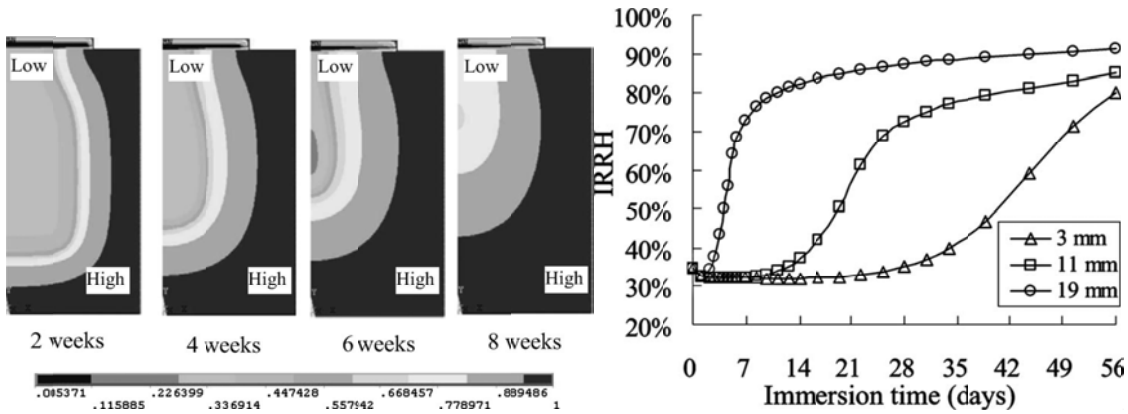

Fig. 1-20 Relative humidity contour and interface region relative humidity at different transverse locations versus immersion time [154].

Tuakta and Büyüköztürk developed another numerical simulation to predict the interface moisture content using Fick's equation [34]. Three-dimensional model was proposed for their both peel and shear specimens and time integration of the transient diffusion analysis was performed with backward Euler method. It was assumed that diffusion occurs at a fixed temperature, and consequently, flux analysis is independent from the temperature. Two analyses were conducted separately at the room temperature and at 50°C. Obtained results proved that by longer immersion in water, more moisture content along the interface can be obtained. In addition, more moisture diffusion was observed at higher temperature. Finally, the correlation between the residual fracture toughness for both of the peel and the shear specimens with the interface moisture content, in terms of the ratio of the transient and the threshold moisture contents, were obtained (Fig. 1-21). As discussed earlier, the average moisture content value along the interface, which was considered as the interface moisture content, does not accurately

represent the entire interface. For this reason, an intrinsic approach is required to overcome this difficulty.

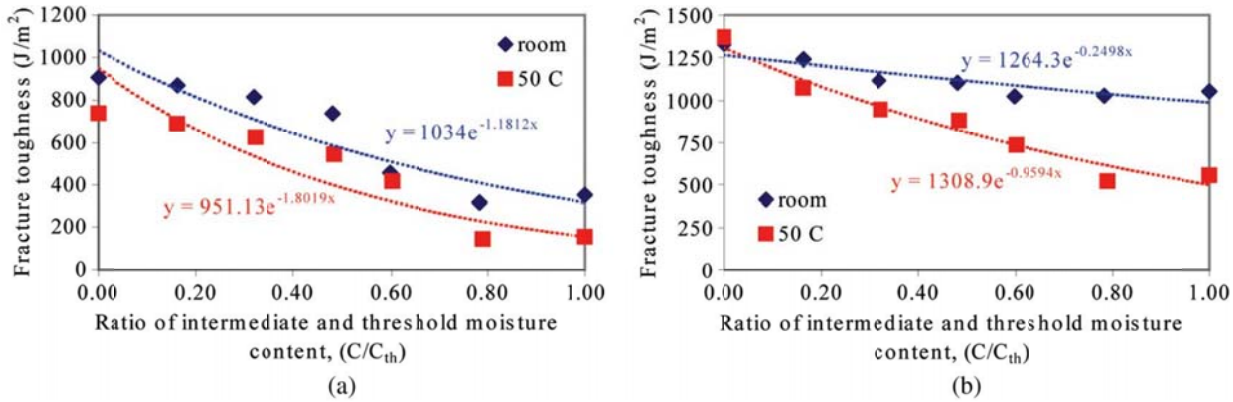

Fig. 1-21 Empirical relationship between fracture toughness and interface moisture content: (a) peel fracture specimens, (b) shear fracture specimens [34].

1.4. Research needs, tasks and dissertation organization

For a sustainable retrofit/rehabilitation of concrete structures using FRP, the durability and the strength of the FRP-to-concrete interface is as important as the properties of the individual layers. Problems such as micro-cracks formation along the interface, and their later propagation can bring about pre-mature failure of the interface, and subsequently, the failure of the entire structural system. In the literatures, a number of researches have been conducted on this problem. However, most of them are on the short-term mechanical behavior of the interface and neglected its long-term properties in presence of aggressive environments.

Investigations of the durability of the FRP-to-concrete interface in aggressive environments should be divided into two separate, but not necessarily independent, categories of analytical and experimental studies. Existing analytical studies have been largely concentrated on the elastic properties of the adhesive (bond) while the experimental investigations have been extensively focused on the critical failure of the degraded bond subjected to harsh conditions. It should be noted that due to the viscoelastic properties of the epoxy adhesive, the long-term stress

distribution along the bond between two adherends can be thoroughly different from the initial one. Redistribution of the stress (either peel or shear) along the interface affects the adhesive bond, and directly influences the crack formation. Even after fracture initiation, viscoelastic behavior of the adhesive bond, play an important role in crack propagation and debonding of the interface, and accordingly, should be investigated. This approach in analytical studies of the epoxy-concrete interface has not been fully investigated. So far, no stress analysis using three-parameter viscoelastic foundation (3PVF) model has been employed for both single-lap and double-lap joint problems. Although in previous studies, a closed-form 3PEF solution for the single-lap joints have been developed, no particular similar solution for the double-lap joints has been suggested.

Existing works showed that small cracks can slowly propagate, even by loads much lower than the critical forces, if environmental conditions such as moisture, temperature, and chemicals are involved. Current EASD studies have only taken into account only submerged specimens in aqueous environment. On the contrary, most of the adhesively bonded joints are exposed to air moisture and not submerged in water. To fill this gap, a new experimental approach is required to independently examine the moisture effect on the gradual and slow fracture propagation along the interface. Applying the silane coupling bonding agent is a practical and feasible method for enhancement of the chemical links between organic and inorganic materials. Nevertheless, its efficiency to improve the epoxy-concrete interface is still under discussion. As a result, experimental studies should be conducted in order to quantify its advantages.

Although the critical failure and the fracture toughness of the adhesive bond in aggressive environments (accelerated conditions) have been widely addressed in many studies, there are a

number of questions that should be appropriately answered. Most of the conducted studies are dependent to their specimens (size, material properties, etc.). Efforts have been made to characterize the bond strength by correlating it with the corresponding interface water moisture; however, non-uniform moisture distribution across the interface provides incomplete insight into the problem. In addition, no practical rehabilitation technique for the epoxy-concrete interface by using coupling agents has been characterized and discussed in literature. Another insufficiency in existing studies is that they generally take the fracture toughness at the time of failure as the bond overall strength. Using a technique such as traction-separation law of the bond can provide a strong insight into the toughness and stiffness of the bond even before the fracture initiation.

In this study, to address above research needs, following tasks in two major categories and seven separate articles were investigated and accomplished:

a) Analytical
    1. Elastic stress analysis of adhesive joints.
    2. Viscoelastic stress analysis of adhesive joints (two articles).
b) Experimental
    1. Subcritical debonding of FRP-to-concrete bonded interface under synergistic effect of load, moisture, and temperature.
    2. Critical debonding of FRP-to-concrete interface.
    3. Traction-separation law of concrete/epoxy interfaces subjected to moisture attack
    4. Effects of specimens and coupling agents on the durability testing results of concrete/epoxy interface.

The major body of this dissertation consists of these seven articles. At the end, the findings are summarized and discussed in the overall conclusion section.

CHAPTER 2

THREE-PARAMETER ELASTIC FOUNDATION MODEL OF DOUBLE-LAP ADHESIVELY BONDED JOINTS

Abstract

Adhesively bonded joints are widely used in composite structures to connect components due to their many advantages compared with other joining methods. However, premature failure due to debonding and peeling of the joint is the major concern of this technique. Existing analytical models of adhesively bonded joints suffers two major drawbacks: 1) not satisfying zero-shear stress boundary conditions at the free edges of the adhesive layer; and 2) failing to distinguish the peel stress along two adherend/adhesive interfaces. In this study, a novel three parameter elastic foundation (3PEF) model is developed to analyze a representative adhesively bonded joint, double-lap joint, which is believed to have relatively low peel stresses. Explicit closed-form expressions of shear and peel stresses along two adhesive/adherend interfaces are yielded. This new model overcomes the major drawbacks of the existing model by satisfying all boundary conditions and predicting different peeling stresses along two adherend/adhesive interfaces. It not only reaches excellent agreement with existing solution and numerical results based on finite element analysis, but also correctly predicts the failure mode of an experimentally tested double-lap joint. The important role of the peel stresses on the failure of the double-lap joint is therefore revealed by this new model, which is not possible by using the classical 2PEF model.

2.1. Introduction

Adhesively bonded joints are widely used in composite structures to connect components for their capabilities to replace conventional methods since they exhibit advantages in providing even distribution of the transmitted load and reducing stress concentration in adherends by eliminating holes [1]. As the adhesives available for bonding have improved, adhesively bonded joints have the potential to replace the use of traditional mechanical fasteners in many structures. However, premature failure due to debonding of the joints is the major concern of this technique. To address this issue, many analytical and numerical solutions have been proposed to evaluate the stress distributions in the adhesively bonded joints. First attempt was made based on the shear-lag model proposed by Volkersen (1938) [2]. In this model, the adherends are assumed in pure tension while the adhesive layer is only under shear force. Stress distribution through the thickness of the joint is also assumed to be constant [3]. The major drawback of this model is that peel stress of the adhesive layer is ignored, which may play an important role in the failure of the joint.

To overcome the shortcomings of Volkersen's model, Goland and Reissner (1944) proposed an improved model, in which the adhesive layer is modeled as a series of uniformly distributed shear and vertical springs [4]. In this way, both the shear and peeling stresses can be captured by this model. Great success and popularity has been achieved by this model (referred to as G-R model thereafter) and many modifications have been proposed on this model [5–17]. For example, Tsai, Oplinger, and Morton modified the G-R model by assuming that the shear stress distribution through the adherends is linear (known as TOM solution) [15]. Martensen and Thomsen proposed a model considering nonlinearity of the adhesive layer [18]. Hart-smith extended the G-R model to account for plasticity of the adhesive layer [5–7].

The G-R model ignores interaction between the shear and vertical springs. Therefore, the adhesive layer in the G-R model is essentially models as a two-parameter elastic foundation (2PEF) [4]. Although relatively simple closed-form solutions of stress can be obtained, the G-R model and all its descendants fail to satisfy the zero-shear-stress boundary conditions at the free edges of the adhesive layer. This can be seen from the governing differential equations of the 2PEF model which are sixth-order. As a result, only six boundary conditions are required (three internal forces acting at each free end), leaving two zero-shear-stress conditions at the free edges of the adhesive layer unsatisfied [19,20]. In addition, 2PEF model assumes that peel stress is a constant through the thickness of the adhesive layer; while experimental studies and numerical simulations suggest that peel stresses along the interface between the adhesive and the outer adherend and the interface between the adhesive and the inner adherend (upper and lower interfaces) are different, even in opposite direction at the edges [3].

To overcome these problems in the G-R model, efforts have been made to model the adhesive layer as a continuum 2-dimensional body [21–24], rather than a two-parameter elastic foundation. However, the resulted solutions are very complicated requiring sophisticated calculations [25]. To simplify these continuum models of the adhesive, Wang and Zhang (2009) proposed to model the adhesive layer as two layers of peel springs connected together through a layer of shear spring. In this way, the adhesive layer is essentially modeled as a three-parameter elastic foundation (3PEF). By using this 3PEF model, Wang and Zhang (2009) obtained a closed-form solution for single-lap joints, which not only satisfies all eight-boundary conditions, but also produces two different peel stresses along the upper and lower interfaces between the adhesive and adherends.

A number of studies have been carried out to establish analytical solutions of interface stresses in double-lap joints. By using Volkersen's single-lap theory [2], de Bruyne (1944) developed the most classical Volkersen/de Bruyne solution which is most widely used for stress analysis of double-lap joints [26]. Hart-Smith (1973a) improved this model by considering the adhesive plasticity, adherends with unbalanced stiffnesses, and thermal difference between the adherends [5]. Tsai et al. (1998) and Tsai and Morton (2010) proposed another improvement by including shear deformations in the adherend [15,27]. Recently, Gustafson et al. (2007) proposed another modification on the adhesive layer so that free edge boundary conditions of the adhesive layer can be satisfied in double-lap joints; while the peel stress is assumed constant through the adhesive layer [28]. Recognizing that stress may vary through the thickness of the adhesive layer, Diaz Diaz et al. (2009) developed a layer-wise model, which can not only meet both the free-edge boundary condition, but also produce different peel stress distributions along two adherend/adhesive interfaces in the joints [29]. However, this model is very difficult to use since eight second-order differential equations must be solved.

Reliable prediction of the locations where a high risk of debonding initiation exist and stress status at these locations is a critical step in designing adhesively bonded joints. To this end, this study proposes a new closed-form solution of interface stresses for double-lap joints. This solution not only satisfies all boundary conditions, but also predicts different peel stress distributions along two adhesive/adherend interfaces in the joint, making it possible to correctly predict the location with highest risk of debonding initiation. Parametric studies have been also carried out to shed new lights on the effect of thickness of the adhesive layer.

2.2. Three-parameter elastic foundation model of a double-lap joint

Figure 1-1(a) shows a typical double-lap joint subject to external loads. Due to symmetry, the whole problem may be reduced to a quarter of a joint, as shown in Fig. 2-1(b). An infinitesimal portion of the overlap in the lower-left quarter of the joint displayed in Fig. 2-1(b) is analyzed for force equilibrium, as shown in Fig. 2-2. Considering the similarity of the adherend along its neutral axis in following analysis, the upper half of the inner adherend is added to Fig. 2-2 to facilitate the formulation.

Both adherends are modeled as Timoshenko's beam. Then the displacement of these two adherends can be written as

$$U_i(x_i, z_i) = u_i(x_i) + z_i\phi_i(x_i), \quad W_i(x_i, z_i) = w_i(x_i), \tag{1}$$

where $u_i(x_i)$,$w_i(x_i)$ and $\phi_i(x_i)$ are the axial displacement, transverse (vertical) displacement, and the rotation angle of the neutral axis, respectively; *i=1,2* denotes the inner adherend (*i=1*) and the outer adherend (*i=2*). $U_i(x_i, z_i)$ and $W_i(x_i, z_i)$ represent the axial and the transverse displacements of the adherends, respectively. Since $x_1=x_2=x$, subscript *i* (*i =1,2*) in displacement functions shown in Eq. (1) will be ignored thereafter.

Both adherends are modeled as Timoshenko's beam. Constitutive equations of both adherends are written as

$$N_i(x) = C_i \frac{du_i(x)}{dx}, \qquad M_i(x) = D_i \frac{d\phi_i(x)}{dx}, \qquad Q_i(x) = B_i\left(\phi_i(x) + \frac{dw_i(x)}{dx}\right), \tag{2}$$

where $N_i(x)$, $M_i(x)$ and $Q_i(x)$ are the axial force, bending moment and transverse shear force of beam *i*, respectively. $C_i = E_i b_i h_i$, $D_i = \frac{E_i B_i h_i^3}{12}$ and $B_i = \kappa G_i b_i h_i$ represent the axial, flexural and shear stiffnesses of the beam *i*, respectively. E_i, $G_i$are the longitudinal and the shear moduli of elasticity of the adherend *i*. b_i and h_i denote the width and the height of beam *i*, respectively; κ is equal to 5/6 for rectangular cross section.

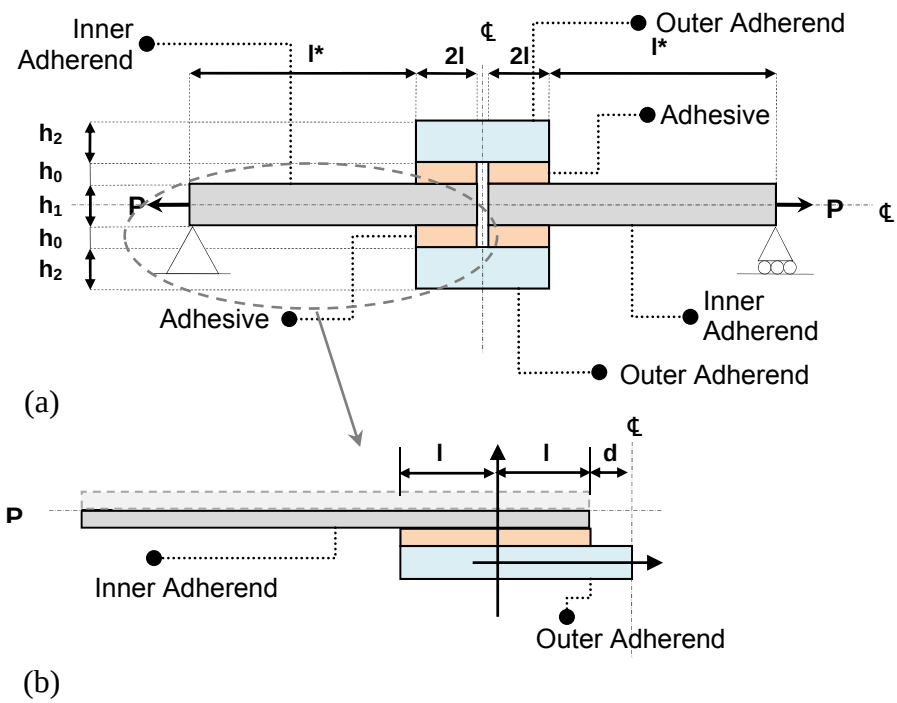

Fig. 2-1 Simply supported double-lap joint beam geometry.

Equilibrium equations of two adherends in Fig. 2-2 can be written as

$$\frac{dN_1(x)}{dx} = 2b\tau(x), \qquad \frac{dM_1(x)}{dx} = 0, \qquad \frac{dQ_1(x)}{dx} = 0, \tag{3a}$$

$$\frac{dN_2(x)}{dx} = -b\tau(x), \qquad \frac{dM_2(x)}{dx} = Q_2(x) - \frac{bh_2\tau(x)}{2}, \qquad \frac{dQ_2(x)}{dx} = -b\sigma_2(x), \tag{3b}$$

where $\tau(x)$ and $\sigma_2(x)$ are the shear stress within the adhesive and the peel stress along the interface between the outer adherend and the adhesive layer (outer interface), respectively. $\tau(x)$ is assumed to be constant through the thickness of the adhesive. $\sigma_1(x)$ is the peel stress along the interface between the inner adherend and the adhesive layer (inner interface) as shown in Fig. 2-2 which does not appear in Eq. (3a) due to symmetry (Fig. 2-2). For the same reason, it can be seen that $M_1(x) = 0$.

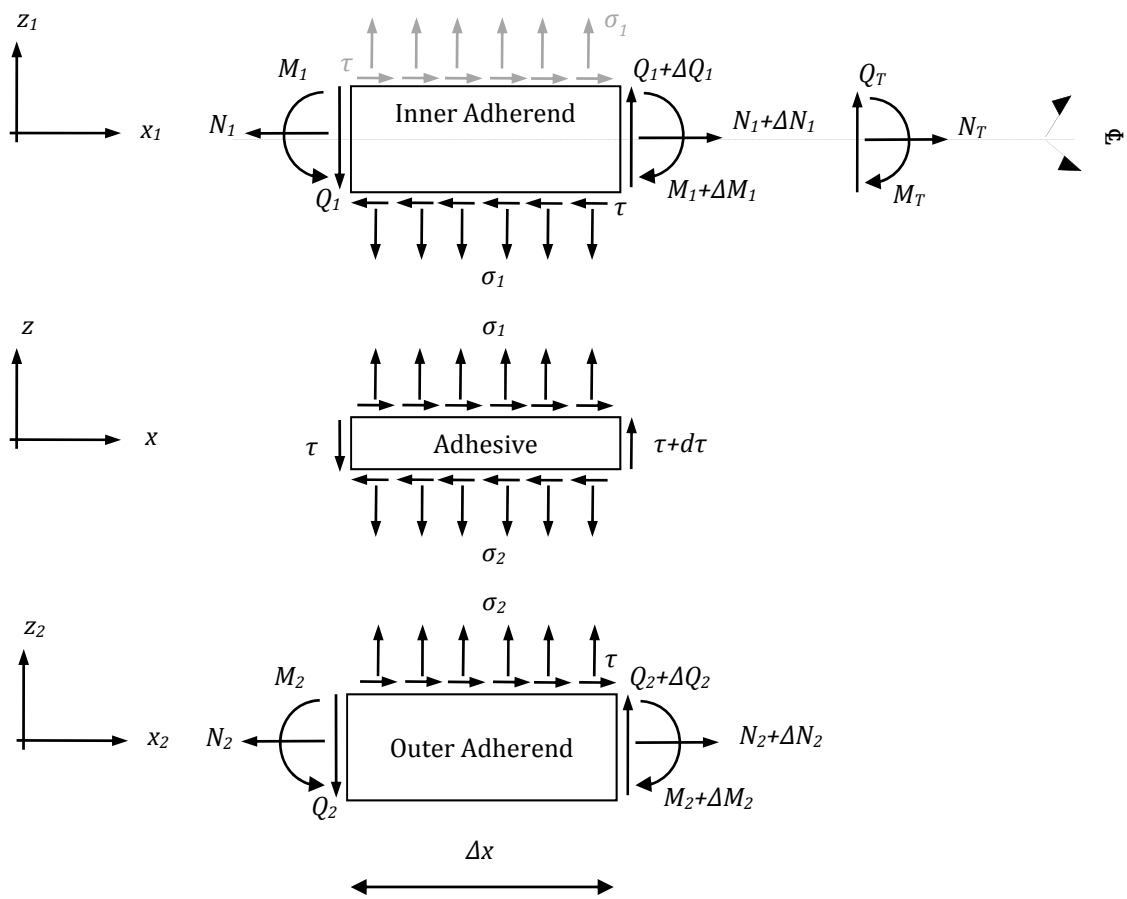

Fig. 2-2 Free body diagram of the assumed quadrant shown in Fig. 2-1(b).

Global equilibrium of the whole cross section requires

$$N_T(x) = N_1(x) + 2N_2(x) = P, \tag{4a}$$

$$M_T(x) = M_1(\mathrm{x}) = 0, \tag{4b}$$

$$Q_T(x) = 0, \tag{4c}$$

where N_T, M_T and Q_T are the resulting axial, bending, and shear forces along the neutral axis of the inner adherend, as shown in Fig. 2-2.

Since the adhesive layer is much softer than the adherends, its axial force and bending moment are neglected, as shown in Fig. 2-3. In the classical 2PEF model, peel stress through the thickness of the adhesive layer is assumed as a constant. Therefore peel stress along two

interfaces, $\sigma_1(x)$ and $\sigma_2(x)$, are identical, as shown in Fig. 2-3. Considering the force equilibrium of the adhesive layer, we have

$$\frac{d\tau(x)}{dx} = \frac{\sigma_2(x)-\sigma_1(x)}{h_a} = 0. \tag{5a}$$

Equation (5a) implies that shear stress is constant along the adhesive layer, which is in contradiction to the shear stress distribution derived from the 2PEF model [25]. In order to fix this inconsistency, two peel stresses $\sigma_1(x)$ and $\sigma_2(x)$ must be different and Eq. (5a) becomes

$$\frac{d\tau(x)}{dx} = \frac{\sigma_2(x)-\sigma_1(x)}{h_a}. \tag{5b}$$

To account for Eq. (5), we can model the adhesive layer as two linear springs with stiffness of $k = \frac{2\,E_a}{h_a}$ connected by a shear layer with shear modulus of G_a as shown in the 3PEF model displayed in Fig. 2-3 [30,31]. Unlike the 2PEF model, in which the transverse (vertical) displacement of the adhesive layer is a constant through the thickness of the adhesive layer, the vertical displacement at the mid-plane (w_a) of the adhesive is different from the ones on the top and bottom surfaces of the adhesive layer

Strain-stress relations of the adhesive layer in the 3PEF model can then be written as

$$\sigma_1(x) = \frac{2E_a}{h_a}\big(w_1(x) - w_a(x)\big), \quad \sigma_2(x) = \frac{2E_a}{h_a}\big(w_a(x) - w_2(x)\big), \tag{6a}$$

$$\tau(x) = \frac{G_a}{h_a}\left(u_1(x) - \frac{h_1}{2}\phi_1(x) - u_2(x) - \frac{h_2}{2}\phi_2(x)\right) + G_a, \tag{6b}$$

where E_a, G_a are the Young's and shear moduli of the adhesive layer, respectively. It can be seen that if the vertical displacement along the mid-plane of the adhesive is equal to the average of those of both adherends (i.e. $w_a = \frac{w_1(x)+w_2(x)}{2}$ as assumed in the 2PEF model), Eq. (6a) will produce two identical peel stresses (i.e. $\sigma_1 = \sigma_2 = \sigma$). Therefore, the classical 2PEF model is a special case of the present 3PEF model. Considering symmetry of the structure, we have

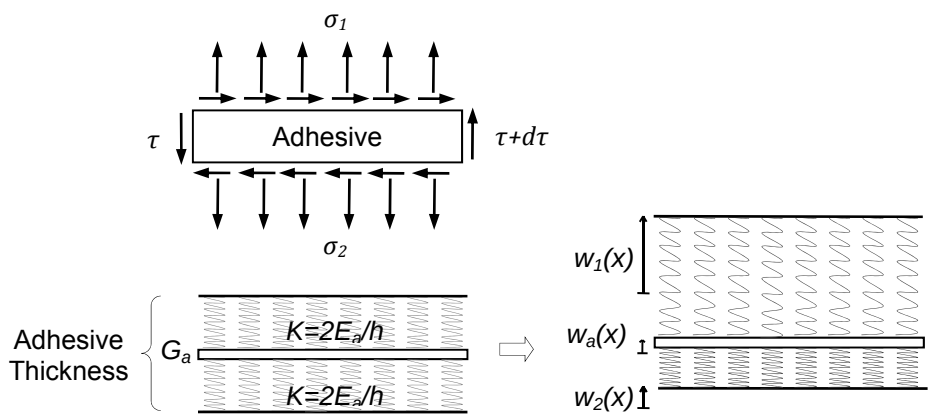

Fig. 2-3 A three-parameter elastic foundation model.

$$w_1(x) = 0, \phi_1(x) = 0. \tag{6c}$$

By considering Eq. (2) and using Eq. (3b) to substitute all stress and strain terms with internal forces, we have

$$\frac{d^2N_2(x)}{dx^2} = -\frac{bG_a}{h_a}\left(\frac{N_1(x)}{C_1} - \frac{N_2(x)}{C_1} - \frac{h_2}{2}\frac{M_2(x)}{D_2}\right) - bG_a\frac{d^2w_a(x)}{dx^2}. \tag{7}$$

Considering Eq. (4) and (6b), the above equation can be rewritten as

$$\frac{d^4M_2(x)}{dx^2} + A_{11}\frac{d^4N_2(x)}{dx^4} + A_{12}\frac{d^2M_2(x)}{dx^2} + A_{13}\frac{d^2N_2(x)}{dx^2} + A_{14}\,M_2(x) + A_{15}\,N_2(x) + A_{16}\,N_T = 0, \tag{8}$$

where

$$A_{11} = -\frac{h_2}{2}, \qquad A_{12} = -\frac{2bE_a}{h_0B_2}, \qquad A_{13} = \frac{2E_a}{h_0G_a}\left(\frac{bG_ah_2}{2B_2} - 1\right), \tag{9}$$

$$A_{14} = \frac{2bE_a}{h_0}\left(\frac{1}{h_0}\frac{h_2}{2D_2}\right) + \frac{1}{D_2}, \qquad A_{15} = \frac{2bE_a}{h_0^2}\left(\frac{2}{C_1} + \frac{1}{C_2}\right), \qquad A_{16} = -\frac{2bE_a}{C_1h_0^2}.$$

By adding two parts of Eq. (6a) together and considering Eq. (2), the following expression is obtained after differentiating twice

$$\frac{d^2\sigma_1(x)}{dx^2} + \frac{d^2\sigma_2(x)}{dx^2} = \frac{2E_a}{h_0}\left(-B_2\frac{dQ_2(x)}{d} + \frac{d\phi_2}{dx}\right). \tag{10}$$

By using Eq. (2), (3) and (5b), the above equation can be simplified as

$$\frac{d^4M_2(x)}{dx^4} + B_{11}\frac{d^4N_2(x)}{dx^2} + B_{12}\frac{d^2M_2(x)}{dx^2} + B_{13}\frac{d^2N_2(x)}{dx^2} + B_{14}\,M_2(x) = 0, \tag{11}$$

where

$$B_{11} = \frac{-h_2+h_0}{2}, \qquad B_{12} = -\frac{bE_a}{h_0B_2}, \qquad B_{13} = \frac{bE_ah_2}{2h_0B_2}, \quad B_{14} = \frac{bE_a}{h_0D_2}. \tag{12}$$

Considering Eq. (8), we can rewrite Eq. (11) in terms of derivatives of $N_2(x)$ by eliminating other terms. Subtracting Eq. (11) from Eq. (8) and cancelling $\frac{d^4M_2(x)}{dx^4}$ yield

$$\frac{d^2M_2(x)}{dx^2} = C_{11}\frac{d^4N_2(x)}{dx^4} + C_{12}\frac{d^2N_2(x)}{dx^2} + C_{13}\,M_2(x) + C_{14}M_2(x) + C_{15}N_T(x) = 0, \tag{13}$$

where

$$C_{11} = -\frac{A_{11}-B_{11}}{A_{12}-B_{12}}, \qquad C_{12} = -\frac{A_{13}-B_{13}}{A_{12}-B_{12}}, \qquad C_{13} = -\frac{A_{14}-B_{14}}{A_{12}-B_{12}}, \tag{14}$$

$$C_{14} = -\frac{A_{15}}{A_{12}-B_{12}}, \qquad C_{15} = -\frac{A_{16}}{A_{12}-B_{12}}.$$

Multiplying Eq. (8) by B_{12} and subtracting Eq. (11) multiplied by A_{12} to eliminate $\frac{d^2M_2(x)}{dx^2}$ gives

$$\frac{d^4M_2(x)}{dx^4} = D_{11}\frac{d^4N_2(x)}{dx^4} + D_{12}\frac{d^2N_2(x)}{dx^2} + D_{13}M_2(x) + D_{14}N_2(x) + D_{15}N_T, \tag{15}$$

where

$$D_{11} = -\frac{A_{11}B_{12}-B_{11}-A_{12}}{B_{12}-A_{12}}, \qquad D_{12} = -\frac{A_{13}B_{12}-B_{13}A_{12}}{B_{12}-A_{12}}, \qquad D_{13} = -\frac{A_{14}B_{12}-B_{14}A_{12}}{B_{12}-A_{12}}, \tag{16}$$

$$D_{14} = -\frac{A_{15}B_{12}}{B_{12}-A_{12}}, \qquad D_{15} = -\frac{A_{16}B_{12}}{B_{12}-A_{12}}.$$

By differentiating Eq. (13) twice and subtracting it from Eq. (15), the following equation is obtained

$$M_2(x) = E_{11}\frac{d^6N_2(x)}{dx^6} + E_{12}\frac{d^4N_2(x)}{dx^4} + E_{13}\frac{d^2N_2(x)}{dx^2} + E_{14}N_2(x) + E_{15}N_T = 0, \tag{17}$$

where

$$E_{11} = \frac{C_{11}}{D_{13}-C_{13}^2}, \qquad E_{12} = \frac{C_{12}+C_{13}C_{11}-D_{11}}{D_{13}-C_{13}^2}, \qquad E_{13} = \frac{(C_{14}+C_{13}C_{12}-D_{12})}{D_{13}-C_{13}^2}, \tag{18}$$

$$E_{14} = \frac{C_{13}C_{14}-D_{14}}{D_{13}-C_{13}^2}, \qquad E_{15} = \frac{C_{13}C_{15}-D_{15}}{D_{13}-C_{13}^2}.$$

In Eq. (17), $M_2(x)$ is expressed in term of $N_2(x)$. Hence, by substituting this equation as well as its derivatives into Eq. (13), the governing equation of the adhesively bonded joint can be obtained as

$$F_{11}\frac{d^8N_2(x)}{dx^8} + F_{12}\frac{d^6N_2(x)}{dx^6} + F_{13}\frac{d^4N_2(x)}{dx^4} + F_{14}\frac{d^2N_2(x)}{dx^2} + F_{15}N_2(x) + F_{16}N_T = 0, \tag{19}$$

where

$$F_{11} = E_{11}, \qquad F_{12} = E_{12} - C_{13}E_{11}, \qquad F_{13} = E_{13} - C_{13}E_{12} - C_{11}, \tag{20}$$

$$F_{14} = E_{14} - C_{13}E_{13} - C_{12}, \qquad F_{15} = -C_{13}E_{14} - C_{14}, \qquad F_{16} = -C_{13}E_{15} - C_{15}.$$

The above governing equation is an eighth-order normal differential equation. Its characteristic equation can be written as

$$F_{11}\bar{X}^8 + F_{12}\bar{X}^6 + F_{13}\bar{X}^4 + F_{14}\bar{X}^2 + F_{15}\bar{X} + F_{16}N_T = 0. \tag{21}$$

Eq. (21) gives eight complex roots $\pm\emptyset_1$, $\pm\emptyset_2$, $\pm\emptyset_3$ and $\pm\emptyset_4$. The general solution of Eq. (19) can be expressed as

$$N_2(x) = N_{2H}(x) + N_{2P}(x), \tag{22a}$$

$$N_{2H}(x) = \sum_{i=1}^{n=4}[a_i\sinh(\emptyset_i x) + b_i\cosh(\emptyset_i x)], \tag{22b}$$

$$N_{2P}(x) = -\frac{F16}{F15}N_T, \tag{22c}$$

where $N_2(x)$, $N_{2H}(x)$ and $N_{2P}(x)$ are the general solution, the hyperbolic solution of the homogenous form of the governing equation, and the particular solution, respectively.

Similarly, the general solution of the bending moment can be obtained considering Eq. (17) as

$$M_2(x) = M_{2H}(x) + M_{2P}(x), \tag{23a}$$

$$M_{2H}(x) = \sum_{i=1}^{n=4} Y_{Mi}[a_i \sinh(\emptyset_i x) + b_i \cosh(\emptyset_i x)], \tag{23b}$$

$$M_{2P}(x) = E15N_T, \tag{23c}$$

$$Y_{Mi} = E11\emptyset_i^6 + E12\emptyset_i^3 + E13\emptyset_i^2 + E14, \tag{23d}$$

where $M_2(x)$, $M_{2G}(x)$ and $M_{2P}(x)$ are the general solution, the hyperbolic solution of the homogenous form of Eq. (17), and the particular solution, respectively.

Considering Eq. (3), the internal shear force can be written as

$$Q_2(x) = \frac{dM_2(x)}{dx} - \frac{h_2}{2}\frac{dN_2(x)}{dx}. \tag{24}$$

By substituting Eqs. (22) and (23) into Eq. (24), the general solution of shear force is given by

$$Q_2(x) = Q_{2H}(x) + Q_{2P}(x), \tag{25a}$$

$$Q_{2H}(x) = \sum_{i=1}^{n=4} Y_{Qi}[a_i \sinh(\emptyset_i x) + b_i \cosh(\emptyset_i x)], \tag{25b}$$

$$Q_{2P}(x) = \frac{dM_{2P}(x)}{dx} - \frac{h_2}{2}\frac{dN_{2P}(x)}{dx}, \tag{25c}$$

$$Y_{Qi} = Y_M\emptyset_i - \frac{h_2}{2}\emptyset_i, \tag{25d}$$

where $Q_2(x)$, $Q_{2H}(x)$ and $Q_{2P}(x)$ are the general solution, the hyperbolic solution, and the particular solution, respectively.

The general solution of the interface stresses along the outer and inner interfaces can be obtained by using Eq. (3) as

$$\sigma_2(x) = \sigma_{2H}(x) + \sigma_{2P}(x), \tag{26a}$$

$$\sigma_{2H}(x) = -\frac{1}{b}\sum_{i=1}^{n=4} Y_{\sigma 2i}[a_i \sinh(\emptyset_i x) + b_i \cosh(\emptyset_i x)], \tag{26b}$$

$$\sigma_{2P} = -\frac{1}{b}\frac{dQ_{2P}(x)}{dx}, \tag{26c}$$

$$Y_{\sigma 2i} = Y_{Q_i}\emptyset_i. \tag{26d}$$

Since

$$\sigma_1(x) = \sigma_2(x) + \frac{h_0}{b}\frac{d^2N_2(x)}{dx^2}, \tag{27}$$

we have

$$\sigma_1(x) = \sigma_{1H}(x) + \sigma_{1P}(x), \tag{28a}$$

$$\sigma_{1H}(x) = \sum_{i=1}^{n=4} Y_{\sigma 1i}[a_i \sinh(\emptyset_i x) + b_i \cosh(\emptyset_i x)], \tag{28b}$$

$$\sigma_{1P} = -\frac{1}{b}\frac{dQ_{2P}(x)}{dx} + \frac{h_0}{b}\frac{d^2N_{2P}(x)}{dx^2}, \tag{28c}$$

$$Y_{\sigma 1i} = Y_{\sigma 2} + \frac{h_0}{b}\emptyset_i^2, \tag{28d}$$

and

$$\tau(x) = \tau_H(x) + \tau_P(x), \tag{29a}$$

$$\tau_H(x) = -\frac{1}{b}\sum_{i=1}^{n=4} Y_{\tau i}[a_i \sinh(\emptyset_i x) + b_i \cosh(\emptyset_i x)], \tag{29b}$$

$$\tau_P(x) = -\frac{1}{b}.\frac{dN_{2P}(x)}{dx}, \tag{29c}$$

$$Y_{\tau i} = \emptyset_i, \tag{29d}$$

where $\sigma_2(x)$, $\sigma_1(x)$ and $\tau(x)$ are general solutions, $\sigma_{2H}(x)$, $\sigma_{1H}(x)$ and $\tau_G(x)$ are hyperbolic solutions, and $\sigma_{2P}(x)$, $\sigma_{1P}(x)$ and $\tau_P(x)$ are particular solutions.

Coefficients a_i and b_i (eight coefficients) can be determined by considering boundary conditions at the two ends of the joint overlap. As shown in Fig. 2-1(a), by assuming that the double-lap joint is supported by hinge and roller supports at two ends, seven boundary conditions can be obtained as

$$N_2(x = -l) = 0, \qquad M_2(x = -l) = 0, \qquad Q_2(x = -l) = 0, \qquad \tau(x = -l) = 0, \tag{30a}$$

$$N_2(x = l) = \frac{P}{2}, \qquad Q_2(x = l) = 0, \qquad \tau(x = l) = 0, \tag{30b}$$

where P is the pulling force applied at the very ends of the joint.

At the symmetric axis where x = $l + d$ as shown in Fig. 2-1, the rotation of the outer adherend is zero, i.e.

$$\phi_2(x = l + d) = 0. \tag{31}$$

By integrating the second constitutive equation in Eq. (2) from $l+d$ to l, the rotation at $x = l$ of the outer adherend can be obtained as

$$\phi_2(x = l) = -\frac{M_2(x=l)}{D_2} d. \tag{32}$$

Since $Q_2 = 0$ at $x = l$, we have

$$-\frac{M_2(x=l)}{D_2} d + \frac{dw_2(x=L)}{dx} = 0. \tag{33}$$

By using Eq. (6), the second term in Eq. (33) can be expressed by

$$\frac{dw_2(x=L)}{dx} = -\frac{h_a}{2E_a}\left(\frac{d\sigma_1(x=l)}{dx} + \frac{d\sigma_2(x=l)}{dx}\right). \tag{34}$$

Substituting Eq. (34) into Eq. (33) provide the eighth boundary conditionS needed to determine all eight coefficients in the solutions.

2.3. Results and verification

To verify the new model, we first study a double-lap joint with unidirectional composite adherends which was studied by Tsai and Morton (2010) [27]. This double-lap joint consists of an inner adherend with thickness of 2 mm and outer adherends with thicknesses of 1 mm with the same Young's modulus of 137 GPa and shear modulus of 4.83 GPa. The adhesive layer has a thickness of 0.15 mm with shear modulus of 0.91 GPa and Poisson ratio of 0.32. The length of the bond is 12.7 mm.

Figure 2-4 compares the shear stress within the adhesive layer obtained by the present solution with those obtained through experimental study, finite element analysis (FEA), and the analytical solution using Tsai, Oplinger and Morton solution TOM, [27]. It can be seen that the present model reaches excellent agreement with experimental result and FEA. Both the present model and FEA can satisfy the zero shear stress boundary condition at the free-edge of the

adhesive layer; while TOM model fails. Since the zero-shear stress zone is very small, experimental measurement cannot capture this feature either due to the limitation of the sensor. Nevertheless, a drop in shear stress near the free edge can be observed from the experimental measurement. According to existing 2PEF model, shear stress should reach its maximum at the free edge, which is clearly contradictory to the experimental observation shown in Fig. 2-4.

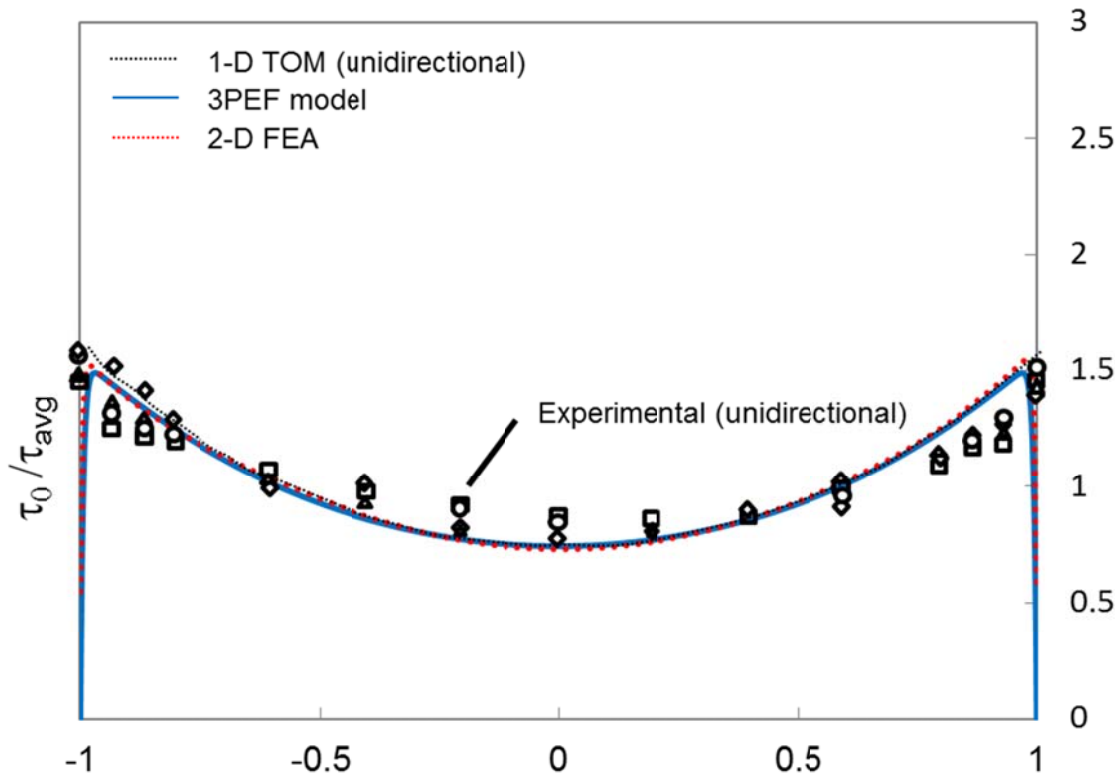

Fig. 2-4 Comparison of the present model with FEA, experimental and analytical (TOM) results obtained by Tsai and Morton [27].

As further verification, a double-lap joint shown in Fig. 2-5 was analyzed by the present method and FEA, which is assumed as accurate solution in this study. The geometry and material properties of the double-lap joint are shown in Tables 2-1 and 2-2, respectively. A linear elastic model of this joint is constructed using commercial finite element software ABAQUS/CAE with 4-node bilinear plane stress quadrilateral elements. Meshing size is ranged between 0.02 mm and 0.2 mm. Refined mesh is used in the regions near the edges of the bond, as shown in Fig. 2-5.

Different thicknesses of the adhesive layer were used in the analysis to examine their effect on the interface stresses.

Table 2-1 Geometrical parameters of the double-lap joint.

	l*	l	h_0	h_1	h_2
Dimension	50 mm	25 mm	0.25 mm 0.5 mm 1 mm 2 mm	5 mm	5 mm

Table 2-1 Mechanical properties of the materials of the joint.

Mechanical properties	Outer adherend	Adhesive	Inner adherend
Modulus of Elasticity E	60GPa	4.82GPa	60GPa
Poisson ratio ν	0.33	0.25	0.33

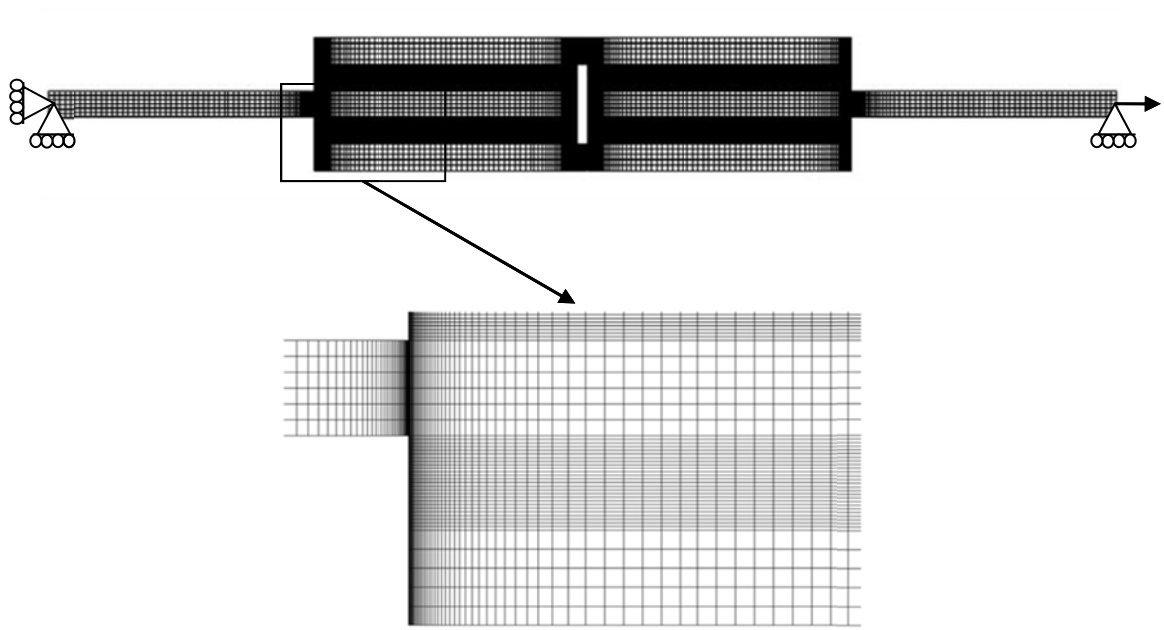

Fig. 2-5 FEA model of a simply supported double-lap joint under axial tension with a close illustration of the lower-left corner meshing.

Figure 2-6 compares the shear stresses obtained by the present 3PEF model and the FEA for different adhesive thicknesses. Excellent agreement with FEA has been achieved by the present model, confirming once again the validity of the new model. Both solutions correctly

predict zero shear stress at the free edge of the adhesive. Small differences between these two solutions exist in the vicinity of the free edges. This is not surprising since the present model simulates two adherends as beams, which are unable to account for the local effect of the boundary. It can be seen that stress concentration near the exterior edge of the interface is higher than that near the inner edge, suggesting that debonding induced by shear stress will be more likely to initiate from the exterior edge rather than from the inner edge.

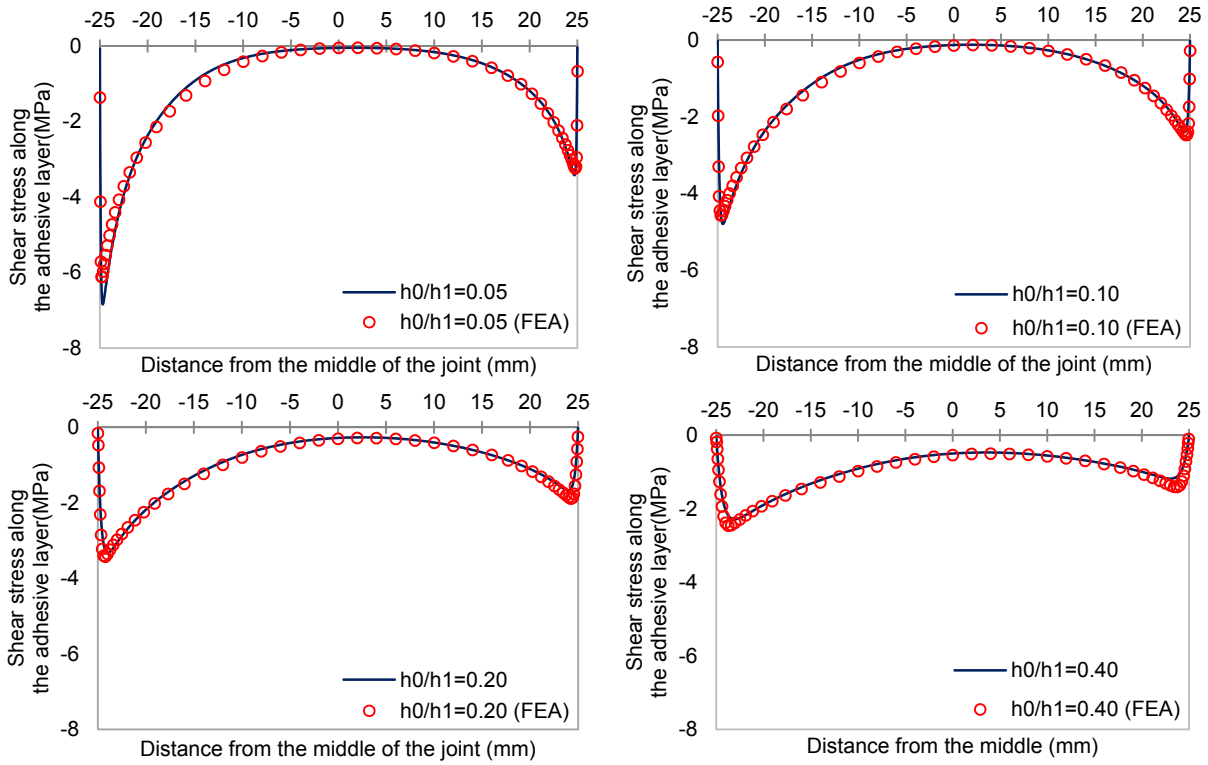

Fig. 2-6 Comparison the shear stress distribution obtained by the present solution and that by the FEA for different thicknesses of the adhesive layer.

Peeling stresses obtained by the present model and by the FEA are presented in Fig. 2-7. Once again, good agreement with FEA has been achieved by the present model. Both FEA and the present model suggest that near the edge of the adhesive layer, peel stresses along the inner and outer adherend-adhesive interfaces are different, as shown in Fig. 2-7. This is different from

the classical 2PEF model, which assumes that the peel stresses are identical along these two interfaces.

The effect of the thickness of the adhesive layer on the shear stress in the adhesive is demonstrated in Fig. 2-8. It can be seen clearly that shear stress concentration near the free edge increases with smaller thickness of the adhesive.

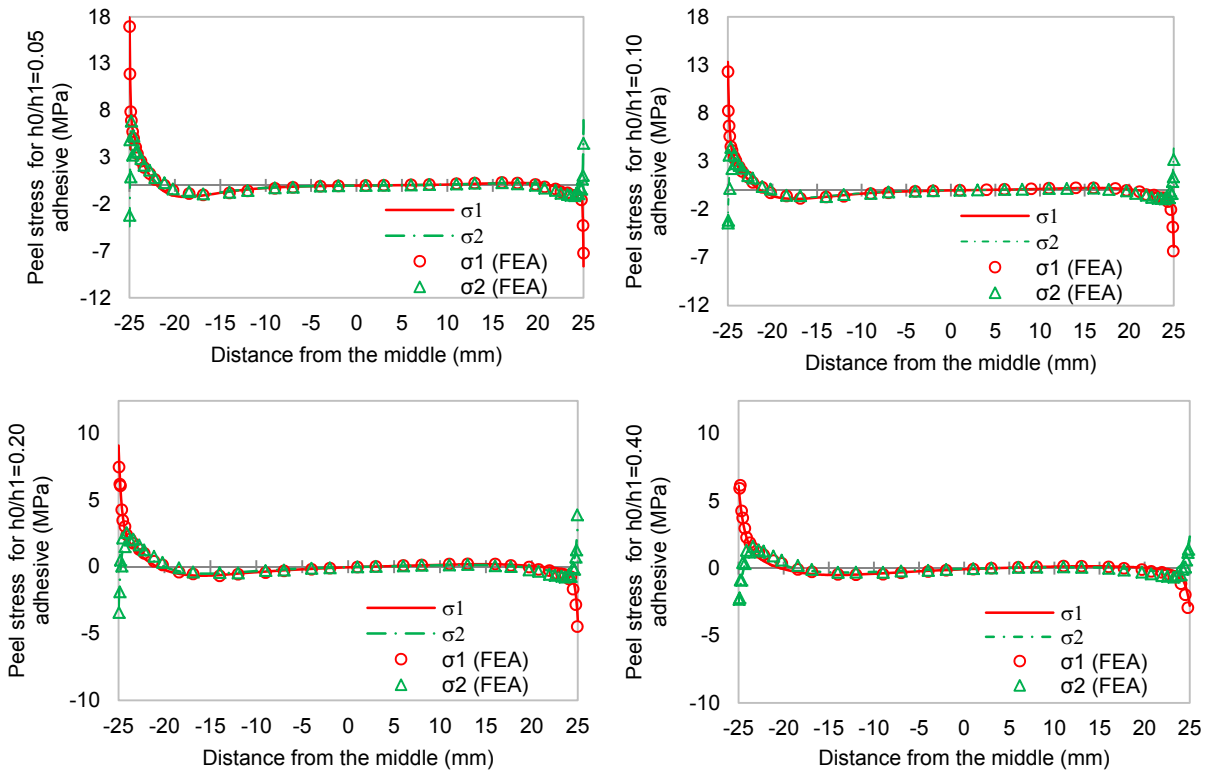

Fig. 2-7 Comparison the peel stresses along two interfaces obtained by the present analytical model and that by the FEA for different thicknesses of the adhesive layer.

Figure 2-9 shows the peel stresses along the inner interface with different thicknesses of the adhesive. While the peel stresses at the middle region of the interface are almost zero and negligible, strong stress concentrations occur near the ends of the interface, and this concentration increases with the thinner adhesive layer. All peel stresses are positive (i.e. tensile) near the exterior end of the interface, as shown in Fig. 2-9(b). While close to the inner end, this peel stresses become negative (i.e. compression) as demonstrated in Fig. 2-9(c). Since debonding

of the joint is more likely to occur under tensile stress, it can be expected that debonding of this interface will initiate near the exterior end.

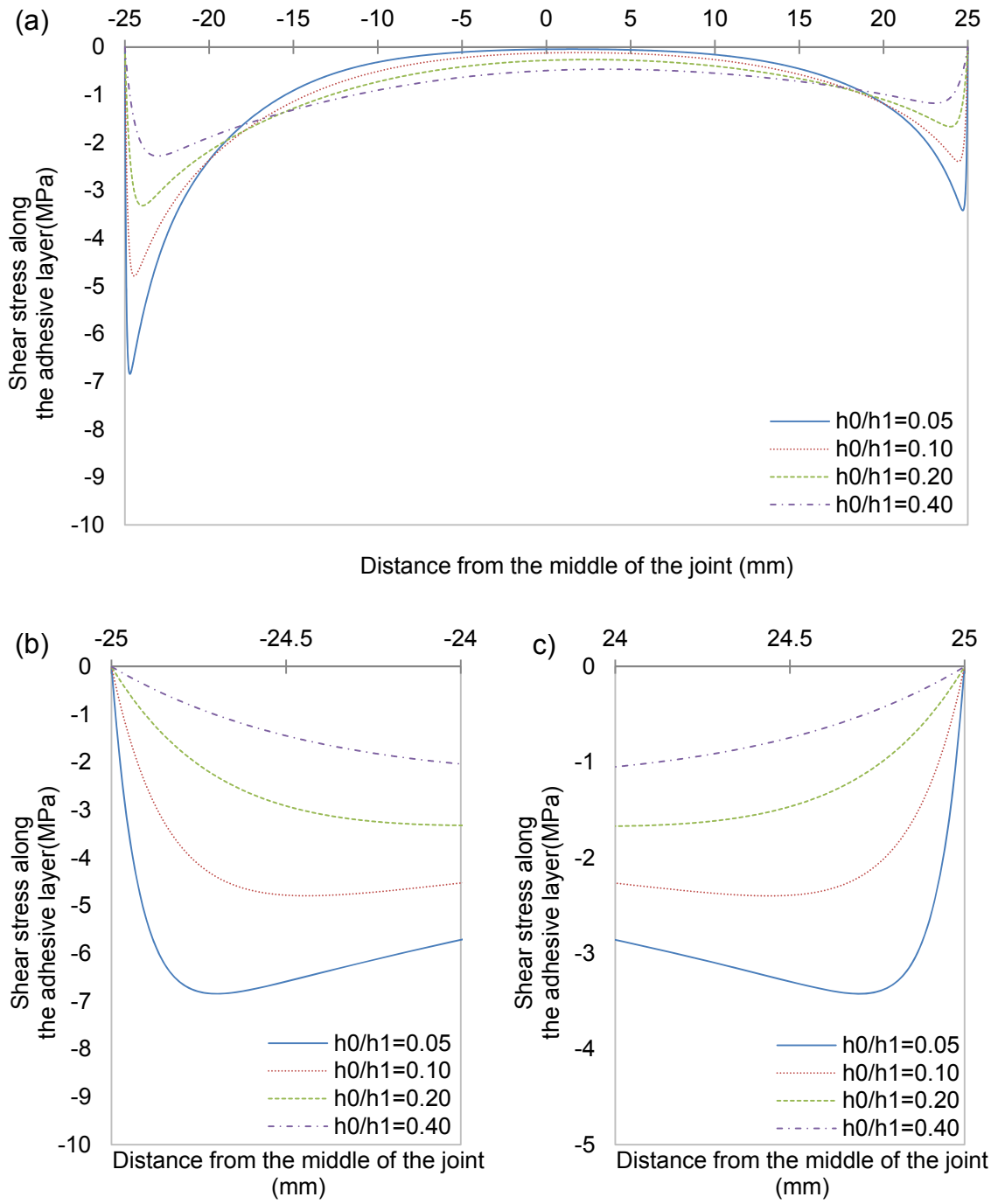

Fig. 2-8 Shear stress distribution of the adhesive layer of double-lap joints with different thicknesses: (a) shear stress distribution along the whole adhesive layer, (b) shear stress at the very left end of the adhesive layer, (c) shear stress at the very right end of the adhesive layer.

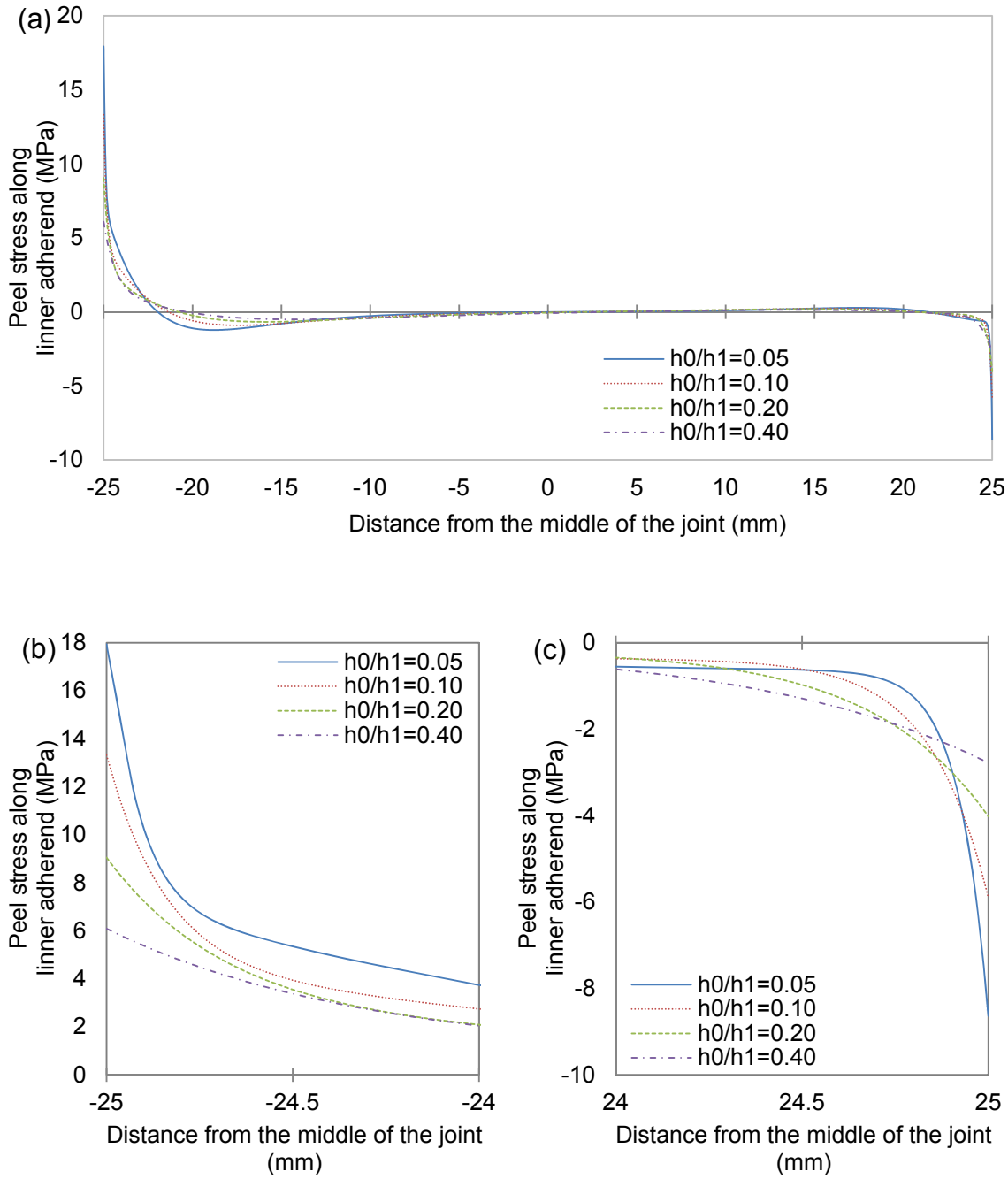

Fig. 2-9 Peel stress distribution along the inner interface of the double-lap joints: (a) peel stress distribution along the whole inner interface, (b) peel stress at the very left end the interface, (c) peel stress at the very right end of the interface.

The peel stresses along the outer interface (interface between the outer adherend and the adhesive layer) are shown in Fig. 2-10(a). It is interesting to observe that high concentration of tensile peel stress at a small region near the exterior end of the interface reduces and eventually becomes compressive approaching the exterior end. This is opposite to the peel stress at the same location along the inner interface shown in Fig. 2-9(a), which is positive. Because debonding is more likely to occur under tensile stress, the difference in the peel stresses along two interfaces suggests that debonding of the joint at the exterior end will more likely to initiate along the inner interface, rather than the outer interface. In the classical 2PEF model, peel stresses along these two interfaces are assumed as the same. As a result, it is unable to tell along which interface the debonding will imitate.

Near the inner end of the outer interface, peel stresses change from strong compressive stress concentration to tensile approaching the inner edge, as shown in Fig. 2-10(c). This is opposite to the peel stress at the same location along the inner interface, which is compressive as shown in Fig. 2-9(c). It is of great importance to identify the presence of tensile peel stress along the interface since the tensile peel stress can lead to debonding failure of the interface. The advantage and necessity of using the present model are clearly demonstrated by this example. If a 2PEF model is used, the peel stress at this location will be found as compressive, which may lead to a wrong conclusion on whether debonding can initiate at this end. The present model clearly shows that debond may initiate at the inner end of the interface along the outer interface, rather than the inner interface.

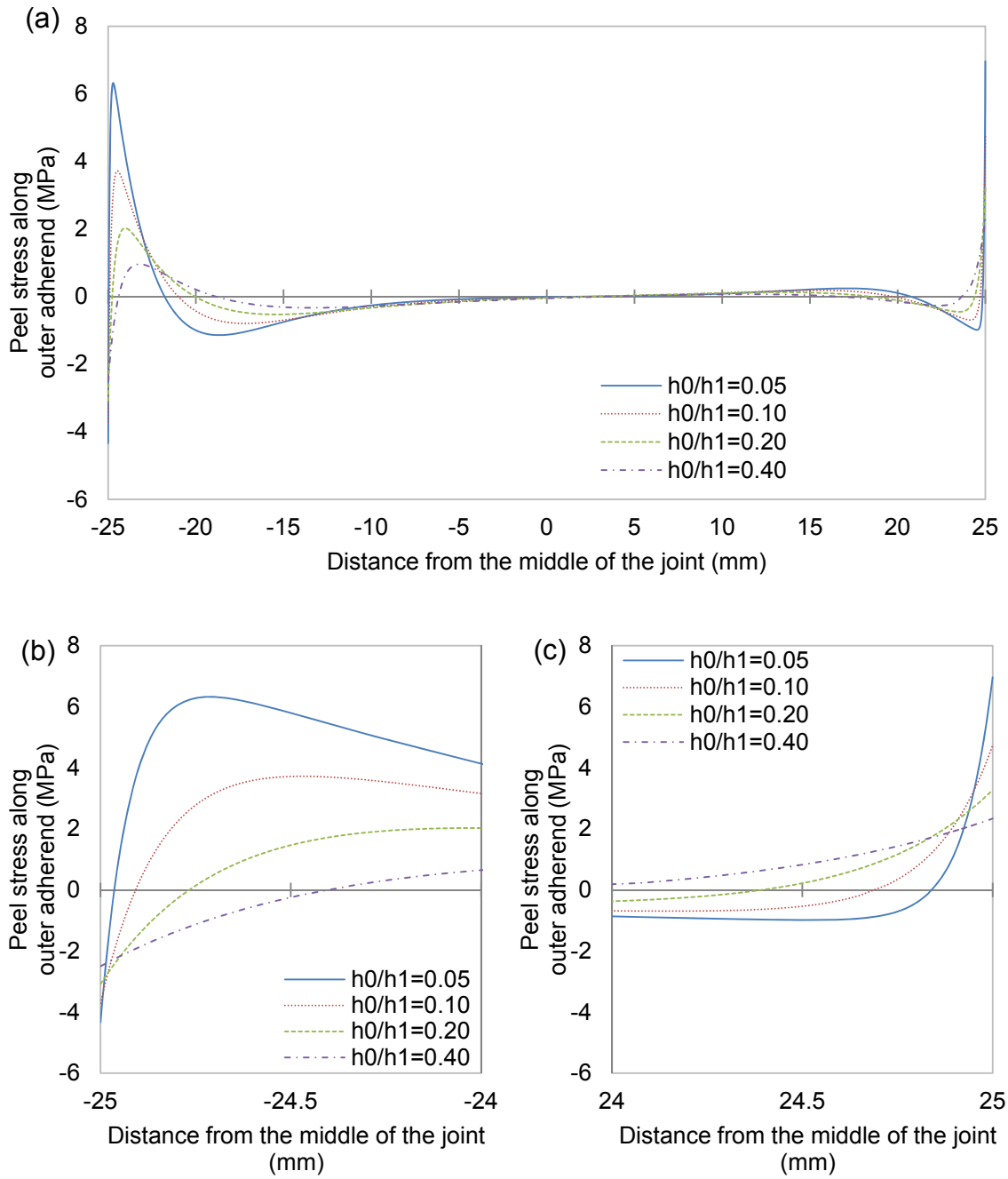

Fig. 2-10 Peel stress distribution along the outer interface of the double lap joints: (a) peel stress distribution along the whole interface, (b) peel stress at the very left end of the interface, (c) peel stress at the very right end of the interface.

Based on interface stress distributions obtained in Fig. 2-9 and Fig. 2-10, we can summarize the possible debonding modes of a typical double-lap joint as shown in Fig. 2-11(a).

Figure 2-11(a) shows the possible debonding mode of the joint caused by shear stress concentration. It can occur in any of four bonds of the joint. Because shear stress concentration is higher near the exterior edge, this debonding is more likely to initiate from the outer edge of the joint. Since peeling stress along the outer and inner interfaces could have different directions according to the present 3PEF model, the possible debonding initiation locations due to peel stresses can be predicted, as illustrated in Fig. 2-11(b). Assuming that only tensile peel stress can cause debonding along the adherend/adhesive interface, debonding should initiate either from the inner interface near the exterior end or from the outer interface near the interior end, as shown in Fig. 2-11(b). These statements can be verified by experimental result shown in Fig. 2-11(c). This shows the failure mode of a double-lap joint observed in experimental study by Tsai and Morton [27]. It can be seen that all the failure initiation location and mode in this sample can be predicted by the present 3PEF model.

2.4. Conclusion

To overcome the flaws in existing analytical solutions, a novel three-parameter elastic foundation model is established for adhesively bonded double-lap joints. Closed-from expression of interface stresses and internal forces of the adherends are obtained. This new model not only satisfies the zero-shear stress boundary condition at the free edge of the adhesive layer, but also produces two different peel stresses along two adherend/adhesive interfaces of the joint. The model is validated by its excellent agreement with existing solution and numerical solutions based on the FEA. By using this model, possible debonding initiation location of the double-lap joints can be correctly predicted, as confirmed by experimental observation.

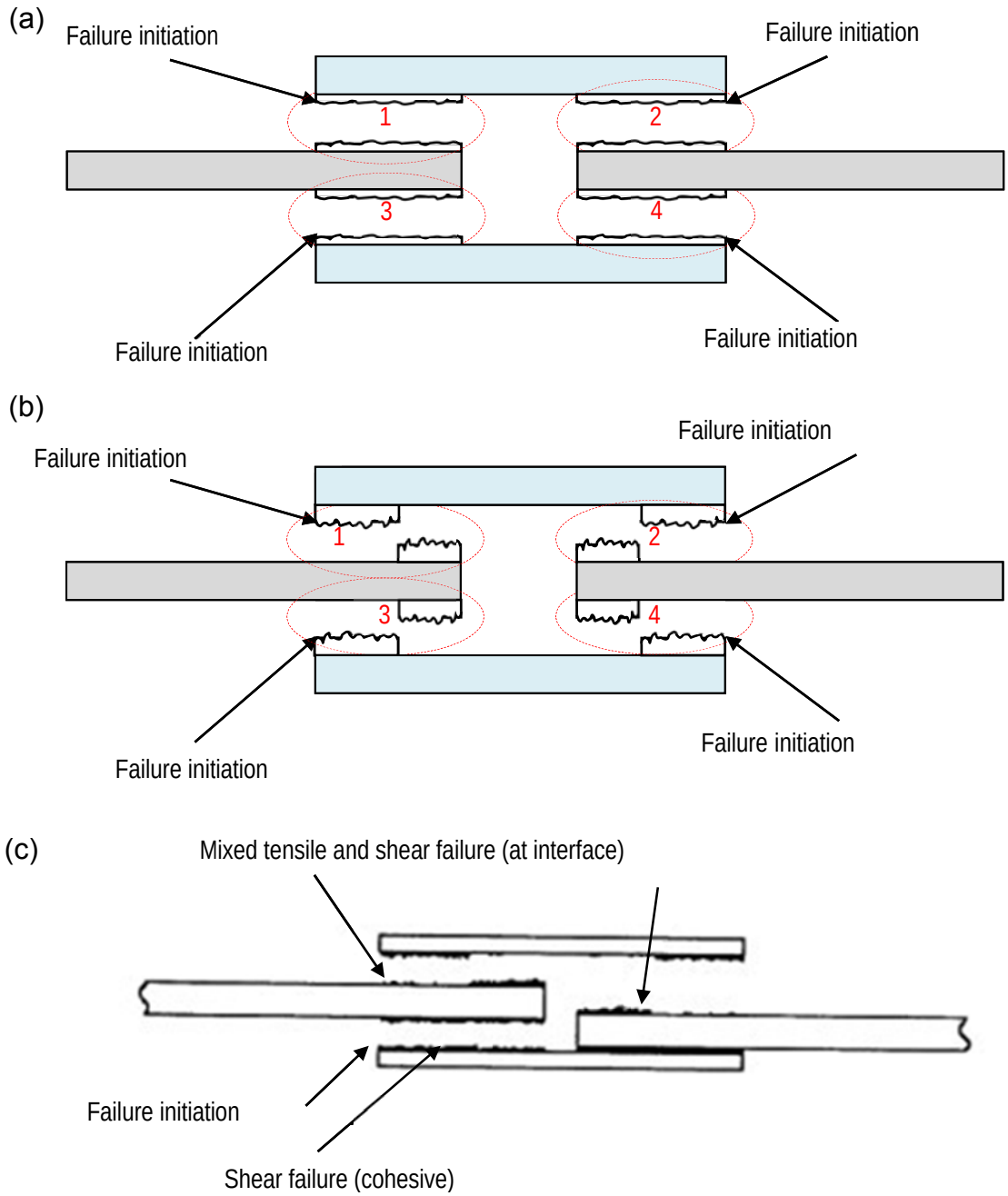

Fig. 2-11 Typical failure modes of a double-lap joint under tensile force: (a) shear failure, (b) tensile failure, (c) mixed tensile and shear failure for a unidirectional model ($[0]_{16}$) [27].

2.5. References

[1] Tong L, Soutis C. Recent advances in structural joints and repairs for composite materials. Springer Science & Business Media; 2013.

[2] Volkersen O. Die Nietkraftverteilung in zugbeanspruchten Nietverbindungen mit konstanten Laschenquerschnitten. Luftfahrtforschung 1938;15:41–7.

[3] Zhu Y, Kedward K. Methods of analysis and failure predictions for adhesively bonded joints of uniform and variable bondline thickness. Office of Aviation Research, Federal Aviation Administration; 2005.

[4] Goland M, Reissner E. The stresses in cemented joints. J Appl Mech 1944;11:A17–27.

[5] Hart-Smith LJ. Adhesive-bonded double-lap joints technical report, NASA CR-112235. Hampton, VA NASA Langley Res Cent 1973.

[6] Hart-Smith LJ. Adhesive-bonded double-lap joints technical report, NASA CR-112237. Hampton, VA NASA Langley Res Cent 1973.

[7] Hart-Smith LJ. Adhesive-bonded single-lap joints technical report, NASA CR-112236. Hampton, VA NASA Langley Res Cent 1973.

[8] Renton JW, Vinson JR. On the behavior of bonded joints in composite material structures. Eng Fract Mech 1975;7:41–60.

[9] Renton WJ, Vinson JR. The efficient design of adhesive bonded joints. J Adhes 1975;7:175–93.

[10] Yuceoglu U, Updike DP. Bending and shear deformation effects in lap joints. J Eng Mech Div 1981;107:55–76.

[11] Pickett AK, Hollaway L. The analysis of elastic-plastic adhesive stress in bonded lap joints in FRP structures. Compos Struct 1985;4:135–60.

[12] Thomsen OT. Elasto-static and elasto-plastic stress analysis of adhesive bonded tubular lap joints. Compos Struct 1992;21:249–59.

[13] Oplinger D. Effects of adherent deflections in single-lap joints. Int J Solids Struct 1994:2565–87.

[14] Tong L. Bond strength for adhesive-bonded single-lap joints. Acta Mech 1996;117:101–13.

[15] Tsai MY, Oplinger DW, Morton J. Improved theoretical solutions for adhesive lap joints. Int J Solids Struct 1998;35:1163–85.

[16] Her S-C. Stress analysis of adhesively-bonded lap joints. Compos Struct 1999;47:673–8.

[17] Luo Q, Tong L. Linear and higher order displacement theories for adhesively bonded lap joints. Int J Solids Struct 2004;41:6351–81.

[18] Mortensen F, Thomsen OT. Analysis of adhesive bonded joints: a unified approach. Compos Sci Technol 2002;62:1011–31.

[19] Delale F, Erdogan F, Aydinoglu MN. Stresses in adhesively bonded joints: a closed-form solution. J Compos Mater 1981;15:249–71.

[20] Wang J. Mechanics and fracture of hybrid material interface bond. 2003.

[21] Allman DJ. A theory for elastic stresses in adhesive bonded lap joints. Q J Mech Appl Math 1977;30:415–36.

[22] Ojalvo IU, Eidinoff HL. Bond thickness effects upon stresses in single-lap adhesive joints. AIAA J 1978;16:204–11.

[23] Chen D, Cheng S. An analysis of adhesive-bonded single-lap joints. J Appl Mech 1983;50:109–15.

[24] Frostig Y, Thomsen OT, Mortensen F. Analysis of adhesive-bonded joints, square-end, and spew-fillet-high-order theory approach. J Eng Mech 1999;125:1298–307.

[25] Wang J, Zhang C. Three-parameter, elastic foundation model for analysis of adhesively bonded joints. Int J Adhes Adhes 2009;29:495–502.

[26] De Bruyne NA. The strength of glued joints. Aircr Eng Aerosp Technol 1944;16:115–8.

[27] Tsai MY, Morton J. An investigation into the stresses in double-lap adhesive joints with laminated composite adherends. Int J Solids Struct 2010;47:3317–25.

[28] Gustafson PA, Bizard A, Waas AM. Dimensionless parameters in symmetric double lap joints: an orthotropic solution for thermomechanical loading. Int J Solids Struct 2007;44:5774–95.

[29] Diaz AD, Hadj-Ahmed R, Foret G, Ehrlacher A. Stress analysis in a classical double lap, adhesively bonded joint with a layerwise model. Int J Adhes Adhes 2009;29:67–76.

[30] Kerr AD. A study of a new foundation model. Acta Mech 1965;1:135–47.

[31] Avramidis IE, Morfidis K. Bending of beams on three-parameter elastic foundation. Int J Solids Struct 2006;43:357–75.

CHAPTER 3

THREE-PARAMETER VISCO-ELASTIC FOUNDATION MODEL OF ADHESIVELY BONDED JOINTS PART I: SINGLE-LAP JOINTS

Abstract

Adhesively bonded joints have been used in industry for many years. Shear and peel stress distributions along the adhesive-adherend interfaces play important roles in the integrity of the joints. This study establishes a new analytical model of these interface stresses in single-lap joints. The major innovation of this model is that the adhesive layer is modeled as a three-parameter viscoelastic foundation using a Standard Linear Solid (SLS) model to account for the viscoelastic behavior of the adhesive. This new model satisfies the zero-shear stress boundary at the free edges of the adhesive and predicts different peel stresses along two adherend/adhesive interfaces. Excellent agreement with FEA has been achieved by the present model, confirming the accuracy of the new model. Both the FEA and the present model show that the shear and peel stresses in the joint reduce with time, suggesting that the present model can properly capture the stress relaxation in adhesively bonded joints induced by the viscoelastic behaviors of the adhesive. Therefore, the present model provides an efficient tool to analyze the time-dependent behaviors of the adhesively bonded single-lap joint which is difficult for FEA. Different relaxation trends of the shear and peel stresses have also been revealed by this study.

3.1. Introduction

Adhesively bonded joints are widely used in composite structures to connect components due to their many advantages compared with other joining methods. However, premature failure due to debonding and peeling of the joint is the major concern of this technique. To address this issue, many analytical and numerical solutions have been proposed to precisely evaluate the stresses in the adhesively bonded joints. Among them, the most successful analytical model was proposed by Goland and Reissner (G-R model) [1], in which the adhesive layer is modeled as a series of uniformly distributed shear and vertical springs without interaction with each other. The G-R model is essentially a two-parameter elastic foundation model (2PEF) which only considers two parameters in the adhesive layer, a shear stress and a peel stress. Based on G-R model, a number of models have been developed for various problems [2–14]. However, all these models ignore the zero-shear-stress at the free ends of the adhesive layer. To overcome this shortcoming, Wang and Zhang (2009) proposed a new model of the adhesive layer. Unlike in the G-R model which assumes the peel stress along two adherend/adhesive interfaces are the same, Wang and Zhang's model removes this assumption and considers these two peel stresses are different [15]. As a result, three stresses (two peel stress and one shear stress) exist in the adhesive layer. To relate these three stresses to the deformation of the adhesive layer, Wang and Zhang model the adhesive layer as two layer of peel springs connected through a layer of shear string, which is essentially same as a three-parameter elastic foundation. Therefore, Wang and Zhang's model is referred to as three-parameter elastic foundation (3PEF), which can be viewed as a direct extension of the two-parameter elastic foundation model used in the G-R model. By adopting this 3PEF model, the zero-shear stress boundary condition at the free edge of the adhesive layer can be satisfied. More

importantly, different peel stress along two adherend/adhesive interfaces are produced by this model, which can predict more precisely where debonding will initiate.

Structural adhesives such as epoxy exhibit viscoelastic properties. Its material properties vary with time under different situations, especially in the regions of high stress concentration [16–19]. Such variation of material properties can induce redistributions of stresses and additional deformation, which could be significant during the service life of the structure and cause potential failure of the joints. Therefore, some efforts have been made to study the viscoelastic behaviors of the adhesive joints [20–36]. It has been shown in most of these studies that the ratio of the shear stress through the adhesive layer to the shear strength is an important contributor to the viscoelastic behavior of the adhesively bonded joints [2]. In the early studies, assumptions such as quasi-elastic approximation were made to simulate the bulk material. In this way, the viscoelastic response of the structures can be approximated as an elastic solution in which the elastic constants are replaced by time-dependent creep or relaxation functions of the materials [37]. Delale and Erdogan developed a viscoelastic solution for a symmetric adhesive joint [22]. Mirman and Knecht proposed another simple viscoelastic model through ignoring the peeling stress of the adhesive layer [17]. Two-parameter models assume both the shear and peel stresses are constant through the thickness of the adhesive layer, which introduces three inherent flaws to the model: (1) the zero-shear stress boundary condition at the free edge of the adhesive layer is not satisfied; (2) the equilibrium equation of the adhesive layer is not satisfied; and (3) the different peel stresses distributions along two adherend/adhesive interfaces are not distinguishable. Recently, a viscoelastic solution capable of predicting both the shear and peeling stresses along the interface was proposed by Zhang and Wang (2011) for a general adhesive joint recently [38].

This study tries to establish a novel three-parameter viscoelastic foundation model (3PVF) for the general adhesive bonded single-lap joints so that the time-dependent stress distribution in the joints can be calculated analytically. This new model is built on the 3PEF model of Zhang and Wang (2009) by considering the viscoelastic behavior of the adhesive layer. Both the symmetric and asymmetric single-lap joints are considered in this paper. Double-lap joints will be addressed in an accompanying paper.

3.2. Three-parameter viscoelastic foundation model (3PVF)

A general single-lap joint with applying loads shown in Fig. 3-1 is considered in this study. Therefore, this joint can be symmetric in which two adherends are identical or asymmetric in which two adherends are different. As shown in Fig. 3-1, the joint consists of three different layers: two adherends with thicknesses of h_1 and h_2, respectively, and one adhesive layer with thickness of h_0. The free body diagram of the overlap area of the joint is shown in Fig. 3-2. Modeling two adherends as Timoshenko's beams, we have

$$U_i(x_i, z_i, t) = u_i\,(x_i, t) + z_i\phi_i(x_i, t),\ W_i(x_i, z_i, t) = w_i(x_i, t), \tag{1}$$

where subscripts $(i=1, 2)$ represent the top and bottom adherends, respectively. $u_i(x_i,t)$, $\phi_i(x_i,t)$ and $w_i(x_i,t)$ are the axial displacement, the rotation and the deflection at the neutral axis of the beam i, respectively. Since $x_1 = x_2 = x$, subscript i ($i = 1, 2$) in displacement functions shown in Eq. (1) will be ignored thereafter. The constitutive equations for each adherend can be written as

$$N_i(x,t) = C_i\frac{\partial u_i(x,t)}{\partial x},\quad M_i(x,t) = D_i\frac{\partial \phi_i(x,t)}{\partial x},\quad Q_i(x,t) = B_i\left(\phi_i(x,t) + \frac{\partial w_i(x,t)}{\partial x}\right), \tag{2}$$

where $N_i(x,t)$, $M_i(x,t)$, $Q_i(x,t)$ are the resultants of the axial force, the bending moment and the transverse shear force in each adherend, respectively; C_i, D_i and B_i are the axial, bending and shear stiffness coefficients of the beam i, respectively, and they can be calculated using the following equation

$$C_i = E_i b h_i,\ D_i = \frac{E_i b h_i^3}{12},\ B_i = \kappa G_i b h_i, \tag{3}$$

E_i and G_i are the longitudinal and the shear modulus of elasticity, and h_i is the thickness of each layer. The width of the joint is equal to b for all layers. κ is the shear correction coefficient and chosen as *5/6* in this study.

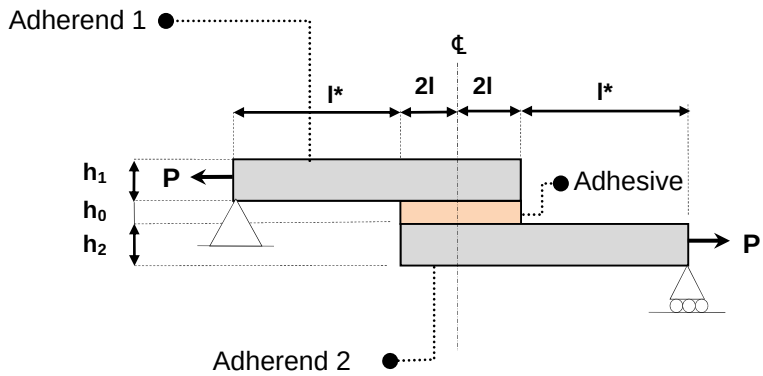

Fig. 3-1 A simply supported single-lap joint.

3.2.1. Asymmetric single-lap joint

Consider an asymmetric joint first. A free body diagram of the joint is shown in Fig. 3-2. This study assumes that the shear stress is a constant through the thickness of the adhesive layer; while the peel stress along the interface between the top adherend (top interface) and the adhesive layer $\sigma_1(x,t)$ and the peel stress along the interface between the bottom adherend and the adhesive layer (bottom interface) $\sigma_2(x,t)$ have different values. Then equilibrium equations of two adherends can be given as

$$\frac{\partial N_1(x,t)}{\partial x} = b\tau(x,t), \qquad \frac{\partial M_1(x,t)}{\partial x} = Q_1(x,t) - \frac{h_1}{2} b\tau(x,t), \qquad \frac{\partial Q_1(x,t)}{\partial x} = b\sigma_1(x,t), \tag{4a}$$

$$\frac{\partial N_2(x,t)}{\partial x} = -b\tau(x,t), \qquad \frac{\partial M_2(x,t)}{\partial x} = Q_2(x,t) - \frac{h_2}{2} b\tau(x,t), \qquad \frac{\partial Q_2(x,t)}{\partial x} = -b\sigma_2(x,t), \tag{4b}$$

$$Q_1(x,t) = \frac{\partial M_1(x,t)}{\partial x} + \frac{h_1}{2}\frac{\partial N_1(x,t)}{\partial x}, \tag{5a}$$

$$Q_2(x,t) = \frac{\partial M_2(x,t)}{\partial x} - \frac{h_2}{2}\frac{\partial N_2(x,t)}{\partial x}. \tag{5b}$$

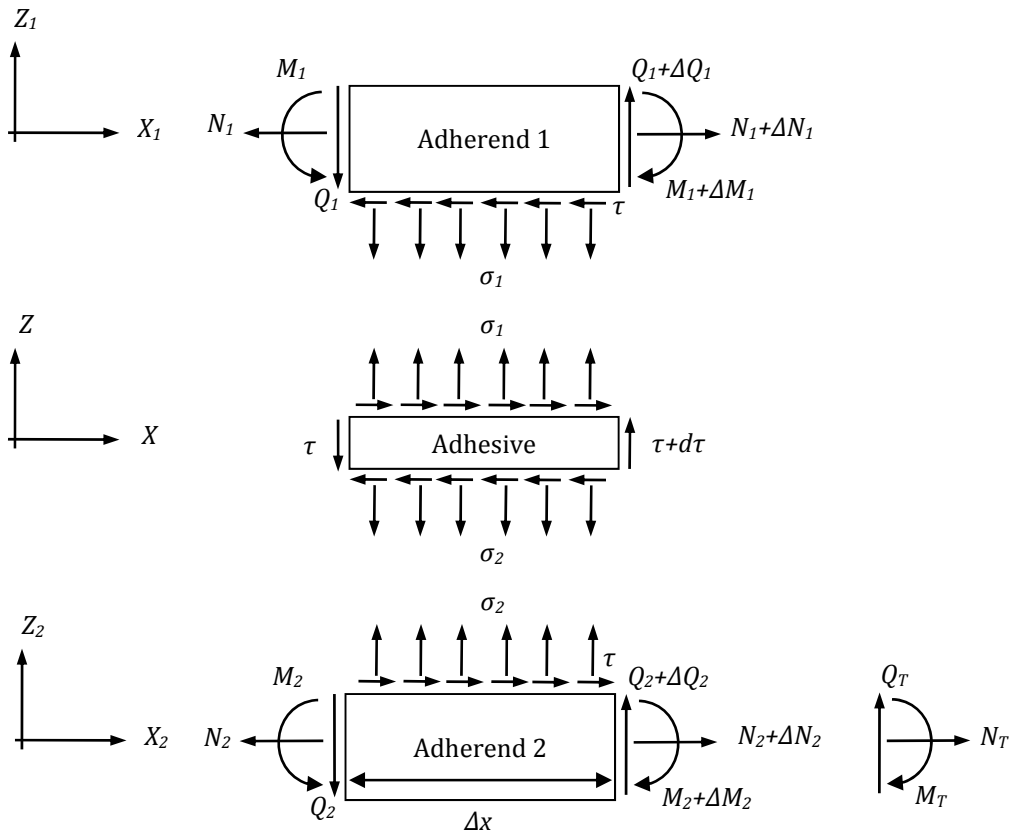

Fig. 3-2 Free body diagram of the adhesively bonded single-lap joint.

As shown in Fig. 3-1, the global equilibrium condition of the joint requires

$$N_T(x,t) = N_1(x,t) + N_2(x,t), \tag{6a}$$

$$M_T(x,t) = M_1(x,t) + M_2(x,t) + N_1(x,t)\left(\frac{h_1+h_2}{2} + h_0\right), \tag{6b}$$

$$Q_T(x,t) = Q_1(x,t) + Q_2(x,t). \tag{6c}$$

Since the adhesive layer is much softer than the adherends, its axial force and bending moment are neglected, as shown in Fig. 3-3(a). Similar to the classical G-R model, the shear stress through the thickness of the adhesive layer is assumed as a constant. Considering the force equilibrium of the adhesive layer shown in Fig. 3-3(a), we have

$$\frac{\partial\tau(x,t)}{\partial x} = \frac{\sigma_2(x,t)-\sigma_1(x,t)}{h_a}. \tag{7}$$

Since $\tau(x,t)$ is not a constant along the whole interface, the left hand side of Eq. (7) is nonzero, suggesting peel stresses $\sigma_1(x,t)$ and $\sigma_2(x,t)$ must be different. To account for Eq. (7), we can model the adhesive layer as two linear springs connected by a shear layer as shown in Fig. 3-3(b). Unlike the 2PEF model, in which the transverse (vertical) displacement of the adhesive layer is a constant through the thickness of the adhesive layer, the new model shown in Fig. 3-3(b) assumes the vertical displacement at the mid-plane (w_a) of the adhesive is different from the ones on the top and bottom surfaces of the adhesive layer. As a result, strains in the upper and lower halves of the adhesive layer can be obtained as

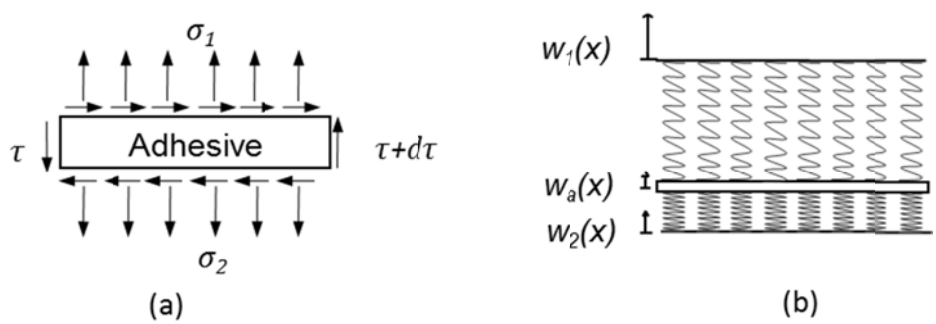

Fig. 3-3 Deformation model of the adhesive layer: (a) stress equilibrium of the adhesive layer, (b) deformation model of the adhesive layer.

$$\gamma_{xz}(x,t) = \frac{1}{h_0}\left(u_1(x,t) - \frac{h_1}{2}\phi_1(x,t) - u_2(x,t) - \frac{h_2}{2}\phi_2(x,t)\right) + \frac{\partial w_a(x,t)}{\partial x}, \tag{8a}$$

$$\varepsilon_{z1}(x,t) = \frac{2}{h_0}\left(w_1(x,t) - w_a(x,t)\right), \tag{8b}$$

$$\varepsilon_{z2}(x,t) = \frac{2}{h_0}\left(w_a(x,t) - w_2(x,t)\right), \tag{8c}$$

$$\varepsilon_x(x,t) = \frac{1}{2}\left(\frac{\partial u_1(x,t)}{\partial x} - \frac{h_1}{2}\frac{\partial\phi_1(x,t)}{\partial x} + \frac{\partial u_2(x,t)}{\partial x} + \frac{h_2}{2}\frac{\partial\phi_2(x,t)}{\partial x}\right), \tag{8d}$$

where $\gamma_{xz}(x, t)$ is the shear strain within the adhesive layer; $\varepsilon_{zk}(x, t)$ (k = 1, 2) are peel strains (normal strain in *z*-direction in Fig. 3-2) within the upper and lower halves of the adhesive layer,

respectively; $\varepsilon_x(x, t)$ is the normal strain in the x-direction of the adhesive layer; $w_a(x,t)$ is the displacement of the mid-plane of the adhesive layer in z-direction. Then the hydrostatic stress-strain state of the adhesive layer for the upper ($k = 1$) and lower ($k = 2$) halves can be expressed as

$$e_k = \frac{1}{3}\left(\varepsilon_x + \varepsilon_y + \varepsilon_{zk}\right), \quad k = 1,2, \tag{9a}$$

$$s_k = \frac{1}{3}(\sigma_x + \sigma_{zk}), \quad k = 1,2, \tag{9b}$$

where ε_x and σ_x represent the normal strains and stresses in the top ($k = 1$) and bottom ($k = 2$) halves of the adhesive layer, respectively. The strains/stress tensor in each half of the adhesive layer can then be decomposed into hydrostatic and deviatoric parts as

$$\left[e_{ij}\right] = \begin{bmatrix} \varepsilon_x & 0 & \frac{\gamma_{xz}}{2} \\ 0 & \varepsilon_y & 0 \\ \frac{\gamma_{xz}}{2} & 0 & \varepsilon_{zk} \end{bmatrix} = \begin{bmatrix} e_k & 0 & 0 \\ 0 & e_k & 0 \\ 0 & 0 & e_k \end{bmatrix} + \begin{bmatrix} \varepsilon_x - e_k & 0 & \frac{\gamma_{xz}}{2} \\ 0 & \varepsilon_y - e_k & 0 \\ \frac{\gamma_{xz}}{2} & 0 & \varepsilon_{zk} - e_k \end{bmatrix}, \quad k = 1,2, \tag{10a}$$

$$\left[s_{ij}\right] = \begin{bmatrix} \sigma_x & 0 & \tau_{xz} \\ 0 & 0 & 0 \\ \tau_{xz} & 0 & \sigma_k \end{bmatrix} = \begin{bmatrix} s_k & 0 & 0 \\ 0 & s_k & 0 \\ 0 & 0 & s_k \end{bmatrix} + \begin{bmatrix} \sigma_x - s_k & 0 & \tau_{xz} \\ 0 & -s_k & 0 \\ \tau_{xz} & 0 & \sigma_k - s_k \end{bmatrix}, \quad k = 1,2. \tag{10b}$$

In Eq. (10b), $\tau_{xz} = \tau(x,t)$. A standard linear solid viscoelastic model (SLS) of Meshgin et al. [32] is used to simulate the viscoelastic behavior of the adhesive layer (Fig. 3-4) [32]. This model consists of a linear spring in parallel with a Maxwell model (an elastic spring and a viscous damper connected in series). In this model, η, the viscous damping coefficient, and k_1 and k_2 , the stiffness coefficients of two springs, are constant. Constitutive equations of any isotropic viscoelastic material, modeled by the SLS model are given by

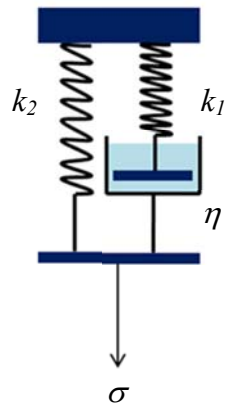

Fig. 3-4 Standard Linear Solid Model [32].

$$P_1(s_{ij}) = Q_1(e_{ij}), \quad (i,j) = 1,2,3, \tag{11a}$$

$$P_2(s_k) = Q_2(e_k), \quad k = 1,2, \tag{11b}$$

$$P_1 = a_1 + \frac{\partial}{\partial t}, \quad Q_1 = b_1 + b_2\frac{\partial}{\partial t}, \tag{11c}$$

where $a_1=k_2/\eta=1/t_0$, $b_1= (k_1.k_2)/\eta=k_1/t_0$, $b_2=k_1+k_2$; and t_0 is the retardation time; P_1 and Q_1 are the differential operators and given by Eq. (11c). By inserting the deviatoric and hydrostatic components of the stress and strain tensors into Eqs. (11a) and (11b), the governing equations can be rewritten as

$$P_1(2\sigma_x - \sigma_k) = Q_1(2\varepsilon_x - \varepsilon_y - \varepsilon_{zk}), \quad k = 1,2, \tag{12a}$$

$$P_2(2\sigma_k - \sigma_x) = Q_1(2\varepsilon_{zk} - \varepsilon_x - \varepsilon_y), \quad k = 1,2, \tag{12b}$$

$$-P_1(\sigma_x + \sigma_k) = Q_1(2\varepsilon_y - \varepsilon_x - \varepsilon_{zk}), \quad k = 1,2, \tag{12c}$$

$$P_1(\tau_{xz}) = \frac{1}{2}Q_1(\gamma_{xz}), \quad k = 1,2, \tag{12d}$$

$$P_2(\sigma_x + \sigma_k) = Q_2(\varepsilon_x + \varepsilon_y + \varepsilon_{zk}), \quad k = 1,2. \tag{12e}$$

Since most viscoelastic materials behave as an elastic material under the hydrostatic pressure state, the governing equation of the hydrostatic tensors can be simplified as

$$P_2 = 1, \quad Q_2 = 3K, \tag{13}$$

where K is the Bulk modulus of the adhesive layer. By the definition, $K = \frac{E_a G_a}{3(3G_a - E_a)}$.

By substituting Eqs. (12e) and (13) into Eqs. (12a) and (12c), ε_y can be eliminated and the following equation is established

$$\begin{aligned}&(2Q_1 + 3KP_1)\big(Q_1(2\varepsilon_x - \varepsilon_{zk}) - P_1(6K(\varepsilon_x + \varepsilon_{zk}) - 3\sigma_k)\big)\\&-(6KP_1 + Q_1)\big(Q_1(\varepsilon_x + \varepsilon_{zk}) - 3KP_1(\varepsilon_x + \varepsilon_{zk})\big) = 0, \qquad k = 1,2.\end{aligned} \tag{14}$$

Substituting Eq. (14) into Eq. (11c) gives

$$\left(a_{10} + a_{11}\frac{\partial}{\partial t} + a_{12}\frac{\partial^2}{\partial t^2}\right)\varepsilon_x + \left(b_{10} + b_{11}\frac{\partial}{\partial t} + b_{12}\frac{\partial^2}{\partial t^2}\right)\varepsilon_{zk} + \left(c_{10} + c_{11}\frac{\partial}{\partial t} + c_{12}\frac{\partial^2}{\partial t^2}\right)\sigma_k = 0, \tag{15}$$

where

$$\begin{aligned}&a_{10} = 3b_1^2 - 9a_1b_1K, && a_{11} = 6b_1b_2 - 9b_1K - 9a_1b_2K, && a_{12} = 3b_2^2 - 9b_2K,\\&b_{10} = -3b_1^2 - 18a_1b_1K, && b_{11} = -6b_1b_2 - 18b_1K - 18a_1b_2K, && b_{12} = -3b_2^2 - 18b_2K,\\&c_{10} = 6a_1b_1 + 9a_1^2K, && c_{11} = 6b_1 + 6a_1b_2 + 18a_1K\,, && c_{12} = 6b_2.\end{aligned}$$

By substituting Eqs. (8) and (4) into Eq. (15) and differentiating both sides of the equation twice yields

$$\begin{aligned}&\left(a_{10} + a_{11}\frac{\partial}{\partial t} + a_{12}\frac{\partial^2}{\partial t^2}\right)\left(\frac{1}{2}\left(\frac{1}{C_1} - \frac{1}{C_2} - \frac{h_2}{2D_2}\left(\frac{h_1+h_2}{2} + h_0\right)\right)\frac{\partial^2 N_1(x,t)}{\partial x^2} - \left(\frac{h_1}{4D_1}\frac{h_2}{4D_2}\right)\frac{\partial^2 M_1(x,t)}{\partial x^2}\right) +\\&\frac{2}{h0}\left(b_{10} + b_{11}\frac{\partial}{\partial t} + b_{12}\frac{\partial^2}{\partial t^2}\right)\left(\frac{1}{B_1}\frac{\partial^2 M_1(x,t)}{\partial x^2} + \frac{1}{B1}\left(\frac{h_1}{2}\right)\frac{\partial^2 N_1(x,t)}{\partial x^2} - \frac{M_1(x,t)}{D_1} - \frac{\partial^2 w_a(x,t)}{\partial x^2}\right) +\\&\frac{1}{b}\left(c_{10} + c_{11}\frac{\partial}{\partial t} + c_{12}\frac{\partial^2}{\partial t^2}\right)\left(\frac{\partial^4 M_1(x,t)}{\partial x^4} + \left(\frac{h_1}{2}\right)\frac{\partial^4 N_1(x,t)}{\partial x^4}\right) = 0,\end{aligned} \tag{16a}$$

$$\begin{aligned}&\frac{2}{h0}\left(b_{10} + b_{11}\frac{\partial}{\partial t} + b_{12}\frac{\partial^2}{\partial t^2}\right)\left(\frac{1}{B_2}\frac{\partial^2 M_1(x,t)}{\partial x^2} + \frac{1}{B2}\left(\frac{h_1}{2} + h_0\right)\frac{\partial^2 N_1(x,t)}{\partial x^2} + \frac{1}{D_2}\Big(M_T(x,t) - M_{1(x,t)} -\right.\\&\left.N_1(x,t)\left(\frac{h_1+h_2}{2} + h_0\right)\Big) + \frac{\partial^2 w_a(x,t)}{\partial x^2}\right) + \frac{1}{b}\left(c_{10} + c_{11}\frac{\partial}{\partial t} + c_{12}\frac{\partial^2}{\partial t^2}\right)\left(\frac{\partial^4 M_1(x,t)}{\partial x^4} + \left(\frac{h_1}{2} +\right.\right.\\&\left.\left.h_0\right)\frac{\partial^4 N_1(x,t)}{\partial x^4}\right) = 0.\end{aligned} \tag{16b}$$

By substituting Eq. (8a) into (12d), the following expression can be obtained

$$P_1(\tau,t)=\frac{1}{2}Q_1\ \left(\frac{1}{\mathrm{h}_0}\left(u_1(x,t)-\frac{h_1}{2}\phi_1(x,t)-u_2(x,t)-\frac{h_2}{2}\phi_2(x,t)\right)+\frac{\partial w_a(x,t)}{\partial x}\right). \tag{17}$$

Differentiating both sides of Eq. (17) with respect to x once, and then substituting Eq. (4) into it gives

$$P_1\left(\frac{1}{b}\frac{\partial^2 N_1(x,t)}{\partial x^2}\right)=\frac{1}{2}Q_1\left(A_{11}M_1(x,t)+A_{12}N_1(x,t)+A_{13}M_T(x,t)+A_{14}N_T(x,t)+\frac{\partial^2 w_a(x,t)}{\partial x^2}\right), \tag{18}$$

where

$$A_{11}=\frac{1}{h_0}\left(\frac{h_2}{2}\ \frac{1}{D_2}-\frac{h_1}{2}\frac{1}{D_1}\right),\qquad A_{12}=\frac{1}{h_0}\left(\frac{1}{C_1}+\frac{1}{C_2}+\frac{h_2}{2}\frac{1}{D_2}\left(\frac{h_1+h_2}{2}+h_0\right)\right),$$

$$A_{13}=-\frac{h_2}{2D_2h_0},\qquad A_{14}=-\frac{1}{C_2h_0}.$$

Applying Laplace transform on both sides of Eq. (18) yields

$$\frac{\partial^2 w_{aL}(x,s)}{\partial x^2}=\frac{B_{11}(s)}{B_{10}(s)}\frac{\partial^2 N_{1L}(x,s)}{\partial x^2}+\frac{B_{12}(s)}{B_{10}(s)}M_{1L}(x,s)+\frac{B_{13}(s)}{B_{10}}N_{1L}(x,s)+\frac{B_{14}(s)}{B_{10}(s)}M_{TL}(x,s)+\frac{B_{15}(s)}{B_{10}(s)}N_{TL}(x,s). \tag{19}$$

where $w_{aL}(x,s)$, $M_{1L}(x,s)$, $N_{1L}(x,s)$, $M_{TL}(x,s)$, and $N_{TL}(x,s)$ are Laplace transforms of $w_a(x,t)$, $M_1(x,t)$, $N_1(x,t)$, $M_T(x,t)$, and $N_T(x,t)$, respectively; and

$$B_{10}(s)=\frac{1}{2}(b_1+b_2s),\qquad B_{11}(s)=\frac{1}{b}(a_1+s),\qquad B_{12}(s)=-\frac{A_{11}}{2}(b_1+b_2s),$$

$$B_{13}(s)=-\frac{A_{12}}{2}(b_1+b_2s),\quad B_{14}(s)=-\frac{A_{13}}{2}(b_1+b_2s),\quad B_{15}(s)=-\frac{A_{14}}{2}(b_1+b_2s).$$

Applying Laplace transform on both sides of Eq. (16) gives

$$B_{21}(s)\partial^4\frac{M_{1L}(x,s)}{\partial x^4}+B_{22}(s)\frac{\partial^4 N_{1L}(x,s)}{\partial x^4}+B_{23}(s)\frac{\partial^2 M_{1L}(x,s)}{\partial x^2}+B_{24}(s)\frac{\partial^2 N_{1L}(x,s)}{\partial x^2}+B_{25}(s)M_{1L}(x,s)+B_{26}(s)\frac{\partial^2 w_{aL}(s)}{\partial x^2}=0, \tag{20a}$$

$$B_{31}(s)\partial^4\frac{M_{1L}(x,s)}{\partial x^4}+B_{32}(s)\frac{\partial^4 N_{1L}(x,s)}{\partial x^4}+B_{33}(s)\frac{\partial^2 M_{1L}(x,s)}{\partial x^2}+B_{34}(s)\frac{\partial^2 N_{1L}(x,s)}{\partial x^2}+$$
$$B_{35}(s)M_{1L}(x,s)+B_{36}(s)N_{1L}(x,s)+B_{37}(s)M_{TL}(s)+B_{38}(s)\frac{\partial^2 w_{aL}(s)}{\partial x^2}=0, \tag{20b}$$

where

$B_{21}(s)=\frac{1}{b}(c_{10}+c_{11}s+c_{12}s^2)$, $B_{22}(s)=\frac{h_1}{2b}(c_{10}+c_{11}s+c_{12}s^2)$,

$B_{23}(s)=-\left(\frac{h_1}{4D_1}+\frac{h_2}{4D_2}\right)(a_{10}+a_{11}s+a_{12}s^2)+(\frac{2}{h_0B_1})(b_{10}+b_{11}s+b_{12}s^2)$,

$B_{24}(s)=\frac{1}{2}\left(\frac{1}{C_1}-\frac{1}{C_2}-\frac{h_2}{2D_2}\left(\frac{h_1+h_2}{2}+h_0\right)\right)(a_{10}+a_{11}s+a_{12}s^2)+(\frac{h_1}{h_0B_1})(b_{10}+b_{11}s+b_{12}s^2)$,

$B_{25}(s)=-\frac{2}{D_1h_0}(b_{10}+b_{11}s+b_{12}s^2)$, $B_{26}(s)=-\frac{2}{h_0}(b_{10}+b_{11}s+b_{12}s^2)$,

$B_{31}(s)=\frac{1}{b}(c_{10}+c_{11}s+c_{12}s^2)$, $B_{32}(s)=\frac{1}{b}\left(\frac{h_1}{2}+h_0\right)(c_{10}+c_{11}s+c_{12}s^2)$,

$B_{33}(s)=-\left(\frac{h_1}{4D_1}+\frac{h_2}{4D_2}\right)(a_{10}+a_{11}s+a_{12}s^2)+\left(\frac{2}{h_0B_2}\right)(b_{10}+b_{11}s+b_{12}s^2)$,

$B_{34}(s)=\frac{1}{2}\left(\frac{1}{C_1}-\frac{1}{C_2}-\frac{h_2}{2D_2}\left(\frac{h_1+h_2}{2}+h_0\right)\right)(a_{10}+a_{11}s+a_{12}s^2)$,

$+\left(\frac{2}{h_0B_2}\right)\left(\frac{h_1}{2}+h_0\right)(b_{10}+b_{11}s+b_{12}s^2)$,

$B_{35}(s)=-\frac{2}{D_2h_0}(b_{10}+b_{11}s+b_{12}s^2)$, $B_{36}(s)=-\frac{2}{h_0D_2}\left(\frac{h_1+h_2}{2}+h_0\right)(b_{10}+b_{11}s+b_{12}s^2)$,

$B_{37}(s)=\frac{2}{D_2h_0}(b_{10}+b_{11}s+b_{12}s^2)$, $B_{38}(s)=\frac{2}{h_0}(b_{10}+b_{11}s+b_{12}s^2)$.

Substituting Eq. (19) into the Eq. (20) yields

$$\partial^4\frac{M_{1L}(x,s)}{\partial x^4}+C_{11}(s)\frac{\partial^4 N_{1L}(x,s)}{\partial x^4}+C_{12}(s)\frac{\partial^2 M_{1L}(x,s)}{\partial x^2}+C_{13}(s)\frac{\partial^2 N_{1L}(x,s)}{\partial x^2}+$$
$$C_{14}(s)M_{1L}(x,s)+C_{15}(s)N_{1L}(s)+C_{16}(s)M_{TL}(x,s)+C_{17}(s)N_{TL}(x,s)=0, \tag{21a}$$

$$\partial^4\frac{M_{1L}(x,s)}{\partial x^4}+C_{21}(s)\frac{\partial^4 N_{1L}(x,s)}{\partial x^4}+C_{22}(s)\frac{\partial^2 M_{1L}(x,s)}{\partial x^2}+C_{23}(s)\frac{\partial^2 N_{1L}(x,s)}{\partial x^2}+$$
$$C_{24}(s)M_{1L}(x,s)+C_{25}(s)N_{1L}(s)+C_{26}(s)M_{TL}(x,s)+C_{27}(s)N_{TL}(x,s)=0, \tag{21b}$$

where

$$C_{11}(s) = \frac{B_{22}(ss)}{B_{21}(s)}, \qquad C_{12}(s) = \frac{B_{23}(s)}{B_{21}(s)}, \qquad C_{13}(s) = \frac{1}{B_{21}(s)}\left(B_{24}(s) + \frac{B_{26}(s)B_{11}(s)}{B_{10}(s)}\right),$$

$$C_{14}(s) = \frac{1}{B_{21}(s)}\left(B_{25}(s) + \frac{B_{26}(s)B_{12}(s)}{B_{10}(s)}\right), \quad C_{16}(s) = \frac{B_{26}(s)B_{14}(s)}{B_{10}(s)B_{21}(s)},$$

$$C_{15}(s) = \frac{B_{26}(s)B_{13}(s)}{B_{10}(s)B_{21}(s)}, \qquad C_{17}(s) = \frac{B_{26}(s)B_{15}(s)}{B_{10}(s)B_{21}(s)},$$

$$C_{21}(s) = \frac{B_{32}(ss)}{B_{31}(s)}, \qquad C_{22}(s) = \frac{B_{33}(s)}{B_{31}(s)}, \qquad C_{23}(s) = \frac{1}{B_{31}(s)}\left(B_{34}(s) + \frac{B_{38}(s)B_{11}(s)}{B_{10}(s)}\right),$$

$$C_{24}(s) = \frac{1}{B_{31}(s)}\left(B_{35}(s) + \frac{B_{38}(s)B_{12}(s)}{B_{10}(s)}\right), \quad C_{25}(s) = \frac{1}{B_{31}(s)}\left(B_{36}(s) + \frac{B_{38}(s)B_{13}(s)}{B_{10}(s)}\right),$$

$$C_{26}(s) = \frac{1}{B_{31}(s)}\left(B_{37}(s) + \frac{B_{38}(s)B_{14}(s)}{B_{10}(s)}\right), \quad C_{27}(s) = \frac{B_{38}(s)B_{15}(s)}{B_{10}(s)B_{31}(s)}.$$

Equation (21) is a fourth-order differential equation in term of $M_{1L}(x,s)$ and $N_{1L}(x,s)$. By subtracting Eq. (21a) from Eq. (21b), we have

$$\frac{\partial^2 M_{1L}(x,s)}{\partial x^2} = D_{11}(s)\frac{\partial^4 N_{1L}(x,s)}{\partial x^4} + D_{12}(s)\frac{\partial^2 N_{1L}(x,s)}{\partial x^2} + D_{13}(s)M_{1L}(x,s) + D_{14}(s)N_{1L}(x,s) + D_{15}(s)M_{TL}(x,s) + D_{16}(s)M_{TL}(x,s), \tag{22}$$

where

$$D_{11}(s) = -\frac{C_{21}(s)-C_{11}(s)}{C_{22}(s)-C_{12}(s)}, \quad D_{12}(s) = -\frac{C_{23}(s)-C_{13}(s)}{C_{22}(s)-C_{12}(s)}, \quad D_{13}(s) = -\frac{C_{24}(s)-C_{14}(s)}{C_{22}(s)-C_{12}(s)},$$

$$D_{14}(s) = -\frac{C_{25}(s)-C_{15}(s)}{C_{22}(s)-C_{12}(s)}, \quad D_{15}(s) = -\frac{C_{26}(s)-C_{16}(s)}{C_{22}(s)-C_{12}(s)}, \quad D_{16}(s) = -\frac{C_{27}(s)-C_{17}(s)}{C_{22}(s)-C_{12}(s)}.$$

Subtracting Eq. (21b) multiplied by $C_{12}(s)$ from Eq. (21a) multiplied by $C_{22}(s)$, gives

$$\frac{\partial^4 M_{1L}(x,s)}{\partial x^4} = E_{11}(s)\frac{\partial^4 N_{1L}(x,s)}{\partial x^4}^2 + E_{12}(s)\frac{\partial^2 N_{1L}(x,s)}{\partial x^2} + E_{13}(s)M_{1L}(x,s) + E_{14}(s)N_{1L}(x,s) + E_{15}(s)M_{TL}(x,s) + E_{16}(s)N_{TL}(x,s). \tag{23}$$

where

$E_{11}(s) = -\frac{C_{11}(s)C_{22}(s)-C_{12}(s)C_{21}(s)}{C_{22}(s)-C_{12}(s)}$, $E_{12}(s) = -\frac{C_{13}(s)C_{22}(s)-C_{12}(s)C_{23}(s)}{C_{22}(s)-C_{12}(s)}$,

$E_{13}(s) = -\frac{C_{14}(s)C_{22}(s)-C_{12}(s)C_{24}(s)}{C_{22}(s)-C_{12}(s)}$, $E_{14}(s) = -\frac{C_{15}(s)C_{22}(s)-C_{12}(s)C_{25}(s)}{C_{22}(s)-C_{12}(s)}$,

$E_{15}(s) = -\frac{C_{16}(s)C_{22}(s)-C_{12}(s)C_{26}(s)}{C_{22}(s)-C_{12}(s)}$, $E_{16}(s) = -\frac{C_{17}(s)C_{22}(s)-C_{12}(s)C_{27}(s)}{C_{22}(s)-C_{12}(s)}$.

By differentiating Eq. (21) twice and substituting it into Eq. (23), we have

$$M_{1L}(x,s) = F_{11}(s)\frac{\partial^6 N_{1L}(x,s)}{\partial x^6} + F_{12}(s)\frac{\partial^4 N_{1L}(x,s)}{\partial x^4} + F_{13}(s)\frac{\partial^2 N_{1L}(x,s)}{\partial x^2} + F_{14}(x,s)N_{1L}(x,s) + F_{15}(s)M_{TL}(x,s) + F_{16}(s)N_{TL}(x,s), \tag{24}$$

where

$F_{11}(s) = \frac{D_{11}(s)}{E_{13}(s)-D_{13}(s)^2}$, $F_{12}(s) = \frac{D_{12}(s)+D_{13}(s)D_{11}(s)-E_{11}(s)}{E_{13}(s)-D_{13}(s)^2}$,

$F_{13}(s) = \frac{D_{14}(s)+D_{13}(s)D_{12}(s)-E_{12}(s)}{E_{13}(s)-D_{13}(s)^2}$, $F_{14}(s) = \frac{D_{13}(s)D_{14}(s)-E_{14}(s)}{E_{13}(s)-D_{13}(s)^2}$,

$F_{15}(s) = \frac{D_{13}(s)D_{15}(s)-E_{15}(s)}{E_{13}(s)-D_{13}(s)^2}$, $F_{16}(s) = \frac{D_{13}(s)D_{16}(s)-E_{16}(s)}{E_{13}(s)-D_{13}(s)^2}$.

Substituting Eq. (24) into Eq. (22), the final governing equation is given by

$$G_{11}(s)\frac{\partial^8 N_{1L}(x,s)}{\partial x^8} + G_{12}(s)\frac{\partial^6 N_{1L}(x,s)}{\partial x^6} + G_{13}(s)\frac{\partial^4 N_{1L}(x,s)}{\partial x^4} + G_{14}(s)\frac{\partial^2 N_{1L}(x,s)}{\partial x^2} + G_{15}(s)N_{1L}(x,s) + G_{16}(s)M_{TL} + G_{17}(s)N_{TL}(x,s) = 0, \tag{25}$$

where

$G_{11}(s) = F_{11}(s)$, $G_{12}(s) = F_{12}(s) - D_{13}(s)F_{11}(s)$, $G_{13}(s) = F_{13}(s) - D_{11}(s) - D_{13}(s)F_{12}(S)$,

$G_{14}(s) = F_{14}(s) - D_{12}(s) - D_{13}(s)F_{13}(s)$, $G_{15}(s) = -D_{14}(s) - D_{13}(s)F_{14}(s)$,

$G_{16}(s) = -D_{15}(s) - D_{13}(s)F_{15}(s)$, $G_{17}(s) = -D_{16}(s) - D_{13}(s)F_{16}(s)$.

The above eighth-order differential equation (the governing equation) is valid for the viscoelastic analysis of the adhesively bonded single lap-joints. Its characteristic equation can be written as

$$G_{11}(s)\bar{X}^8 + G_{12}(s)\bar{X}^6 + G_{13}(s)\bar{X}^4 + G_{14}(s)\bar{X}^2 + G_{15}(s) = 0. \tag{26}$$

Eq. (26) gives the roots $\pm\emptyset_1(s)$, $\pm\emptyset_2(s)$, $\pm\emptyset_3(s)$, and $\pm\emptyset_4(s)$. Then general solution of Eq. (25) can be expressed obtained as

$$N_{1L}(x,s) = N_{1LH}(x,s) + N_{1LP}(x,s), \tag{27a}$$

$$N_{1LH}(x,s) = \sum_{i=1}^{n=4}[\alpha_i(s)\sinh(\emptyset_i(s)x) + \beta_i(s)\cosh(\emptyset_i(s)x)], \tag{27b}$$

$$N_{1LP}(x,s) = -\frac{G_{16}(s)}{G_{15}(s)}M_{TL}(x,s) - \frac{G_{17}(s)}{G_{15}(s)}N_{TL}(x,s). \tag{27c}$$

where $N_{1L}(x,s)$, $N_{1LH}(x,s)$ and $N_{1LP}(x,s)$ are the general solution, the hyperbolic solution of the homogenous solution and the particular solution of the adherend 1, respectively.

In the same way, the general solution of the bending moment of beam 1 can be obtained considering Eq. (24) as

$$M_{1L}(x,s) = M_{1LH}(x,s) + M_{1LP}(x,s), \tag{28a}$$

$$M_{1LH}(x,s) = \sum_{i=1}^{n=4} Y_{M1i}(s)[\alpha_i(s)\sinh(\emptyset_i(s)x) + \beta_i(s)\cosh(\emptyset_i(s)x)], \tag{28b}$$

$$M_{1LP}(x,s) = F_{15}(s)M_{TL}(x,s) + F_{16}(s)N_{TL}(x,s), \tag{28c}$$

$$Y_{M1i}(s) = F_{11}(s)\emptyset_i^6(s) + F_{12}(s)\emptyset_i^3(s) + F_{13}(s)\emptyset_i^2(s) + F_{14}(s), \tag{28d}$$

where $M_{1L}(x,s)$, $M_{1LH}(x,s)$ and $M_{1LP}(x,s)$ are the general solution, the hyperbolic solution (the homogeneous form), and the particular solution of the adherend 1, respectively. Considering Eq. (5), the shear force of the adherend 1 can be written as

$$Q_{1L}(x,s) = \frac{\partial M_{1L}(x,s)}{\partial x} + \frac{h_1}{2}\frac{\partial N_{1L}(x,s)}{\partial x}. \tag{29}$$

The Laplace transform of the internal forces of the adherend 2 can be obtained by considering Eq. (6) as

$$N_{2L}(x,s) = N_{TL}(x,s) - N_{1L}(x,s), \tag{30}$$

$$M_{2L}(x,s) = M_{TL}(x,s) - M_{1L}(x,s) - N_{1L}(x,s)\left(\frac{h_1+h_2}{2} + h_0\right), \tag{31}$$

$$Q_{2L}(x,s) = \frac{\partial M_{2L}(x,s)}{\partial x} - \frac{h_2}{2}\frac{\partial N_{2L}(x,s)}{\partial x}, \tag{32}$$

where $N_{2L}(x,s)$, $M_{2L}(x,s)$, and $Q_{2L}(x,s)$ are the general solutions of the adherend 2.

Considering Eqs. (4) and (32), general solutions of the stresses along the adhesive-adherend interfaces can be obtained as

$$\sigma_{1L}(x,s) = \frac{1}{b}\frac{\partial Q_{1L}(x,s)}{dx}, \tag{33}$$

$$\sigma_{2L}(x,s) = -\frac{1}{b}\frac{\partial Q_{2L}(x,s)}{\partial x}, \tag{34}$$

$$\tau_L(x,s) = \frac{1}{b}\frac{\partial N_{1L}(x,s)}{dx}, \tag{35}$$

where $\sigma_{1L}(x,s)$, $\sigma_{2L}(x,s)$ and $\tau_L(x,s)$ are the general solutions. Coefficients α_i and β_i (eight coefficients) can be determined by considering boundary conditions at the two ends of the joint overlap.

Although by using any computational software the inverse Laplace transform can be solved, in this study, the method presented by Zakian is employed. The method gives an explicit technique to numerically calculate the Inverse Laplace transform on any assumed function [39], [40]. Using the Zakian's technique, the internal forces and the stresses along the interfaces can be derived from their Laplace forms with respect to x and t.

By assuming the single-lap joint is simply supported and that the external forces are applied instantly and kept constant with time, as shown in Fig.1, the boundary conditions can be written as

$$N_1(-l,t) = PH(t), \quad Q_1(-l,t) = \frac{-P}{2(l+l^*)}\left(\frac{h_1+h_2}{2}+h_0\right)H(t), \quad M_1(-l,t) = \frac{-Pl^*}{2(l+l^*)}\left(\frac{h_1+h_2}{2}+h_0\right)H(t), \quad \tau(-l,t) = 0, \tag{36a}$$

$$N_1(l,t) = 0, \quad Q_1(l,t) = 0, \quad M_1(l,t) = 0, \quad \tau(l,t) = 0, \tag{36b}$$

where P is the pulling force applied at the very ends of the joint, $H(t)$ is the Heaviside function.

3.2.2. Symmetric single-lap joint

Equation (25) is valid for asymmetric joints. For symmetric joints, coefficients such as D_{11} to D_{16} and E_{11} to E_{16} will have zero denominators, resulting in undefined values. Therefore, a new formulation for symmetric joints is presented in this section. Since both adherends are identical, we have $C_1=C_2=C$, $B_1=B_2=B$ and $D_1=D_2=D$.

We can decompose the deformations, beam forces, and interface stresses into two parts as

$$f_R = \frac{1}{2}(f_1 + f_2),\ \ f_S = \frac{1}{2}(f_1 - f_2), \tag{37}$$

where f_i can be any one of u_i, w_i, ϕ_i, Q_i, N_i, M_i, σ_i. In this way, we can rewrite the constitutive equations as

$$N_R(x,t) = C\frac{\partial u_R(x,t)}{\partial x}, \qquad M_R(x,t) = D\frac{\partial \phi_R(x,t)}{\partial x}, \qquad Q_R(x,t) = B\left(\phi_R(x,t) + \frac{\partial w_R(x,t)}{\partial x}\right), \tag{38a}$$

$$N_S(x,t) = C\frac{\partial u_S(x,t)}{\partial x}, \qquad M_S(x,t) = D\frac{\partial \phi_S(x,t)}{\partial x}, \qquad Q_S(x,t) = B\left(\phi_S(x,t) + \frac{\partial w_S(x,t)}{\partial x}\right). \tag{38b}$$

Considering Eq. (4), equilibrium equations can be rewritten as

$$\frac{\partial N_R(x,t)}{\partial x} = 0, \qquad \frac{\partial M_R(x,t)}{\partial x} = Q_R(x,t) - \frac{h}{2}b\tau(x,t), \quad \frac{\partial Q_R(x,t)}{\partial x} = b\sigma_S(x,t), \tag{39a}$$

$$\frac{\partial N_S(x,t)}{\partial x} = b\tau(x,t), \quad \frac{\partial M_S(x,t)}{\partial x} = Q_S(x,t), \qquad \frac{\partial Q_S(x,t)}{\partial x} = b\sigma_R(x,t), \tag{39b}$$

$$Q_R(x,t) = B\left(\phi_R(x,t) + \frac{\partial w_R(x,t)}{\partial x}\right), \tag{40a}$$

$$Q_S(x,t) = B\left(\phi_S(x,t) + \frac{\partial w_S(x,t)}{\partial x}\right). \tag{40b}$$

In the same way, the decoupled global equilibrium equations of the symmetric single-lap joint can be rewritten as

$$N_T(x,t) = 2N_R(x,t), \tag{41a}$$

$$M_T(x,t) = 2M_R(x,t) + (N_R(x,t) + N_S(x,t))(h + h_0), \tag{41b}$$

$$Q_T(x,t) = 2Q_R(x,t). \tag{41c}$$

The strain components shown in Eq. (8) for the asymmetric joint can be rewritten for the symmetric joint as

$$\gamma(x,t) = \frac{1}{h_0}\left(2u_S(x,t) - h\phi_R(x,t)\right) + \frac{\partial w_a(x,t)}{\partial x}, \tag{42a}$$

$$\varepsilon_R(x,t) = \frac{2w_S(x,t)}{h_0}, \tag{42b}$$

$$\varepsilon_S(x,t) = \frac{2}{h_0}\left(w_R(x,t) - w_a(x,t)\right), \tag{42c}$$

$$\varepsilon_x(x,t) = \frac{1}{2}\left(2\frac{\partial u_R(x,t)}{\partial x} - h\frac{\partial \phi_S(x,t)}{\partial x}\right). \tag{42d}$$

Similarly, Eq. (16) can be rewritten for the symmetric joint as

$$\left(a_{10} + a_{11}\frac{\partial}{\partial t} + a_{12}\frac{\partial^2}{\partial t^2}\right)\left(\frac{1}{C}\frac{\partial^2 N_R(x,t)}{\partial x^2} - \frac{h}{2D}\frac{\partial^2 M_S(x,t)}{\partial x^2}\right) + \frac{2}{h_0}\left(b_{10} + b_{11}\frac{\partial}{\partial t} + b_{12}\frac{\partial^2}{\partial t^2}\right)\left(\frac{1}{B}\frac{\partial^2 M_S(x,t)}{\partial x^2} - \frac{M_S(x,t)}{D}\right) + \frac{1}{b}\left(c_{10} + c_{11}\frac{\partial}{\partial t} + c_{12}\frac{\partial^2}{\partial t^2}\right)\left(\frac{\partial^4 M_S(x,t)}{\partial x^4}\right) = 0, \tag{43a}$$

$$\frac{2}{h_0}\left(b_{10} + b_{11}\frac{\partial}{\partial t} + b_{12}\frac{\partial^2}{\partial t^2}\right)\left(-\frac{h_0}{2B}\frac{\partial^2 N_S(x,t)}{\partial x^2} + \frac{h+h_0}{2D}N_S(x,t) - \frac{M_T(x,t)}{2D} + \frac{h+h_0}{4D}N_T(x,t) - \frac{\partial^2 w_a(x,t)}{\partial x^2}\right) + \frac{1}{b}\left(c_{10} + c_{11}\frac{\partial}{\partial t} + c_{12}\frac{\partial^2}{\partial t^2}\right)\left(-\frac{h_0}{2}\frac{\partial^4 N_S(x,t)}{\partial x^4}\right) = 0. \tag{43b}$$

Applying Laplace transform to Eq. (43) yields

$$B_{41}(s)\frac{\partial^4 M_{SL}(x,s)}{\partial x^4} + B_{42}(s)\frac{\partial^2 M_{SL}(x,s)}{\partial x^2} + B_{43}(s)M_{SL}(x,s) = 0, \tag{44a}$$

$$B_{51}(s)\frac{\partial^4 N_{SL}(x,s)}{\partial x^4} + B_{52}(s)\frac{\partial^2 N_{SL}(x,s)}{\partial x^2} + B_{53}(s)N_{SL}(x,s) + B_{54}(s)M_{TL}(x,s) + B_{55}(s)N_{TL}(x,s) + B_{56}(s)\frac{\partial^2 w_{aL}(x,s)}{\partial x^2} = 0, \tag{44b}$$

where

$$B_{41}(s) = \frac{1}{b}(c_{10} + c_{11}s + c_{12}s^2),$$

$$B_{42}(s) = -\left(\frac{h}{2D}\right)(a_{10} + a_{11}s + a_{12}s^2) + \left(\frac{2}{h_0 B}\right)(b_{10} + b_{11}s + b_{12}s^2),$$

$$B_{43}(s) = -\frac{2}{D_2 h_0}(b_{10} + b_{11}s + b_{12}s^2),$$

$$B_{51}(s) = -\frac{h_0}{2b}(c_{10} + c_{11}s + c_{12}s^2), \quad B_{52}(s) = -\frac{1}{B}(b_{10} + b_{11}s + b_{12}s^2),$$

$B_{53}(s) = \frac{h+h_0}{h_0 D}(b_{10} + b_{11}s + b_{12}s^2)$, $\quad B_{54}(s) = -\frac{1}{h_0 D}(b_{10} + b_{11}s + b_{12}s^2)$,

$B_{55}(s) = \frac{h+h_0}{2h_0 D}(b_{10} + b_{11}s + b_{12}s^2)$, $\quad B_{56}(s) = -\frac{2}{h_0}(b_{10} + b_{11}s + b_{12}s^2)$.

Substituting Eqs. (39b) and (42a) into Eq. (12d) and differentiating both sides yields

$$P_1\left(\frac{1}{b}\frac{\partial^2 N_S(x,t)}{\partial x^2}\right) = \frac{1}{2}Q_1\left(\frac{1}{h_0}\left(\frac{2}{C}N_S(x,t) - \frac{h}{D}M_R(x,t)\right) + \frac{\partial^2 w_a(x,t)}{\partial x^2}\right). \tag{45}$$

Substituting the total equilibrium equations of Eq. (42) into Eq. (45) gives

$$P_1\left(\frac{1}{b}\frac{\partial^2 N_S(x,t)}{\partial x^2}\right) = \frac{1}{2}Q_1\left(A_{21}N_S(x,t) + A_{22}M_T(x,t) + A_{23}N_T(x,t) + \frac{\partial^2 w_a(x,t)}{\partial x^2}\right), \tag{46}$$

where

$$A_{21} = \frac{1}{h_0}\left(\frac{2}{C} + \frac{h(h+h_0)}{2D}\right),\ A_{22} = \frac{h(h+h_0)}{4Dh_0}, A_{23} = -\frac{h}{2Dh_0}.$$

By applying Laplace transform to Eq. (46), we have

$$\frac{\partial^2 w_{aL}(x,s)}{\partial x^2} = \frac{B_{61}(s)}{B_{60}(s)}\frac{\partial^2 N_{SL}(x,s)}{\partial x^2} + \frac{B_{62}(s)}{B_{60}}N_{SL}(x,s) + \frac{B_{63}(s)}{B_{60}(s)}M_{TL}(x,s) + \frac{B_{64}(s)}{B_{60}(s)}N_{TL}(x,s), \tag{47}$$

where

$B_{60}(s) = \frac{1}{2}(b_1 + b_2 s)$, $\quad B_{61}(s) = \frac{1}{b}(a_1 + s)$, $\quad B_{62}(s) = -\frac{A_{21}}{2}(b_1 + b_2 s)$,

$B_{63}(s) = -\frac{A_{22}}{2}(b_1 + b_2 s)$, $\quad B_{64}(s) = -\frac{A_{23}}{2}(b_1 + b_2 s)$.

Substituting Eq. (47) into Eq. (44b) gives

$$C_{31}(s)\frac{\partial^4 N_{SL}(x,s)}{\partial x^4} + C_{32}(s)\frac{\partial^2 N_{SL}(x,s)}{\partial x^2} + C_{33}(s)N_{SL}(s) + C_{34}(s)M_{TL}(x,s) + C_{35}(s)N_{TL}(x,s) = 0, \tag{48}$$

where

$C_{31}(s) = B_{51}(x,s)$, $\quad C_{32}(s) = B_{52}(x,s) + \frac{B_{56}(s)B_{11}(s)}{B_{10}(s)}$, $\quad C_{33}(s) = B_{53}(x,s) + \frac{B_{56}(s)B_{13}(s)}{B_{10}(s)}$,

$C_{34}(s) = B_{54}(x,s) + \frac{B_{56}(s)B_{14}(s)}{B_{10}(s)}$, $\quad C_{35}(s) = B_{55}(x,s) + \frac{B_{56}(s)B_{15}(s)}{B_{10}(s)}$.

Equations (44a) and (48) are the governing equations in term of $M_{SL}(x,s)$ and $N_{SL}(x,s)$, respectively. Both of them are forth-order differential equations. Eight boundary conditions are needed to determine coefficients in the solution, same as in the case of the asymmetric joints. The characteristic equations can be written as

$$B_{41}(s)\bar{X}^4 + B_{42}(s)\bar{X}^2 + B_{43}(s) = 0, \tag{49a}$$

$$C_{31}(s)\bar{Y}^4 + C_{32}(s)\bar{Y}^2 + C_{33}(s) = 0. \tag{49b}$$

Equation (49a) gives four roots $\emptyset_1(s)$, $\emptyset_2(s)$, $\emptyset_3(s)$, and $\emptyset_4(s)$, and Eq. (49b) gives another four roots $\emptyset_5(s)$, $\emptyset_6(s)$, $\emptyset_7(s)$, and $\emptyset_8(s)$, respectively. Then the general solutions can be obtained as

$$M_{SL}(x,s) = M_{SLH}(x,s), \tag{50a}$$

$$M_{SLH}(x,s) = \sum_{i=1}^{n=4}[\gamma_i(s)e^{\emptyset_i(s).x}], \tag{50b}$$

$$N_{SL}(x,s) = N_{SLH}(x,s) + N_{SLP}(x,s), \tag{51a}$$

$$N_{SLH}(x,s) = \sum_{i=5}^{n=8}[\gamma_i(s)e^{\emptyset_i(s).x}], \tag{51b}$$

$$N_{SLP}(x,s) = -\frac{C_{34}(s)}{G_{33}(s)}M_{TL}(x,s) - \frac{C_{35}(s)}{C_{33}(s)}N_{TL}(x,s). \tag{51c}$$

Considering Eq. (39b) $Q_{SL}(x,s)$ can be found as

$$\frac{\partial M_{SL}(x,s)}{\partial x} = Q_{SL}(x,s). \tag{52}$$

By using equilibrium equations of Eq. (41), we can have $N_{RL}(x,s)$, $M_{RL}(x,s)$ and $Q_{RL}(x,s)$

$$N_{RL}(x,s) = \frac{1}{2}N_{TL}(x,s), \tag{53}$$

$$M_{RL}(x,s) = \frac{1}{2}\Big(M_{TL}(x,s) - \big(N_{SL}(x,s) + N_{RL}(x,s)\big)(h + h_0)\Big), \tag{54}$$

$$Q_{RL}(x,s) = \frac{1}{2}Q_{TL}(x,s). \tag{55}$$

According to Eq. (35), the Laplace transform of the forces in both adherends are obtained as

$$N_{1L}(x,s) = N_{RL}(x,s) + N_{SL}(x,s), \tag{56}$$

$$M_{1L}(x,s) = M_{RL}(x,s) + M_{SL}(x,s), \tag{57}$$

$$Q_{1L}(x,s) = Q_{RL}(x,s) + Q_{SL}(x,s), \tag{58}$$

$$N_{2L}(x,s) = N_{RL}(x,s) - N_{SL}(x,s), \tag{59}$$

$$M_{2L}(x,s) = M_{RL}(x,s) - M_{SL}(x,s), \tag{60}$$

$$Q_{2L}(x,s) = Q_{RL}(x,s) - Q_{SL}(x,s). \tag{61}$$

Internal forces of the adherends can be obtained by taking inverse Laplace transform of Eqs. (56-61). The rest of the method remains the same as the asymmetric solution. Boundary conditions can be applied to the model in the same way as well.

3.3. Verification and comparisons

As verifications, the analytical results are compared with the numerical results obtained by finite element analysis (FEA). A single-lap joint studied by Wang and Zhang [15] is analyzed using both the present solutions and FEA, as shown in Fig. 3-5. The geometry and material properties of the joints are shown in Table 3-1 and Table 3-2. The results of the viscoelastic analysis are obtained at 5, 10 and 30 days. To evaluate the elastic behavior of the joints, the non-transient instant analysis at time 0 is also determined. Commercial software ABAQUS/CAE is used to conduct FEA, as shown in Fig. 3-5. A user's subroutine (UMAT) is used to model the viscoelastic material of the adhesive. Denote the initial shear modulus of elasticity denotes by G_0, and the ultimate shear modulus by G_∞. As a numerical example, we take $G_\infty = \frac{1}{3} G_0$ and $t_0 = 5(days)$. The viscoelastic parameters can be obtained as follow

$$a_1 = \frac{1}{t_0} = \frac{1}{5}, \tag{62a}$$

$$b_1 = \frac{k_1}{t_0} = \frac{2G_\infty}{5}, \tag{62b}$$

$$b_2 = 2(G_0 - G_\infty). \tag{62c}$$

For each numerical example, a plane stress model is constructed with 4-node bilinear stress quadrilateral elements. A meshing pattern of elements with size ranged between 0.02 mm and 0.2 mm in longitudinal direction is chosen. Refined mesh is used in the regions near the edges and within the interfaces to capture more accurate stress distributions.

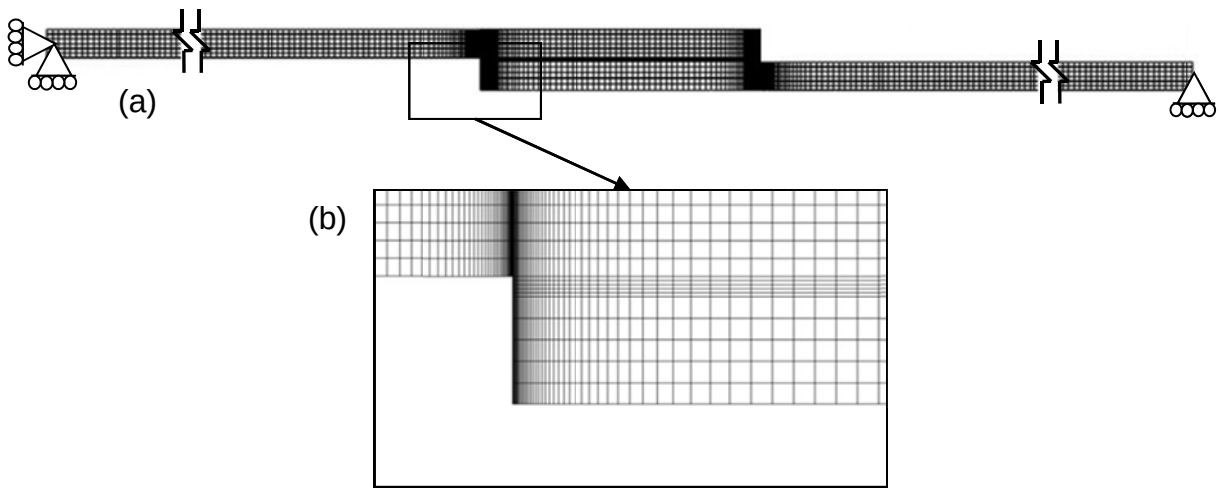

Fig. 3-5 Finite element model of (a) simply supported single-lap joint under axial tension, (b) close illustration of the lower-left corner.

Table 3-1 Geometrical parameters of the single-lap joint.

	l	l*	h_0	h_1	h_2
Dimension	25 mm	150 mm	0.20 mm	5 mm	5 mm

Table 3-2 Mechanical properties of the single-lap joint.

	Asymmetric joint			Symmetric joint		
Layers	Adherend 1	Adherend 2	Adhesive	Adherend 1	Adherend 2	Adhesive
E (GPa)	60	30	2.50	60	60	4.82
ν	0.30	0.30	0.25	0.33	0.33	0.25

3.3.1. Asymmetric single-lap joint

Figure 3- 6 compares the shear stresses along the adhesive layer obtained by the present 3PVF model and the FEA for the asymmetric single-lap joint. Excellent agreement with FEA is reached by the present model, confirming the accuracy of the model. Both methods can satisfy the zero-shear stress boundary condition at the free edge of the adhesive. It can be seen from Fig. 3-6 that the shear stress concentrations near the ends of the interface reduce with time due to the viscoelastic behavior of the adhesive.

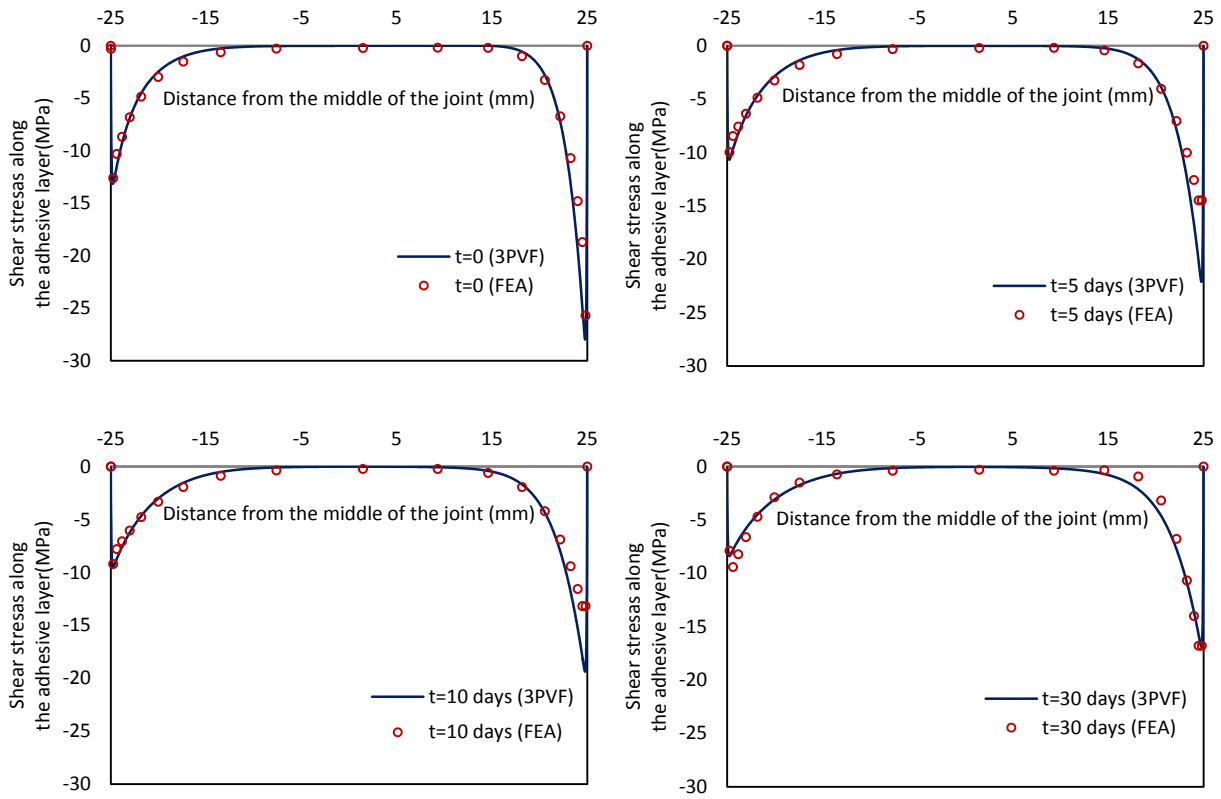

Fig. 3-6 Comparison the 3PVF model with the FEA on shear stress distribution in an asymmetric single-lap joint.

The time-dependent stress distributions of the asymmetric joint are further demonstrated in Figs.3-7 and 3-8. As shown in Fig. 3-7(a), the shear stress reaches its maximum at a very small distance to the end, which is in agreement with some experimental observation. The viscoelastic

behavior of the adhesive layer is clearly shown in this figure by remarkable shear stress relaxation. As shown in Fig. 3-7(b) and Fig. 3-7(c), the shear stress drops up to 35% and 40% near the left and right ends, respectively, after 30 days.

Fig. 3-8(a) shows the peel stress obtained by the 3PVF model along the top adherend/adhesive interface. The peel stress in the middle region of the interface is close to zero; however, significant peel stress concentrations occur at the two ends of the interface. Fig. 3-8(b) and (c) show the close-up of peel stresses close to the left and right ends of the interface, respectively. It can be seen that the peel stress at the left end of the interface is positive (tensile); while at the right end, it changes rapidly from positive at a small distance to the end to negative (compression) at the end. Since the interface is more vulnerable under tension, it can be expected that debonding is more likely to initiate at the left end, rather than at the right one. Stress relaxation induced by the viscoelastic behavior of the adhesive layer is clearly revealed in this figure by the reduction of the maximum peel stress with time.

The peel stress along the bottom adherend/adhesive interface is presented in Fig. 3-9. As shown in Fig. 3-9(b) and Fig. 3-9(c), peel stress reaches a positive maximum at the left end, but reduces sharply from a high value at a small distance from the left end to close zero at the left end. In such a case, debonding is more likely to initiate at the right end, rather than the left end.

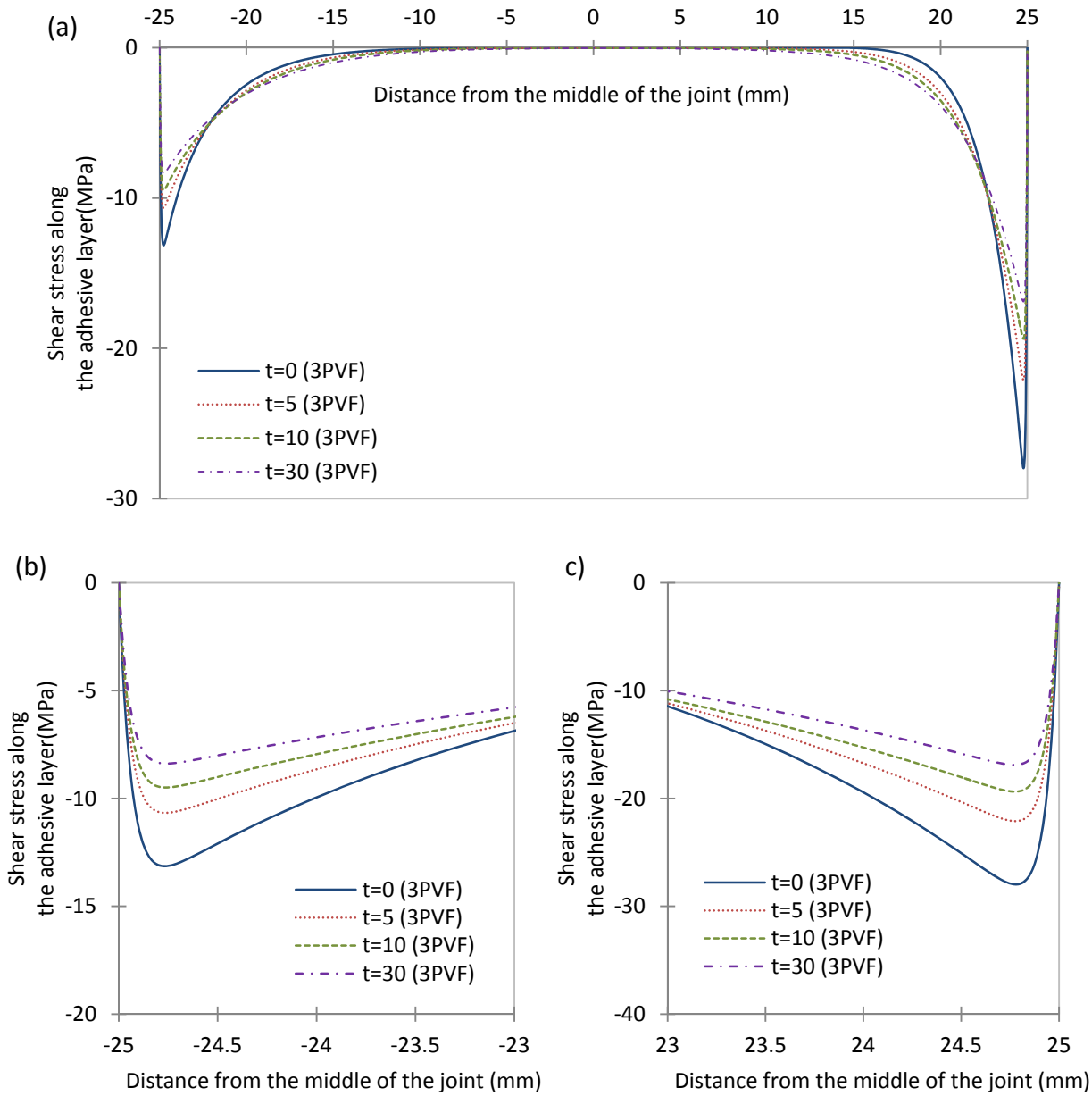

Fig. 3-7 Time-dependent shear stress distribution of the asymmetric single-lap joint in the adhesive layer: (a) shear stress distribution along the whole interface, (b) shear stress at the very left edge of the adhesive layer, (c) shear stress at the very right edge of the adhesive layer.

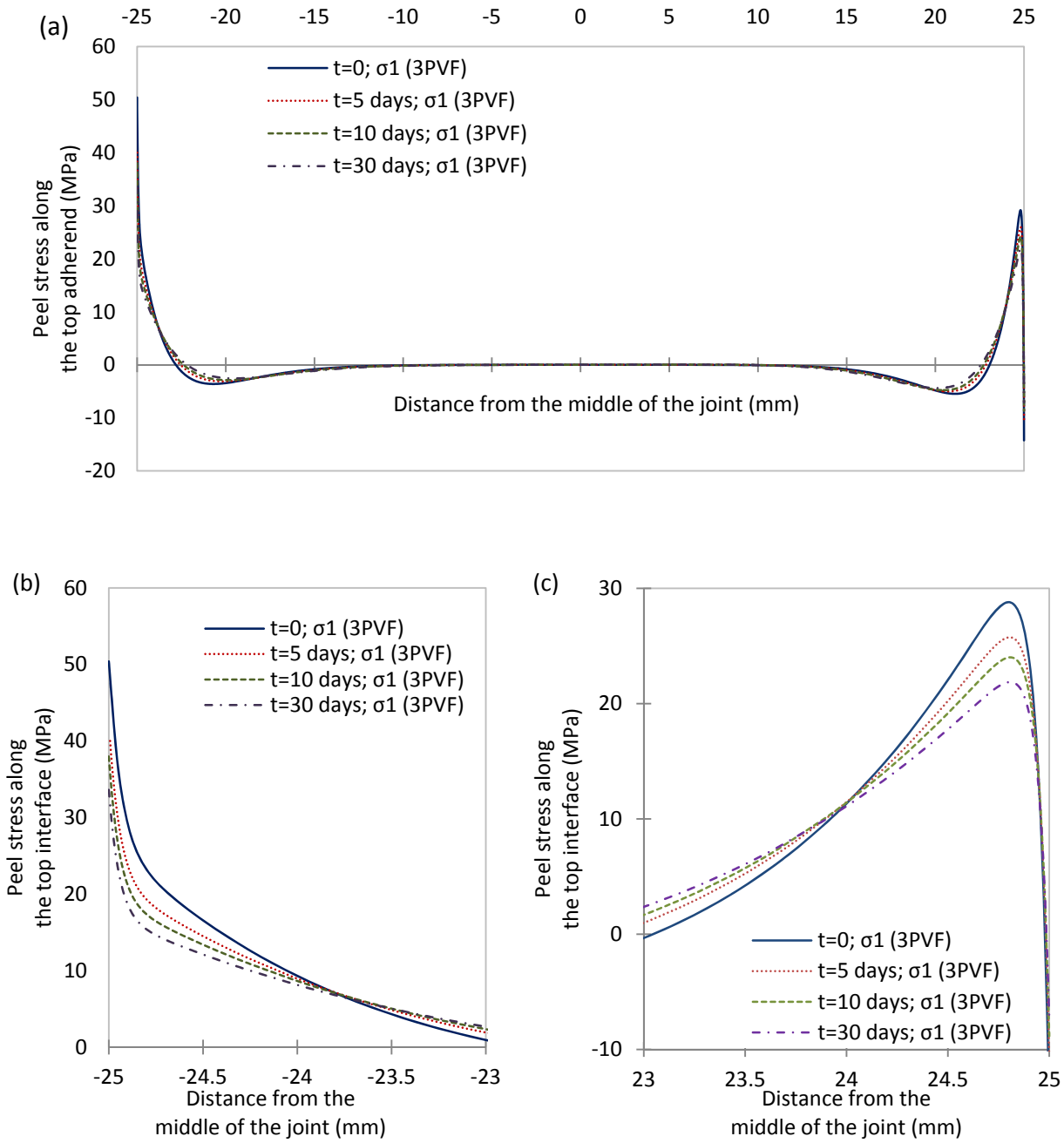

Fig. 3-8 Time-dependent peel stress distribution of the asymmetric single-lap joint along the top interface: (a) peel stress distribution along the whole interface, (b) peel stress at the very left edge of the interface, (c) peel stress at the very right edge of the interface.

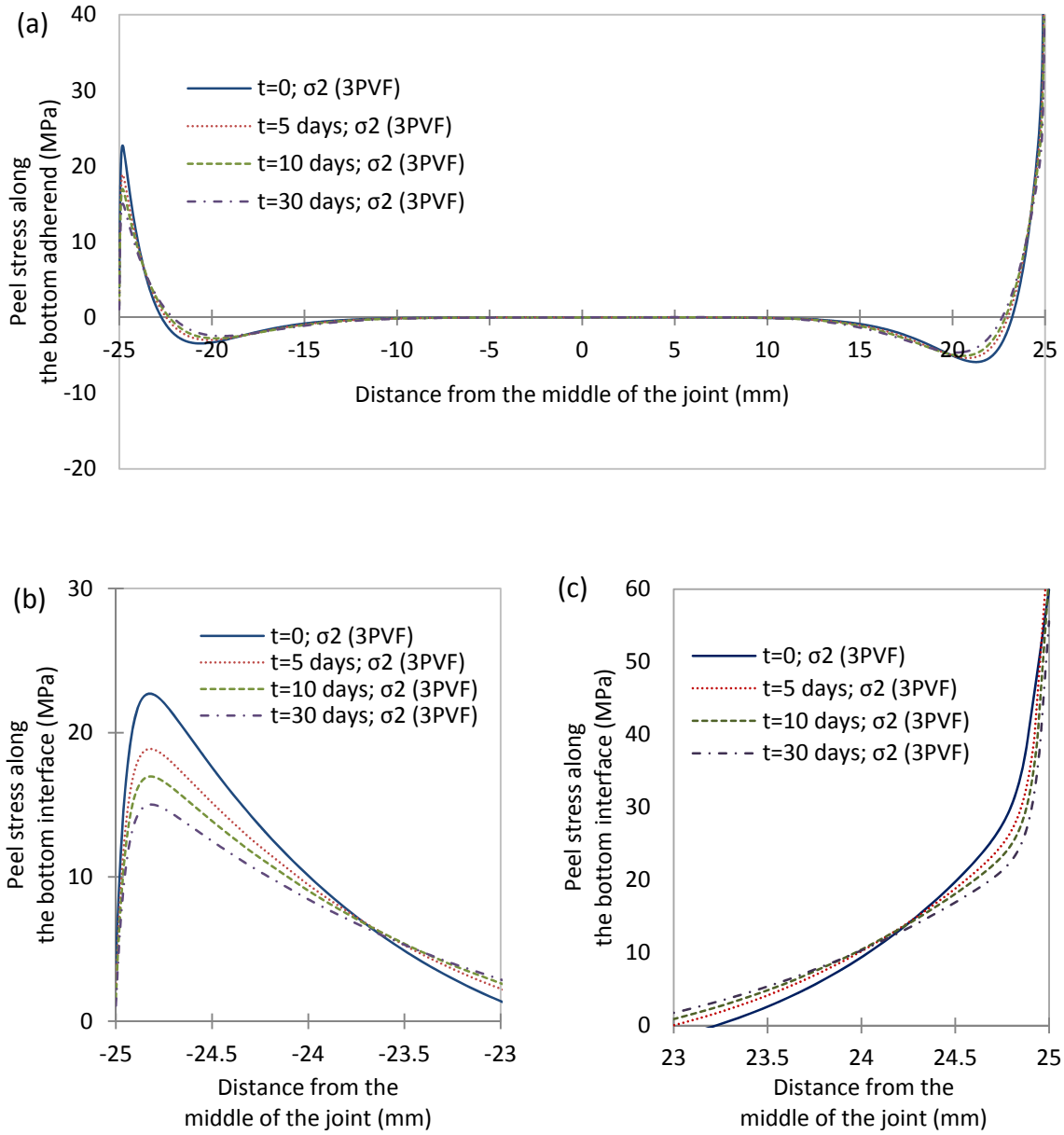

Fig. 3-9 Time-dependent peel stress distribution of the asymmetric single-lap joint along the bottom interface: (a) peel stress distribution along the whole interface, (b) peel stress at the very left edge of the interface, (c) peel stress at the very right edge of the interface

3.3.2. Symmetric single-lap joint

Figure 3-10 compares the shear stresses of the symmetric single-lap joint obtained by the 3PVF model and the FEA. Overall, excellent agreement with FEA has been achieved by the 3PVF model, confirming the validity of the 3PEF model. The present model slightly overestimates the

shear stress at the ends, particularly at the ages of 10 and 30 days. Because of the geometry and material symmetries of the joint, the shear stress distribution within the adhesive is also symmetric with respect to the vertical center line. Similar to the asymmetric joint, the shear stress concentration in this joint also reduces with time due to the viscoelastic behavior of the adhesive. Peel stress distributions along two interfaces obtained from the 3PVF model and the corresponding FEA are shown in Fig. 3-11. Analytical solution agrees well with the FEA, except in small areas close to the ends of the interface. A stress relaxation behavior similar to the asymmetric joint is observed and the peak peel stress concentrations reduce with time.

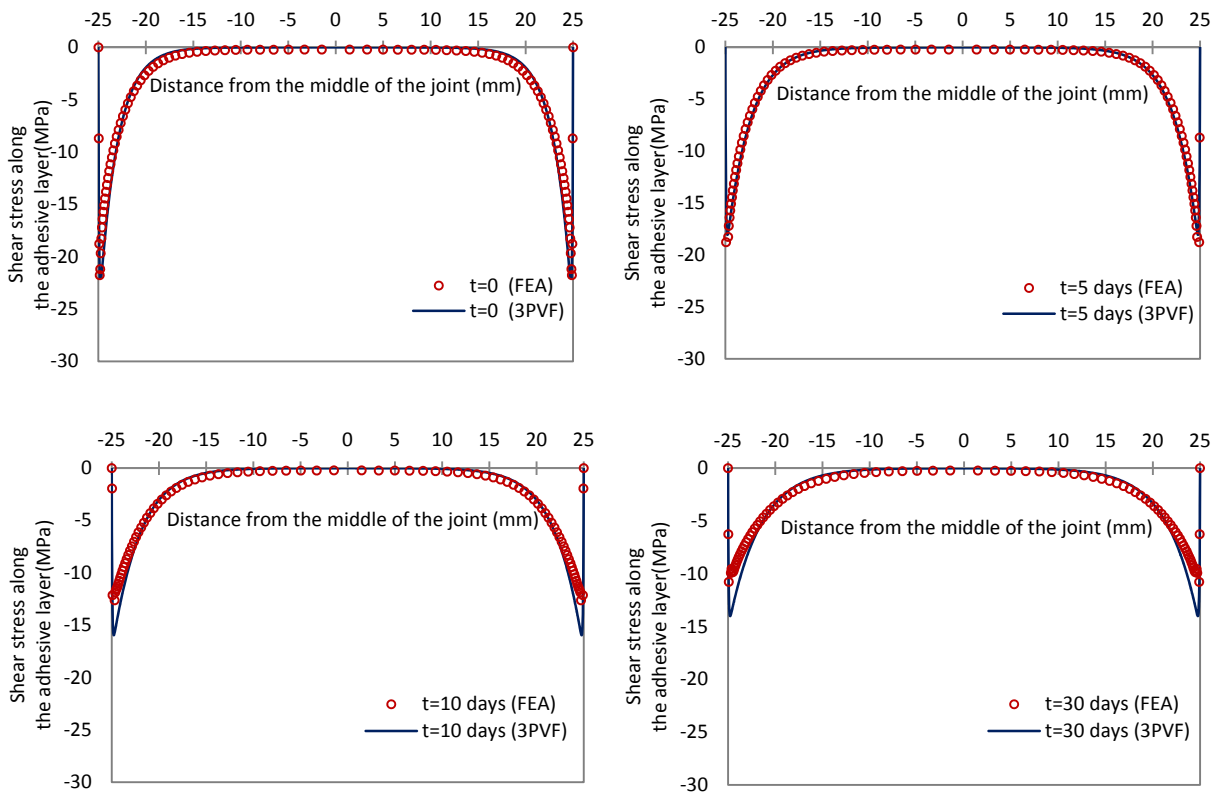

Fig. 3-10 Comparison between the 3PVF model and FEA on shear stress distribution within the adhesive layer of the symmetric single-lap joint.

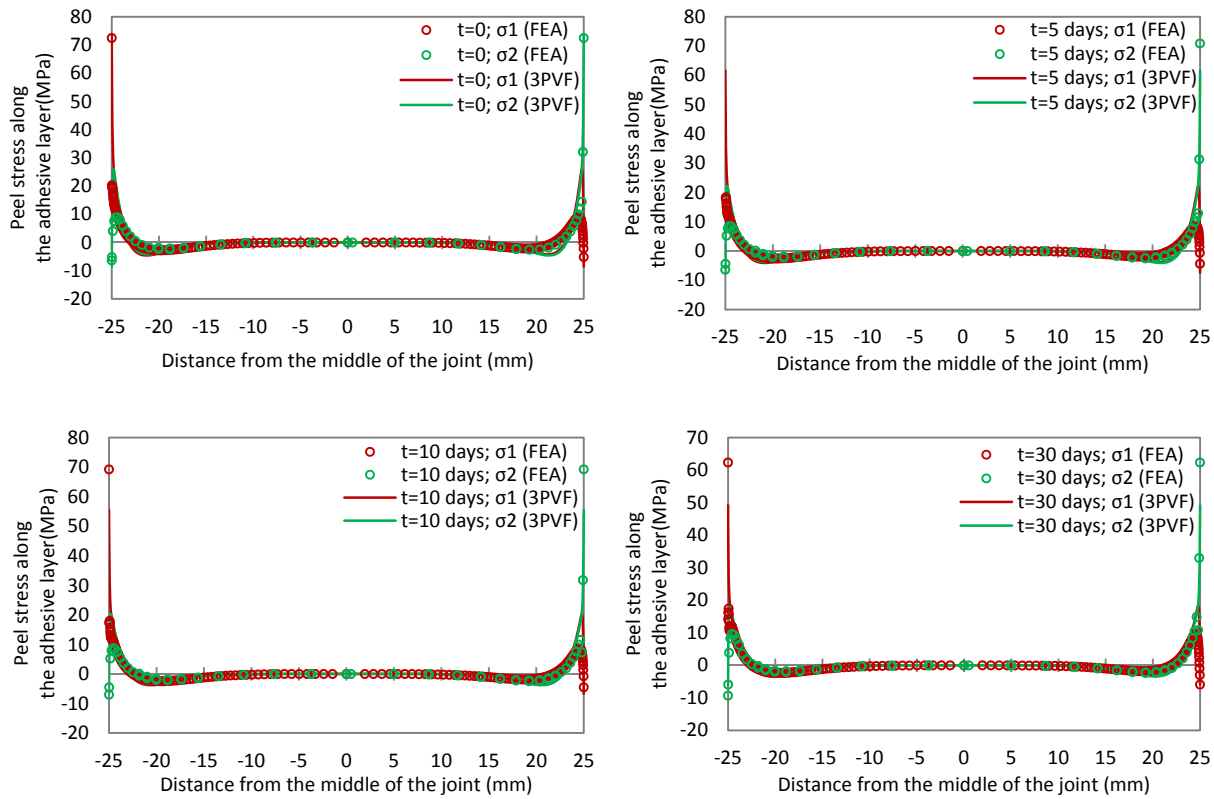

Fig. 3-11 Comparison between the 3PVF model and FEA on peel stress distribution along two adherend/adhesive interfaces of the symmetric single-lap joint.

3.4. Conclusion

In this study, an analytical model was established to analyze the stress redistributions due to the viscoelastic behavior of the adhesive in general single-lap joints. In this model, the adherends are modeled as elastic Timoshenko's beams; while the adhesive layer is modeled as a three-parameter viscoelastic foundation. A viscoelastic rheological model, the SLS model is used to model the viscoelastic behavior of the adhesive layer. Closed-form solutions of interface stresses are obtained and compared with finite element analysis using ABAQUS. Excellent agreements with the FEA have been achieved by the present model on interface shear and peel stresses, suggesting that the present model can produce sufficient accuracy on stress distribution in the viscoelastic joints. Both the FEA and the present model show that the shear and peel stresses in the

joint reduce with time. However, shear and peel stress relaxations exhibits different trends. Shear stress appears to reduce with time significantly; while relatively smaller reduction of peel stress is observed. This study shows that the present model provides an efficient tool to analyze the time-dependent behaviors of the adhesively bonded joint which is difficult for FEA.

3.5. References

[1] Goland M, Reissner E. The stresses in cemented joints. J Appl Mech 1944;11:A17–27.

[2] Zhang C. Mechanics and subcritical cracking of FRP-concrete interface 2011.

[3] Hart-Smith LJ. Adhesive-bonded double-lap joints. National Aeronautics and Space Administration; 1973.

[4] Renton JW, Vinson JR. On the behavior of bonded joints in composite material structures. Eng Fract Mech 1975;7:41–60.

[5] Renton WJ, Vinson JR. The efficient design of adhesive bonded joints. J Adhes 1975;7:175–93.

[6] Yuceoglu U, Updike DP. Bending and shear deformation effects in lap joints. J Eng Mech Div 1981;107:55–76.

[7] Pickett AK, Hollaway L. The analysis of elasto-plastic adhesive stress in adhesive bonded lap joints in F.R.P.-structures. Compos Struct 1985:135–60.

[8] Thomsen OT. Elasto-static and elasto-plastic stress analysis of adhesive bonded tubular lap joints. Compos Struct 1992;21:249–59.

[9] Oplinger D. Effects of adherent deflections in single-lap joints. Int J Solids Struct 1994:2565–87.

[10] Tong L. Bond strength for adhesive-bonded single-lap joints. Acta Mech 1996;117:101–13.

[11] Tsai MY, Oplinger DW, Morton J. Improved theoretical solutions for adhesive lap joints. Int J Solids Struct 1998;35:1163–85.

[12] Her S-C. Stress analysis of adhesively-bonded lap joints. Compos Struct 1999;47:673–8.

[13] Luo Q, Tong L. Linear and higher order displacement theories for adhesively bonded lap joints. Int J Solids Struct 2004;41:6351–81.

[14] Mortensen F, Thomsen OT. Analysis of adhesive bonded joints: a unified approach. Compos Sci Technol 2002;62:1011–31.

[15] Wang J, Zhang C. Three-parameter, elastic foundation model for analysis of adhesively bonded joints. Int J Adhes Adhes 2009;29:495–502.

[16] Brinson HF. The viscoelastic constitutive modelling of adhesives. Composites 1982;13:377–82.

[17] Mirman BA, Knecht S. Creep strains in an elongated bond layer. Components, Hybrids, Manuf Technol IEEE Trans 1990;13:914–28.

[18] Ferrier E, Hamelin P. Influence of Time-Temperature-Loading on Carbon Epoxy Reinforcement for Concrete Structures. ACI Spec Publ 1999;188.

[19] Dean G. Modelling non-linear creep behaviour of an epoxy adhesive. Int J Adhes Adhes 2007;27:636–46.

[20] Weitsman Y. Interfacial stresses in viscoelastic adhesive-layers due to moisture sorption. Int J Solids Struct 1979;15:701–13.

[21] Weitsman Y. An Investigation of Non-Linear Viscoelastic Effects on Load Transfer in a Symmetric Double-Lap Joint. J Adhes 1981;11:279–89.

[22] Delale F, Erdogan F. Viscoelastic analysis of adhesively bonded joints. J Appl Mech 1981;48:331–8.

[23] Savoia M, Ferracuti B, Mazzotti C. Creep deformation of fiber reinforced plastics-plated reinforced concrete tensile members. J Compos Constr 2005;9:63–72.

[24] Diab H, Wu Z. Nonlinear constitutive model for time-dependent behavior of FRP-concrete interface. Compos Sci Technol 2007;67:2323–33.

[25] Peretz D, Weitsman Y. The Nonlinear Thermoviscoelastic Characterizations of FM□73 Adhesives. J Rheol 1983;27:97–114.

[26] Knauss WG, Emri IJ. Non-linear viscoelasticity based on free volume consideration. Comput Struct 1981;13:123–8.

[27] Choi K-K, Meshgin P, Taha MMR. Shear creep of epoxy at the concrete–FRP interfaces. Compos Part B Eng 2007;38:772–80.

[28] Pickett AK, Hollaway L. The analysis of elastic-plastic adhesive stress in bonded lap joints in FRP structures. Compos Struct 1985;4:135–60.

[29] Ascione F, Berardi VP, Feo L, Giordano A. An experimental study on the long-term behavior of CFRP pultruded laminates suitable to concrete structures rehabilitation. Compos Part B Eng 2008;39:1147–50.

[30] Schaffer BG, Adams DF. Nonlinear viscoelastic analysis of a unidirectional composite material. J Appl Mech 1981;48:859–65.

[31] Ghoneim H, Chen Y. A viscoelastic-viscoplastic constitutive equation and its finite element implementation. Comput Struct 1983;17:499–509.

[32] Meshgin P, Choi K-K, Taha MMR. Experimental and analytical investigations of creep of epoxy adhesive at the concrete–FRP interfaces. Int J Adhes Adhes 2009;29:56–66.

[33] Ferrier E, Michel L, Jurkiewiez B, Hamelin P. Creep behavior of adhesives used for external FRP strengthening of RC structures. Constr Build Mater 2011;25:461–7.

[34] Choi K-K, Taha MMR, Masia MJ, Shrive PL, Shrive NG. Numerical investigation of creep effects on FRP-strengthened RC beams. J Compos Constr 2010;14:812–22.

[35] Meaud C, Jurkiewiez B, Ferrier E. Investigation of creep effects in strengthened RC structures through double lap shear testing. Compos Part B Eng 2011;42:359–66.

[36] Houhou N, Benzarti K, Quiertant M, Chataigner S, Fléty A, Marty C. Analysis of the nonlinear creep behavior of concrete/FRP-bonded assemblies. J Adhes Sci Technol 2014;28:1345–66.

[37] Schapery RA. A method of viscoelastic stress analysis using elastic solutions. J Franklin Inst 1965;279:268–89.

[38] Zhang C, Wang J. Viscoelastic analysis of FRP strengthened reinforced concrete beams. Compos Struct 2011;93:3200–8.

[39] Zakian V. Rational approximation to transfer-function matrix of distributed system. Electron Lett 1970;6:474–6.

[40] Zakian V. Optimisation of numerical inversion of Laplace transforms. Electron Lett 1970;6:677–9.

CHAPTER 4

THREE-PARAMETER VISCO-ELASTIC FOUNDATION MODEL OF ADHESIVELY BONDED JOINTS PART II: DOUBLE-LAP JOINTS

Abstract

This study proposes a new analytical model to calculate the peel and shear stresses in double-lap joints. In this model, the adherends are modeled as elastic Timoshenko's beams; while the adhesive layer is modeled as a three-parameter viscoelastic (3PVF) foundation. A viscoelastic rheological model, the standard linear solid model is used to model the viscoelastic behavior of the adhesive layer. Closed-form solutions of interface stresses are obtained and compared with finite element analysis using ABAQUS. This new model presents a major improvement of existing analytical solutions through: satisfying all boundary conditions and producing different peel stresses along two adherend/adhesive interfaces. Excellent agreements with the FEA have been achieved by the present model, suggesting that the present model can produce sufficient accuracy on stress distribution in the viscoelastic joints. Therefore, the present model provides an efficient tool to analyze the time-dependent behaviors of the adhesively bonded joint which is difficult for FEA. Both the FEA and the present model show that the shear and peel stresses in the joint reduce with time due to the viscoelasticity of the adhesive layer. It has been found that shear and peel stress relaxations exhibit different features. Significant shear stress reduction with time has been observed; while the maximum peel stresses is barely affected.

4.1. Introduction

Adhesively bonded joints have many advantages over other methods of fastening in providing even distribution of the transmitted load and reducing stress concentration in adherends by eliminating holes [1]. Premature failure due to debonding of the joints induced by excessive stress within the adhesive and along the adherend/adhesive interfaces is the major concern of this technique. To address this issue, many analytical and numerical solutions have been proposed to evaluate the stress distributions in the adhesively bonded joints, as summarized in an accompanying paper [2].

Most existing analytical studies on adhesively bonded joints focus on single-lap joints. A relatively fewer studies have been carried out to establish analytical solutions of interface stresses in double-lap joints. The most widely used stress analysis model for double-lap joints [3] was developed by de Bruyne (1944) using Volkersen's single-lap theory [4]. Hart-Smith (1973) [5] improved this model by considering the adhesive plasticity, adherends with unbalanced stiffnesses, and thermal difference between the adherends [5]. Tsai et al. (1998) [6] and Tsai and Morton (2010) [7] proposed another improvement by including shear deformations in the adherend. Recently, Gustafson et al. (2007) [8] proposed another modification on the adhesive layer so that free edge boundary conditions of the adhesive layer can be satisfied in double-lap joints; while the peel stress is assumed constant through the adhesive layer. Recognizing that stress may vary through the thickness of the adhesive layer, Diaz Diaz et al. (2009) [9] developed a layer-wise model, which can not only meet both the free-edge boundary condition, but also produce different peel stress distributions along two adherend/adhesive interfaces in the joints. A novel three-parameter elastic foundation (3PEF) model was recently established by Amidi and Wang [10] for

the double-lap joints. The major advantages of this new model include: 1) satisfying all boundary conditions; and 2) producing different peel stresses along two adherend/adhesive interfaces.

All analytical models for double-lap joints are based on elastic analysis. Structural adhesives such as epoxy exhibit viscoelastic properties. Its material properties vary with time under different situations, especially in the regions of high stress concentration [11–14]. Such variation of material properties can induce redistributions of stresses and additional deformation, which could be significant during the service life of the structure and cause potential failure of the joints. To address this issue, this study present a three-parameter viscoelastic foundation (3PVF) model for double-lap joints, based on which the time-dependent stress distribution in the joints can be calculated analytically.

4.2. Three-parameter viscoelastic foundation model for double-lap joints

Consider a typical double-lap joint subject to external loads shown in Fig. 4-1(a). Due to symmetry, the whole problem may be reduced to a quarter of a joint, as shown in Fig. 4-1(b). This quarter joint consists of three different layers: two adherends with thicknesses of h_1 and h_2, respectively, and one adhesive layer with thickness of h_0. Modeling two adherends as Timoshenko's beams, we have

$$U_i(x_i, z_i, t) = u_i\,(x_i, t) + z_i\phi_i(x_i, t),\ W_i(x_i, z_i, t) = w_i(x_i, t), \tag{1}$$

where subscripts $(i=1, 2)$ represent the top and bottom adherends, respectively. $u_i(x_i,t)$, $\phi_i(x_i,t)$ and $w_i(x_i,t)$ are the axial displacement, the rotation and the deflection at the neutral axis of the beam i, respectively. Since $x_1 = x_2 = x$, subscript i ($i = 1, 2$) in displacement functions shown in Eq. (1) will be ignored thereafter. The constitutive equations for each adherend can be written as

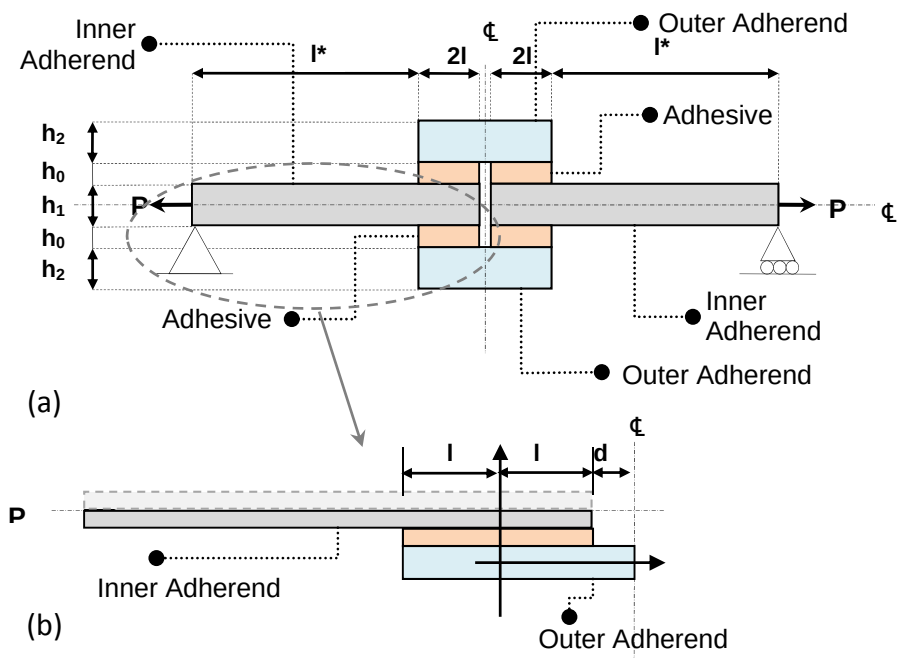

Fig. 4-1 A simply supported double-lap joint.

$$N_i(x,t) = C_i \frac{\partial u_i(x,t)}{\partial x}, \quad M_i(x,t) = D_i \frac{\partial \phi_i(x,t)}{\partial x}, \quad Q_i(x,t) = B_i \left(\phi_i(x,t) + \frac{\partial w_i(x,t)}{\partial x}\right), \tag{2}$$

where $N_i(x,t)$, $M_i(x,t)$, $Q_i(x,t)$ are the resultants of the axial force, the bending moment and the transverse shear force in each adherend, respectively; C_i, D_i and B_i are the axial, bending and shear stiffness coefficients of the beam i, respectively, and they can be calculated using the following equation

$$C_i = E_i b h_i, \; D_i = \frac{E_i b h_i^3}{12}, \; B_i = \kappa G_i b h_i. \tag{3}$$

E_i and G_i are the longitudinal and the shear modulus of elasticity, and h_i is the thickness of each layer. The width of the joint is equal to b for all layers. κ is the shear correction coefficient and chosen as *5/6* in this study.

An infinitesimal portion of the overlap in the lower-left quarter of the joint displayed in Fig. 4-1(b) is analyzed for force equilibrium, as shown in Fig. 4-2. The upper half of the inner

adherend is added to Fig. 4-2 so that the force equilibrium equations can be established more conveniently as

$$\frac{dN_1(x,t)}{dx} = 2b\tau(x,t), \quad \frac{dM_1(x,t)}{dx} = 0, \quad \frac{dQ_1(x,t)}{dx} = 0, \tag{4a}$$

$$\frac{dN_2(x,t)}{dx} = -b\tau(x,t), \quad \frac{dM_2(x,t)}{dx} = Q_2(x,t) - \frac{bh_2\tau(x,t)}{2}, \quad \frac{dQ_2(x,t)}{dx} = -b\sigma_2(x,t), \tag{4b}$$

where $\tau(x,t)$ and $\sigma_2(x,t)$ are the shear stress within the adhesive and the peel stress along the interface between the outer adherend and the adhesive layer (outer interface), respectively. $\tau(x,t)$ is assumed to be constant through the thickness of the adhesive. $\sigma_1(x,t)$ is the peel stress along the interface between the inner adherend and the adhesive layer (inner interface), which does not appear in Eq. (4a) due to symmetry, as shown in Fig. 4-2. For the same reason, it can be seen that $M_1(x,t) = 0$.

The global equilibrium of the entire cross section requires

$$N_T(x,t) = N_1(x,t) + 2N_2(x,t), \tag{5a}$$

$$M_T(x,t) = 0, \tag{5b}$$

$$Q_T(x,t) = 0, \tag{5c}$$

where $N_T(x,t)$, $M_T(x,t)$ and $Q_T(x,t)$ are the resultant axial, bending and shear forces along the neutral axis of the inner adherend.

Since the adhesive layer is much softer than the adherends, its axial force and bending moment are neglected, as shown in Fig. 4-3(a). Similar to the many existing solutions, this study assumes that the shear stress through the thickness of the adhesive layer is a constant. Considering the force equilibrium of the adhesive layer shown in Fig. 4-3(a), we have

$$\frac{\partial\tau(x,t)}{\partial x} = \frac{\sigma_2(x,t) - \sigma_1(x,t)}{h_a}. \tag{6}$$

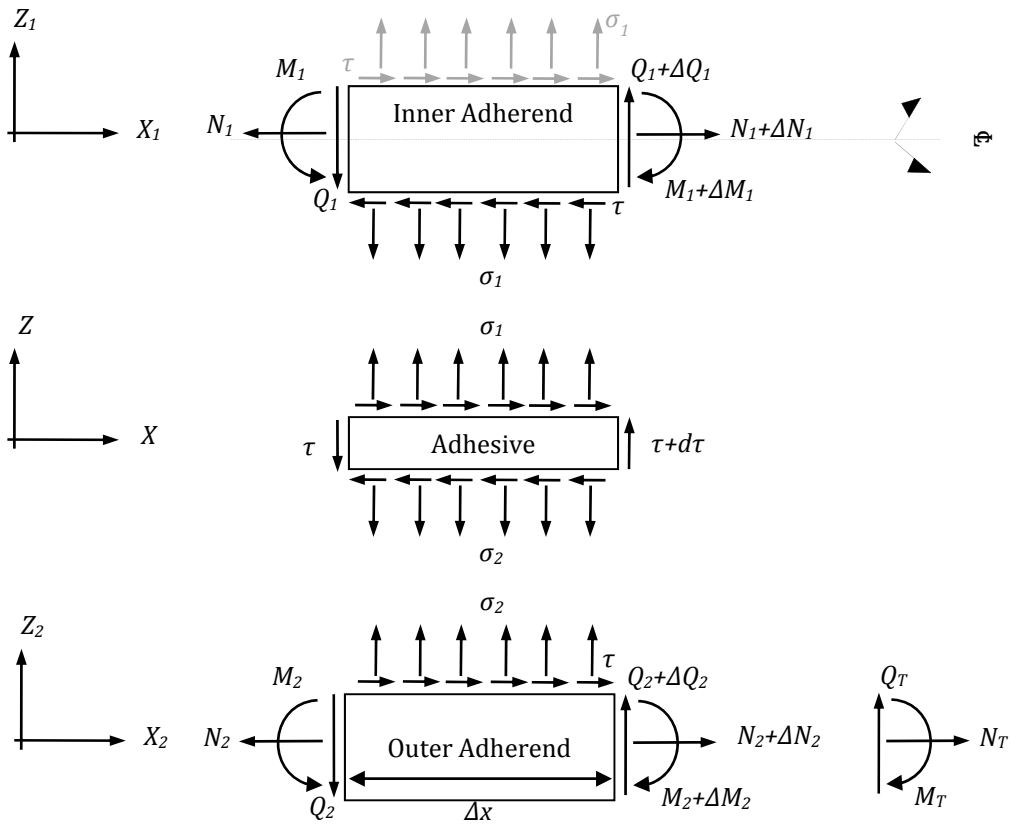

Fig. 4-2 Free body diagram of the assumed quadrant shown in Fig. 4-1(b).

Since $\tau(x,t)$ is not a constant along the whole interface, the left hand side of Eq. (6) is nonzero, suggesting peel stresses $\sigma_1(x,t)$ and $\sigma_2(x,t)$ must be different. To account for Eq. (6), we can model the adhesive layer as two linear springs connected by a shear layer as shown in Fig. 4-3(b). Unlike the two-parameter elastic/viscoelastic foundation model [15], in which the transverse (vertical) displacement of the adhesive layer is a constant through the thickness of the adhesive layer, the new model shown in Fig. 4-3(b) assumes the vertical displacement at the mid-plane ($w_a(x,t)$) of the adhesive is different from the ones on the top and bottom surfaces of the adhesive layer. As a result, strains in the upper and lower halves of the adhesive layer can be obtained as

$$\gamma_{xz}(x,t) = \frac{1}{h_0}\left(u_1(x,t) - u_2(x,t) - \frac{h_2}{2}\phi_2(x,t)\right) + \frac{\partial w_a(x,t)}{\partial x}, \tag{7a}$$

$$\varepsilon_{z1}(x,t) = -\frac{2}{h_0} w_a(x,t), \tag{7b}$$

$$\varepsilon_{z2}(x,t) = \frac{2}{h_0}\left(w_a(x,t) - w_2(x,t)\right), \tag{7c}$$

$$\varepsilon_x(x,t) = \frac{1}{2}\left(\frac{\partial u_1(x,t)}{\partial x} + \frac{\partial u_2(x,t)}{\partial x} + \frac{h_2}{2}\frac{\partial \phi_2(x,t)}{\partial x}\right). \tag{7d}$$

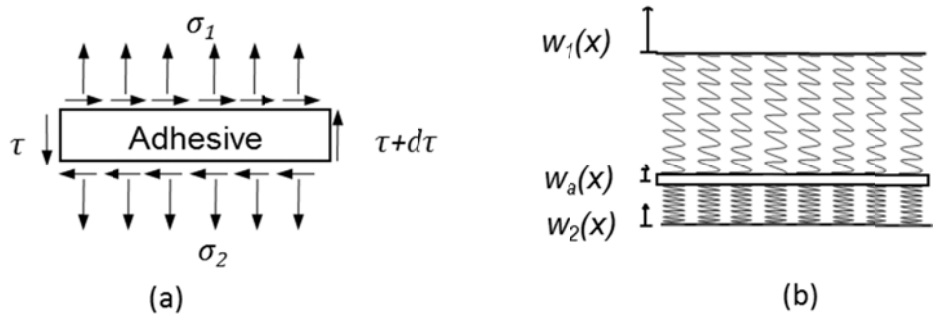

Fig. 4-3 Deformation model of the adhesive layer: (a) stress equilibrium of the adhesive layer, (b) deformation model of the adhesive layer.

where $\gamma_{xz}(x, t)$ is the shear strain within the adhesive layer; $\varepsilon_{yk}(x, t)$ (k = 1, 2) are peel strains (normal strain in *z*-direction in Fig. 4-3(b)) within the upper and lower halves of the adhesive layer, respectively; $\varepsilon_x(x, t)$ is the normal strain in the *x*-direction of the adhesive layer; $w_a(x,t)$ is the displacement of the mid-plane of the adhesive layer in *z*-direction. It can be seen that Eqs. 7(b) and 7(c) assume that peel strain through the upper and bottom halves of the adhesive layers are constant.

The hydrostatic stress-strain state of the adhesive layer for the upper ($k = 1$) and lower ($k = 2$) halves can be expressed as

$$e_k = \frac{1}{3}\left(\varepsilon_x + \varepsilon_y + \varepsilon_{zk}\right), \quad k = 1,2, \tag{8a}$$

$$s_k = \frac{1}{3}\left(\sigma_x + \sigma_{zk}\right), \quad k = 1,2, \tag{8b}$$

where ε_x and σ_x represent the normal strains and stresses in the top ($k = 1$) and bottom ($k = 2$) halves of the adhesive layer, respectively. The strains/stress tensor in each half of the adhesive layer can then be decomposed into hydrostatic and deviatoric parts as

$$[e_{ij}] = \begin{bmatrix} \varepsilon_x & 0 & \frac{\gamma_{xz}}{2} \\ 0 & \varepsilon_y & 0 \\ \frac{\gamma_{xz}}{2} & 0 & \varepsilon_{zk} \end{bmatrix} = \begin{bmatrix} e_k & 0 & 0 \\ 0 & e_k & 0 \\ 0 & 0 & e_k \end{bmatrix} + \begin{bmatrix} \varepsilon_x - e_k & 0 & \frac{\gamma_{xz}}{2} \\ 0 & \varepsilon_y - e_k & 0 \\ \frac{\gamma_{xz}}{2} & 0 & \varepsilon_{zk} - e_k \end{bmatrix}, \qquad k = 1,2, \tag{9a}$$

$$[s_{ij}] = \begin{bmatrix} \sigma_x & 0 & \tau_{xz} \\ 0 & 0 & 0 \\ \tau_{xz} & 0 & \sigma_k \end{bmatrix} = \begin{bmatrix} s_k & 0 & 0 \\ 0 & s_k & 0 \\ 0 & 0 & s_k \end{bmatrix} + \begin{bmatrix} \sigma_x - s_k & 0 & \tau_{xz} \\ 0 & -s_k & 0 \\ \tau_{xz} & 0 & \sigma_k - s_k \end{bmatrix}, \qquad k = 1,2. \tag{9b}$$

where $\tau_{xz} = \tau(x,t)$. The adhesive is modeled by a standard linear solid viscoelastic model (SLS), as used in Part I paper [2]. As shown in Fig. 4-4, SLS model consists of a linear spring in parallel with a Maxwell model (an elastic spring and a viscous damper connected in series). In this model, η, the viscous damping coefficient, and k_1 and k_2, the stiffness coefficients of two springs, are constant. The constitutive equations of the adhesive layer can be written as

$$P_1(s_{ij}) = Q_1(e_{ij}), \qquad (i,j) = 1,2,3, \tag{10a}$$

$$P_2(s_k) = Q_2(e_k), \qquad k = 1,2, \tag{10b}$$

$$P_1 = a_1 + \frac{\partial}{\partial t}, \qquad Q_1 = b_1 + b_2 \frac{\partial}{\partial t}, \tag{10c}$$

$$P_2 = 1, \qquad Q_2 = 3K, \tag{10d}$$

where $a_1 = k_2/\eta = 1/t_0$, $b_1 = (k_1.k_2)/\eta = k_1/t_0$, $b_2 = k_1 + k_2$, $K = \frac{E_a G_a}{3(3G_a - E_a)}$; t_0 is the retardation time; P_1 and Q_1 are the differential operators and given by Eq. (10c). P_2 and Q_2 are another two differential operators and given by Eq. (10d) based on the assumption that the adhesive layer behaves as an elastic material under the hydrostatic pressure state, which is common for most isotropic viscoelastic materials. Substituting Eqs. (8) and (9) into Eqs. (10a) and (10b) gives

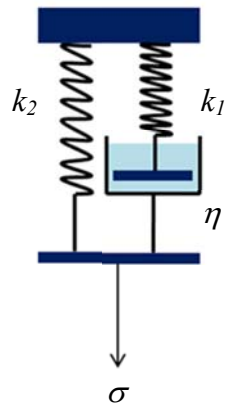

Fig. 4-4 Standard Linear Solid Model [16].

$$P_1(2\sigma_x - \sigma_k) = Q_1\left(2\varepsilon_x - \varepsilon_y - \varepsilon_{zk}\right), \qquad k = 1,2, \tag{11a}$$

$$P_2(2\sigma_k - \sigma_x) = Q_1\left(2\varepsilon_{zk} - \varepsilon_x - \varepsilon_y\right), \qquad k = 1,2, \tag{11b}$$

$$-P_1(\sigma_x + \sigma_k) = Q_1\left(2\varepsilon_y - \varepsilon_x - \varepsilon_{zk}\right), \qquad k = 1,2, \tag{11c}$$

$$P_1(\tau_{xz}) = \frac{1}{2}Q_1(\gamma_{xz}), \qquad k = 1,2, \tag{11d}$$

$$P_2(\sigma_x + \sigma_k) = Q_2\left(\varepsilon_x + \varepsilon_y + \varepsilon_{zk}\right), \qquad k = 1,2. \tag{11e}$$

By substituting Eqs. (11e) and (10d) into Eqs. (11a) and (11c) to eliminate ε_y, we have

$$\begin{aligned}&(2Q_1 + 3KP_1)\left(Q_1(2\varepsilon_x - \varepsilon_{zk}) - P_1(6K(\varepsilon_x + \varepsilon_{zk}) - 3\sigma_k)\right)\\ &-(6KP_1 + Q_1)\left(Q_1(\varepsilon_x + \varepsilon_{zk}) - 3KP_1(\varepsilon_x + \varepsilon_{zk})\right) = 0, \qquad k = 1,2.\end{aligned} \tag{12}$$

Substituting Eq. (12) into Eq. (10c) gives

$$\left(a_{10} + a_{11}\frac{\partial}{\partial t} + a_{12}\frac{\partial^2}{\partial t^2}\right)\varepsilon_x + \left(b_{10} + b_{11}\frac{\partial}{\partial t} + b_{12}\frac{\partial^2}{\partial t^2}\right)\varepsilon_{zk} + \left(c_{10} + c_{11}\frac{\partial}{\partial t} + c_{12}\frac{\partial^2}{\partial t^2}\right)\sigma_k = 0, \tag{13}$$

where

$a_{10} = 3b_1^2 - 9a_1b_1K,$ $\quad a_{11} = 6b_1b_2 - 9b_1K - 9a_1b_2K,$ $\quad a_{12} = 3b_2^2 - 9b_2K,$

$b_{10} = -3b_1^2 - 18a_1b_1K,$ $\quad b_{11} = -6b_1b_2 - 18b_1K - 18a_1b_2K,$ $\quad b_{12} = -3b_2^2 - 18b_2K,$

$c_{10} = 6a_1b_1 + 9a_1^2K,$ $\quad c_{11} = 6b_1 + 6a_1b_2 + 18a_1K,$ $\quad c_{12} = 6b_2.$

Substituting Eq. (7) into Eq. (13), we have

$$\frac{1}{2}\left(a_{10}+a_{11}\frac{\partial}{\partial t}+a_{12}\frac{\partial^2}{\partial t^2}\right)\left(\frac{\partial \mathrm{u}_{1(\mathrm{x,t})}}{\partial x}+\frac{\partial \mathrm{u}_2(\mathrm{x,t})}{\partial \mathrm{x}}+\frac{\mathrm{h}_2}{2}\frac{\partial \phi_2(\mathrm{x,t})}{\partial \mathrm{x}}\right)$$
$$+2\left(b_{10}+b_{11}\frac{\partial}{\partial t}+b_{12}\frac{\partial^2}{\partial t^2}\right)\left(-\frac{\mathrm{w_a(x,t)}}{\mathrm{h_0}}\right)+\left(c_{10}+c_{11}\frac{\partial}{\partial t}+c_{12}\frac{\partial^2}{\partial t^2}\right)\sigma_1(\mathrm{x,t})=0, \tag{14a}$$

$$\frac{1}{2}\left(a_{10}+a_{11}\frac{\partial}{\partial t}+a_{12}\frac{\partial^2}{\partial t^2}\right)\left(\frac{\partial u_1(x,t)}{\partial x}+\frac{\partial u_2(x,t)}{\partial x}+\frac{h_2}{2}\frac{\partial \phi_2(x,t)}{\partial x}\right)$$
$$+2\left(b_{10}+b_{11}\frac{\partial}{\partial t}+b_{12}\frac{\partial^2}{\partial t^2}\right)\left(\frac{w_a(x,t)-w_2(x,t)}{h_0}\right)+\left(c_{10}+c_{11}\frac{\partial}{\partial t}+c_{12}\frac{\partial^2}{\partial t^2}\right)\sigma_2(x,t)=0. \tag{14b}$$

By differentiating both sides of Eq. (14) twice and considering Eqs. (4), (5), and (6), we have

$$\left(a_{10}+a_{11}\frac{\partial}{\partial t}+a_{12}\frac{\partial^2}{\partial t^2}\right)\left(\frac{1}{2}\left(-\frac{2}{C_1}+\frac{1}{C_2}\right)\frac{\partial^2 N_2(x,t)}{\partial x^2}+\left(\frac{h_2}{4D_2}\right)\frac{\partial^2 M_2(x,t)}{\partial x^2}\right)$$
$$+\frac{2}{h0}\left(b_{10}+b_{11}\frac{\partial}{\partial t}+b_{12}\frac{\partial^2}{\partial t^2}\right)\left(-\frac{\partial^2 w_a(x,t)}{\partial x^2}\right)$$
$$+\frac{1}{b}\left(c_{10}+c_{11}\frac{\partial}{\partial t}+c_{12}\frac{\partial^2}{\partial t^2}\right)\left(-\frac{\partial^4 M_2(x,t)}{\partial x^4}+\left(\frac{h_2}{2}+h_0\right)\frac{\partial^4 N_2(x,t)}{\partial x^4}\right)=0, \tag{15a}$$

$$\left(a_{10}+a_{11}\frac{\partial}{\partial t}+a_{12}\frac{\partial^2}{\partial t^2}\right)\left(\frac{1}{2}\left(-\frac{2}{C_1}+\frac{1}{C_2}\right)\frac{\partial^2 N_2(x,t)}{\partial x^2}+\left(\frac{h_2}{4D_2}\right)\frac{\partial^2 M_2(x,t)}{\partial x^2}\right)$$
$$+\frac{2}{h0}\left(b_{10}+b_{11}\frac{\partial}{\partial t}+b_{12}\frac{\partial^2}{\partial t^2}\right)$$
$$\left(-\frac{1}{B_2}\frac{\partial^2 M_2(x,t)}{\partial x^2}+\left(\frac{h_2}{2B2}\right)\frac{\partial^2 N_2(x,t)}{\partial x^2}+\frac{M_2(x,t)}{D_2}+\frac{\partial^2 w_a(x,t)}{\partial x^2}\right)$$
$$+\frac{1}{b}\left(c_{10}+c_{11}\frac{\partial}{\partial t}+c_{12}\frac{\partial^2}{\partial t^2}\right)\left(-\frac{\partial^4 M_2(x,t)}{\partial x^4}+\left(\frac{h_2}{2}\right)\frac{\partial^4 N_2(x,t)}{\partial x^4}\right)=0. \tag{15b}$$

Substituting Eq. (7a) into (11d) gives

$$P_1\big(\tau(x,t)\big)=\frac{1}{2}Q_1\left(\frac{1}{\mathrm{h_0}}\left(u_1(x,t)-u_2(x,t)-\frac{h_2}{2}\phi_2(x,t)\right)+\frac{\partial w_a(x,t)}{\partial x}\right). \tag{16}$$

Differentiating both sides of Eq. (16) and then substituting Eqs. (2) and (5)into it gives

$$P_1\left(-\frac{1}{b}\frac{\partial^2 N_2(x,t)}{\partial x^2}\right)=\frac{1}{2}Q_1\left(A_{31}M_2(x,t)+A_{32}N_2(x,t)+A_{33}N_T(x,t)+\frac{\partial^2 w_a(x,t)}{\partial x^2}\right), \tag{17}$$

where

$$A_{31}=-\frac{h_2}{2h_0D_2},\qquad A_{32}=-\frac{1}{h_0}\left(\frac{2}{C_1}+\frac{1}{C_2}\right),\qquad A_{33}=\frac{1}{C_1h_0}.$$

Applying Laplace transform to both sides of Eq. (17) yields

$$\frac{\partial^2 w_{aL}(x,s)}{\partial x^2}= \tag{18}$$
$$\frac{B_{71}(s)}{B_{70}(s)}\frac{\partial^2 N_{2L}(x,s)}{\partial x^2}+\frac{B_{72}(s)}{B_{70}(s)}M_{2L}(x,s)+\frac{B_{73}(s)}{B_{70}}N_{2L}(x,s)+\frac{B_{74}(s)}{B_{70}(s)}N_{TL}(x,s),$$

where $w_{aL}(x,s)$, $M_{1L}(x,s)$, $N_{1L}(x,s)$, $M_{TL}(x,s)$, and $N_{TL}(x,s)$ are Laplace transforms of $w_a(x,t)$, $M_1(x,t)$, $N_1(x,t)$, $M_T(x,t)$, and $N_T(x,t)$, respectively; and

$$B_{70}(s)=\frac{1}{2}(b_1+b_2s),\qquad B_{71}(s)=\frac{1}{b}(a_1+s),\qquad B_{72}(s)=-\frac{A_{31}}{2}(b_1+b_2s),$$

$$B_{73}(s)=-\frac{A_{32}}{2}(b_1+b_2s),\qquad B_{74}(s)=-\frac{A_{33}}{2}(b_1+b_2s).$$

Similarly, applying Laplace transform to Eq. (15), we have

$$B_{81}(s)\partial^4\frac{M_{2L}(x,s)}{\partial x^4}+B_{82}(s)\frac{\partial^4 N_{2L}(x,s)}{\partial x^4}+B_{83}(s)\frac{\partial^2 M_{2L}(x,s)}{\partial x^2}, \tag{19a}$$
$$+B_{84}(s)\frac{\partial^2 N_{2L}(x,s)}{\partial x^2}+B_{85}(s)\frac{\partial^2 w_{aL}(s)}{\partial x^2}=0,$$

$$B_{91}(s)\partial^4\frac{M_{2L}(x,s)}{\partial x^4}+B_{92}(s)\frac{\partial^4 N_{2L}(x,s)}{\partial x^4}+B_{93}(s)\frac{\partial^2 M_{2L}(x,s)}{\partial x^2}, \tag{19b}$$
$$+B_{94}(s)\frac{\partial^2 N_{2L}(x,s)}{\partial x^2}+B_{95}(s)M_{2L}(x,s)+B_{96}(s)\frac{\partial^2 w_{aL}(s)}{\partial x^2}=0,$$

where $M_{2L}(x,s)$ and $N_{2L}(x,s)$ are Laplace transforms of $M_2(x,t)$ and $N_2(x,t)$, respectively; and

$$B_{81}(s)=-\frac{1}{b}(c_{10}+c_{11}s+c_{12}s^2),B_{82}(s)=\frac{1}{b}\left(\frac{h_{12}}{2}+h_0\right)(c_{10}+c_{11}s+c_{12}s^2),$$

$$B_{83}(s)=\left(\frac{h_2}{4D_2}\right)(a_{10}+a_{11}s+a_{12}s^2),$$

$$B_{84}(s)=\frac{1}{2}\left(-\frac{2}{C_1}+\frac{1}{C_2}-\frac{h_2}{2D_2}\left(\frac{h_1+h_2}{2}+h_0\right)\right)(a_{10}+a_{11}s+a_{12}s^2)+\left(\frac{h_1}{h_0B_1}\right)(b_{10}+b_{11}s+b_{12}s^2),$$

$$B_{85}(s) = -\frac{2}{h_0}(b_{10} + b_{11}s + b_{12}s^2), B_{91}(s) = -\frac{1}{b}(c_{10} + c_{11}s + c_{12}s^2),$$

$$B_{92}(s) = \left(\frac{h_2}{2b}\right)(c_{10} + c_{11}s + c_{12}s^2),$$

$$B_{93}(s) = \left(\frac{h_2}{4D_2}\right)(a_{10} + a_{11}s + a_{12}s^2) - \left(\frac{2}{h_0B_2}\right)(b_{10} + b_{11}s + b_{12}s^2),$$

$$B_{94}(s) = \frac{1}{2}\left(\frac{-2}{C_1} + \frac{1}{C_2}\right)(a_{10} + a_{11}s + a_{12}s^2) + \left(\frac{h_2}{h_0B_2}\right)(b_{10} + b_{11}s + b_{12}s^2),$$

$$B_{95}(s) = \frac{2}{D_2h_0}(b_{10} + b_{11}s + b_{12}s^2), B_{96}(s) = \frac{2}{h_0}(b_{10} + b_{11}s + b_{12}s^2).$$

Substituting Eq. (18) into Eq. (19) yields

$$\partial^4\frac{M_{2L}(x,s)}{\partial x^4} + C_{41}(s)\frac{\partial^4 N_{2L}(x,s)}{\partial x^4} + C_{42}(s)\frac{\partial^2 M_{2L}(x,s)}{\partial x^2} + C_{43}(s)\frac{\partial^2 N_{2L}(x,s)}{\partial x^2} + C_{44}(s)M_{2L}(x,s) + C_{45}(s)N_{2L}(s) + C_{46}(s)N_{TL}(x,s) = 0, \tag{20a}$$

$$\frac{\partial^4 M_{2L}(x,s)}{\partial x^4} + C_{51}(s)\frac{\partial^4 N_{2L}(x,s)}{\partial x^4} + C_{52}(s)\frac{\partial^2 M_{2L}(x,s)}{\partial x^2} + C_{53}(s)\frac{\partial^2 N_{2L}(x,s)}{\partial x^2} + C_{54}(s)M_{2L}(x,s) + C_{55}(s)N_{2L}(s) + C_{56}(s)N_{TL}(x,s) = 0, \tag{20b}$$

where

$$C_{41}(s) = \frac{B_{82}(ss)}{B_{81}(s)}, \quad C_{42}(s) = \frac{B_{83}(s)}{B_{81}(s)}, \quad C_{43}(s) = \frac{1}{B_{81}(s)}\left(B_{84}(s) + \frac{B_{85}(s)B_{71}(s)}{B_{70}(s)}\right),$$

$$C_{44}(s) = \frac{B_{85}(s)B_{72}(s)}{B_{70}(s)B_{81}(s)}, \quad C_{45}(s) = \frac{B_{86}(s)B_{73}(s)}{B_{70}(s)B_{81}(s)}, \quad C_{46}(s) = \frac{B_{86}(s)B_{74}(s)}{B_{70}(s)B_{81}(s)},$$

$$C_{51}(s) = \frac{B_{92}(ss)}{B_{91}(s)}, \quad C_{52}(s) = \frac{B_{93}(s)}{B_{91}(s)}, \quad C_{53}(s) = \frac{1}{B_{91}(s)}\left(B_{94}(s) + \frac{B_{96}(s)B_{71}(s)}{B_{70}(s)}\right),$$

$$C_{54}(s) = \frac{1}{B_{91}(s)}\left(B_{95}(s) + \frac{B_{96}(s)B_{72}(s)}{B_{70}(s)}\right), \quad C_{55}(s) = \frac{B_{96}(s)B_{73}(s)}{B_{70}(s)B_{91}(s)}, \quad C_{56}(s) = \frac{B_{96}(s)B_{74}(s)}{B_{70}(s)B_{91}(s)}.$$

By subtracting Eq. (20a) from Eq. (20b), the following expression is obtained

$$\frac{\partial^2 M_{2L}(x,s)}{\partial x^2} = D_{21}(s)\frac{\partial^4 N_{2L}(x,s)}{\partial x^4} + D_{22}(s)\frac{\partial^2 N_{2L}(x,s)}{\partial x^2} + D_{23}(s)M_{2L}(x,s) + D_{24}(s)N_{2L}(x,s) + D_{25}(s)N_{TL}(x,s), \tag{21}$$

where

$D_{21}(s) = -\frac{C_{51}(s)-C_{41}(s)}{C_{52}(s)-C_{42}(s)}$, $D_{22}(s) = -\frac{C_{53}(s)-C_{43}(s)}{C_{52}(s)-C_{42}(s)}$, $D_{23}(s) = -\frac{C_{54}(s)-C_{44}(s)}{C_{52}(s)-C_{42}(s)}$,

$D_{24}(s) = -\frac{C_{55}(s)-C_{44}(s)}{C_{52}(s)-C_{42}(s)}$, $D_{25}(s) = -\frac{C_{56}(s)-C_{46}(s)}{C_{52}(s)-C_{42}(s)}$,

By subtracting Eq. (20b) multiplied by $C_{42}(s)$ from Eq. (20a) multiplied by $C_{52}(s)$, we have

$$\frac{\partial^4 M_{2L}(x,s)}{\partial x^4} = E_{21}(s)\frac{\partial^4 N_{2L}(x,s)}{\partial x^4}^2 + E_{22}(s)\frac{\partial^2 N_{2L}(x,s)}{\partial x^2} + E_{23}(s)M_{2L}(x,s) + E_{24}(s)N_{2L}(x,s) + E_{25}(s)N_{T\mathrm{L}}(x,s), \tag{22}$$

where

$E_{21}(s) = -\frac{C_{41}(s)C_{52}(s)-C_{42}(s)C_{51}(s)}{C_{52}(s)-C_{42}(s)}$, $E_{22}(s) = -\frac{C_{43}(s)C_{52}(s)-C_{42}(s)C_{53}(s)}{C_{52}(s)-C_{42}(s)}$,

$E_{23}(s) = -\frac{C_{44}(s)C_{52}(s)-C_{42}(s)C_{54}(s)}{C_{52}(s)-C_{42}(s)}$, $E_{24}(s) = -\frac{C_{45}(s)C_{52}(s)-C_{42}(s)C_{55}(s)}{C_{52}(s)-C_{42}(s)}$,

$E_{25}(s) = -\frac{C_{46}(s)C_{52}(s)-C_{42}(s)C_{56}(s)}{C_{52}(s)-C_{42}(s)}$.

Differentiating Eq. (21) twice and substituting it into Eq. (22) yields

$$M_{2L}(x,s) = F_{21}(s)\frac{\partial^6 N_{2L}(x,s)}{\partial x^6} + F_{22}(s)\frac{\partial^4 N_{2L}(x,s)}{\partial x^4} + F_{23}(s)\frac{\partial^2 N_{2L}(x,s)}{\partial x^2} + F_{24}(x,s)N_{2L}(x,s) + F_{25}(s)N_{TL}(x,s), \tag{23}$$

where

$F_{21}(s) = \frac{D_{21}(s)}{E_{23}(s)-D_{23}(s)^2}$, $F_{22}(s) = \frac{D_{22}(s)+D_{23}(s)D_{21}(s)-E_{21}(s)}{E_{23}(s)-D_{23}(s)^2}$,

$F_{23}(s) = \frac{D_{24}(s)+D_{23}(s)D_{22}(s)-E_{22}(s)}{E_{23}(s)-D_{23}(s)^2}$, $F_{24}(s) = \frac{D_{23}(s)D_{24}(s)-E_{24}(s)}{E_{23}(s)-D_{23}(s)^2}$,

$F_{25}(s) = \frac{D_{23}(s)D_{25}(s) - E_{25}(s)}{E_{23}(s) - D_{23}(s)^2}$.

By substituting Eq. (23) into Eq. (21), the governing equation is obtained as

$$G_{21}(s)\frac{\partial^8 N_{2L}(x,s)}{\partial x^8}+G_{22}(s)\frac{\partial^6 N_{2L}(x,s)}{\partial x^6}+G_{23}(s)\frac{\partial^4 N_{2L}(x,s)}{\partial x^4}+G_{24}(s)\frac{\partial^2 N_{2L}(x,s)}{\partial x^2}$$
$$+G_{25}(s)N_{2L}(x,s)+G_{26}(s)N_{TL}(x,s)=0, \tag{24}$$

where

$G_{21}(s)=F_{21}(s)$, $G_{22}(s)=F_{22}(s)-D_{23}(s)F_{21}(s)$,

$G_{23}(s)=F_{23}(s)-D_{21}(s)-D_{23}(s)F_{22}(S)$, $G_{24}(s)=F_{24}(s)-D_{22}(s)-D_{23}(s)F_{23}(s)$,

$G_{25}(s)=-D_{24}(s)-D_{23}(s)F_{14}(s)$, $G_{26}(s)=-D_{25}(s)-D_{23}(s)F_{25}(s)$.

The characteristic equation of Eq. (24) can be written as

$$G_{21}(s)\bar{X}^8+G_{22}(s)\bar{X}^6+G_{23}(s)\bar{X}^4+G_{24}(s)\bar{X}^2+G_{25}(s)=0. \tag{25}$$

Eq. (25) gives the roots $\pm\emptyset_1(s)$, $\pm\emptyset_2(s)$, $\pm\emptyset_3(s)$, and $\pm\emptyset_4(s)$. Then general solution of Eq. (24) can be expressed obtained as

$$N_{2L}(x,s)=N_{2LH}(x,s)+N_{2LP}(x,s), \tag{26a}$$

where

$$N_{2LH}(x,s)=\sum_{i=1}^{n=4}[\alpha_i(s)\sinh(\emptyset_i(s)x)+\beta_i(s)\cosh(\emptyset_i(s)x)], \tag{26b}$$

$$N_{2LP}(x,s)=-\frac{G_{26}(s)}{\mathrm{G}_{25}(\mathrm{s})}N_{TL}(x,s). \tag{26c}$$

In the same way, the rest of the beam forces and the interface stresses can be expressed as

$$M_{2L}(x,s)=M_{2LH}(x,s)+M_{2LP}(x,s), \tag{27a}$$

where

$$M_{2LH}(x,s)=\sum_{i=1}^{n=4}Y_{M2i}(s)[\alpha_i(s)\sinh(\emptyset_i(s)x)+\beta_i(s)\cosh(\emptyset_i(s)x)], \tag{27b}$$

$$M_{2LP}(x,s)=F_{25}(s)N_{TL}(x,s), \tag{27c}$$

$$Y_{M2i}(s)=F_{21}(s)\emptyset_i^6(s)+F_{22}(s)\emptyset_i^3(s)+F_{23}(s)\emptyset_i^2(s)+F_{24}(s), \tag{27d}$$

and,

$$N_{1L}(x,s)=N_{TL}(x,s)-2N_{2L}(x,s). \tag{28}$$

$Q_{2L}(x,s)$ can be found from the relationship provided in Eq. (4b). The Laplace transformed shear stress within the adhesive layer and the peel stresses along two interfaced can be as

$$\sigma_{2L}(x,s) = -\frac{1}{b}\frac{\partial Q_{2L}(x,s)}{\partial x}, \tag{29a}$$

$$\tau_L(x,s) = \frac{1}{b}\frac{\partial N_{1L}(x,s)}{dx}, \tag{29b}$$

$$\sigma_{1L}(x,s) = \sigma_{2L}(x,s) + \frac{h_0}{b}\frac{d^2 N_{2L}(x,s)}{dx^2}. \tag{29c}$$

Eight coefficients α_i and β_i can be determined by considering boundary conditions at the two ends of the overlap portion of the joint. Same method used in the case of the single-lap joint is adopted to conduct the inverse Laplace transform of the above solutions.

Considering simply supported boundary conditions shown in Fig. 4-1 and assuming that the external forces are applied instantly and kept constant with time, the boundary conditions can be written as

$$N_2(x=-l,t) = 0, \quad M_2(x=-l,t) = 0, \quad Q_2(x=-l,t) = 0, \quad \tau(x=-l,t) = 0, \tag{30a}$$

$$N_2(x=l,t) = \frac{P}{2}H(t), \quad Q_2(x=l,t) = 0, \quad \tau(x=l,t) = 0, \tag{30b}$$

where P is the pulling force applied at the very ends of the joint; $H(t)$ is the Heaviside function.

At the symmetric axis where x = $l + d$ as shown in Fig. 4-1, the rotation of the outer adherend is zero, i.e.

$$\phi_2(x=l+d,t) = 0. \tag{31}$$

By integrating the second constitutive equation in Eq. (2) from $l+d$ to l, the rotation at $x = l$ of the outer adherend can be obtained as

$$\phi_2(x=l,t) = -\frac{M_2(x=l,t)}{D_2}d. \tag{32}$$

Since $Q_2 = 0$ at $x = l$, we have

$$-\frac{M_2(x=l,t)}{D_2}d+\frac{\partial w_2(x=L,t)}{\partial x}=0. \tag{33}$$

Adding Eq. (14a) to Eq. (14b), we have

$$\left(a_{10}+a_{11}\frac{\partial}{\partial t}+a_{12}\frac{\partial^2}{\partial t^2}\right)\left(\frac{\partial u_1(x=l,t)}{\partial x}+\frac{\partial u_2(x=l,t)}{\partial x}+\frac{h_2}{2}\frac{\partial \phi_2(x=l,t)}{\partial x}\right)+2\left(b_{10}+b_{11}\frac{\partial}{\partial t}+b_{12}\frac{\partial^2}{\partial t^2}\right)\left(\frac{-w_2(x=l,t)}{h_0}\right)+\left(c_{10}+c_{11}\frac{\partial}{\partial t}+c_{12}\frac{\partial^2}{\partial t^2}\right)\left(\sigma_1(x=l,t)+\sigma_2(x=l,t)\right)=0. \tag{34}$$

Differentiating Eq. (34) once with respect to x and subsituting Eq. (2) and (33) gives another boundary condition needed to determine all the coefficients

$$\left(a_{10}+a_{11}\frac{\partial}{\partial t}+a_{12}\frac{\partial^2}{\partial t^2}\right)\left(\frac{1}{C_1}\frac{\partial N_1(x=l,t)}{\partial x}+\frac{1}{C_2}\frac{\partial N_2(x=l,t)}{\partial x}+\frac{h_2}{2D_2}\frac{\partial M_2(x=l,t)}{\partial x}\right)+2\left(b_{10}+b_{11}\frac{\partial}{\partial t}+b_{12}\frac{\partial^2}{\partial t^2}\right)\left(\frac{M_2(x=l,t)}{D_2}\frac{d}{h_0}\right)+\left(c_{10}+c_{11}\frac{\partial}{\partial t}+c_{12}\frac{\partial^2}{\partial t^2}\right)\left(\frac{\partial \sigma_1(x=l,t)}{\partial x}+\frac{\partial \sigma_2(x=l,t)}{\partial x}\right)=0. \tag{35}$$

4.3. Verification and parametric studies

As verifications, the present model is compared with the numerical analysis using finite element analysis (FEA), which is assumed accurate in this study. A simply supported double-lap joint shown in Fig. 4-5 is analyzed by both methods. The geometry and material properties of the joint are shown Table 4-1 and Table 4-2. Commercial software ABAQUS/CAE is used to conduct FEA. A user's subroutine (UMAT) is used to model the viscoelastic material of the adhesive. For each numerical example, a plane stress model is constructed with 4-node bilinear stress quadrilateral elements. A meshing pattern of elements with size ranged between 0.02 mm and 0.2 mm in longitudinal direction is chosen. Refined mesh is used in the regions near the edges and within the interfaces to capture more accurate stress distributions, as shown in Fig. 4-5.

Denote the initial shear modulus of elasticity denotes by G_0, and the ultimate shear modulus by G_∞. As a numerical example, we take $G_\infty=\frac{1}{3}G_0$ and $t_0=5(days)$. The viscoelastic parameters can be obtained as follow

$$a_1 = \frac{1}{t_0} = \frac{1}{5}, \tag{36a}$$

$$b_1 = \frac{k_1}{t_0} = \frac{2G_\infty}{5}, \tag{36b}$$

$$b_2 = 2(G_0 - G_\infty). \tag{36c}$$

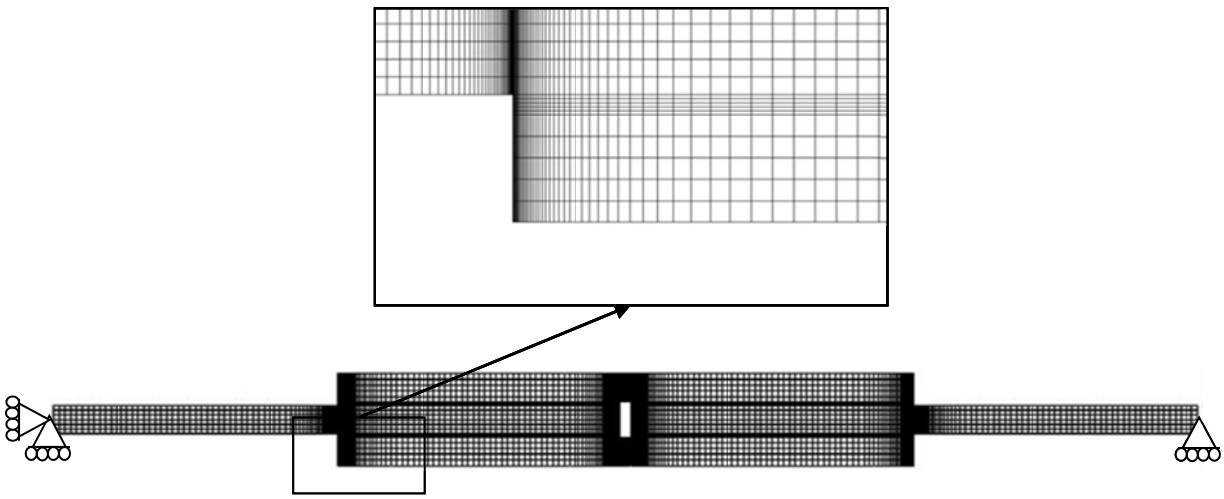

Fig. 4-5 Finite element model of a simply supported double-lap joint under tension.

Table 4-1 Geometrical parameters of the double-lap joint.

	l	l*	h_0	h_1	h_2
Dimension	25 mm	50 mm	0.20 mm	5 mm	5 mm

Table 4-2 Mechanical properties of the materials of the joint.

Mechanical properties	Outer adherend	Adhesive	Inner adherend
Modulus of Elasticity E	60GPa	4.82GPa	60GPa
Poisson ratio ν	0.33	0.25	0.33

Figure 4-6 compares the shear stress in the double-lap joint obtained by the present 3PVF model and the one obtained by the FEA. In this figure, shear stresses within the adhesive layer are calculated at 5, 10 and 30 days. The non-transient instant analysis at time 0 is also carried out to

evaluate the elastic behavior of the joints. Figure 4-6 clearly shows that the present 3PVF model reaches excellent agreement with FEA. It can be seen that both methods can satisfy the zero-shear stress boundary conditions at the free edges of the adhesive layer. Figure 4-7 compares the peel stresses obtained by the present model and the ones obtained by FEA. Once again, excellent agreement with FEA has been achieved by the present model on predicting the peel stress distributions of the joint. Both solutions show that peel stress distributions along the inner and outer interfaces are different. All these suggest that the present 3PVF model provides an improved and efficient tool to analyze the viscoelastic behavior of the adhesive joints.

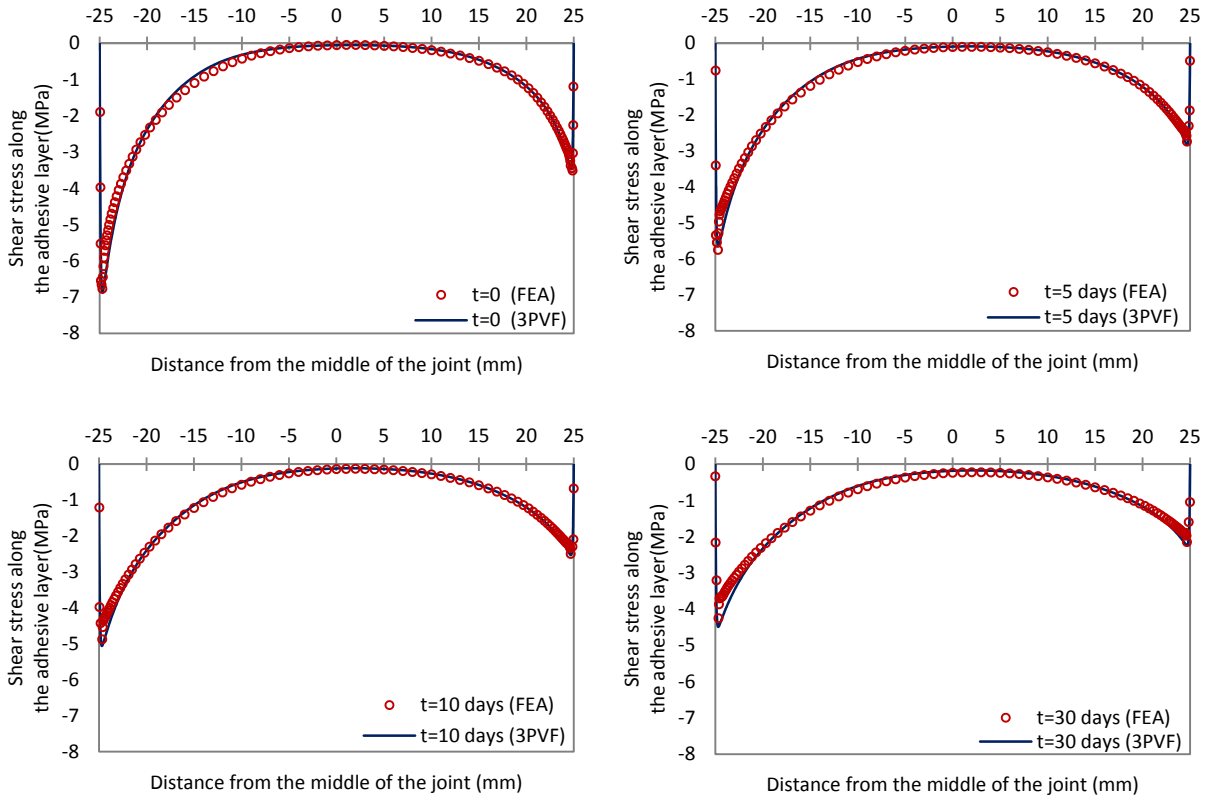

Fig. 4-6 Comparison of shear stress in the adhesive layer of the double-lap joint obtained by the present 3PVF model and FEA.

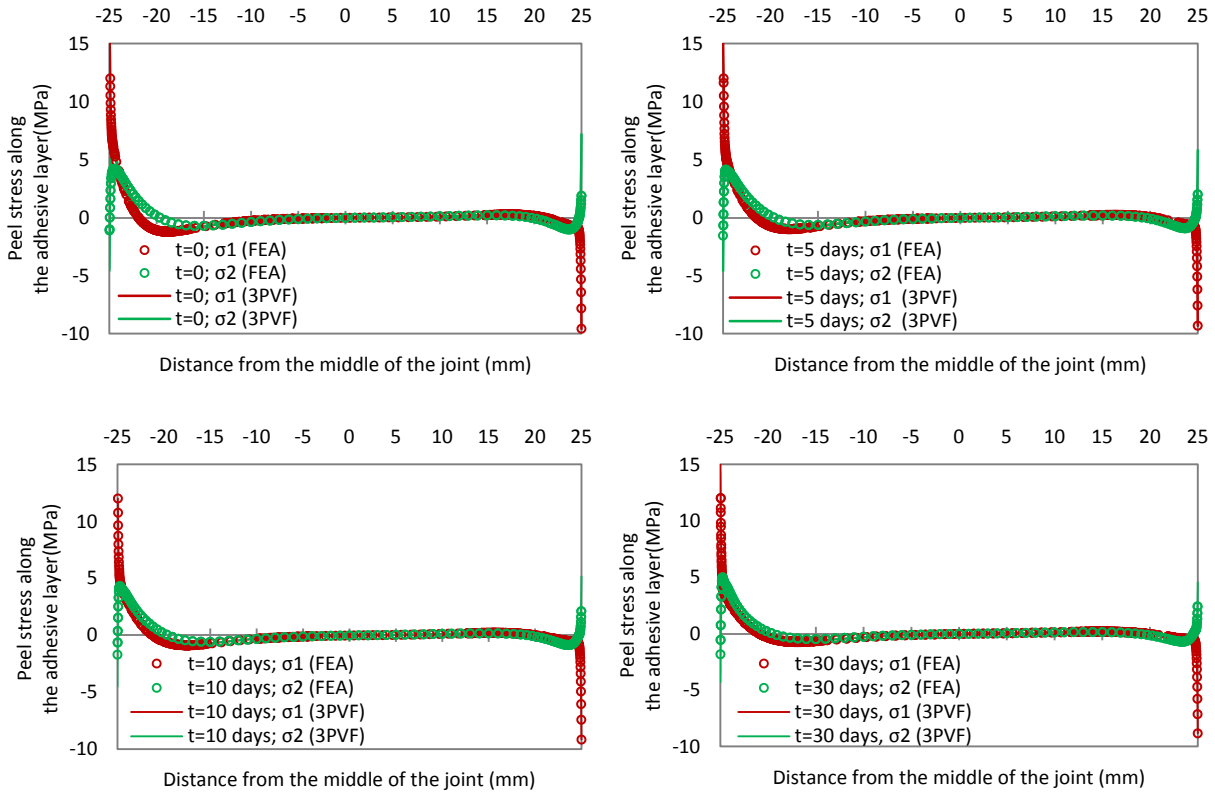

Fig. 4-7 Comparison of the peel stresses in the double-lap joint obtained by the present model and the FEA.

The time-dependent stress distributions of the double-lap joint are further demonstrated Figs. 4-8 and 4-9. Figure 4-8 shows that shear stress concentration is higher near the left end than that near the right end, suggesting that debonding induced by shear stress is more likely to occur near the left end than the right end. Remarkable shear stress relaxation due to the viscoelastic behavior of the adhesive layer is clearly shown in Fig. 4-8. It shows that maximum shear stress drops up to 40% after 30 days based on the mechanical properties used in this study.

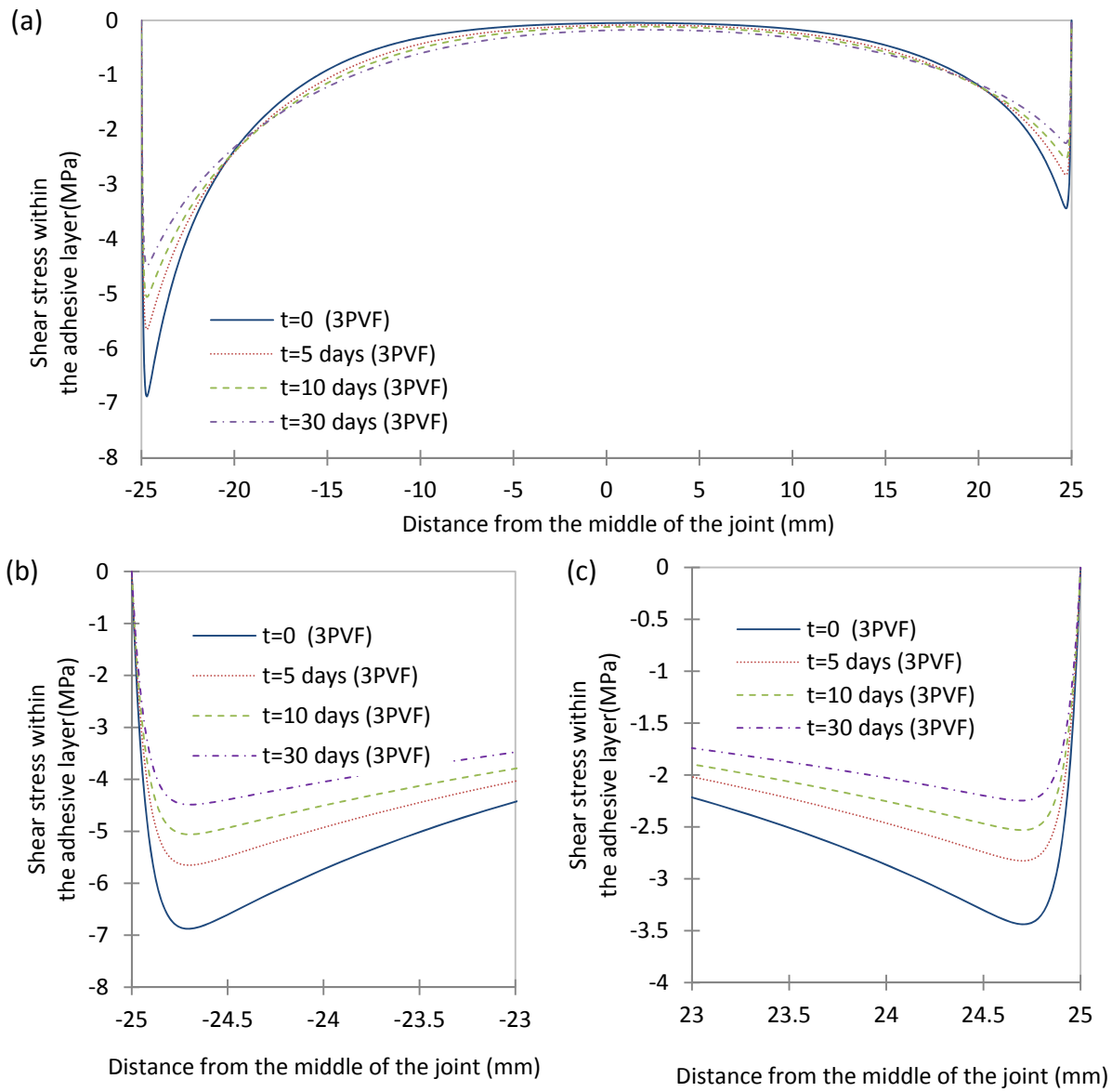

Fig. 4-8 Time-dependent shear stress within the adhesive layer of the double-lap joint: (a) Shear stress distribution along the whole interface, (b) shear stress at the very left edge of the adhesive layer, (c) shear stress at the very right edge of the adhesive layer.

The peel stress along the inner interface at different time is shown in Fig. 4-9(a). It can be seen that the peel stress in the middle region of the interface is close to zero; however, significant peel stress concentrations occur at the two ends of the interface. Figures 4-9(b) and 4-9(c) show the close-ups of peel stresses close to the left and right ends of the interface, respectively. It can be

seen that the peel stress concentration near the ends is even higher than that of the shear stress, suggesting that peel stress should be considered in the analysis of the double-lap joints. It is interesting to note that the peel stress at the left end of the interface is positive (tensile); while at the right end, it is negative (compression). Since the interface is more vulnerable under tension, it can be expected that debonding is more likely to initiate at the left end, rather than at the right one. Stress relaxation induced by the viscoelastic behavior of the adhesive layer is clearly revealed in this figure by the reduction of the maximum peel stress with time.

The peel stress along the outer interface is presented in Fig. 4-10. It is very interesting to see that although the peel stress is positive near the left end, it reduces sharply from a high value at a small distance from the left end to negative at the left end, as shown in Fig. 4-10(b). Near the right end of the interface, peel stress exhibits an opposite trend. As shown in Fig. 4-10(c), the peel stress appears to be negative near the end, but sharply changes to positive approaching the end. This suggests that along the outer interface, debonding is more likely to initiate from the right end, rather the left end. Compared Figs. 4-9 and 4-10, it can be seen that the peel stresses along two interfaces have different signs at the edges of the interface. Capturing this difference is very important to predict the possible debonding location. Unfortunately, this cannot be done by existing solutions since both peel stresses are assumed the same in these solutions.

Both Figs. 4-9 and 4-10 show that peel stress also relaxs with time as the shear stress. However, it can be seen that the relaxation rate is much slower. In addition, the maximum peel stress at the end of the interface seems not reducing very much with time. This suggests that although viscoelasticity of the adhesive layer can reduce the shear stress concentration within the adhesive layer, it has very little effect on peel stress concentration.

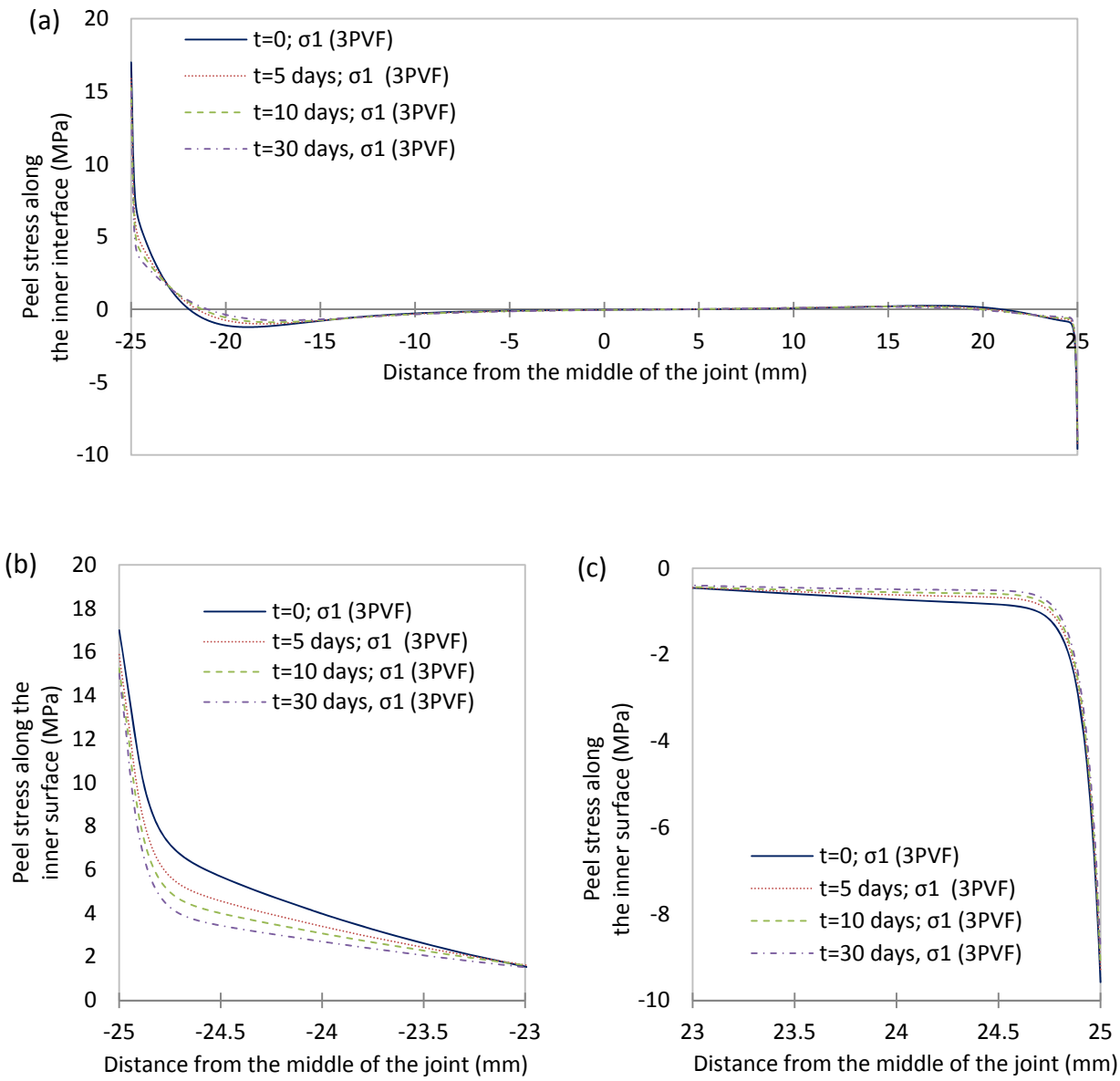

Fig. 4-9 Time-dependent peel stress along the inner surface of the double-lap joint: (a) Peel stress distribution along the whole inner interface, (b) peel stress at the very left edge of the interface, (c) peel stress at the very right edge of the interface.

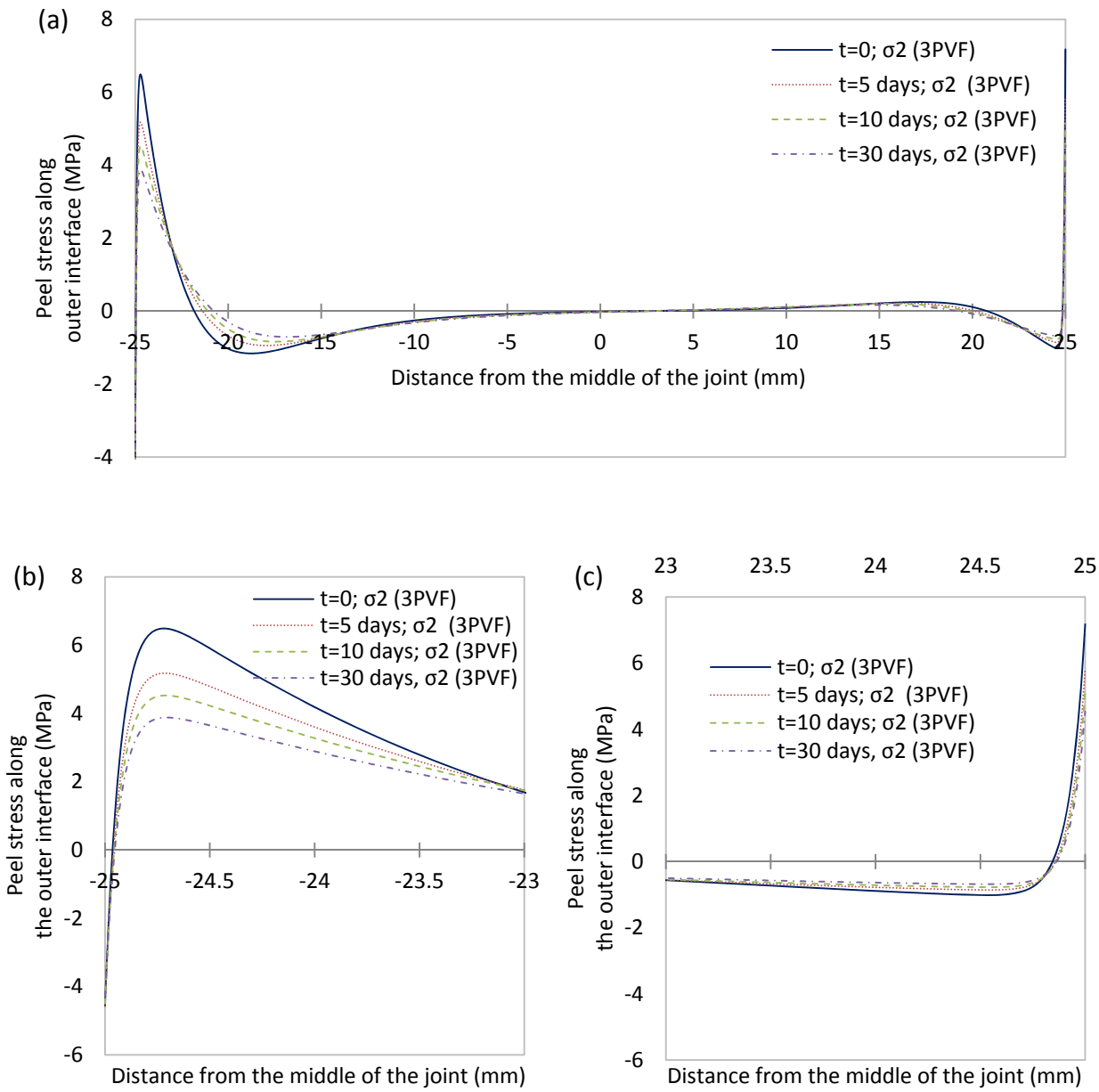

Fig. 4-10Time-dependent normal stress distribution of the double-lap joint along the interface between outer adherend and adhesive layer: (a) Total normal stress distribution, (b) normal stress at the very left edge of the interface, (c) normal stress at the very right edge of the interface.

4.4. Conclusions

This study presents a novel analytical model to analyze the stress redistributions in double-lap single-lap joints due to the viscoelastic behavior of the adhesive. In this model, the adherends are modeled as elastic Timoshenko's beams; while the adhesive layer is modeled as a three-

parameter viscoelastic foundation. A viscoelastic rheological model, the SLS model is used to model the viscoelastic behavior of the adhesive layer. Closed-form solutions of stresses within the adhesive layer and the resultant forces in adherends are obtained in Laplace transformed shape. An efficient numerical method, Zakian's algorithm, is used to conduct inverse Laplace transform. To verify the present analytical solutions, the analytical solution is compared with finite element analysis using a subroutine UMAT. Excellent agreements with the FEA have been achieved by the present model on interface shear and peel stresses, suggesting that the present model can produce sufficient accuracy on stress distribution in the viscoelastic double-lap joints. Both the FEA and the present model show that the viscoelasticity of the adhesive can reduce the stress concentrations within the joint. However, the maximum peel stress is almost not affected.

4.5. References

[1] Tong L, Soutis C. Recent advances in structural joints and repairs for composite materials. Springer Science & Business Media; 2013.

[2] Amidi S, Wang J. Three-parameter visco-elastic foundation model of adhesively bonded joints part i: single-lap joints 2016.

[3] De Bruyne NA. The strength of glued joints. Aircr Eng Aerosp Technol 1944;16:115–8.

[4] Volkersen O. Die Nietkraftverteilung in zugbeanspruchten Nietverbindungen mit konstanten Laschenquerschnitten. Luftfahrtforschung 1938;15:41–7.

[5] Hart-Smith LJ. Adhesive-bonded double-lap joints technical report, NASA CR-112235. Hampton, VA NASA Langley Res Cent 1973.

[6] Tsai MY, Oplinger DW, Morton J. Improved theoretical solutions for adhesive lap joints. Int J Solids Struct 1998;35:1163–85.

[7] Tsai MY, Morton J. An investigation into the stresses in double-lap adhesive joints with laminated composite adherends. Int J Solids Struct 2010;47:3317–25.

[8] Gustafson PA, Bizard A, Waas AM. Dimensionless parameters in symmetric double lap joints: an orthotropic solution for thermomechanical loading. Int J Solids Struct 2007;44:5774–95.

[9] Diaz AD, Hadj-Ahmed R, Foret G, Ehrlacher A. Stress analysis in a classical double lap, adhesively bonded joint with a layerwise model. Int J Adhes Adhes 2009;29:67–76.

[10] Amidi S, Wang J. Three-parameter elastic foundation model of double-lap adhesively bonded joints. Compos Part B Eng 2016.

[11] Brinson HF. The viscoelastic constitutive modelling of adhesives. Composites 1982;13:377–82.

[12] Mirman BA, Knecht S. Creep strains in an elongated bond layer. Components, Hybrids, Manuf Technol IEEE Trans 1990;13:914–28.

[13] Ferrier E, Hamelin P. Influence of Time-Temperature-Loading on Carbon Epoxy Reinforcement for Concrete Structures. ACI Spec Publ 1999;188.

[14] Dean G. Modelling non-linear creep behaviour of an epoxy adhesive. Int J Adhes Adhes 2007;27:636–46.

[15] Zhang C, Wang J. Viscoelastic analysis of FRP strengthened reinforced concrete beams. Compos Struct 2011;93:3200–8.

[16] Meshgin P, Choi K-K, Taha MMR. Experimental and analytical investigations of creep of epoxy adhesive at the concrete–FRP interfaces. Int J Adhes Adhes 2009;29:56–66.

CHAPTER 5

SUBCRITICAL DEBONDING OF FRP-TO-CONCRETE BONDED INTERFACE UNDER SYNERGISTIC EFFECT OF LOAD, MOISTURE, AND TEMPERATURE

Abstract

External bonding of fiber reinforced polymers (FRPs) has played an important role in rehabilitation and retrofitting of aged reinforced concrete structures in the last two decades. However, the long-term durability of the FRP-to-concrete bonded interface is still an unresolved issue, which hampers the widespread use of these techniques. An environment-assisted subcritical debonding testing (EASD) program using a static wedge specimen is carried out in this study to evaluate the long-term durability of the FRP-to-concrete interface subjected to the synergistic effect of mechanical load, moisture, and temperature. Unlike commonly used critical debonding-based testing methods, EASD allows for interaction among mechanical load and environmental conditions (moisture and temperature), providing more insight into the degradation mechanisms of the interface between the concrete and the strengthening material. A commercially available coupling agent, γ-GPS was used to treat the concrete surface to improve the durability of the interface. This is because the coupling agent can introduce covalent bonds between the epoxy and concrete, which is much stronger than the hydrogen bonds formed between the epoxy and the concrete without coupling agents. Testing results shows that the moisture and temperature have significant effects on the subcritical debonding of the interface. A failure mode change from cohesive failure in the concrete in the air to the adhesive failure along the epoxy-concrete interface in aqueous condition was observed in the subcritical debonding of

the FRP-to-concrete interface. EASD testing data confirms that the durability of the epoxy-concrete interface can be significantly enhanced by coupling agent treatment.

5.1. Introduction

External bonding carbon fiber reinforced polymers (CFRPs) to concrete structures using structural adhesives has emerged as an effective and popular method for retrofitting/rehabilitating the civil infrastructures due to many outstanding properties of CFRPs, such as high corrosion resistance, high strength-to-weight ratio, and ease of handling. A FRP-to-concrete adhesively bonded interface consisting of the FRP, the structural adhesive, and the adjoining concrete layer is formed in this technique. Debonding of this interface is one of the most common failure modes of the CFRP external bonding technique. A large body testing results are available in the literature on the short-term behavior of this interface [1]. The long-term durability of this FRP-to-concrete interface is mainly examined through experimental studies [2,3,4,5,6,7,8,9]. In these studies, various specimens were used to evaluate the strengths of the interface before and after environmental conditions [8,10,11,12]. Grace and Grace (2005) identified that moisture could do the most damage to the FRP-to-concrete interface. This observation was corroborated by Au and Büyüköztürk (2006) and Ouyang & Wan (2008), in which substantial loss of the fracture toughness of the interface induced by moisture was observed. More importantly, the debonding locus was found to switch from within the concrete cover in its dry state to a path along the adhesive-concrete interface in its wet state [8,13]. This change of failure mode suggests that the interphase of the FRP-to-concrete interface, the region adjacent to the adhesive/concrete interface becomes the weakest link under the attack of moisture over an extended period of time. Therefore, improvement on the moisture resistance of this interface can lead to better durability of the FRP-to-concrete joint under moisture attack.

5.1.1. Environment-assisted subcritical debonding of the FRP-to-concrete interface

An inherent problem of these existing durability studies of the FRP-to-concrete interface is that only the loads occurred at the time of catastrophic failure are measured. Debonding of this interface, as shown in a recent study [14], is a slow process of crack growing assisted by reactive environmental species at an energy release rate G, which is only a fraction of the critical crack energy release rate G_c. This slow crack growth is a long-term process of synergistic action of environments such as moisture and temperature and mechanical loads. The catastrophic interface debonding (critical crack) is only the ending point of this process. The slow crack growth in adhesive joints in aggressive environments is referred to as environment-assisted subcritical debonding (EASD) [15,16].

EASD of the FRP-to-concrete bonded interface under static loading is triggered by specific environmental conditions that encourage time-dependent crack growth processes. For example, water molecules can permeate the adhesive or concrete and preferentially migrate to the interfacial region. These water molecules can reduce the bonding strength of the adhesive-concrete interface through a displacement mechanism [17]. With the presence of water, the synergistic interaction of strained adhesive bonds and water molecules shown in Fig. 5-1 can cause debonding to grow slowly along the interface between the epoxy and concrete even though the driving mechanical force is below the critical value.

EASD behavior is often described by the relationship of debond (or crack) growth rate, da/dt, versus the driving energy release rate at the crack tip, G. An illustration of this curve is shown in Fig. 5-2. This curve generally consists of three regions, each representing a specific debond growth mechanism. Starting from the far right side in Region III shown in Fig. 5-2 where the curve is nearly vertical, debonding growth rate increases very fast as G approaches to the

critical value G_c. Once G reaches G_c, debonding protrudes in a critical manner. In this region, the debonding growth rate is so fast that the environmental species have no sufficient time to travel to the crack tip. As a result, no interaction between environmental species and mechanical loading is allowed in this stage. Large volume of existing experimental studies on the strength and durability of the FRP-to-concrete interface are limited to this stage. Reducing the mechanical loading can reduce the debonding growth rate accordingly, and the debonding enters Region II in Fig. 5-2. In this region, debonding growth rate is slow enough so that the environmental species can reach the debonding tip to trigger the interaction between the environmental species and the strained adhesive bonds. This interaction will be lost if the debonding growth rate exceeds the transport speed of the environment species. Therefore, the debonding growth rate in this region is controlled by the transport of the environmental species, and cannot be increased through increasing mechanical loading. Reducing the mechanical loading further so that the debonding growth rate is lower than that of the transport of the environmental species, the debonding process enters Region I. Since the transport speed of the environment species is higher than that of debonding growth rate, environment species are always present at the debonding tip. Therefore, the interaction between the environmental species and adhesive bonds is allowed in this region. The debonding growth rate in the region is dependent on both the reaction rate of the environmental species and the applied mechanical load, G.

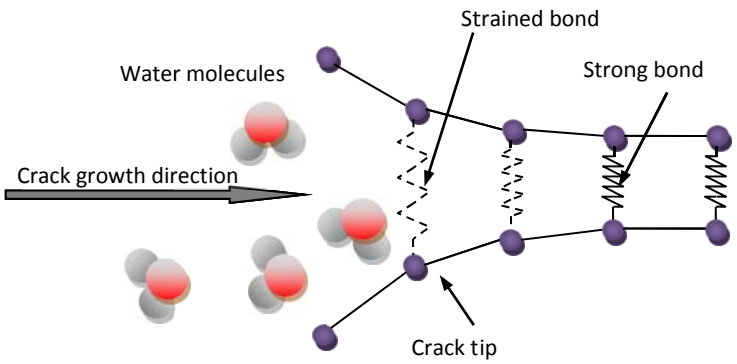

Fig. 5-1 Reaction of water with a strained crack tip bond to propagate the crack at the driving forces below the critical fracture energy.

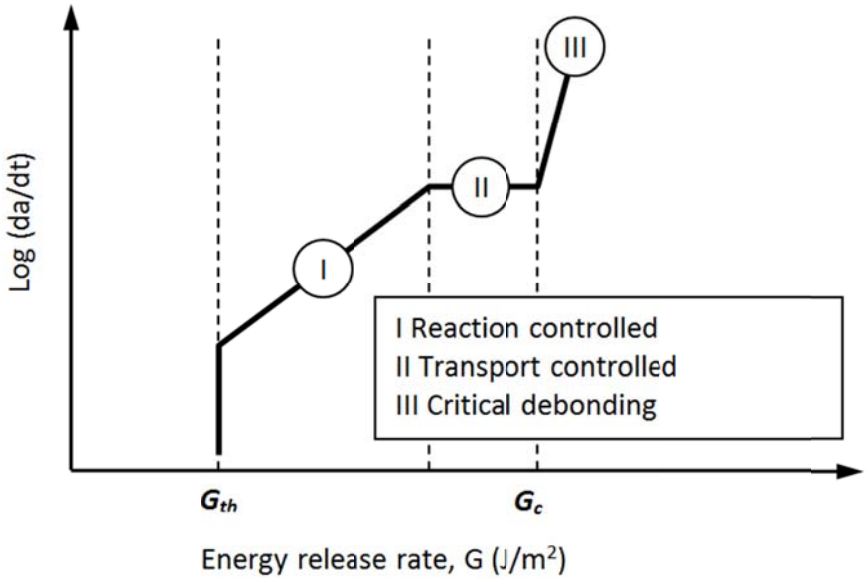

Fig. 5-2 Crack growth velocity as a function the strain energy release rate.

Often a situation arises wherein the strain at the crack tip is not large enough to overcome the activation energy of the reaction with the exposed environmental species resulting in a sharp transition out of the reaction region. This performance is known as threshold. When the driving energy release rate, G, is less than the debond-growth threshold value, G_{th}, debond-growth/cracking is assumed dormant. The absence of a debond-growth threshold has very

important implications for interface reliability, resulting in continued growth of interfacial defects even at very low loads. This behavior is also shown in Fig. 5-2.

Critical debonding testing is used in existing studies to evaluate the strength and durability of FRP-to-concrete interface in aggressive environments through accelerating aging. The major drawback of this method is that the real mechanism of deterioration may be masked since the interaction between the environmental species and mechanical loads can be lost in the critical debonding-based testing. Little information of the degradation mechanism of the interface under environmental species attack can be obtained from the testing. It has also been shown that critical debonding-based testing can lead to a different failure mode from that of real applications. As demonstrated in many studies (e.g., [18,19,20]), interface debonding may shift from adhesive failure at slow growth rate under service loads to cohesive failure at high growth rate under critical failure.

Compared with the existing critical-debonding based approach, EASD testing enjoys a few advantages in characterizing the long-term durability of the FRP-to-concrete interface. i) Interaction with environmental species is allowed in EASD due to slow debonding growth rate, making it possible to measure important parameters of the reaction kinetics at the crack tip and to deepen our understanding of the degradation mechanism of the interface. ii) EASD closely simulates the failure occurring in real-life applications under the synergistic action of mechanical and environmental loadings. iii) The transport of the environmental species is separated from the reaction at the crack tip in EASD. Therefore, degradation rate of the interface induced by the environmental species can be accurately quantified. Testing results are specimen-independent. 4) EASD takes shorter time because the time-consuming process of conditioning specimens is unnecessary. Since the durability of the interface is generally more important than the ultimate

bond strength in harsh and changing environments, EASD provides a far more useful indicator of interface quality than the ultimate bond strength or fracture toughness.

In our previous studies [14,21], EASD of the CFRP-to-concrete interface was carried out using wedge-driven testing in an ambient environment, tap water, deicing salt, alkaline solutions, and at different temperatures. Testing results suggest that water, alkaline, and deicing salt solutions can substantially reduce the energy release rate at the crack tip needed to drive the subcritical debonding growth along the epoxy-concrete interface. Under the same mechanical driving energy, water, deicing salt and alkaline solutions can accelerate the subcritical debonding growth along the epoxy-concrete interface by many times. Elevated temperature can significantly accelerate the debonding growth rate. The major debonding mode of the environment-assisted subcritical debonding in aqueous conditions is mainly adhesive along the epoxy-concrete interface, which is different from the cohesive failure within the concrete observed in the critical debonding-based studies. This change of failure mode is caused by two possible reasons: low loading rate in the test and interaction with environmental species.

Existing EASD testing of FRP-to-concrete interface is limited to aqueous conditions, which is different from the environment the structure is exposed under service condition. Under service condition, the FRP-to-concrete interface is usually exposed to open air at different humidity levels and temperatures. It is unclear whether the FRP-to-concrete interface deteriorates in air in the similar way as in water. The subcritical debonding behavior of the FRP-to-concrete interface in air subjected to synergistic effects of moisture and temperature may provide answer to this question.

5.1.2. Enhance durability of the FRP-to-concrete interface using silane coupling agent

Most studies on the durability of the FRP-to-concrete joints are limited to the evaluation of the mechanical properties of the bond. Acknowledging that significant reduction of bond strength can be lost due to the existence of environmental species (say, 60% strength reduction has been observed due to existence of water [22]), it is of great importance for real application to enhance the resistance of the FRP-to-concrete bonded interface to the attack of environmental species. Considering that the epoxy-concrete interface is the weakest link of the FRP-to-concrete joint during environmental attack, enhancing the water-resistance of the interface is the most effective method to improve the durability of the FRP-to-concrete bonded interface.

The need for bonding technique to improve the long-term durability of the interface between the organic polymers and inorganic surfaces, particularly metals, goes back to 1940 when it was observed that glass-resin composites lost most of their strength after exposure for a long time to moisture. It was understood that the bond between dissimilar materials (polymers and minerals) cannot be water-resistant unless a third intermediate material called coupling agent applied within the interface [23]. Organofunctional silane coupling agents are commonly used as mediator to bind organic materials to inorganic materials [24]. Significant enhancement of durability can be reached by using silane agents for adhesive joints with metal adherends [25,26,27,28,29,30,31,32]. Ye et al. (1998) applied a silane primer to enhance the strength of the FRP-to-concrete bonded interface [33]. They found that applying silane primers improved the bonding strength of the FRP-to-concrete interface with poorly treated concrete surfaces. When the adhesive is applied to well-treated concrete surfaces, however, the enhancing effect of the silane coupling agent on the bond strength diminishes. This is because the bond strength between the adhesive and well-treated concrete surface is higher than the neighboring concrete. As a

result, the measured strength of the FRP-to-concrete interface is actually the strength of the substrate concrete, not the interface [33]. In such a case, traditional critical-cracking based method cannot be used to estimate the contribution of the coupling agent on the strength of the FRP-to-concrete joint. No studies have focused on the role of silane primer in durability of the FRP-to-concrete interface.

Once silane is used as primer to treat the surface of concrete substrate, there are two possible mechanisms which will enhance the durability of the FRP-to-concrete interface significantly. 1) Covalent chemical bonds Si-O-Si between the concrete (of which the major component is silicate bond Si-O-Si) and epoxy can be formed as shown by the in Fig. 5-3 [33]. These covalent bonds are much stronger than the hydrogen bonds between epoxy and concrete when epoxy primer is used. 2) A hydrophobic organosilicate layer at the surface of concrete can be formed which can effectively reduce the ingress and subsequent hydrolysis.

As shown in Fig. 5-3, a possible mechanism for the environmental-assisted subcritical debonding of the epoxy-concrete interface when silane coupling agent is used can be written as Eq. (1)

$$SiOSi + H_2O \xleftrightarrow{H^+} 2SiOH. \tag{1}$$

The hydrolysis reaction at the crack tip along the interface of the interface in Fig. 5-3 is significantly different from what happens to untreated interface as shown in Fig. 5-1. It means that crack growth for FRP-to-concrete bond when silane coupling agent is used should be different from those untreated concrete surface.

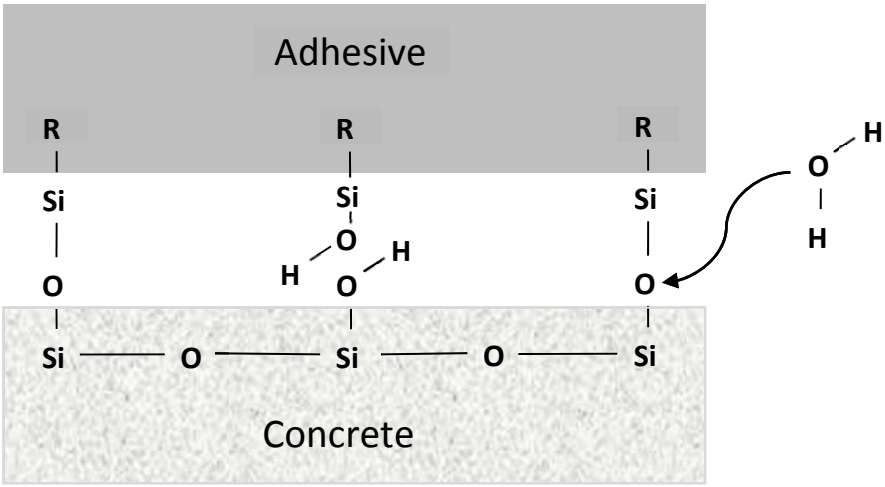

Fig. 5-3 Schematic of covalent bonds and water attack at adhesive to concrete interface treated with silane coupling agent.

5.2. Materials and testing

Water is widely known as the most invasive environment to damage and degrade the bond of the adhesive joints [11]. EASD tests on FRP-to-concrete interface in ambient environment, tap water, as well as other extreme environmental conditions such as deicing salt, and alkaline solutions were studied in the past [14]. In this study, EASD testing has been carried out to evaluate the synergistic effect of mechanical load, relative humidity, and temperature levels on the durability of the joints. To this end, a series of tests were conducted at three different temperature levels. For each temperature level, specimens were subjected to three different relative humidity levels. EASD testing of the FRP-to-concrete interface in tap water has also been carried out to compare with the testing results in air.

5.2.1. Specimen manufacturing

Static wedge testing (Fig. 5-4) was adopted to carry out EASD in this study to allow for continuous measurement of the crack growth and the interaction between the environmental species and mechanical load in a timely and easily reproducible manner. The FRP-to-concrete

interface specimen consists of a carbon FRP (CFRP) strip, an epoxy adhesive layer, and a concrete block, as shown in Fig. 5-4. A steel wedge with thickness of Δ is inserted into the pre-crack between the epoxy and the concrete block to create a crack with length of a (which is the distance between the crack tip to the contact point of the wedge to the CFRP sheet. This testing was successfully used in our previous study [21]. A quarter-bridge strain gauge was gently applied on the surface of the FRP sheet between the contact point with the wedge and the tip of the crack as shown in Fig. 5-4. In this figure, L_a is the nominal crack length measured from the edge of the specimen to the crack tip; a is the effective crack length measured from the contact point with the wedge to the crack tip; and a_0 is the distance between the contact point with the wedge and the centroid of the strain gauge. The width of the specimen is 50.8 mm, which is the same as the width of the commercial available CFRP sheet.

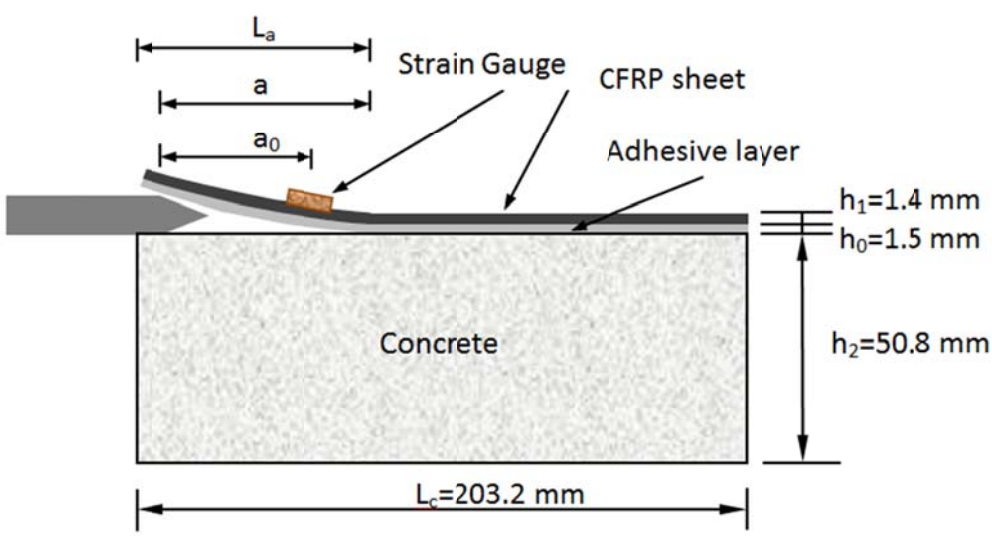

Fig. 5-4 Testing specimen.

The concrete blocks used in this study were made from ordinary Portland cement and aggregates with maximum size of 9.525 mm (3/8 in). The blocks were cast and cured following ASTM C33 and ASTM C192 using steel molds with dimensions 50.8 x 50.8 x 203.2 mm (2 x 2 x 8 in.). Manufactured concrete blocks were first cured for 28 days and then dried in the

laboratory for an additional two weeks. The mean 28-day compressive strength of the block measured using 100 x 200 mm cylinder was 44.5 MPa. The CFRP sheets used in the specimens is commercially available with dimensions of 1.4 x 50.8 x 140 mm. The dimensions and mechanical properties of the CFRP sheets are shown in Tab. 1 according to the manufacturer. The recommended structural adhesive for the available carbon FRP sheets is Tyfo TC. This adhesive consists of two parts A and B which are resin and hardener, respectively. The geometries and mechanical properties of the adhesive layer are given in Tab. 2. The bonding sides of the concretes were sandblasted for about 5 minutes to provide appropriate rough surfaces for bonding. After sandblasting, the bonding surfaces were first cleaned by high pressure air and then wiped with a wet cloth. The bonding sides of CFRP sheets were already sanded by manufacturer. All contaminants were cleaned from the sheet with acetone using soft cloth.

All mechanical properties related to the CFRP and epoxy adhesive used in this research are shown in Table 5-1 and Table 5-2.

Table 5-1 Mechanical properties of CFRP.

Laminate Width	Laminate Thickness	Cross Sectional Area	Tensile Strength	Tensile Modulus of Elasticity	Ultimate Strain
50.8 *mm*	1.397 *mm*	71.10 mm^2	2413 *MPa*	131,000 *MPa*	0.0187 *%*

Table 5-2 Mechanical properties of Epoxy.

Compressive Strength	Epoxy layer Width	Epoxy layer Thickness	Cross Sectional Area	Tensile Strength	Tensile Modulus	Flexural Modulus	Flexural Strength
28.2 *MPa*	50.8 *mm*	1.397 *mm*	71.0 mm^2	22.7 *MPa*	1,200 *MPa*	1.23 *GPa*	45.8 *MPa*

To ensure a uniform thickness of the adhesive layer, four spacers with thickness of 1.5 mm were placed at each corner of the concrete bonding surfaces. A 3 mm pre-crack was made by

covering the pre-cracked area of the concrete specimen with Teflon tape. Components A and B of the adhesive were mixed gently following the manufacturer's instruction for about 5 minutes until they fully dissolved into each other. A thin layer of epoxy was brushed onto the bonding surface of the CFRP sheet. Then the CFRP sheet was carefully placed on the bonding surface of the concrete block on which the epoxy was applied already. A pressure was applied to the CFRP sheet to ensure good bonding between the epoxy and the CFRP sheet and squeeze out excessive epoxy. After cleaning the excessive epoxy so that bond-line can be clearly seen, a uniform pressure was applied over the specimen for two weeks to allow for sufficient curing time for the adhesive and ensure the maximum bonding strength. After curing both lateral sides of the specimens were grinded to prevent possible adhesive bridging between the epoxy and the concrete, and to provide clear images for crack length measurement using digital camera. A foil strain gauge was temporarily positioned at designated area and fixed by a small piece of adhesive tape.

For all EASD tests, initial effective crack length a was chosen between 25 and 35 mm based on experimental results gained from multiple preliminary tests. The specimens were connected to a data acquisition system (DAQ) and then calibrated following the instructions provided by the strain gauge manufacturer and the data-logging software (NI LabVIEW SignalExpress by National Instruments).

5.2.2. Application of the silane coupling agent

A commercially available silane primer based on γ- glycidoxypropyltrimethoxysilane (γ - GPS) was used in this study to enhance the durability between the adhesive and the concrete. Similar procedures were used in existing studies for preparation and applying the primer on inorganic substrates with some differences in the concentration of silane solution, pre-hydrolysis

time and curing time of the treated specimens. Ye et al (1998) showed that applying 1% aqueous solution of silane coupling agent on concrete surfaces can enhance of the bonding strength between the adhesive and concrete. A study on of adhesively bonded aluminum alloy joints shows that treating the alloy by silane coupling agent with a concentration of 1% at *pH* 5 and hydrolyzed for 1 h prior to application can most effectively enhance the durability of the interface [28]. Therefore, 1% silane solution (aqueous) was prepared. After hydrolyzing for 1 hour in room temperature, the silane solution was continuously brushed onto the bonding surface of the concrete block for a period of 10 minutes. The treated concrete blocks were then immediately dried in a preheated oven at 93 °C for 1 hour. Then the dried were removed from the oven and cool down to ambient temperature in the laboratory. The treated concrete blocks were then used to manufacture the CFRP-to-concrete bonded interface specimens in the similar way described before.

5.2.3. Experiment setup

The testing system consists of a stainless steel fixture for the specimen, a digital camera, and a data acquisition system to monitor the strain from the strain gauge, as shown in Fig. 5-5. A steel wedge fabricated according to ASTM standard D3762-98 was inserted into the pre-crack and then driven into the interface between the adhesive and the concrete substrate at a proper position to reach an equal effective initial crack length *a* for all the specimens. Thereafter, the specimens were restrained in the steel frame. The induced slow crack propagation along the interface was monitored by a digital microscope camera and a strain gauge, as shown in Fig. 5-5. In our previous studies [14,21], crack length was directly read from the microscope images at the crack tip. However, bridging effect of the adhesive makes this measurement very difficult, and sometimes unreliable. Therefore, a strain gauge is used to measure the strain of the CFRP sheet,

based on which, the effective crack length can be calculated using beam theory. To this end, the debonded CFRP-adhesive layer was modeled as a composite beam cantilevered at the crack tip. Then strain measured by the strain gauge can be determined by

$$\varepsilon = \frac{Mc}{D}, \tag{2}$$

where, $M = Pa_0$ *is* bending moment at the location of the strain gauge, in which P is shear reactive force from the wedge; D and c are bending stiffness of the CFRP-adhesive composite beam, and the distance of the top surface to the neutral axis of the composite beam, respectively. With a shear force P applied at the contact point with the wedge, the deflection at this point which is equal to the thickness of the wedge Δ, can be calculated as:

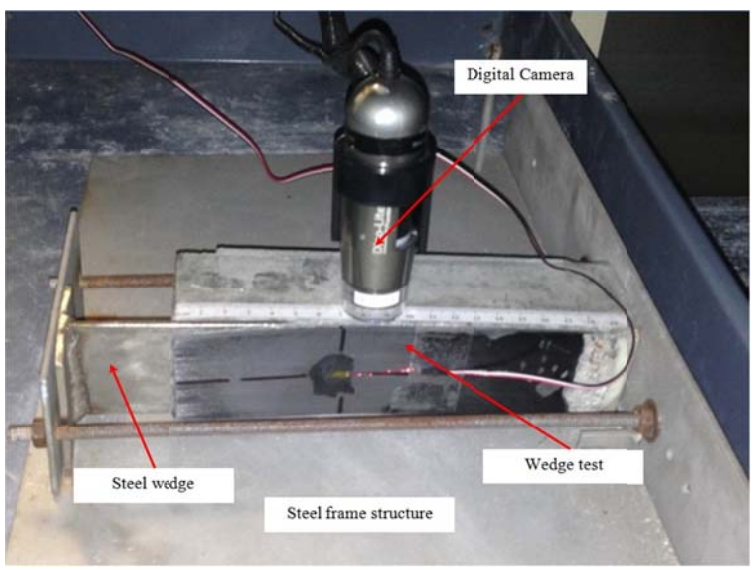

Fig. 5-5 Testing set-up.

$$\Delta = \frac{Pa^3}{3D}, \tag{3}$$

where a is the crack length shown in Fig. 5-4. Combining Eqs. (2) and (3), we can obtain the crack length a based on measured strain ε as

$$a = \sqrt[3]{\frac{3\Delta a_0}{\varepsilon}}. \quad (4)$$

Equation (4) provides an indirect way to determine the crack length using one strain gauge.

To calibrate this in-direct crack length measuring method, subcritical debonding growth of a specimen without treated with silane soaked in water at 23.9°C were measured by using both the strain gauge and a digital microscope camera as shown in Fig. 5-5. In water, the subcritical crack growth length is much longer than in air, making it easier to read crack length using the digital microscope. The crack lengths increasing with time determined by these two methods were compared in Fig. 5-6. It can be seen that excellent agreement can be reached by these two methods, at the early stage of the testing when the debonding grows relatively fast. At the later stage when crack grows slower, the indirect measurement method using a strain gauge gives a longer crack length than the direct measurement based on digital camera. This may be caused by creep of the specimen. Since most meaningful data on subcritical debonding are provided by the early stage, the indirect measurement based on strain gauge is satisfactory in this study. The creep will have more profound effect on the threshold value of the subcritical debonding. Study is undergoing to separate the effect of creep on the deformation of the CFRP beam from the crack length.

Armed with measured crack length *a*, the strain energy release rate at the crack tip can be calculated as [14]

$$G = \frac{9D\Delta^2}{2ba^4}, \quad (5)$$

where, *b* is with of the specimen.

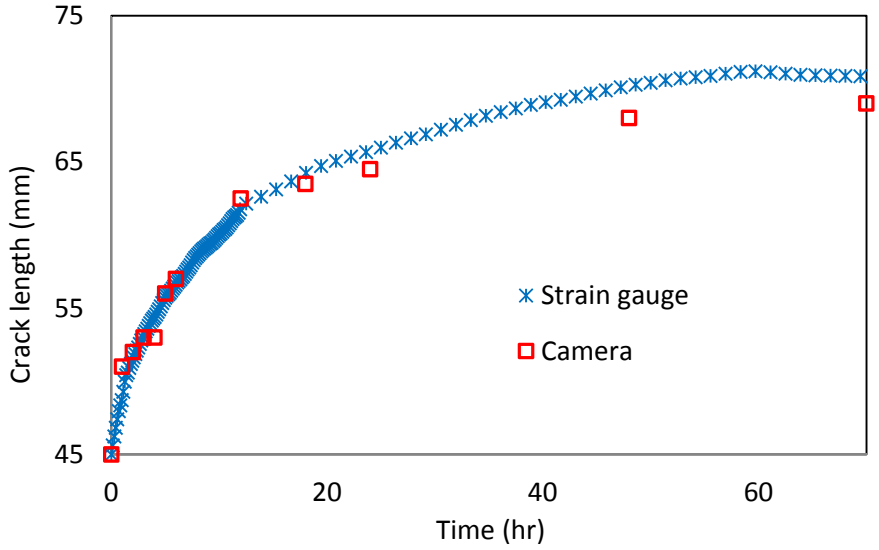

Fig. 5-6 Comparison of crack length determined by the indirect method using a strain gauge and the direct method using a digital microscope for a specimen without silane treatment tested in water at 23.9°C.

5.2.4. Testing plan

All EASD tests were conducted in a walk-in environmental chamber in which both temperature and humidity can be controlled. Three different temperature levels (23.9^{0}C, 32.2^{0}C and 43.3^{0}C) were used in the testing to evaluate the temperature effect on the subcritical debonding of the interface. For temperatures of 23.9^{0}C and 32.2^{0}C, three different relative humidity levels (50%, 70% and 95%) were used to evaluate the influence of the humidity on the crack growth. At 23.9^{0}C, EASD was also conducted in tap water. At the extreme high temperature level (43.3^{0}C), only two different relative humidity levels, 50% and 65% were used because higher humidity levels cannot be reached at this temperature by the walk-in environmental chamber.

5.3. Testing results and discussions

5.3.1. EASD testing of the CFRP-to-concrete bonded interface at 23.9°C

Fig. 5-7-Fig. 5-8 show results of EASD testing at 23.9°C for specimens without/with silane coupling agent treatment. Crack growth lengths shown in these figures were calculated by Eq. (4) and confirmed by the measurements obtained by the digital microscope.

Fig. 5-7 compares the crack grows with time in tap water and three different relative humidity levels. One can easily find that the interface debonding grows much faster and longer in tap water than in air at three different relative humidity levels, as shown in Fig. 5-7(a). This suggests that tap water has much more detrimental effect on the bond between the epoxy and the concrete than air with high humidity. Fig. 5-7(b) shows the effect of the relative humidity on the debonding growth of the specimens without/with silane coupling agent. Two distinct features can be identified from this figure. Firstly, the interface debonding grows faster at higher relative humidity. This is within our expectation since more water molecules are available to attack the interface bond during EASD testing at high relative humidity. Secondly, silane coupling agent can effectively reduce the growth rate of the subcritical debonding in the specimens due to the possible covalent bonds formed between the epoxy and the concrete generated due to the silane.

All testing curves in Fig. 5-7 show that the debonding rate is higher in the beginning, but decreases substantially with time and levels out to a very slow growth rate at the end of the testing. This is because that the energy release rate at the tip of the crack reduces with the crack length as shown in Eq.(5). Since the crack length increases with time, the energy release rate at the crack tip reduces with time. Once the energy release rate is lower than a threshold for the subcritical debonding to grow, interface debonding stops, as can be seen in Fig. 5-7.

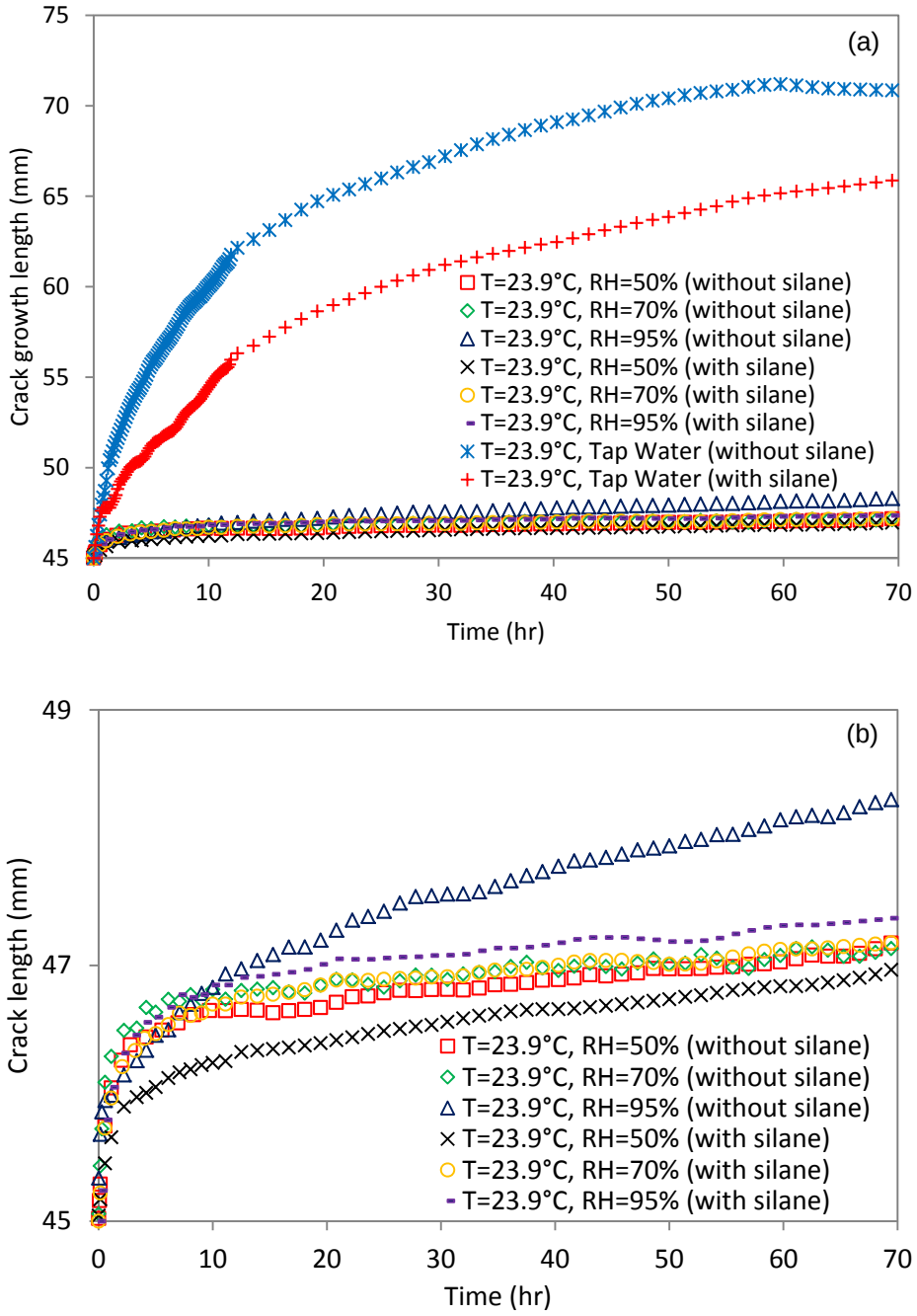

Fig. 5-7 Crack grows with time at 23.9°C: (a) in tap water and in air with different relative humidity levels, (b) Close-up of crack growing at different relative humidity levels.

Crack growth rate verse energy release rate at the crack tip curves are presented in Fig. 5-8. From this figure, we can see clearly that interface debonding grows at energy release rate much lower than the critical energy release rate of this interface, which was determined as 2.5

N/mm in our previous study [14], confirming that subcritical debonding indeed exists. From these curves, one can easily identify the Region I of the subcritical debonding as indicated in Fig. 5-8a and the threshold energy release rate G_{th} for each case. For the case in tap water, Region II can be identified too. Both Fig. 5-7a and Fig. 5-8(a) suggest that subcritical debonding of the FRP-to-concrete bonded interface in tap water is significantly different from in air. A very lower threshold value of energy release rate is needed for the subcritical debonding of the interface to initiate and propagate in tap water than in air regardless relative humidity levels. Similarly, the energy release rate needed to drive the debonding in region I is much lower than that in air. The debonding growth rate increases with energy release rate at a faster rate in air than in tap water, implying that debonding mechanisms in air may be different from that in tap water. Fig. 5-8(b) compares the effect of humidity levels and silane coupling agent on the subcritical debonding of the interface. Higher relative humidity level can increase the crack growth rate and reduce the threshold value of the energy release rate needed to trigger the subcritical debonding. The effect of silane treatment is also revealed by this figure: the debonding growth rate is reduced by the application of silane, confirming that silane can effective enhance the resistance of the interface from the attack of moisture.

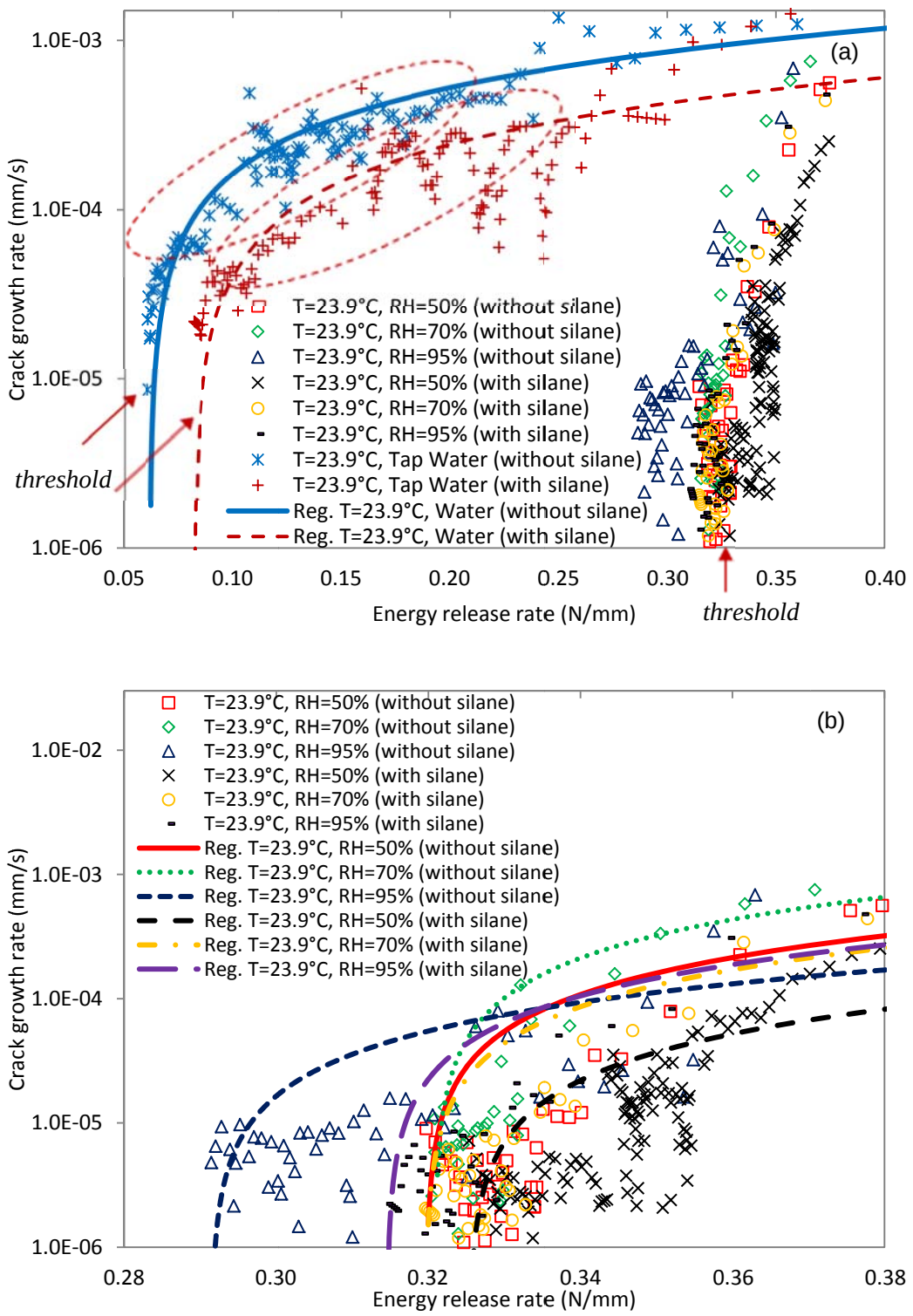

Fig. 5-8 Subcritical debonding of interface at 23.9°C: (a) in tap water and at different relative humidity levels, (b) in air with different relative humidity levels.

5.3.2. EASD testing of the CFRP-to-concrete bonded interface at 32.2°C (90°F)

Results EASD of specimens tested at 32.2°C at three different relative humidity levels are shown in Fig. 5-9-Fig. 5-10. Fig. 5-9 shows the crack length versus time for specimens with and without applying silane. Compared with Fig. 5-7(b), it can be seen that the crack lengths are significantly larger at this temperature than that at lower temperature (23.9°C). At higher relative humidity level, crack growth is generally faster at the beginning and the crack length is longer at the end of the testing. Clearly, relative humidity can largely influence the subcritical debonding and subsequently affect the durability of the adhesive to the concrete interface. In comparison with debonding of the specimens untreated with silane, the debonding length of the specimens treated with silane is shorter as expected. Fig. 5-10 shows the crack growth rate varying with the energy release rate at the crack tip at 32.2°C. Two distinct regions (I and II) are much more distinguishable and the threshold value of the energy release rate (G_{th}) can be clearly recognized in all cases. The effects of the relative humidity and silane coupling agent on the subcritical debonding at this temperature is similar to that at 23.9°C. Compared with Fig. 5-8(b), it can be seen that raising the temperature to 32.2°C significantly reduces the energy release rate needed to drive the subcritical debonding, as indicated by the reduced threshold value of the energy release rate at the same humidity level.

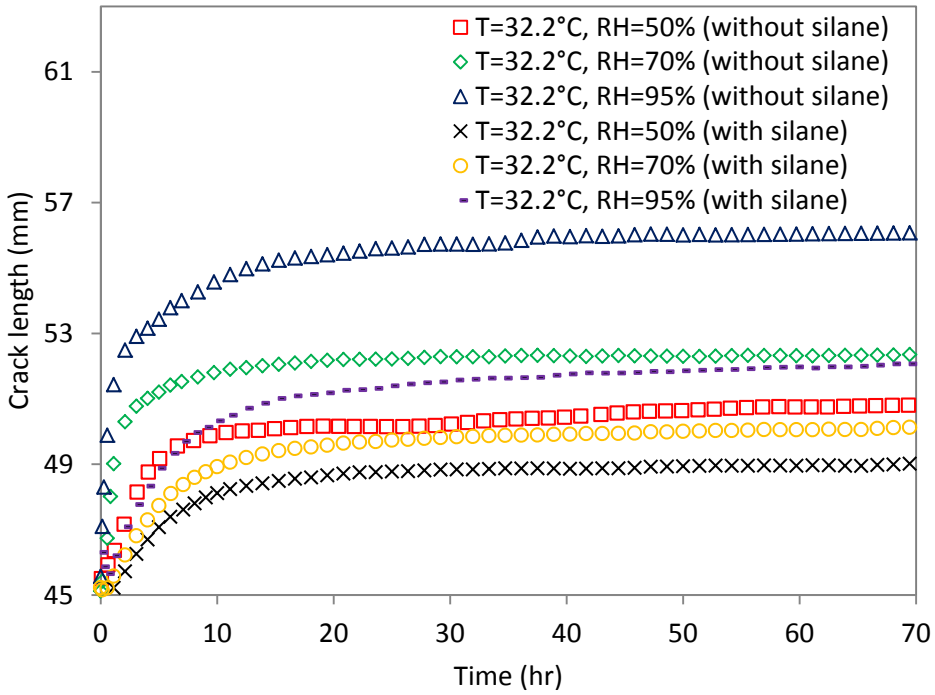

Fig. 5-9 Crack grows with time at different relative humidity levels at 32.2°C.

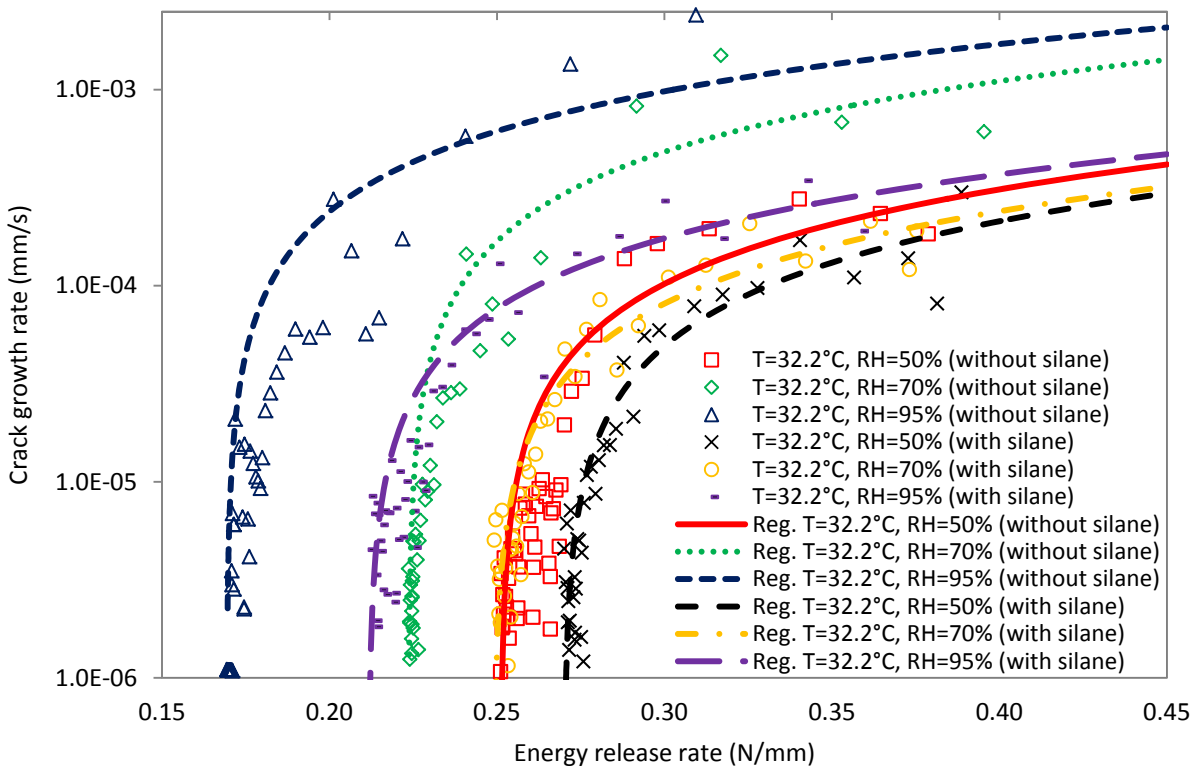

Fig. 5-10 Subcritical debonding of the FRP-to-concrete joints at 32.2°C.

5.3.3. EASD of FRP-to- concrete interface at 43.3°C (110°F)

EASD testing of the FRP-to-concrete interface at high temperature 43.3°C (110°F) are shown in Fig. 5-11-Fig. 5-12. Only two different relative humidity levels at 50% and 65% were used in the testing due to the limitation of the environmental chamber. At this temperature, debonding growth shows a different feature compared with previous two cases. As shown in Fig. 5-11a, the debonding grows much faster at the beginning of the testing and slows down quickly. As a result, the maximum crack growth rate in this case is higher than that at 23.9°C and 32.2°C, as shown in Fig. 5-11. However, further examining the very beginning of the debonding growth, one can find that the debonding growth is rather slow with the first one hour and then suddenly accelerated, as shown in Fig. 5-11(b). This phenomenon was not observed at lower testing temperature because the testing temperature could be very close to the T_g of the adhesive. Significant creep deformation and stress redistribution could happen within the specimen at this high temperature. As a result, the debonding growth with time shows a different trend from those at lower temperatures. The effect of this high temperature is also reflected in the crack growth rate versus energy release rate curve, as shown in Fig. 5-12. In this figure, an unexpected region in which crack growth rate reduces with energy release rate appears. More study will be carried out to understand the mechanism of this region.

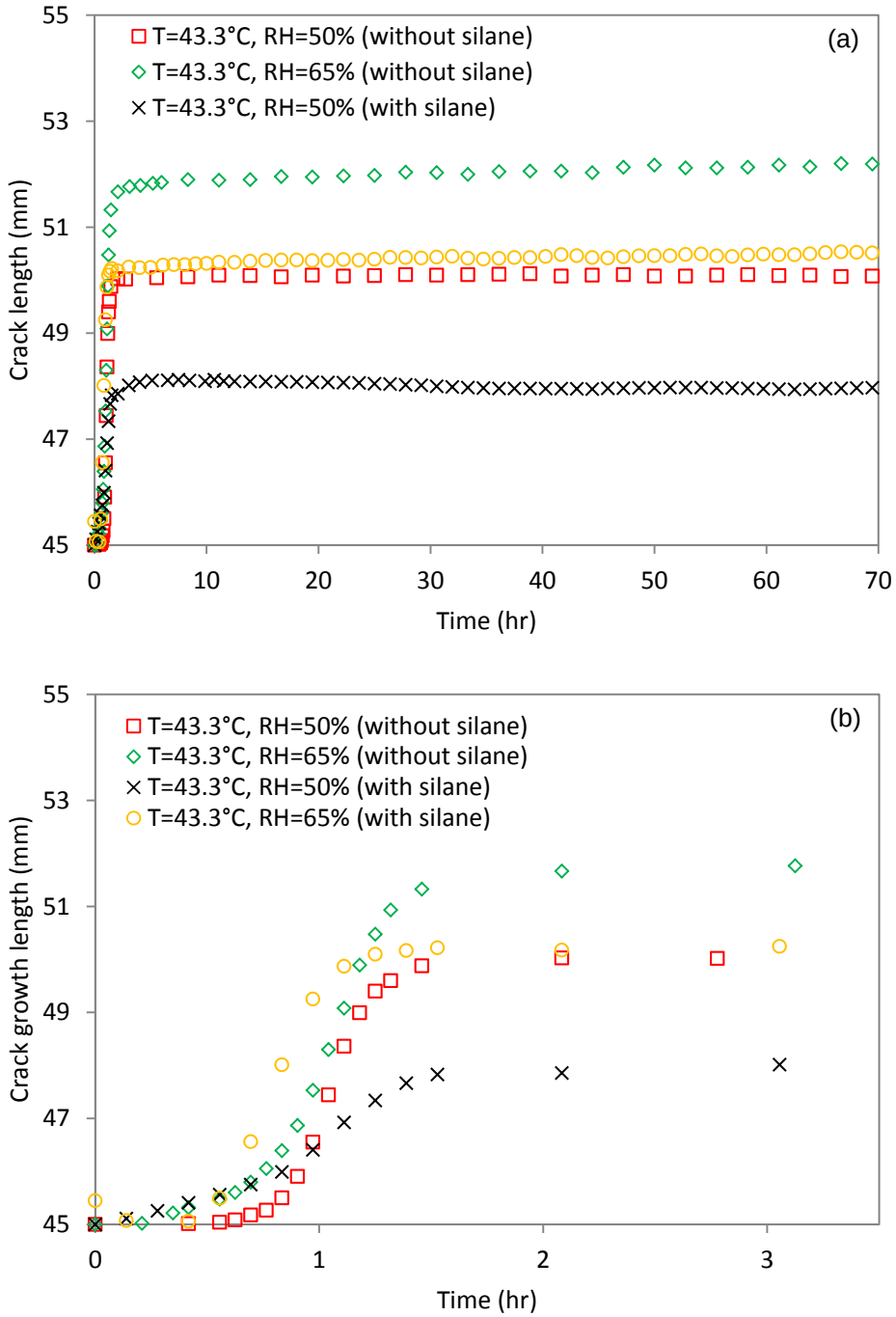

Fig. 5-11 Crack length with time at 43.3°C: (a) Long-term results, (b) at the beginning of the test.

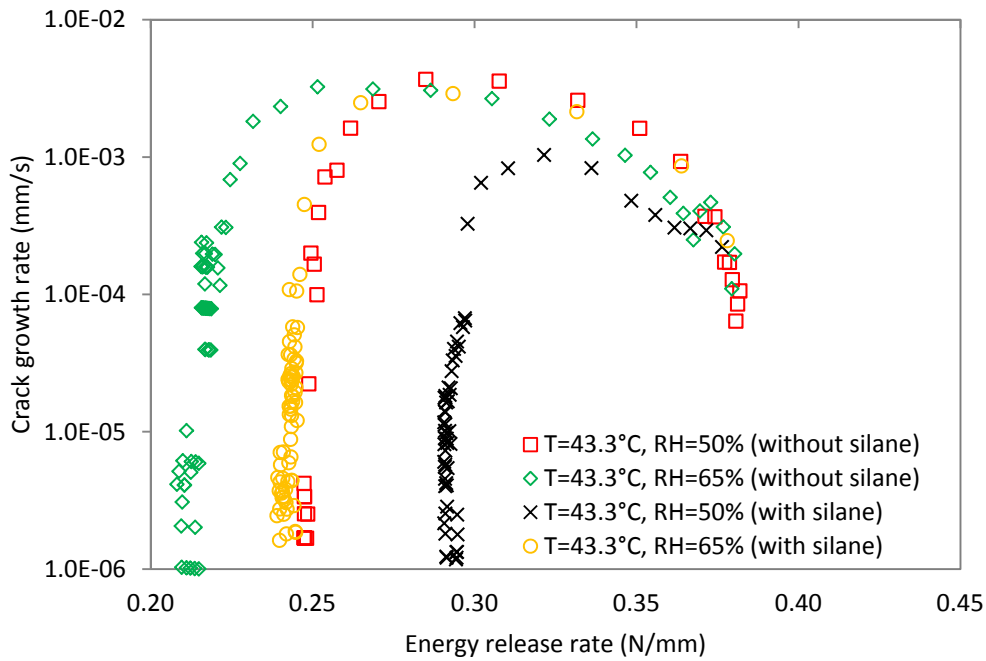

Fig. 5-12 Subcritical debonding of FRP-to-concrete joint at 43.3°C.

5.3.4. Fitting the EASD testing results

To describe the synergistic effect of mechanical loads, moisture, and temperature on the subcritical debonding of the FRP-to-concrete interface, the experimental data were fitted to an empirical expression modified from Paris Law

$$\frac{da}{dt} = m(G)^n \left[\frac{1-\left(\frac{G_{th}}{G}\right)^{n1}}{1-\left(\frac{G}{G_c}\right)^{n2}}\right], \tag{6}$$

where m, n, n_1 and n_2 are empirical regression coefficients and are determined by fitting the Eq. (6) in to experimental data. Equation (6) has been successfully used to fit the time-dependent debonding of adhesive joints with metal adherend [34,35]. The fitted curves for all tests conducted at 23.9°C and 32.2°C are shown in Fig. 5-8 and Fig. 5-10. No fitting was tried for data obtained at 43.3°C because of the observed softening behavior in the region II. For each test, G_{th} is unique and can be determined based on the obtained subcritical data. G_c which is the

maximum energy release rate at critical debonding is thoroughly dependent on mechanical forces and was determined in our previous study as 2.59 N/mm [14].

Overall, Eq. (6) provides excellent fitting for all the testing data, as shown in Fig. 5-8 and Fig. 5-10. Table 5-3 presents all the fitting parameters in Eq. (6) for each test shown in Fig. 5-8 and Fig. 5-10. It can be seen that generally, the threshold G_{th} reduces with relative humidity levels and temperatures. The effect of silane coupling agent on the subcritical debonding of the interface is also reflected by G_{th} value. As shown in Table 5-3, all specimens treated by silane exhibit a higher G_{th}. Significant difference on regression parameters can be found between the subcritical debonding in air and in tap water. In tap water, G_{th} is much lower and n is significantly higher than those in air. This may suggest that different failure mechanisms or mode has been triggered in subcritical debonding in tap water than in air regardless the relative humidity levels.

Table 5-3 Data fitting parameters based on Eq. (6).

Testing	G_{th} (N/mm)	m ($x10^{-2}$)	n ($x10^{-2}$)	n_1 ($x10^{-2}$)	n_2 ($x10^{-2}$)
T=23.9°C, RH=50% (without silane)	0.315	2.37	10.81	2.41	17.02
T=23.9°C, RH=70% (without silane)	0.316	3.35	10.70	3.39	16.06
T=23.9°C, RH=95% (without silane)	0.286	1.42	10.97	1.46	17.98
T=23.9°C, Water (without silane)	0.062	2.24	13.33	1.01	20.17
T=23.9°C, RH=50% (with silane)	0.320	1.30	10.94	1.32	18.11
T=23.9°C, RH=70% (with silane)	0.315	2.12	10.84	2.16	17.20
T=23.9°C, RH=95% (with silane)	0.310	2.09	10.85	2.13	17.24
T=23.9°C, Water (with silane)	0.082	2.20	11.73	0.61	20.24
T=32.2°C, RH=50% (without silane)	0.251	1.43	10.89	1.45	17.68
T=32.2°C, RH=70% (without silane)	0.224	2.43	10.88	2.44	17.61
T=32.2°C, RH=95% (without silane)	0.169	2.49	10.88	2.50	17.59
T=32.2°C, RH=50% (with silane)	0.270	1.29	10.92	1.34	18.18
T=32.2°C, RH=70% (with silane)	0.249	1.25	10.97	1.30	18.26
T=32.2°C, RH=95% (with silane)	0.212	1.35	11.07	1.38	18.25

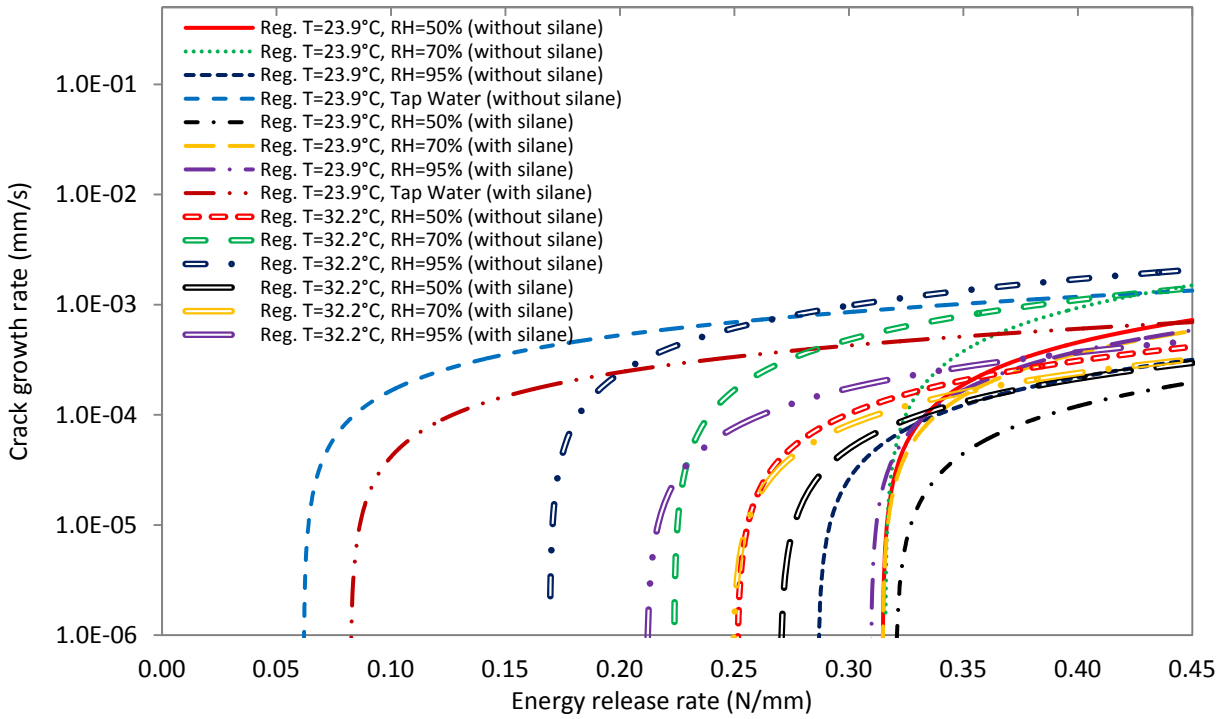

Fig. 5-13 Fitting curves of subcritical debonding under synergistic effect of mechanical loads, moisture, and temperature.

Figure 5-13 summarizes all the fitting curves of the subcritical debonding of the FRP-to-concrete interface tested in this study. The synergistic effects of the mechanical loads, moisture and temperature can be seen clearly from this figure. The effect of the silane coupling agent on the subcritical debonding of the interface can be observed too. A straightforward fracture-mechanics-based method for service-life prediction may be developed on the basis of subcritical-debonding test results as outlined in our previous study [14].

5.3.5. Discussions

5.3.5.1. Failure mode of EASD

Our previous study [14] showed that failure mode of the subcritical debonding of the FRP-to-concrete interface is cohesive in ambient environment and adhesive in aqueous condition. It is unclear whether high temperature and high humidity level can lead to different

failure mode of the interface. To answer this question, the failure modes of EASD tests conducted in this study were examined by splitting the FRP strips from the tested specimens. The debonded epoxy sides of four representative specimen surfaces are shown in Fig. 5-14. Three regions can be identified from these fractured epoxy side from right to left, which are initial crack zone, subcritical debonding zone, and the splitting zone. The first region is the initial crack surfaces induced by inserting the wedge to its designed position before the testing. This region is covered by concrete for all specimens, suggesting that debonding in this region is a cohesive failure within the concrete caused by inserting the steel wedge into the specimen to create a desired initial debonding length. This is in agreement with the existing critical debonding-based studies. The subcritical debonding zone is induced by the slow crack growth during the EASD testing. No distinguishable difference can be found in this zone from the initial crack zone for all the specimens tested in air. This suggests that subcritical debonding of the FRP-to-concrete interface in air is cohesive and failure locus is within concrete regardless the relative humidity and temperature. The splitting zone is induced by fast splitting the FRP strip from the tested specimens. This zone is covered by concrete for all three specimens tested in air. The cohesive failure mode in this zone is clearly induced by the fast splitting of the FRP from the specimen which is a critical debonding process. For the specimen tested in tap water, it can be seen clearly that a failure mode change occurred at the beginning of the subcritical debonding. The failure locus shifted from within the concrete to the interface between the epoxy and the concrete since very little concrete is attached to the epoxy, as shown in Fig. 5-14(d). A transitional zone can be observed between the initial crack zone and the subcritical debonding zone in which the concrete attached to epoxy diminishes with the growth of the subcritical debonding. In the splitting zone,

more concrete is attached to concrete, suggesting that debonding mode changes to cohesive again because of high debonding rate in this zone.

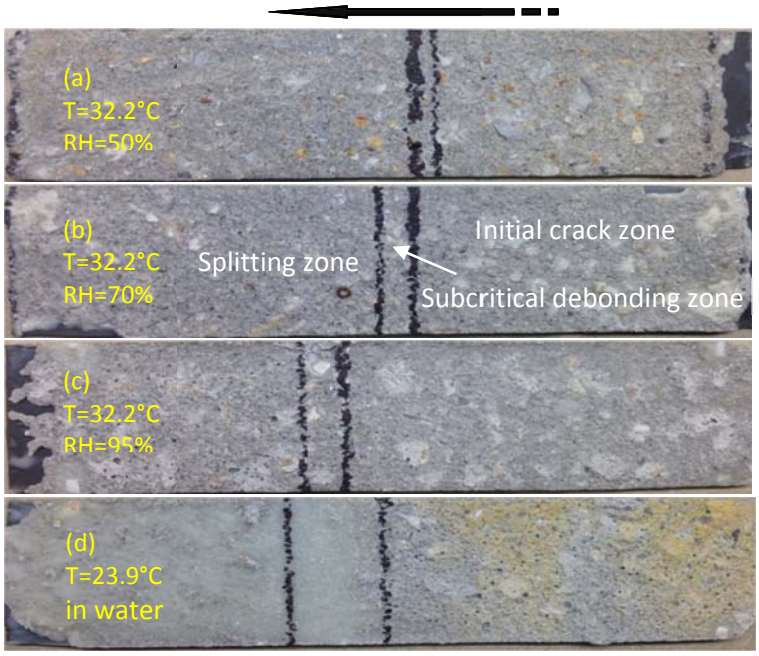

Fig. 5-14 Debonded epoxy side of the tested specimens.

5.3.5.2. Effect of silane treatment on the moisture resistance of the interface

The significant effect of the silane surface treatment has been demonstrated in the subcritical debonding testing shown in Fig. 5-7-Fig. 5-13. To further understand the mechanism of the silane treatment on enhancing the durability of the interface, thin slices of the FRP-to-concrete interface were cut from the specimens and conditioned in tap water for 7 days. After that, the specimens were dried and the interface area between the epoxy and concrete of the thin specimens were examined by scanning electron microscope (SEM).

Figure 5-15(a) shows the SEM image of the interface area between the epoxy and concrete without silane treatment after soaking in water in 7 days. A crack induced by water soaking and subsequent drying can be found at the interface between the epoxy and concrete, as indicated by the carbon mapping in this area shown in Fig. 5-15(b). In this figure, the upper half with higher

concentration of carbon is the epoxy, and the lower half with lower concentration of carbon is concrete. Fig. 5-15(c) shows the oxygen mapping in this interface area. Since oxygen is mainly in water, the concentration of oxygen can be viewed as an indicator of water content. No difference on oxygen content can be identified from this figure, suggesting that water content on both the epoxy and the concrete sides are identical.

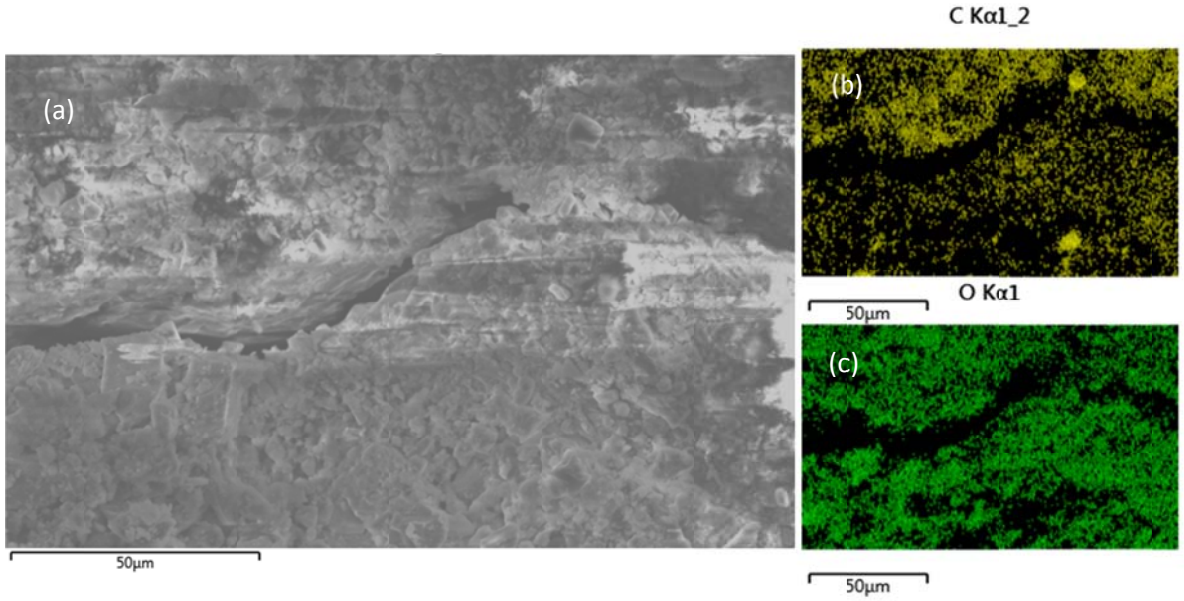

Fig. 5-15 water-induced damage in epoxy-concrete interface untreated with silane: (a) SEM image of interface crack induced by soaking in water for 7 days, (b) C mapping of the interface, (c) O mapping of the interface.

Fig. 5-16(a) shows the SEM image of the interface area between the epoxy and concrete with silane treatment after soaking in water in 7 days. No interface cracks can be found on this image, as indicated by the carbon mapping in this area shown in Fig. 5-16(b). However, a few micro-cracks can be found in the adjacent concrete. This suggests that the interface treated with silane may have higher resistance to the water attack so that cracks can only occur in the concrete layer. Oxygen mapping of this interface area shows oxygen content is significantly lower in the epoxy side, which indicates that water content in the epoxy side is much lower than that in the

concrete side. This difference in water content may be caused by the hydrophobicity on the surface of concrete generated by silane treatment which reduces the water ingress into the epoxy layer.

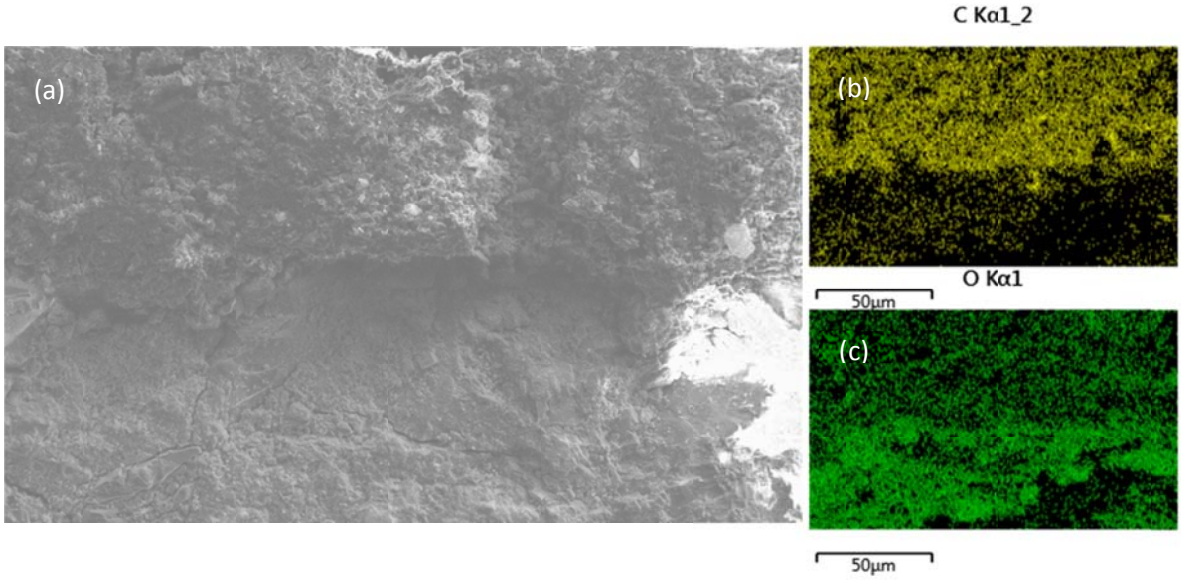

Fig. 5-16 water-induced damage in epoxy-concrete interface treated with silane: (a) SEM image of interface crack induced by soaking in water for 7 days, (b) C mapping of the interface, (c) O mapping of the interface

5.3.5.3. Swelling of the epoxy

It is well known that significant swelling in polymers can occur after absorbing moisture. This swelling is also observed in the subcritical debonding testing carried out in this study, as shown in Fig. 5-17. Fig. 5-17(a) shows the specimen before the testing, and Fig. 5-17(b) shows the same location one hour after the testing. Significant amount of swelling of the epoxy layer can be observed under the digital microscope. Such a high swelling in the epoxy layer will introduce significant stress concentration along the epoxy-concrete interface and affect the energy release rate *G* at the crack tip. It should be pointed out all the *G* shown in the subcritical debonding testing data in this study do not consider the effect of the swelling of the epoxy.

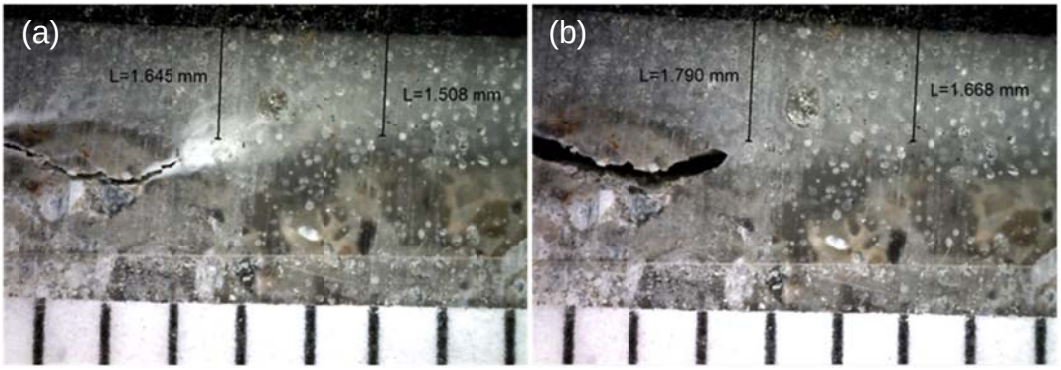

Fig. 5-17 Swelling of the epoxy layer subjected to 43.3°C and RH of 65%: (a) before testing, (b) one hour after testing.

5.4. Conclusions

The synergistic effects of the mechanical loads, moisture and temperature on the durability of FRP-to-concrete bonded interface were evaluated by subcritical debonding testing using a static wedge specimen. Following conclusions can be drawn based on this study:

1) Humidity and temperature can accelerate the subcritical debonding, suggesting that subcritical debonding testing is a good tool to examine the synergistic effects of mechanical loads, moisture and temperature on the durability of the FRP-to-concrete bonded interface.

2) Treatment with silane coupling agent can improve the durability of the FRP-to-concrete interface as indicated by reduced total length and its growth rate of the subcritical debonding of the specimen treated by silane.

3) The relationship between the subcritical debonding rate and energy release rate at the crack tip can be fitted by Eq. (6). Based on this equation, service-life predication of the interface can be established.

4) Significant difference exists between the subcritical debonding of the FRP-to-concrete interface in aqueous condition and in air. Much longer debonding length and its growth rate were

observed in water than in air. Failure mode also shifts from cohesive failure in concrete in air to adhesive along the interface between the epoxy and concrete in tap water.

In addition, this study also shows that hydrophobicity induced by the silane and swelling of the epoxy can play roles in the durability of the FRP-to-concrete interface. These two factors are related to the surface chemistry and the anomalous diffusion of moisture in epoxy, respectively. Unfortunately, all existing studies fail to account for these important factors. In order to fully understand the deterioration mechanism and develop a mechanism-based life-prediction model for the FRP-to-concrete bonded interface, these two factors must be considered. Much more severe deterioration and different failure mode of the FRP-to-concrete bonded interface in aqueous conditions than in air regardless of the relative humidity levels may suggest that our current durability testing on the FRP-to-concrete interface based soaking the specimens in water could exaggerate the deterioration of the interface in service condition which is in air.

5.5. References

[1] J. Yao, J. G. Teng, and J. F. Chen, "Experimental study on FRP-to-concrete bond joints," *Composites Part B: Engineering* , vol. 36, no. 2, pp. 99-113, 2005.

[2] V. Karbhari and M. Engineer, "Effect of environmental exposure on the external strengthening of concrete with composites-short term bond durability," *Journal of Reinforced Plastics and Composites*, vol. 15, no. 12, pp. 1194-1216, 1996.

[3] L. Bizindavyi, K. Neale, and M. Erki, "Experimental investigation of bonded fiber reinforced polymer-concrete joints under cyclic loading," *Journal of Composites for Construction*, vol. 7, no. 2, pp. 127-134, 2003.

[4] R. Krishnaswamy and M. Lopez, "Time performance of concrete-CFRP bond under the effects of freeze-thaw cycles and sustained loading," in *85th Annual Meeting, Transportation Research Board*, Washington, DC: National Academies, 2006.

[5] K. A. Harries, J. Aidoo, and A. Zorn, "Deterioration of FRP-to-concrete bond under failure loading," *Advances in Structural Engineering*, vol. 9, no. 6, pp. 779-789, 2006.

[6] J. F. Davalos, S. S. Kodkani, I. Ray, and C. Lin, "Fracture evaluation of GFRP-concrete interfaces for freeze-thaw and wet-dry cycling," *Journal of Composite Materials*, no. 42,

pp. 1439-1466, 2008.

[7] J. Dai, E. Kato, M. Iwanami, and H. Yokata, "Durability of carbon strand sheet to concrete bond interface under moisture condition," in *Forth Int. Conf. on FRP Composites in Civil Eingineering, International Institute for FRP in Construction (IIFC),* Zurich, Switzerland, 2008.

[8] C. Au and O. Büyüköztürk, "Peel and shear fracture characterization of debonding in FRP plated concrete affected by moisture," *Journal of Composites for Construction*, vol. 10, no. 1, pp. 35-47, 2006.

[9] B. Wan, M. F. Petrou, and K. A. Harries, "The effect of the presence of water on the durability of bond between CFRP and concrete," *Journal of Reinforced Plastics and Composites*, no. 25, pp. 875-890, 2006.

[10] V. ,. C. J. ,. H. D. Karbhari, et al., "Durability Gap Analysis for Fiber-Reinforced Polymer Composites in Civil Infrastructure," *Journal of Composites for Construction*, vol. 7, pp. 238-247, 2003.

[11] N. F. Grace and M. Grace, "Effect of repeated loading and long term humidity exposure on flexural response of CFRP strengthened concrete beams," *International Institute for FRP in Construction*, pp. 547-554, 2005.

[12] K. Benzarti, S. Chataigner, M. Quiertant, C. Marty, and C. Aubagnac, "Accelerated ageing behaviour of the adhesive bond between concrete specimens and CFRP overlays," *Construction and building materials*, vol. 25, no. 2, pp. Benzarti,K,Chataigner,S,Quiertant,M,Marty,C,&Aubagnac,C(2011)Acceleratedageingbehaviourofthe523-538, 2011.

[13] Z. Ouyang and B. Wan, "Experimental and numerical study of moisture effects on the bond fracture energy of FRP/concrete joints," *Journal of Reinforced Plastics and Composites*, no. 27, pp. 205-223, 2008.

[14] C. Zhang, J. Wang, and K. J. Fridley, "Environment-Assisted Subcritical Debonding of Epoxy-Concrete Interface," *Journal of Composites for Construction*, vol. 16, no. 5, pp. 563-571, 2012.

[15] S. Wiederhorn, "Moisture assisted crack growth in ceramics," *International Journal of Fracture*, no. 4, pp. 171-177, 1968.

[16] R. Dauskardt, M. Lane, Q. Ma, and N. Krishna, "Adhesion and debonding of multi-layer thin film structures," *Engineering Fracture Mechanics*, no. 61, pp. 141-162, 1998.

[17] S. Shimizu, T. Yanagimoto, and M. Sakai, "Pyramidal indentation load-depth curve of

viscoelastic materials," *Journal of Material Research*, no. 16, pp. 4075-4086, 1999.

[18] M. Rakestraw, M. Taylor, D. Dillard, and T. Chang, "Time dependent crack growth and loading rate effects on interfacial and cohesive fracture of adhesive joints," *112. Rakestraw, M.D., Taylor, M.W., and Dillard, D.A., 1995. Time dependent crack groJournal of Adhesion*, no. 55, pp. 123-149, 1995.

[19] H. Diab and Z. Wu, "Nonlinear constitutive model for time-dependent behavior of FRP-concrete interface," *Composites Science and Technology*, no. 67, pp. 2323-2333, 2007.

[20] H. K. Singh, et al., "Subcritical delamination in epoxy bonds to silicon and glass adherends: Effect of temperature and preconditioning," *The Journal of Adhesion*, no. 84, pp. 619-637, 2008.

[21] E. Jennings, J. Wang, K. Fridley, and C. Chen, "Temperature Effect on Subcritical Crack Growth in CFRP Externally Bonded Concrete Systems," in *28th Annual Technical Conference of the American Society for Composites*, State College, Pennsylvania, 2013.

[22] O. Büyüköztürk, C. Au, A. Reyes, V. Barzov, and I. Jacobi, "Failure Behavior of FRP Bonded Concrete Affected by Interface Fracture. Part 2. Moisture Degradation in FRP Bonded Concrete Systems: An Interface Fracture Approach.," 2004.

[23] E. P. Plueddemann, *Silane coupling agents*. New York: Plenum Press, 1982.

[24] A. Namkanisorn, A. Ghatak, M. Chaudhury, and D. Berry, "A kinetic approach to study the hydrolytic stability of polymer-metal adhesion," *Journal of Adhesion Science and Technology*, vol. 15, pp. 1725-1745, 2001.

[25] C. Korenberg, A. Kinloch, and J. Watts, "Crack growth of structural adhesive joints in humid environments," *Journal of Adhesion*, vol. 80, no. 3, pp. 169-201, 2004.

[26] A. Kinloch, C. Korenberg, K. Tan, and J. Watts, "Crack growth in structural adhesive joints in aqueous environments," *Journal of Material Science*, no. 42, pp. 6353-6370, 2007.

[27] M. Sautrot*, M. Abel, J. Watts, and J. Powell, "Incorporation of an adhesion promoter in structural adhesives: Aspects of durability and interface chemistry," *Journal of Adhesion*, vol. 81, pp. 163-187, 2005.

[28] M. Abel, et al., "Understanding the relationship between silane application conditions, bond durability and locus of failure," *International Journal of Adhesion and Adhesives*, vol. 26, pp. 2-15, 2006.

[29] D. H. Berry and A. Namkanisorn, "Fracture toughness of a silane coupled polymer-metal

interface: silane concentration effects," *Journal of Adhesion*, vol. 81, pp. 347-370, 2005.

[30] A. Rattana, M. Abel, and J. F. Watts, "Degradation of interfacial chemistry of epoxy/silane/aluminum interfaces as a result of aqueous attack," *Journal of Adhesion*, vol. 81, pp. 963-988, 2005.

[31] B. B. Johnsen, K. Olafsen, A. Stori, and K. Vinje, "Silanization of adhesively bonded aluminum alloy AA6060 with g-glycidoxypropyltrimethoxysilane. II. Stability in degradation environments," *Journal of Adhesion Science and Technology*, no. 17, pp. 1283-1298, 2003.

[32] S. Shokoohi, A. Arefazar, and R. Khosrokhavar, "Silane coupling agents in polymer-based reinforced composites: a review," *Journal of Reinforced Plastics and Composites*, vol. 27, pp. 473-485, 2008.

[33] L. Ye, K. Friedrich, C. Weimer, and Y. Mai, "Surface treatments and adhesion bonding between concrete and a CFRP composite," *Advanced Composite Materials*, vol. 7, no. 1, pp. 47-61, 1998.

[34] R. H. Martin and G. B. Murri, "Characterization of mode I and mode II delamination growth and thresholds in AS4/PEEK composites," *ASTM STP*, no. 1059 , pp. 251-270, 1990.

[35] A. J. Kinloch and S. O. Osiyemi, "Predicting the fatigue life of adhesively-bonded joints," *The Journal of adhesion*, vol. 43, no. 1-2, pp. 79-90, 1993.

CHAPTER 6

CRITICAL DEBONDING OF FRP-TO-CONCRETE INTERFACE

Abstract

Fiber reinforced polymer (FRP) composites have emerged as one the foremost structural materials in retrofit/rehabilitation of concrete structural members in the last decades. A large number of studies have widely focused on the short-term behavior of the FRP-retrofitted structures. However, wide-application of these materials in civil infrastructures is still facing major obstacles due to issues such as long-term durability and failure mechanism in presence of aggressive environments. Few investigation conducted on the FRP-to-concrete joints determined that the epoxy-concrete interface is the most critical region in the bond, particularly when moisture effect is involved. A couple of normal tri-layer FRP-to-concrete specimens are conditioned in water for different periods of time. In addition, silane coupling bonding agent, which is known for its ability to from strong covalent bonds between organic and inorganic materials, is applied on some of the specimens. These covalent bonds can substitute regular hydrogen links between the epoxy adhesive and the concrete substrate, and therefore, improve the bond. Some dry or wet specimens are debonded in either wedge driving or pulling tests to examine their mode-I and mode-II fracture toughness, respectively. Moisture contents along the interface are numerically determined using a finite element method and Fick's law of diffusion in which diffusion coefficients are experimentally obtained. Then, the fracture energy values are plotted against the corresponding moisture. Overall results ascertain that using silane coupling

agent, and drying specimens, to some part regain the strength for the bond; nevertheless, it is not capable of recovering all the strength. Failure mechanisms of debonded specimens indicate that the interface debonding of the untreated specimens is adhesive. In contrary, the debonding surface changes to the cohesive failure by using silane, or drying specimens before the test.

6.1. Introduction

Civil infrastructures are in urgent need of repair and strengthening throughout the world. Changes in the design codes, deterioration, structural defects, seismic conditions, all can be responsible for premature failure or ineffectiveness of structural elements. ASCE 2013 Report Card for America's Infrastructure estimates the U.S. would need to spend $3.6 trillion on aging infrastructures by 2020 [1]. Fiber reinforced polymer (FRP) composites have developed as one of the most fast growing structural materials in different engineering fields from, aerospace and automotive industries to civil engineering and infrastructural applications in the last decades. One of the revolutionary applications of FRP in civil engineering, particularly in civil infrastructures, is strengthening and rehabilitation of aging and damaged concrete structures [2]–[6].

Although in recent studies the short-term behavior of the FRP-to-concrete bond in retrofitted infrastructures has been investigated thoroughly, very little attention has been paid to long-term characteristics of the FRP-retrofitted concrete elements, particularly when aggressive environmental threats such as moisture and water invasion are involved [7]–[9] . A large number of short-term experimental tests under controlled and dry laboratory conditions showed that the most common failure mode in the FRP-to-concrete bonded joints occurs through the concrete in vicinity of the epoxy-concrete interface (cohesive failure) [10]. Many researchers focused experimentally on the long-term behavior of the FRP-to-concrete interface [11]–[18].

Experimental studies on the interface between the epoxy and concrete in FRP strengthened structures concluded that exposure to moisture for a long time is the foremost factor that can degrade the interface [7], [14], [15],[19], [20]. It has also been found out that the debonding locus shifts from the concrete cover to the epoxy- concrete interface.

This shift of debonding mode of the FRP-to-concrete bonded joint from cohesive to adhesive after conditioning in water was found contrary to the crack kink criterion theory proposed by He and Hutchinson [21], Au and Büyüköztürk [14], and Lau and Büyüköztürk [22]. According to He and Hutchinson [21], the debonding crack along the epoxy-concrete interface should kink to the concrete cover. They hypothesized that this contradiction can be resulted from two possible reasons: the plasticization, by formation of a layer of epoxy penetrated inside the cover concrete, or the weakening adhesive force between the epoxy and concrete [14]. No experimental evidence was suggested to examine these hypotheses. Later, Büyüköztürk et al. proposed a molecular dynamics (MD) approach to give a better understanding in this matter [23]. It was shown that water molecules can attack secondary bonds between adhesive and substrate by hydrolysis, and reduce the energy barrier (i.e. the required energy to separate silica-epoxy system) by approximately 15%. Although the MD model was successful to simulate the debonding mechanism, existing experimental results show much severe degradation in facture energy than MD simulation. Tuakta and Büyüköztürk showed that continuous moisture condition of specimens can significantly reduce both the mode-I and mode-II fracture toughness after early weeks [24]. They also examined the effect of drying the water conditioned specimen on the fracture toughness of the FRP-to-concrete specimens by exposing the specimens to a number of wet-dry cycles. Their testing results show that drying the specimen can improve the fracture

toughness of the interface. The original bond strength of the interface, however, cannot be fully recovered

6.2. Research scopes and organization

Although a number of different environmental conditions can affect the bond strength and fracture toughness of an epoxy-to-concrete bond, this study focuses on the effect of water invasion only. To this end, the fracture toughness of FRP-to-concrete bonded joints before and after conditioning in water will be determined by two methods. In the first method, mode-I and mode-II fracture toughness of the FRP (CFRP)-to-concrete interface are determined by a wedge driving test and a pulling test, respectively. The testing specimens and loading wedge are the same as those previously used by authors for the environment-assisted subcritical debonding (EASD) of the FRP-to-concrete bond [25]. The water diffusivity in materials used in the specimens such as concrete block, cured epoxy layer and CFRP plates are experimentally determined.

Organofunctional silane coupling agents (SiH_4) for many years have been proved to be useful to enhance the bond between an organic material such as epoxy and inorganic materials such as metal, particularly bond between epoxy and aluminum [26]–[33]. Also, some promising results by adding silane bonding agent between concrete and epoxy have been reported [25], [34]. In this study the role of silane bonding agent in improving the fracture toughness of the bond will also be investigated.

6.3. Materials and testing

The same specimen used in our previous study on the subcritical debonding of the epoxy-concrete interface is adopted for the wedge driving test (Fig. 6-1) [25]. The specimen consists of a layer of CFRP pre-cured plate, a layer of epoxy adhesive and a concrete block. A

pre-crack with a length about 3 mm (1/8 inch) is produced by applying a thick Teflon tape on the concrete block to assist crack initiation through the interface between the epoxy and the concrete. A steel wedge with thickness of Δ will be driven into the interface crack. As shown in Fig. 6-1, a is the effective length between the wedge contact point and the crack tip. The concrete block of the specimen has a width of 50.8 mm (2 inch) which is equal to the width of the commercially available CFRP plate.

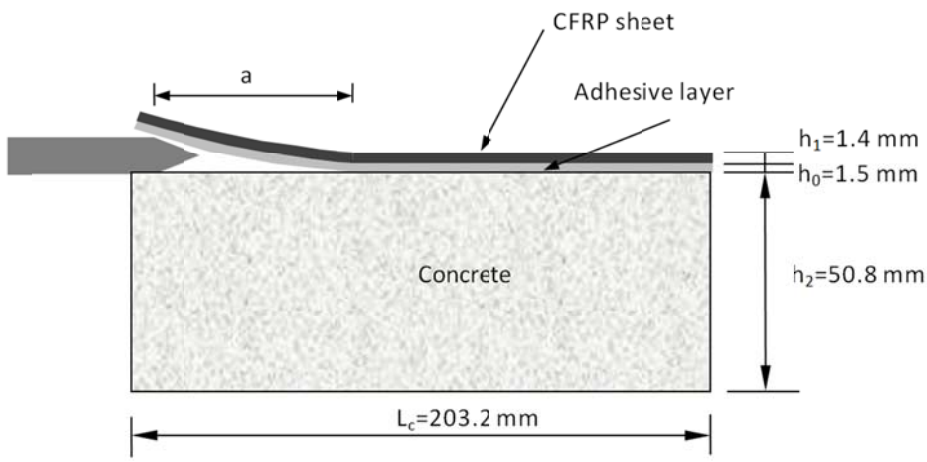

Fig. 6-1 Wedge driving test specimen.

The concrete blocks were cast and then cured for 28 days following ASTM C33/C33M and ASTM C192,C192M [35], [36], and then dried in a laboratory at room temperature (23°C) for more than two weeks. The mean 28-day compressive strength of the block in 100 x 200 mm cylinders was measured as 44.5 MPa. Geometries and mechanical properties of CFRP plates and the Tyfo TC adhesive for binding between concrete and CFRP plate are shown in Table 6-1 and Table 6-2, respectively.

Pulling specimen is identical to the wedge driving specimen except that the length of the CFRP plate is 76.2 mm (3 inch) longer (Fig. 6-2) and a pre-crack of 50.9 mm (2 inch) is induced between the epoxy-concrete interface to guarantee better debonding.

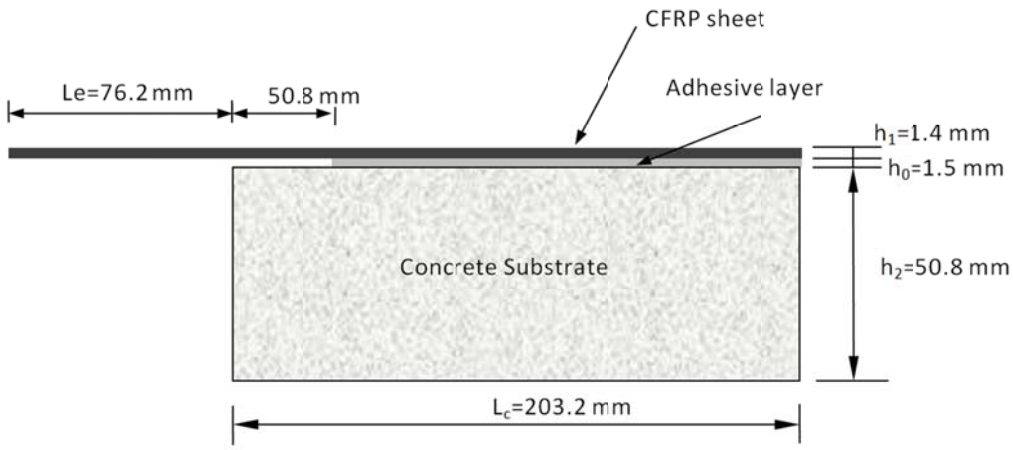

Fig. 6-2 Pulling test specimen.

Table 6-1 Mechanical properties of CFRP.

Laminate Width	Laminate Thickness	Cross Sectional Area	Tensile Strength	Tensile Modulus of Elasticity	Ultimate Strain
50.8 mm	1.397 mm	71.10 mm2	2413 MPa	131,000 MPa	0.0187 %

Table 6-2 Mechanical properties of Epoxy.

Compressive Strength	Epoxy layer Width	Epoxy layer Thickness	Cross Sectional Area	Tensile Strength	Tensile Modulus	Flexural Modulus	Flexural Strength
28.2 MPa	50.8 mm	1.50 mm	76.2 mm2	22.7 MPa	1,200 MPa	1.23 GPa	45.8 MPa

6.3.1. Fracture toughness of the CFRP-to-concrete specimens conditioned in water

6.3.1.1. Experimental set-up

The test system consists of a home-made steel fixture, a digital camera for monitoring the crack growth, and a servo-controlled hydraulic loading frame (MTS810) to apply load. All

specimens were conditioned in water for different durations to simulate different levels of deterioration induced by water. The test set-up is shown in Fig. 6-3.

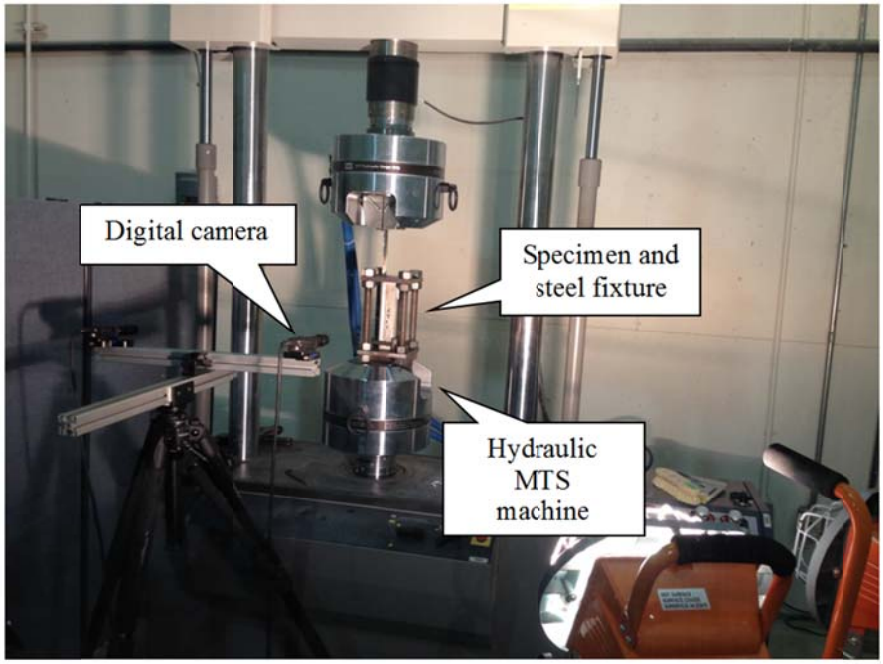

Fig. 6-3 Experimental set-up for fracture toughness tests of CFRP-to-concrete specimens.

6.3.1.2. Wedge driving test

Specimens were first installed in the home-made steel fixture, and then the fixture was placed on the MTS loading frame in the lower grip as shown in Fig. 6-3. A 3.175 mm (0.125 in) thick steel wedge fabricated according to ASTM D3762-03 [37] was then fixed in the upper grip and placed into the pre-crack between the epoxy and the concrete interface. The wedge was driven into the crack at an intermediate speed of 2.54 mm/minute (0.00167 inch/second) by using the MTS machine. A high resolution digital camera was used to monitor the crack growth by taking high-quality images at the crack tip every one second, as shown in Fig. 6-4(a). From the captured images, the length of the propagated crack was calculated by calculating the distance between the crack tip and the wedge contact point. The mode-I energy release rate (ERR) at the crack tip can be calculated as [38]:

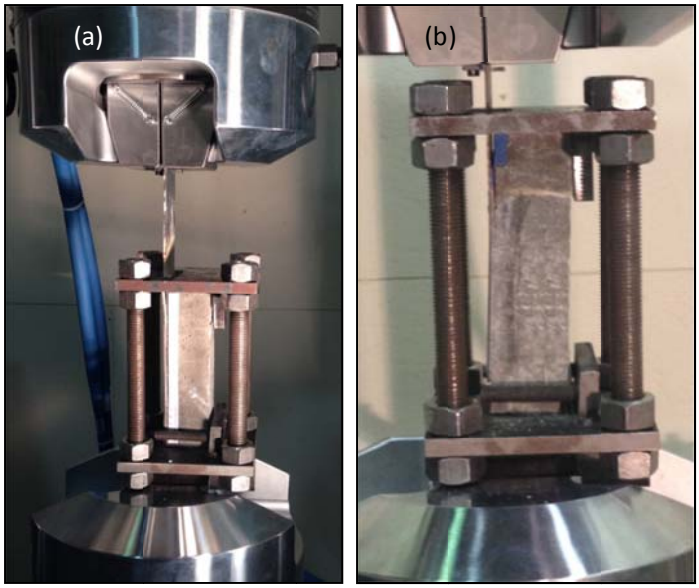

Fig. 6-4 Specimens setup: (a) the wedge driving test setup, (b) the pulling test setup.

$$G_I = \frac{9D\Delta^2}{2ba^4}, \quad (1)$$

where, b, D, and Δ are width of the specimen, bending stiffness of the CFRP-adhesive composite beam, and wedge thickness at the contact point, respectively.

6.3.1.3. Pulling test

The same steel fixture used in the wedge driving test was employed to firmly confined specimens to prevent any sliding or rotation of the concrete block during the pulling test. The free edge of the CFRP plate was then pulled at a slow speed of 0.45 mm/minute (0.0003 inch/second) by the upper grip of the MTS machine. The testing set-up is demonstrated in Fig. 6-4(b). The applied force by the loading cell and slip of the CFRP plate were recorded. The area under the force-slip graph (Fig. 6-5) divided by the area of the bond is used to calculate the applied mode-II fracture energy release rate needed to separate the CFRP-adhesive from the concrete for each specimen

$$G_{II} = \frac{1}{b.L_{eff}} \int_0^{s_c} P.ds, \quad (2)$$

where L_{eff} is the effective length of the bond (can be determined by measuring the length of the debonded adhesive), P is applied pulling force and s in the slip of the debonded CFRP-adhesive section. In this equation, s_c stands for the maximum slip at the time of debonding.

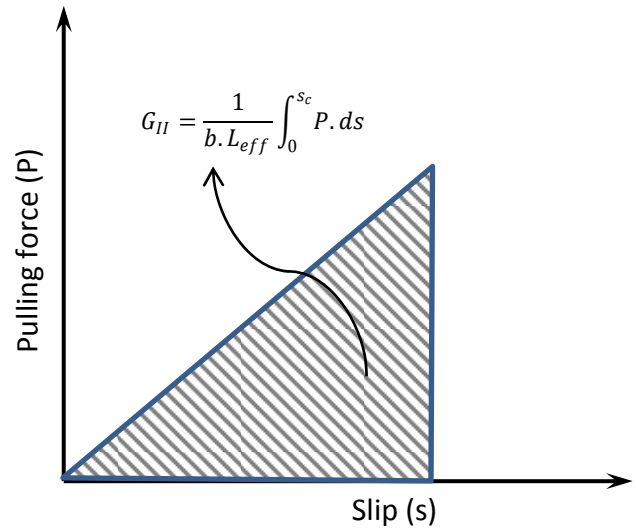

Fig. 6-5 Calculation of the mode-II fracture energy release rate from the pulling test.

6.3.1.4. Moisture diffusion simulation

A conditioned specimen in water is exposed to water molecule invasion from all sides (Fig. 6-6). Then moisture transfers all the way through the specimens to the inner parts and eventually reaches entire epoxy-concrete interface. The governing equation of moisture diffusion can be expressed considering by Fick's second law and Darcy's law [39]

$$\frac{\partial H(x,z,t)}{\partial t} = \nabla(D_w^i\big(C(x,z,t) \times \nabla H(x,z,t)\big), \quad (3)$$

where $H(x, z, t)$ is the relative humidity in the specimen, $D^i_w (i = 1, 2, 3)$ are moisture diffusivity (diffusion coefficient) of CFRP, epoxy, and concrete, respectively and t denotes the diffusion time. x and z are the axes of the coordinate system originated at the interface shown in Fig. 6-6. Moisture continuity conditions along the CFRP-epoxy and epoxy-concrete interfaces require

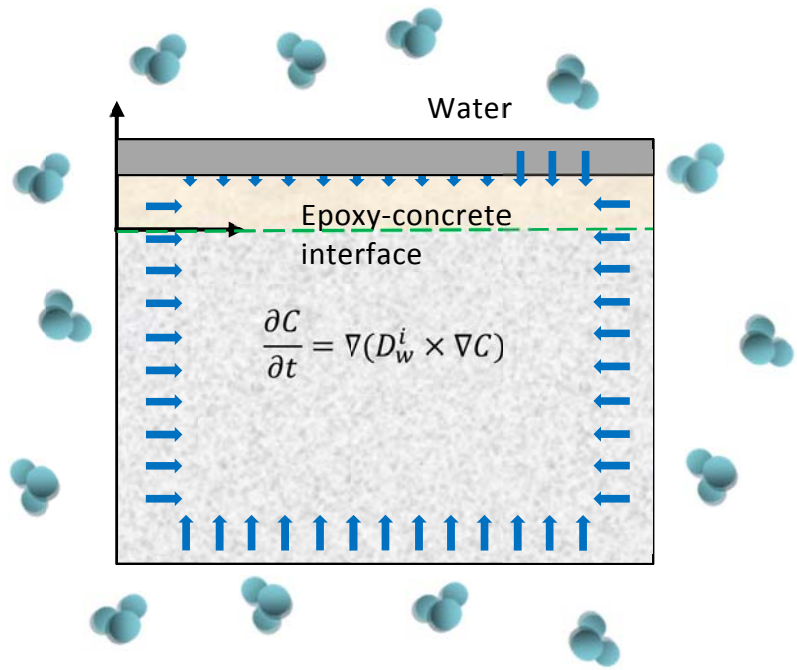

Fig. 6-6 Schematic illustration of the water diffusion from the CFRP-to-concrete bond towards the epoxy-concrete interface.

$$\frac{\partial H(x,z,t)}{\partial z}\nabla(D_w^i\big(C(x,z,t)\big) = \frac{\partial H(x,z,t)}{\partial z}\nabla(D_w^{i+1}\big(C(x,z,t)\big), \qquad i = 1,2,3. \tag{4}$$

It would be difficult to find a closed-form solution for the water diffusion using Eq. (3); however, a numerical finite element method employed by Ouyang and Wan (2009) is used to simulate three-dimension models of CFRP-to-concrete specimens [39].

A series of absorption tests were carried out to determine the moisture diffusivities needed for this simulation. To this end, thin rectangular specimens were cut from the same materials (CFRP, epoxy and concrete) used in the fracture toughness tests. CFRP plates used in this study were pre-cured unidirectional carbon fibers with epoxy matrix. Since the thickness of the applied CFRP plate is much smaller compared to the length and width of the bond, we can assume that the majority of water diffuses perpendicularly to the mid-plane of the CFRP, instead of a three-dimension problem. In this way, it can be reduced to a one-dimension diffusivity test. A CFRP plate was cut into four 51 × 58 mm rectangular pieces. They were then abraded by a

clean sand-paper to remove any dust or solid particles. After abrasion, the average thickness of these specimens is 0.8 mm. A thin layer of epoxy with thickness of 1.55 mm was cured for two weeks. Then it was cut in the same way to four 49×51 mm pieces. From a 28-day cured concrete block, four 48 by 51 mm pieces with average thickness of 3 mm were cut using an electric water-saw. Final absorption test samples are shown in Fig. 6-7.

Four sides of each sample were covered with a water absorption sealant to minimize water diffusion from other sides and guarantee one-dimensional flux. The moisture content of a material during absorption can be obtained as [40]

$$M = G(M_m - M_i) + M_i, \tag{5}$$

where, M_i and M_m are the initial moisture content and the maximum moisture content, respectively. G is a dependent parameter and can be achieved as [40]

$$G = \frac{M - M_i}{M_m - M_i} = \frac{8}{\pi^2}.\sum_{j=0}^{\infty}\frac{\exp\left[-(2j+1)^2.\pi^2\left(D_w^i.\frac{t}{S^2}\right)\right]}{(2j+1)^2}. \tag{6}$$

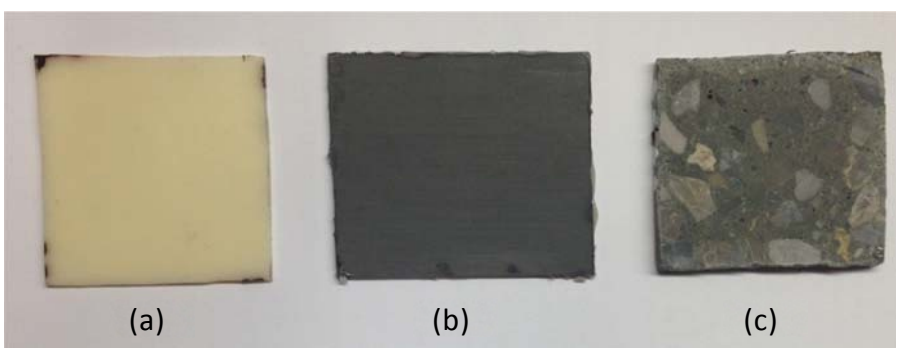

Fig. 6-7 Samples used in water absorption test: (a) epoxy sample, (b) CFRP sample, (c) Concrete sample.

Above equation can be simplified as [40]

$$G = 1 - \exp\left[7.3\left(D_w^i . \frac{t}{s^2}\right)^{0.75}\right], \quad (7)$$

where t is the time and s is the thickness for the material exposed to the same environment on both sides. Moisture diffusivities will be obtained by fitting experimental data to the expression of Eq. (7).

6.3.1.5. Testing plan

Before conducting tests on conditioned specimens, some control specimens, which were maintained at ambient condition after manufacturing, were tested. All conditioned CFRP-to-concrete specimens were submerged in tanks filled with tap water maintained at temperature of 23.89°C (75^{0}F). Three different periods of conditioning (one, three and six months) were chosen for both untreated specimens and specimens treated with silane (before applying epoxy and CFRP palate) to evaluate the effect of water ingress duration on the crack growth length for wedge driving test and on the fracture energy. In addition to the wet specimens tested after removing from the water tank, some of the specimens were dried at room temperature (23°C) for two days and then tested in the same way as wet specimens in order to study the reversal effect of the fracture toughness.

Absorption test specimens were first dried in an oven at 45°C until no change in the mass is observed. After registering the dried-weight and assuming the initial moisture content M_i =0, all specimens were conditioned in a water tank at room temperature (23°C). At different times, specimens were weighed using a digital lab scale after removing the surface moisture with a moistened cloth to obtain moisture content. After that, they were returned to the tank for further conditioning. This procedure was repeated until no evident change of mass was discovered.

6.4. Testing results and discussion

6.4.1. Wedge driving and pulling tests

Results of degradation of the CFRP-to-concrete induced by conditioning in water tank are shown in Fig. 6-8. After 1 month conditioning in water, mode-I fracture toughness of the interface has been reduced to only 35% of the control specimen for the specimen without surface treatment with silane coupling agent. This fracture toughness can be further reduced to 22% after conditioning in water for two months. After that, no significant reduction of the fracture toughness can be observed for extended water conditioning, suggesting that most deterioration caused by water can be done within two months conditioning. Similarly, significant reduction in the fracture toughness can be observed for the specimens treated with silane coupling agent too after conditioning in water for one month. Their residual fracture toughness, which is 51% of that of the control specimen, is much higher than the specimens without silane treatment, confirming that silane coupling agent can improve the durability of the interface due to strong covalent bonds formed between the epoxy and the concrete surface. If specimens were dried in laboratory for two days before testing, a slight increase in fracture toughness can be observed for all specimens in comparison with those tested without drying. This suggests that some of the lost interface strength is reversible, which is in agreement with the observation of Tuakta and Büyüköztürk [24]. The According to [24], this reversible portion of the fracture toughness is due to the plasticization of the adhesive induced by moisture. Similar gain of fracture toughness can be observed for the specimens treated with silane after drying in the laboratory for two days.

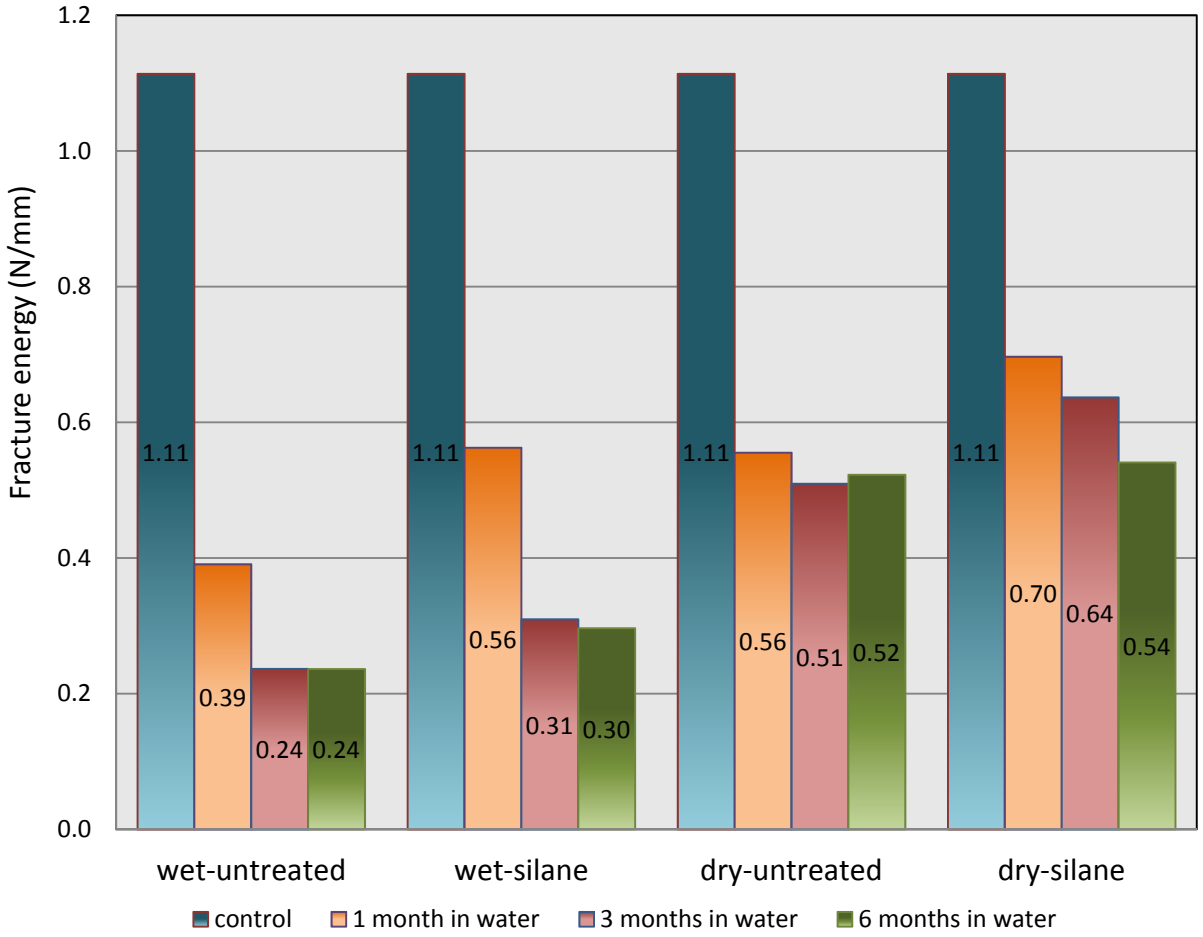

Fig. 6-8 Effect of water conditioning, duration and being wet or dry at the time of test, on mode-I fracture toughness of untreated or treated specimens with silane coupling agent.

Fig. 6-9 compares the mode-II fracture toughnesses of the specimens conditioned in water for extended time and the control specimens. Similar to the case of mode-I loading, conditioning in water can significantly degrade the CFRP-to-concrete interface. However, the residual mode-II fracture toughness, which is 41% of the control specimen, appears slightly higher than that of the mode-I. This may be because that mechanical interlock plays a larger role in the mode-II fracture toughness than mode-I fracture toughness. Unlike in the case of mode-I loading shown in Fig. 6-8, one month water conditioning is sufficient to deteriorate the mode-II fracture toughness to its minimum. No significant reduction of mode-II fracture toughness can be observed after one month conditioning in water. Once again, treating surface with silane

coupling agent has a beneficial effect on the residual fracture toughness of the CFRP-to-concrete interface, as shown in Fig. 6-9.

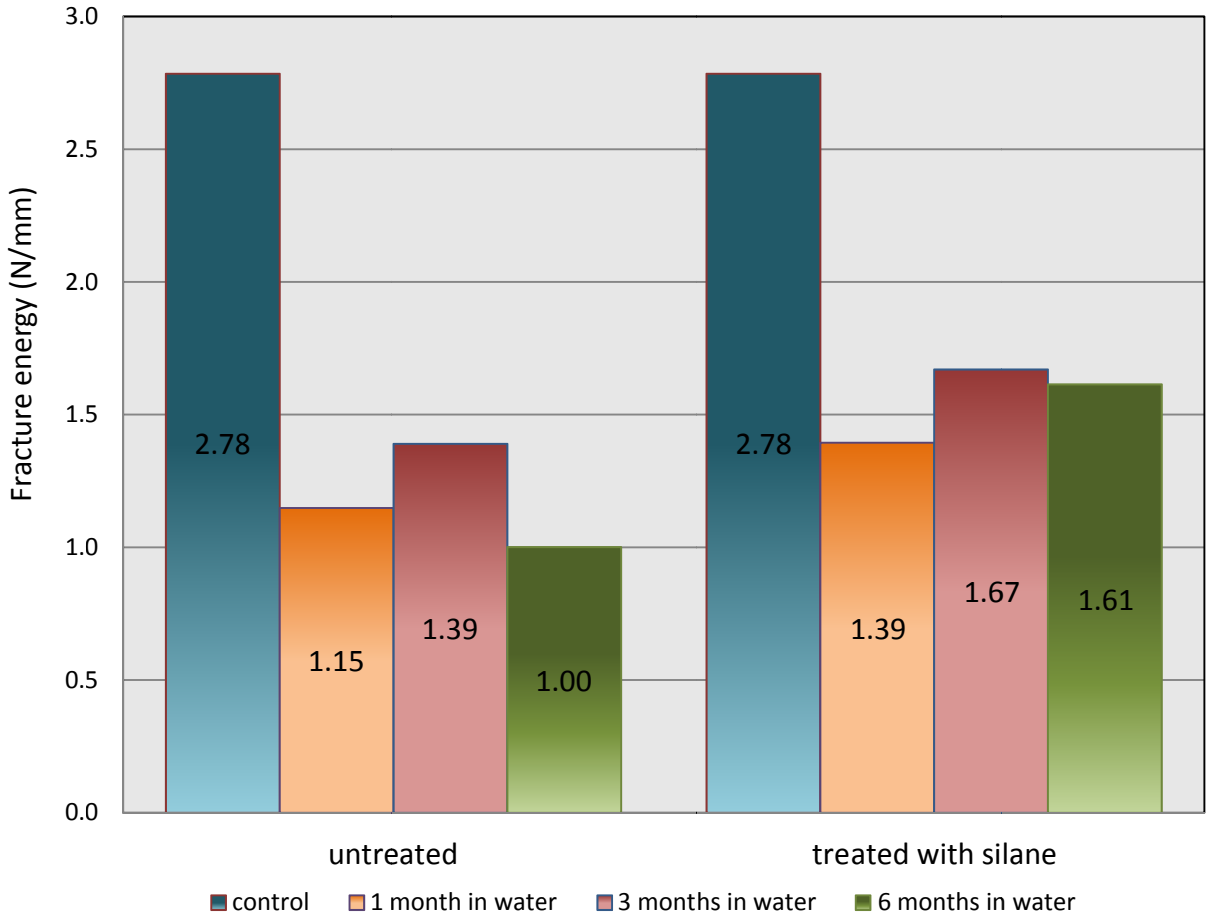

Fig. 6-9 Effect of water conditioning on mode-II fracture energy release rate for untreated or treated specimens with silane coupling agent.

The failure modes of specimens conditioned in water for three months under mode-I loading are shown in Fig. 6-10. In this figure, the epoxy part of the specimen is shown. Fig. 6-10(a) shows the specimen without silane treatment has a very clean epoxy surface, suggesting that debonding exhibits an adhesive failure through the epoxy-concrete interface. As comparison, very thin layer of concrete can be observed on the epoxy layer of the specimen treated with silane, indicating that the failure is cohesive through the adjacent concrete substrate for this specimen. This is not surprising since silane can create some covalent bonds between the epoxy

and the concrete interface, which makes it difficult for water molecules to displace the adhesive from the concrete surface. If the specimen without silane treatment were dried in laboratory for two days before testing, a mixed adhe1ive and cohesive failure mode can be observed as shown in Fig. 6-10(c). It can be seen that the inner part of the surface mostly shows adhesive failure, while the outer bound of the interface exhibits a cohesive failure. This is due to the nature of the drying process in the specimen, in which more water can be evaporated in the exterior portions of the interface than the inner part. As a result, more strength can be recovered in the outer bound of the interface of the specimen than the inner part, leading to mixed failure mode observed in Fig. 6-10(c). As confirmation, the inner part of the specimen was found still wet after testing.

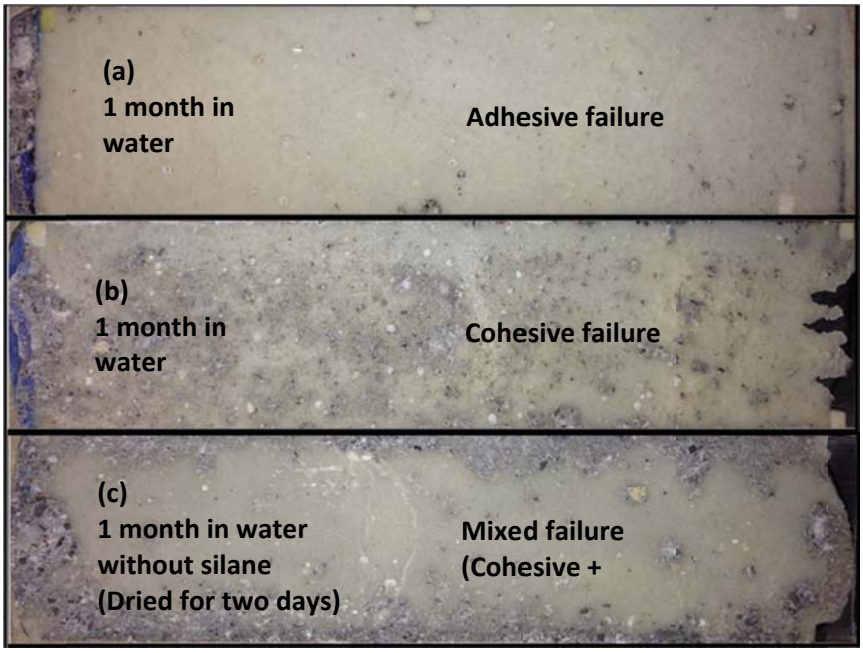

Fig. 6-10 Debonded epoxy side of the tested specimens under mode-I loading.

6.4.2. Moisture diffusion simulation

The gain of moisture content of the absorption specimens, are presented with respect to the square root of time per unit thickness in Fig. 6-11. Proposed numerical fitting based on Fick's law match the experimental data very well. However, CFRP and epoxy show some non-Fickian

trends if the absorption is sufficiently long. They can take more water and gain more moisture content with absorption time. Moisture diffusivities for materials used in this study are derived from the fitting of Fickian model from Eq. (7) with the experimental data (Table 6-3).

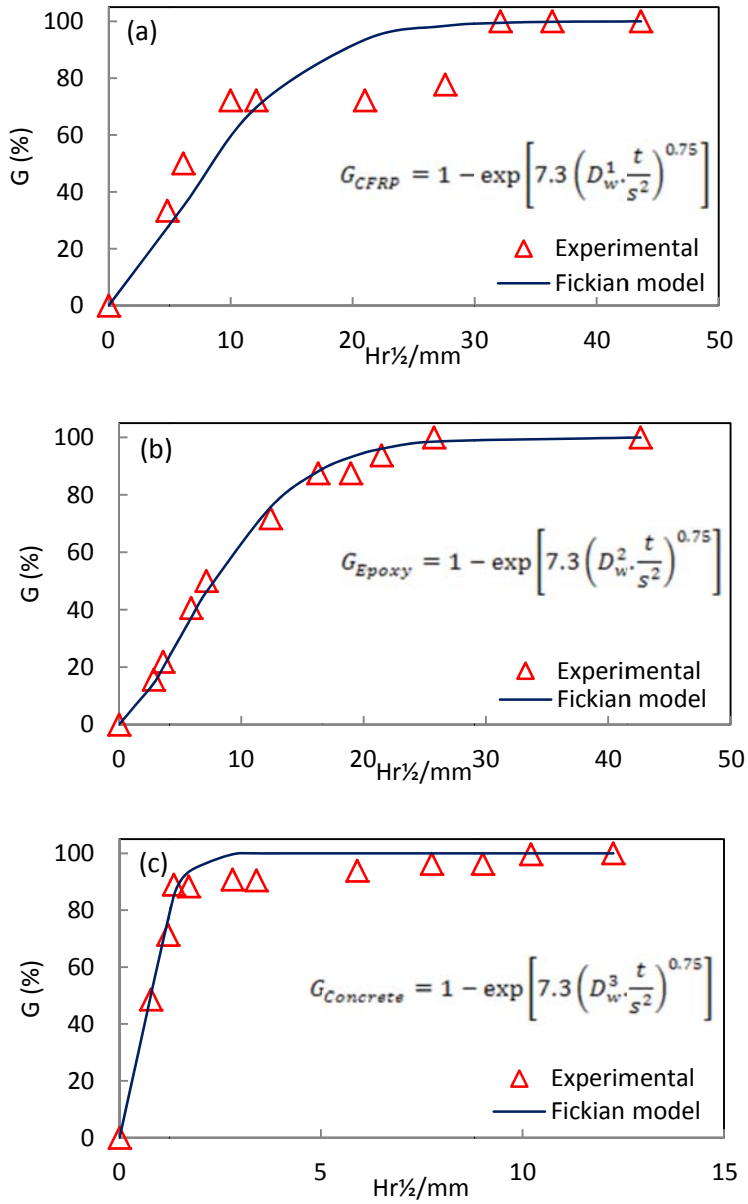

Fig. 6-11 Experimental and Fickian absorption model for (a) CFRP, (b) Epoxy, (c) Concrete at room temperature (23°C).

Table 6-3 Experimental diffusivities of materials used in fracture toughness tests.

Material	CFRP	Epoxy	Concrete
Diffusivity (10^{-5} mm^2/sec)	0.0170	0.0203	2.54

Moisture diffusion in the CFRP-to-concrete specimen can be numerically simulated using ABAQUS/CAE (Fig. 6-12). DC3D8 elements (8-node linear brick for heat transfer) were used. A numerical technique was employed to convert a heat-flux problem to a moisture diffusion one. A refined mesh with element size of 1 mm close to the epoxy-concrete interface was adopted for all three materials.

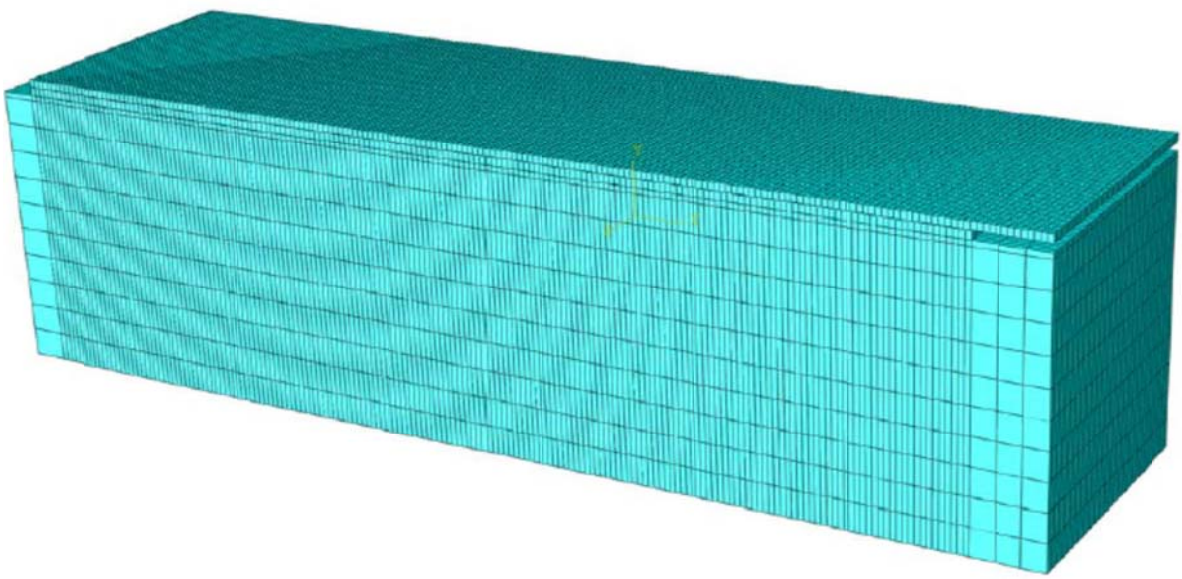

Fig. 6-12 FEA model used for moisture diffusion along the epoxy-concrete interface.

In this simulation, the boundary conditions for all outer surfaces were set as environmental RH =100%. The Concrete, CFRP and epoxy adhesive were assumed initially dry with 0% RH. Diffusion Coefficients of Concrete, CFRP, and Epoxy are given in Table 6-3 and thicknesses are 50.9 mm, 1.4 mm and 1.5 mm, respectively.

Fig. 6-13 and Fig. 6-14 show the relative humidity contour of a specimen submerged in water from one month to six months in transverse and longitudinal sections, respectively. It can be seen that along the epoxy-concrete interface, the relative humidity is not uniform, which clearly is due to the geometry of the specimen. Diffusion path, which is the distance from the outside of the specimen to a specific location inside the specimen, is the main contributor to the uneven distribution of moisture content within the interface. As a result, the closer a region along the interface to the external water source is the higher interface relative humidity (I_{RH}) it has. Fig. 6-15 illustrates the *IRH* for a specimen from one month to six months conditioning in water in both the transverse and the longitudinal directions.

It can be seen that the moisture content in a large portion of the interface is still below 20% by the first month. This non-uniform distribution of the moisture content along the interface makes it difficult to interpret the degradation testing data obtained in Fig. 6-8 and Fig. 6-9. This difficulty also exists in all existing studies on the deterioration of the epoxy-concrete interface attacked by water. In this study, the residual strength of the interface is expressed as an average of moisture contents along the interface.

By taking average of all moisture contents obtained through the interface between the concrete and the epoxy layer at each time, we are able to correlate the I_{RH} with the fracture toughness obtained from the wedge driving test (mode-I) and the pulling test (mode-II). The results are presented in Fig. 6-16. An exponential expression can be used to describe behavior of the interface residual fracture toughness in either mode-I or mode-II with respect to the moisture content

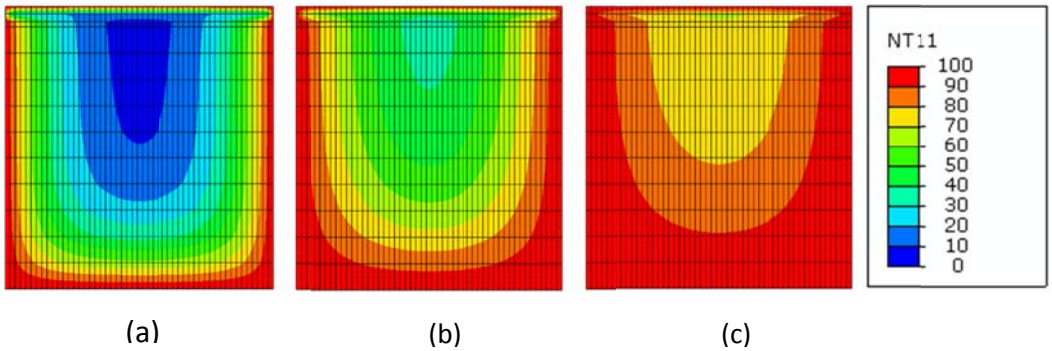

Fig. 6-13 Relative humidity contour versus immersion time: (a) 1-month transverse section, (b) 3-month transverse section, (c) 6-month transverse.

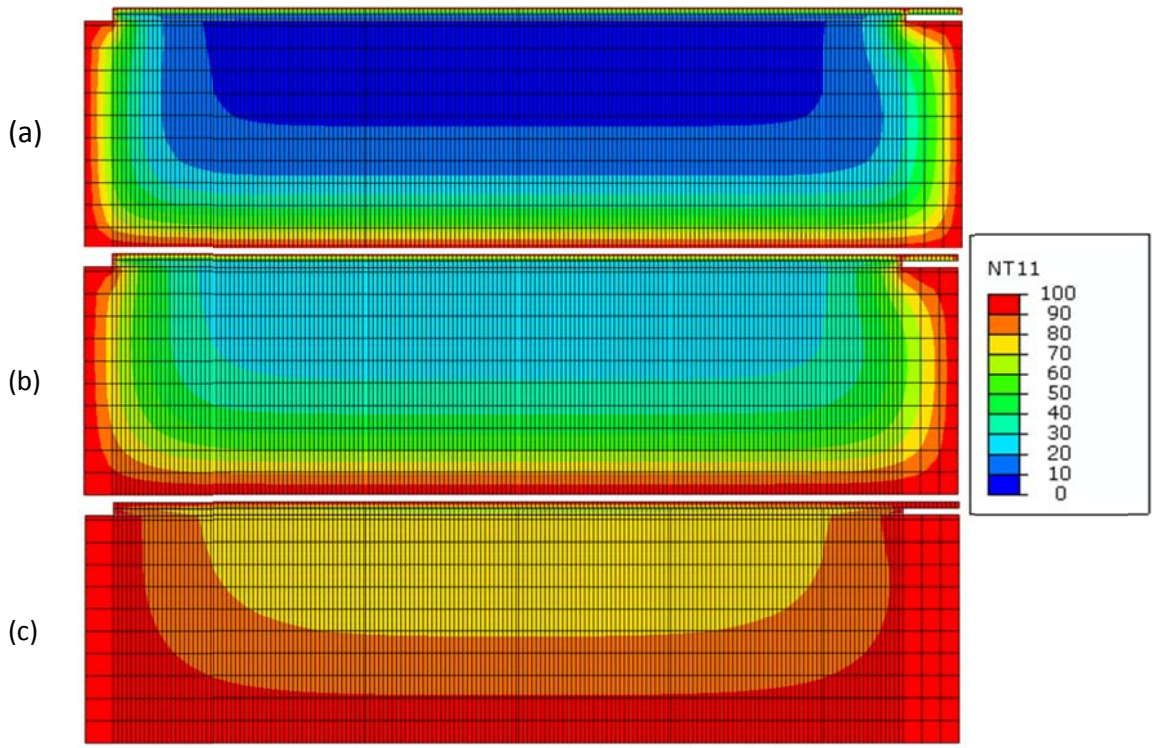

Fig. 6-14 Relative humidity contour versus immersion: (a) 1-month longitudinal section, (b) 3-month longitudinal section, (c) 6-month longitudinal section.

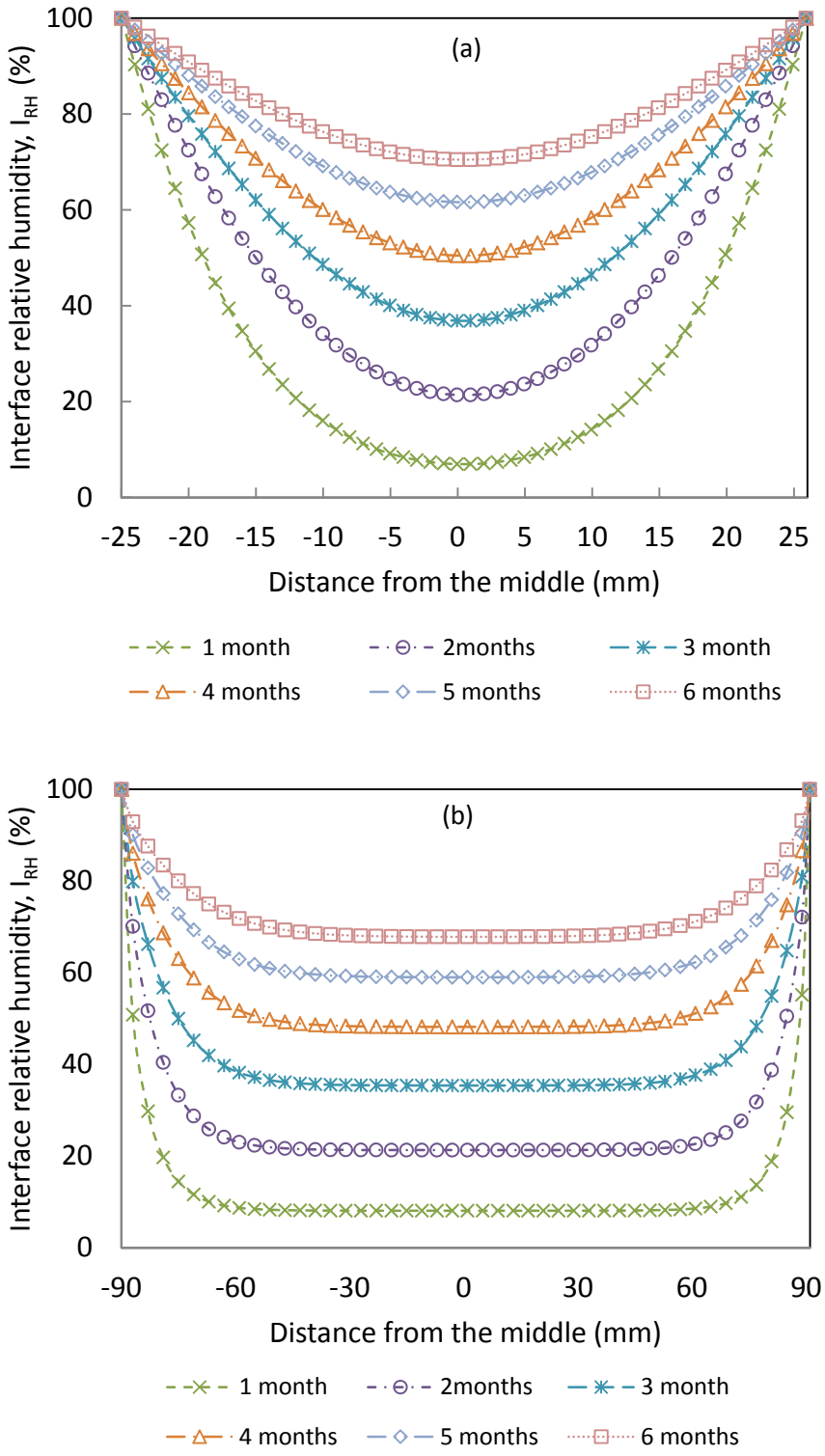

Fig. 6-15 Interface relative humidity along the epoxy-concrete interface: (a) Transverse section, (b) Longitudinal section.

$$G_I \; or \; G_{II} = \alpha . e^{(-\beta . I_{RH})}, \tag{8}$$

where α and β are parameters to be determined by fitting Eq. (8) to the experimental data (Table 6-4). As expected, wet-untreated specimen shows a rapid tendency to lose its mode-I fracture toughness with higher average I_{RH}, while surface treatment with silane bonding agent can increase the toughness a little bit.

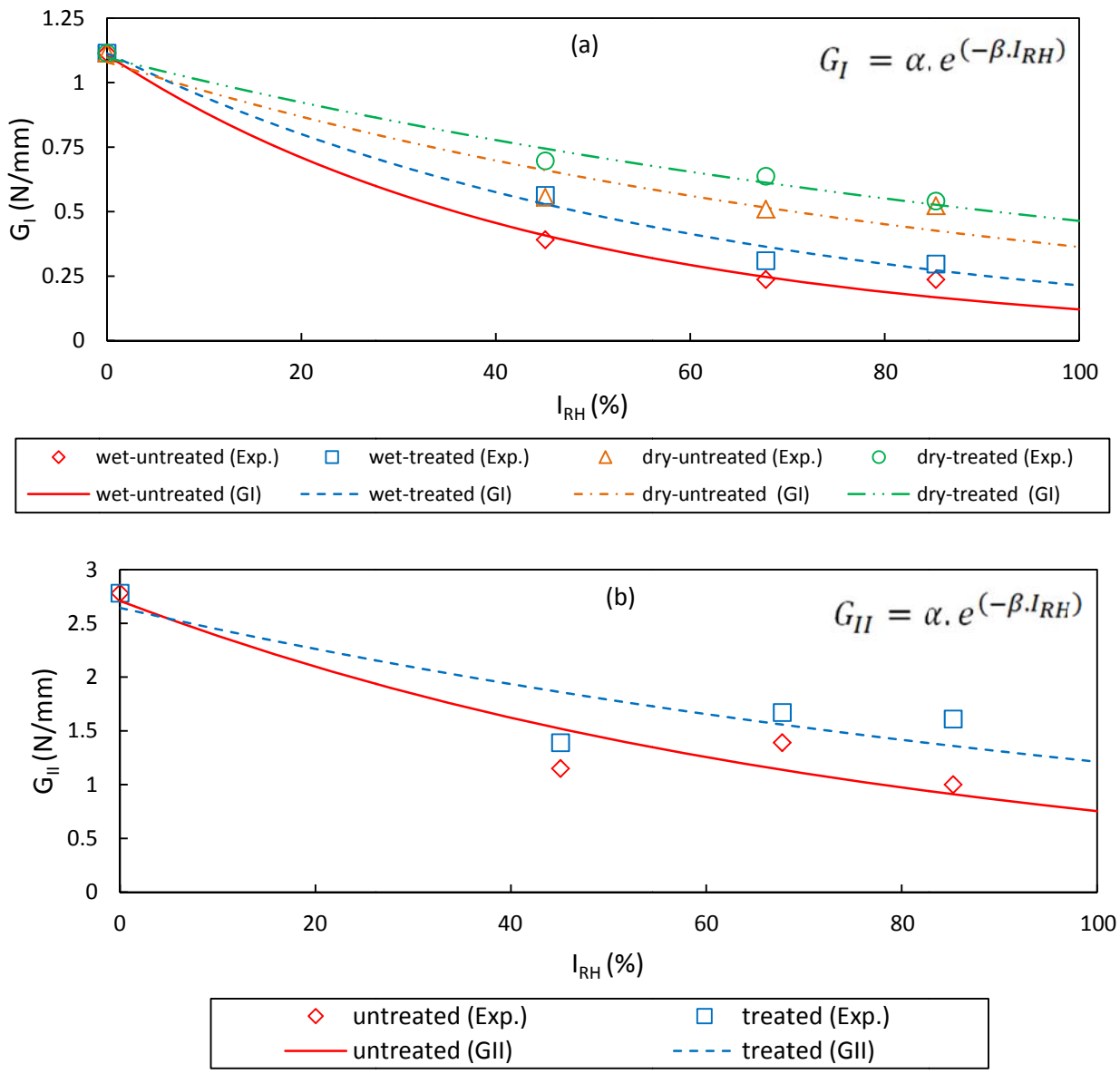

Fig. 6-16 The relationship between the fracture energy release rate and the average interface relative humidity along the epoxy-concrete interface: (a) Mode-I fracture, (b) Mode-II fracture.

Table 6-4 Parameters of the relationship between the fracture energy and the I_{RH}.

Parameters	Mode-I Fracture				Mode-II fracture	
	Wet-untreated	Wet-treated	Dry-untreated	Dry-treated	untreated	treated
α	1.10	1.11	1.08	1.10	2.71	2.64
B	2.21	1.65	1.09	0.86	1.28	0.78

6.5. Conclusions

In this study, the critical debonding of FRP-to-concrete interface was investigated using two fracture mechanics methods. The wedge driving test (for the mode-I fracture), and the pulling test (for the mode-II) were carried out to measure the fracture toughness of a number of the FRP-to-concrete interface specimens conditioned in water. It was found that within the first month of the conditioning, the specimens lose more than half of their both mode-I and mode-II fracture toughness. Even though, the mode-II fracture toughness is stronger than that of the mode-I since mechanical interlock plays more important role in mode-II fracture. The strength reduction of the interface seems to reach its maximum after three-month conditioning in water. No further reduction of the fracture toughness of the interface for any longer conditioning time in water more than 3 months was observed. It was shown that using silane coupling agent can improve the residual fracture toughness of the interface subjected to water attack. A study on the mode-I failure mode showed that while the interface debonding for specimens conditioned in water is adhesive, applying silane coupling argent changes this adhesive failure to the cohesive one (i.e. within the concrete substrate). Also it was observed that drying specimens shifts the mode to the mixed failure (i.e. cohesive/adhesive failure). An exponential expression was used to fitting the experimental relationship between the residual fracture toughness and the interface relative humidity.

6.6. References

[1] A. W. Herrmann, "ASCE 2013 Report Card for America's Infrastructure," in *IABSE Symposium Report*, 2013, vol. 99, no. 33, pp. 9–10.

[2] V. M. Karbhari, F. Seible, and G. A. Hegemier, "On the Use of Fiber Reinforced Composites for Infrastructure Renewal—A Systems Approach," in *Materials for the New Millennium*, 1996, pp. 1091–1100.

[3] A. Sharif, G. J. Al-Sulaimani, I. A. Basunbul, M. H. Baluch, and B. N. Ghaleb, "Strengthening of initially loaded reinforced concrete beams using FRP plates," *ACI Struct. J.*, vol. 91, no. 2, 1994.

[4] P. A. Ritchie, D. A. Thomas, L.-W. Lu, and G. M. Conelly, "External reinforcement of concrete beams using fiber reinforced plastics," *ACI Struct. J.*, vol. 88, no. 4, 1991.

[5] C. E. Bakis, A. Ganjehlou, D. I. Kachlakev, M. Schupack, P. N. Balaguru, D. J. Gee, V. M. Karbhari, D. W. Scott, C. A. Ballinger, and T. R. Gentry, "Guide for the design and construction of externally bonded FRP systems for strengthening concrete structures," *Rep. by ACI Comm.*, vol. 440, no. 2002, 2002.

[6] Ce. Bakis, L. C. Bank, Vl. Brown, E. Cosenza, J. F. Davalos, J. J. Lesko, A. Machida, S. H. Rizkalla, and T. C. Triantafillou, "Fiber-reinforced polymer composites for construction-state-of-the-art review," *J. Compos. Constr.*, vol. 6, no. 2, pp. 73–87, 2002.

[7] N. F. Grace and M. Grace, "Effect of repeated loading and long term humidity exposure on flexural response of CFRP strengthened concrete beams," in *Proceedings of the International Symposium on Bonded behavior of FRP in Structures (BBFS 2005), Chen and Teng (eds)*, 2005, pp. 539–546.

[8] V. M. Karbhari, Jw. Chin, D. Hunston, B. Benmokrane, T. Juska, R. Morgan, J. J. Lesko, U. Sorathia, and D. Reynaud, "Durability gap analysis for fiber-reinforced polymer composites in civil infrastructure," *J. Compos. Constr.*, vol. 7, no. 3, pp. 238–247, 2003.

[9] M. L. Porter and K. Harries, "Future directions for research in FRP composites in concrete construction," *J. Compos. Constr.*, vol. 11, no. 3, pp. 252–257, 2007.

[10] J. G. Teng, S. T. Smith, J. Yao, and J. F. Chen, "Intermediate crack-induced debonding in RC beams and slabs," *Constr. Build. Mater.*, vol. 17, no. 6, pp. 447–462, 2003.

[11] S. U. Al-Dulaijan, M. M. Al-Zahrani, A. Nanni, and T. E. Boothby, "Effect of environmental pre-conditioning on bond of FRP reinforcement to concrete," *J. Reinf. Plast. Compos.*, vol. 20, no. 10, pp. 881–900, 2001.

[12] J. F. Davalos, S. S. Kodkani, I. Ray, and C. Lin, "Fracture evaluation of GFRP—concrete interfaces for freeze—thaw and wet-dry cycling," *J. Compos. Mater.*, vol. 42, no. 14, pp. 1439–1466, 2008.

[13] K. V Subramaniam, M. Ali-Ahmad, and M. Ghosn, "Freeze–thaw degradation of FRP–concrete interface: impact on cohesive fracture response," *Eng. Fract. Mech.*, vol. 75, no. 13, pp. 3924–3940, 2008.

[14] C. Au and O. Büyüköztürk, "Peel and shear fracture characterization of debonding in FRP plated concrete affected by moisture," *J. Compos. Constr.*, vol. 10, no. 1, pp. 35–47, 2006.

[15] O. Büyüköztürk and T.-Y. Yu, "Understanding and assessment of debonding failures in FRP–concrete systems," in *17th International congress on advances in civil engineering, Yildiz Technical University, Istanbul, Turkey*, 2006.

[16] J. Lyons, D. Laub, V. Giurgiutiu, M. Petrou, and H. Salem, "Effect of hygrothermal aging on the fracture of composite overlays on concrete," *J. Reinf. Plast. Compos.*, vol. 21, no. 4, pp. 293–309, 2002.

[17] P. Mukhopadhyaya, R. N. Swamy, and C. J. Lynsdale, "Influence of aggressive exposure conditions on the behaviour of adhesive bonded concrete–GFRP joints," *Constr. Build. Mater.*, vol. 12, no. 8, pp. 427–446, 1998.

[18] V. M. Karbhari and M. Engineer, "Effect of environmental exposure on the external strengthening of concrete with composites-short term bond durability," *J. Reinf. Plast. Compos.*, vol. 15, no. 12, pp. 1194–1216, 1996.

[19] Z. Ouyang and B. Wan, "Experimental and Numerical Study of Moisture Effects on the Bond Fracture Energy of FRP/Concrete Joints," *J. Reinf. Plast. Compos.*, 2007.

[20] B. Wan, "The Effect of the Presence of Water on the Durability of Bond between CFRP and Concrete," *J. Reinf. Plast. Compos.*, vol. 25, no. 8, pp. 875–890, 2006.

[21] M.-Y. He and J. W. Hutchinson, "Kinking of a crack out of an interface," *J. Appl. Mech.*, vol. 56, no. 2, pp. 270–278, 1989.

[22] D. Lau and O. Büyüköztürk, "Fracture characterization of concrete/epoxy interface affected by moisture," *Mech. Mater.*, vol. 42, no. 12, pp. 1031–1042, 2010.

[23] O. Büyüköztürk, D. Lau, and C. Tuakta, "Durability and long-term performance modeling of frp-concrete systems," in *The 6th International Conference on FRP Composites in Civil Engineering-CICE*, 2012.

[24] C. Tuakta and O. Büyüköztürk, "Conceptual model for prediction of FRP-concrete bond strength under moisture cycles," *J. Compos. Constr.*, vol. 15, no. 5, pp. 743–756, 2011.

[25] S. Amidi and J. Wang, "Subcritical Debonding of FRP-to-Concrete Bonded Interface under Synergistic Effect of Load, Moisture, and Temperature," 2015.

[26] C. F. Korenberg, A. J. Kinloch, and J. F. Watts, "Crack growth of structural adhesive joints in humid environments," *J. Adhes.*, vol. 80, no. 3, pp. 169–201, 2004.

[27] S. Shokoohi, A. Arefazar, and R. Khosrokhavar, "Silane coupling agents in polymer-based reinforced composites: a review," *J. Reinf. Plast. Compos.*, vol. 27, no. 5, pp. 473–485, 2008.

[28] B. B. Johnsen, K. Olafsen, A. Stori, and K. Vinje, "Silanization of adhesively bonded aluminum alloy AA6060 with γ-glycidoxypropyltrimethoxysilane. II. Stability in degrading environments," *J. Adhes. Sci. Technol.*, vol. 17, no. 9, pp. 1283–1298, 2003.

[29] A. Rattana, M.-L. Abel, and J. F. Watts, "Degradation of interfacial chemistry of epoxy/silane/aluminium interfaces as a result of aqueous attack," *J. Adhes.*, vol. 81, no. 9, pp. 963–988, 2005.

[30] D. H. Berry and A. Namkanisorn, "Fracture toughness of a silane coupled polymer-metal interface: Silane concentration effects," *J. Adhes.*, vol. 81, no. 3–4, pp. 347–370, 2005.

[31] M.-L. Abel, R. D. Allington, R. P. Digby, N. Porritt, S. J. Shaw, and J. F. Watts, "Understanding the relationship between silane application conditions, bond durability and locus of failure," *Int. J. Adhes. Adhes.*, vol. 26, no. 1, pp. 2–15, 2006.

[32] M. Sautrot*, M.-L. Abel, J. F. Watts, and J. Powell, "Incorporation of an adhesion promoter in a structural adhesive: aspects of durability and interface chemistry," *J. Adhes.*, vol. 81, no. 2, pp. 163–187, 2005.

[33] A. J. Kinloch, C. F. Korenberg, K. T. Tan, and J. F. Watts, "Crack growth in structural adhesive joints in aqueous environments," *J. Mater. Sci.*, vol. 42, no. 15, pp. 6353–6370, 2007.

[34] L. Ye, K. Friedrich, C. Weimer, and Y.-W. Mai, "Surface treatments and adhesion bonding between concrete and a CFRP composite," *Adv. Compos. Mater.*, vol. 7, no. 1, pp. 47–61, 1998.

[35] "ASTM C33/C33M, Standard Specification for Concrete Aggregates." ASTM International, West Conshohocken, PA, 2013.

[36] "ASTM C 192/C192M, Standard Practice for Making and Curing Concrete Test Specimens in the Laboratory." ASTM International, West Conshohocken, PA, 2014.

[37] "ASTM D3762-03, Standard Test Method for Adhesive-Bonded Surface Durability of Aluminum (Wedge Test)." ASTM International, West Conshohocken, PA, 2010.

[38] C. Zhang, “Mechanics and subcritical cracking of FRP-concrete interface.” The University of Alabama TUSCALOOSA, 2011.

[39] Z. Ouyang and B. Wan, “Modeling of moisture diffusion in FRP strengthened concrete specimens,” *J. Compos. Constr.*, vol. 12, no. 4, pp. 425–434, 2008.

[40] C.-H. Shen and G. S. Springer, “Moisture absorption and desorption of composite materials,” *J. Compos. Mater.*, vol. 10, no. 1, pp. 2–20, 1976.

[41] H. N. Linsbauer and E. K. Tschegg, “Fracture energy determination of concrete with cube-shaped specimens,” *Zement und Bet.*, vol. 31, pp. 38–40, 1986.

[42] E. Brühwiler and F. H. Wittmann, “The wedge splitting test, a new method of performing stable fracture mechanics tests,” *Eng. Fract. Mech.*, vol. 35, no. 1, pp. 117–125, 1990.

[43] E. Denarie, V. E. Saouma, A. Iocco, and D. Varelas, “Concrete fracture process zone characterization with fiber optics,” *J. Eng. Mech.*, vol. 127, no. 5, pp. 494–502, 2001.

[44] J. Skoček and H. Stang, “Inverse analysis of the wedge-splitting test,” *Eng. Fract. Mech.*, vol. 75, no. 10, pp. 3173–3188, 2008.

[45] J. Skoček and H. Stang, “Application of optical deformation analysis system on wedge splitting test and its inverse analysis,” *Mater. Struct.*, vol. 43, no. 1, pp. 63–72, 2010.

[46] S. Zeng, “Synthesis and characterization of geopolymers using locally available fly ashes,” The University of Alabama, 2014.

[47] “ASTM:C39/C39M-15a, Standard Test Method for Compressive Strength of Cylindrical Concrete Specimens,” *ASTM International*. ASTM International, West Conshohocken, PA, pp. 1–7, 2015.

[48] S. AMIDI and J. WANG, “Engineering FRP-to-Concrete Bonded Joints for Better Durability,” in *Proceedings of the American Society for Composites 2014-Twenty-ninth Technical Conference on Composite Materials*, 2014.

[49] A. K. Dastjerdi, E. Tan, and F. Barthelat, “Direct measurement of the Cohesive Law of adhesives using a rigid double cantilever beam technique,” *Exp. Mech.*, vol. 53, no. 9, pp. 1763–1772, 2013.

[50] C. Pedersen, *New production processes, materials and calculation techniques for fiber reinforced concrete pipes*. Technical University of Denmark, Department of Structural Engineering and Materials, 1996.

[51] P. Casanova and P. Rossi, “Analysis and design of steel fiber reinforced concrete beams,” *ACI Struct. J.*, vol. 94, no. 5, 1997.

[52] Q. D. Yang and M. D. Thouless, “Mixed-mode fracture analyses of plastically-deforming adhesive joints,” *Int. J. Fract.*, vol. 110, no. 2, pp. 175–187, 2001.

CHAPTER 7

DIRECT MEASUREMENT OF TRACTION-SEPARATION LAW OF CONCRETE/EPOXY INTERFACES SUBJECTED TO MOISTURE ATTACK UNDER MODE-I LOADING

Abstract

Cohesive zone model (CZM) has been commonly used to simulate the failure process of the fiber reinforced polymers (FRPs)-to-concrete bonded joints, which plays a critical role in the success of external bonding of FRPs to reinforced concretes for strengthening/retrofitting. In the CZM method, a proper traction-separation law based on the physical behaviors of the material must be provided. However, no method is available to measure the traction-separation law of the concrete/epoxy interface under mode-I loading. To address this gap, this study proposes a novel testing method to directly measure the traction-separation law of the concrete/epoxy interface. This method uses a wedge splitting test specimen which requires not only simple testing set-ups, but also produces stable crack propagation in the specimen. By adopting a rigid body moment assumption, the traction in the concrete/epoxy interface is expressed as a function of the applied load and the crack opening displacement. As a result, this method can directly calculate the relationship between the traction and the separation of the concrete/epoxy interface through simply recording the crack opening displacement and the applied load during the test. The success of the new method has been confirmed through experimental study. Testing results show the traction-separation law of the concrete/epoxy concrete under mode-I loading can be approximated by a tri-linear law. The new method is also used to evaluate the long-term

durability of concrete/epoxy interface subjected to moisture attack. It has been found that the conditioning the interface specimens in water can significantly reduce the tensile strength and fracture toughness of the interface. The effectiveness of applying silane coupling agent to enhance the durability of the concrete/epoxy interface has also been confirmed by this new testing method.

7.1. Introduction

There is a world-wide need to rehabilitate and improve civil infrastructures. To this end, new construction materials and methods are being intensely investigated to alleviate current problems and provide better and more reliable future services. ASCE 2013 Report Card for America's Infrastructure estimates the U.S. would need to spend $3.6 trillion on aging infrastructures by 2020 [1]. This national need presents a unique opportunity for research, implementation and development of advanced materials such as fiber reinforced polymers (FRPs) that can provide longer service-life and lower life-cycle costs than conventional materials alone. One of the most popular applications of FRPs in civil engineering, particularly in civil infrastructures, is external bonding of FRP plates or sheets for strengthening and rehabilitation of aging and damaged concrete structures [2].

The interface between the FRP and conventional materials plays a critical role in this strengthening method by providing effective stress transfer from the existing structures to externally bonded FRP plates or sheets and keeping integrity and durability of the composite performance of FRP strengthened concrete structures. The sudden loss of bond due to delamination of the FRP from the substrate concrete can lead to premature failure of the structure. A sound understanding of FRP-to-concrete bond behavior is needed for safe and economic design of externally bonded FRP systems. It has been demonstrated that the relative

deformation between FRP and concrete and the debonding of the bond mainly happens within a thin layer of adhesive and the adjacent concrete in FRP-to-concrete bond, which is referred to as "concrete/epoxy interface" in this study [3]. In order to determine the ultimate load transfer capacity and effective bond length of FRP external bonding, the integrity and durability of this interface must be obtained.

Due to the existence of stress singularity, fracture mechanics was chosen by many researchers as a suitable approach to characterize the behavior of the concrete/epoxy interface. Extensive studies have been carried out by using linear elastic fracture mechanics (LEFM) model [4,5] and nonlinear fracture mechanics models [6–17] to study the concrete/epoxy interface. The latter fracture model is also known as cohesive zone model (CZM) [10] in which a nonlinear traction-separation constitutive law of the interface is used. The nonlinear traction-separation law of the interface is also referred to as bond slip-stress law. This may be due to the fact that all the cohesive zone model developed so far for the FRP-to-concrete bonds are only limited to mode-II loading [8–11,13,18].

CZM pioneered by Dugdale [19] and Barenblatt [20], is gaining more and more attentions and popularities nowadays in modeling fracture process with large-scale fracture process zone. In CZM, the locally damaged materials forming a narrow band of localized deformation may be modeled by nonlinear springs which represent the major physical variables. Compared with the single-parameter fracture approach of LEFM, which ignores the microscopic details and discloses little what happens within the damage zone, the CZM takes the behavior of fracture processing zone into consideration and provides a way to examine the "inner problem" of understanding, characterizing and modeling the failure processes that actually lead to energy dissipation. What is more, the CZM unifies the crack initiation and growth into one model and

can be easily formulated and implemented in numerical simulation, such as the "interface element" method in finite element code [21].

The very first step of CZM procedures is to determine the traction-separation law within the cohesive zone. Usually, a hypothesized and idealized function is assumed for the traction-separation law of a cohesive zone, and the cohesive zone parameters are then determined by fitting the presumed cohesive zone model to a set of experiment data. In this sense, they may only be called "cohesive zone model" rather than "cohesive law or constitutive equation" [22]. To realize the benefit of CZM in modeling and design of FRP-strengthened structures, it is necessary to experimentally characterize the cohesive zone of the FRP-to-concrete interface.

The traction-separation law of the concrete/epoxy under mode-II loading has been studied extensively. Typically, a single lap-shear test is used in the literature [6,18] to study this law. In this test, strain gauges are instrumented on the outer surface of FRP strip so that the strain distribution of the FRP can be measured. The shear stress distribution along the concrete/epoxy interface is then calculated by the measured strain gradient of the FRP plate multiplied by the Young's modulus and thickness of the FRP [18]. This method can provide a relatively approximate measurement of the traction-separation law of the interface under mode-II loading due to the severe strain concentration near the crack tip. This method was improved by Dai et al. [23]. By assuming that a unique relationship exists between the FRP strain ε and slip δ. Dai et al. found that the bond slip-stress law of the interface can be directly obtained as the pulling force in the FRP plate multiplied by the derivative of the strain in the FRP plate with respect to the slip at the crack tip. This method avoids the difficulty and error in measuring the strain gradient in the FRP plate. The soundness of Dai et al.'s method was confirmed in theory by Wang [13], which demonstrated that Dai et al. method is essentially a special case of a more general method, the J-

integral method [24,25]. According to J-integral method, the bond stress can be calculated as the derivative of J-integral (which is equal to the energy release rate at the crack tip) with respect to the separation of the interface at the crack tip. However, as pointed out by Achintha and Burgoyne [26], "these tests do not provide meaningful fracture parameters that can be used in the analysis because the tests provide an estimate of Mode-II fracture energy whereas a Mode-I fracture triggers debonding."

A few methods to determine the fracture toughness of the concrete/epoxy interface under mode-I loading are available, including modified double cantilever beam method [4,5] and modified three-point bend test method [27]. None of these methods can produce the traction-separation law of the concrete/epoxy interface under mode-I loading. To address this gap in the literature, this study presents a simple method to directly measure the traction-separation law of the concrete/epoxy interface under mode-I loading using a wedge splitting test (WST).

The long-term behaviors of the concrete/epoxy interface subjected to aggressive environments threats such as moisture and water invasion have become the focus of recent studies [5,28–30]. Experimental studies shows that exposure to moisture for a long time is the foremost factor that can degrade the interface. Substantial loss of the fracture toughness of the interface induced by moisture was observed. More importantly, Au and Büyüköztürk [5] found that the debonding locus shifts from within the concrete cover in its dry state to along the adhesive-concrete interface in its wet state. This change of failure mode was confirmed by Ouyang and Wan [31].

In this study, the proposed new testing method will be used to evaluate the effect of water invasion on the concrete/epoxy interface. To this end, the traction-separation laws of the concrete/epoxy interface before and after conditioning in water will be determined by WST.

Organofunctional silane coupling agents (SiH_4) for many years have been proved to be useful to enhance the bond between an organic material such as epoxy and inorganic materials such as metal, particularly bond between epoxy and aluminum [32–35]. Also, some promising results by adding silane bonding agent between concrete and epoxy have been reported [36,37]. In this study the role of silane bonding agent in improving the fracture toughness of the bond will also be investigated by the proposed method.

7.2. Materials and testing

7.2.1. Wedge splitting test

The wedge splitting test (WST) technique was proposed by Linsbauer and Tschegg [38]. Later Brühwiler and Wittmann used it to create stable crack propagation in concrete specimens [39]. This technique has become popular recently and been used in many studies [40–42]. WST is chosen in this study because of its advantages over other popular fracture testing methods. Firstly, the testing set up for WST is very simple. Secondly, the specimen is easy to fabricate and therefore, even can be done on-site or drilled from the structure. Lastly and most importantly, the crack propagation in this specimen is stable, which eliminates the difficult task to control the crack growth in the other existing methods such as three-point bending test [27].

The WST specimen consists of three parts: two identical concrete blocks, and a thin layer of cured epoxy bonding these two concrete blocks together, as shown in Fig. 7-1. The concrete blocks have a size of 25.4 mm in thickness and 70mm in height and 75 mm in length. A rectangular piece with size of 15 mm × 24.2 mm is cut from one corner of the block, as shown in Fig. 7-1. The concrete blocks were made of ordinary Portland cement (OPC) and fine sands, cast and cured according to ASTM C33/C33M [43] and ASTM C192/C192M [44]. According to ASTM C39 [45] the 28-day compressive strength of concrete was measured as 28 MPa using 100 x 200 mm cylinder samples. The bonding side of each concrete block was sandblasted to

provide suitable rough surface, and then cleaned by high pressure air, and finally, wiped with a wet cloth. Before applying the epoxy layer, a pre-crack band with length of 15.9mm is designated at the top of the specimens. Tyfo TC epoxy was then used to bond two concrete blocks together and cured for two weeks, as shown in Fig. 7-1. For properly bonded FRP-to-concrete joints, debonding is unlikely to occur along the interface between the FRP and the adhesive layer. Therefore, no FRP sheet was used in the specimen shown in Fig. 7-1.

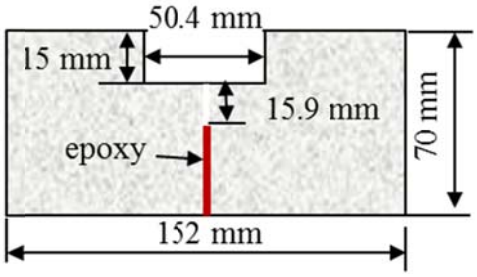

Fig. 7-1 Geometry of the wedge splitting test specimen.

A commercially available silane coupling agent based on γ-glycidoxypropyltrimethoxysilane (γ-GPS) was used in this study to enhance the durability between the adhesive and the concrete. Ye et al [36] showed that applying 1% aqueous solution of silane coupling agent on concrete surfaces can enhance the bonding strength between the adhesive and concrete. A study on adhesively bonded aluminum alloy joints shows that treating the alloy by silane coupling agent with a concentration of 1% at pH 5 and hydrolysis for 1 hour prior to application, can most effectively enhance the durability of the interface [33]. Therefore, 1% silane solution (aqueous) was prepared. After hydrolysis for 1 hour in room temperature, the silane solution was continuously brushed onto the bonding surface of the concrete block for 10 minutes. The treated concrete blocks were then immediately dried in a preheated oven at 93 °C for one hour. Then the dried blocks were removed from the oven and cooled down to ambient

temperature in the laboratory. The treated concrete blocks were then used to manufacture WST specimens in the similar way described before.

The testing set-up for the WST is shown in Fig. 7-2(a). The specimen is placed on a roller support mounted on a MTS machine. A steel wedge with two identical parallel plates is fixed at the top of the specimen to transfer the vertical force P_v applied by the MTS machine to two parallel roller supports at the top of the pre-crack region (Fig. 7-2(b)). A splitting force P_{sp} which is the horizontal component of the forces acting on the specimen P_N and friction force μP_N can be generated to drive two rollers apart (Fig. 7-2(b)), leading to a mode-I fracture in the specimen.

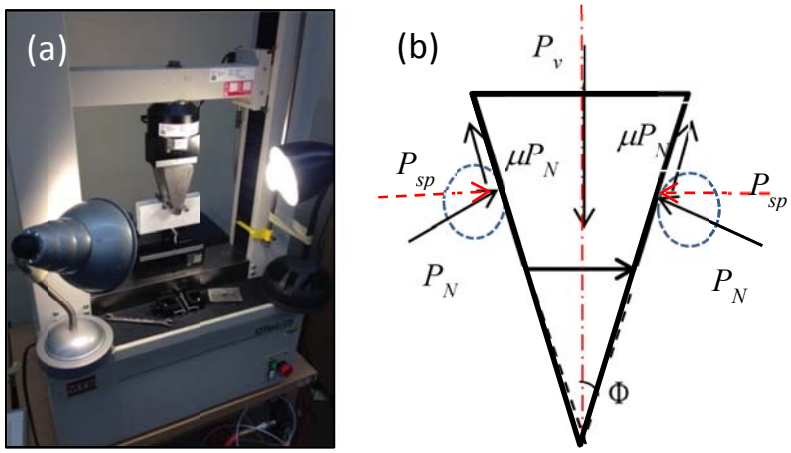

Fig. 7-2 Wedge splitting test: (a) Testing set-up, (b) Free-body diagram of the wedge.

The testing could be displacement controlled, or crack opening displacement (COD) controlled (an additional clip gauge for crack mouth opening displacement measurement is needed). Brühwiler and Wittamann [39] showed that when the following condition is met, the WST is stable under the displacement control

$$l_{ch} > K \cdot L \cdot \left(k_p/k_M + 1\right), \quad (1)$$

where l_{ch} is the characteristic length of the material, k_p and k_M are the stiffness of the specimen and the loading machine; K is the constant depending on the specimen geometry; and L is the

cantilever length of the wedge splitting specimen. Brühwiler and Wittmann [39] showed that stable fracture can be performed on all materials, except the "completely brittle one".

7.2.2. Crack opening displacement (COD) measurement using DIC

A robust full-field measurement method, Digital Imagine Correlation (DIC) method is used to directly measure the crack opening of the specimen. DIC is a full-field deformation measurement technique that extracts the full-field displacement data by comparing a pair of digital images of a specimen surface before and after deformation. In this method, image of the body could be represented by a discrete function: value between 0 and 255 of its grey levels. In order to correlate the intensity distribution of the deformed image to the un-deformed image, the images are divided into small subsets called pattern (see the initial pattern ABCD in Fig. 7-3). The displacement field is assumed homogeneous inside each pattern. A discrete function $f(x,y)$ is used to represent the initial image of the body before deformation, which is transformed in another discrete function $f^*(x^*,y^*)$ after deformation, as shown in Fig. 7-3. Then the cross correlation coefficient can be calculated as

$$C = 1 - \frac{\Sigma[f(x,y)\cdot f^*(x^*,y^*)]}{[\Sigma[f^2(x,y)\cdot f^{*2}(x^*,y^*)]]^{1/2}}. \quad (2)$$

By minimizing the correlation function over a subset image region, in-plane displacements, u and v, and the displacement gradients, du/dx, du/dy, dv/dx, and dv/dy are determined, which are in turn used for further analysis.

With DIC, the whole displacement field of the specimen can be obtained, from which the difference in horizontal displacement of any arbitrary point can be calculated. If two points are chosen on the crack surface, then the difference in their horizontal displacements gives the separation (COD) at these two points.

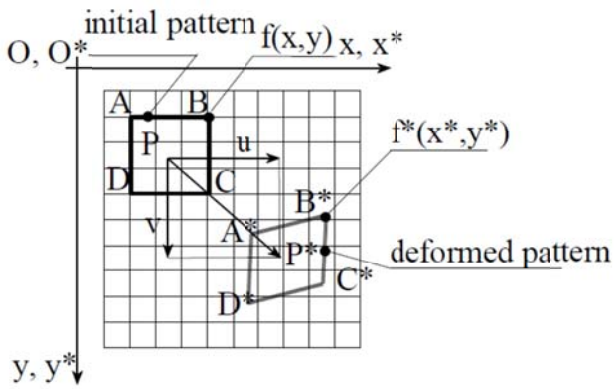

Fig. 7-3 Pattern, displacements, and discrete functions used in DIC.

7.2.3. Testing plan

Wedge splitting test specimens were first conditioned in water tank at room temperature (23°C) for 4, 8 and 16 weeks before testing. In addition to the untreated specimens, specimens treated with silane coupling agent were also conditioned in water and then tested to evaluate the role of covalent bonds provided by silane in improving the resistance to water invasion of the concrete/epoxy interface. As a reference, a control group of specimens were conditioned in the ambient environment (with temperature (23°C) and relative humidity level of 50%). Four duplicated specimens were used for each test. The data reported in this study are average of these duplicated specimens.

7.2.4. Direct measurement of the traction-separation law and fracture toughness under mode-I loading

Inspired by the rigid double cantilever beam technique used for adhesive by Dastjerdi et al [46] a new direct measurement method of the traction-separation law of the concrete/epoxy interface using WST is proposed. Since concrete block is much stiffer than the adhesive layer, it has been commonly assumed that the most deformation of the FRP-to-concrete bonded joints occurs within the adhesive layer and the interface. Similarly, we can assume that the major deformation is within the adhesive layer and the interface in this WST specimen. Then the

movement of the left and right concrete blocks of the specimen can be approximated as rotating about the symmetric axis like rigid bodies during testing, as shown in Fig. 7-4. In such a case, we can assume that crack opening *w(y)* at position *y* (Fig. 7-4) can be expressed by a linear function as

$$w(y) = \frac{\delta}{h} y, \tag{3}$$

where δ is the COD at the mouth of the crack, and h is the crack length. Dastjerdi et al. [46] have confirmed through theoretical analysis that such a rigid body assumption of the specimen is reasonable for short and stiff beam, which is the case of the WST specimen used here.

Since each half of the specimen can rotate about the vertical symmetric axis as a rigid body, its free-body diagram can be presented as shown in Fig. 7-4. In this figure, the peel stress within the interface is presented by $\sigma(w(y))$, which is a function of the separation of *w(y)* of the interface. The equilibrium condition of the wedge in the vertical direction shown in Fig. 7-2(b) gives

$$\eta P_N \cos\Theta + P_N \sin\Phi = \frac{P_v}{2}, \tag{4}$$

where η is the friction constant between the roller and the wedge, P_N is the reaction force from the roller to the wedge. Considering the equilibrium condition of the roller shown in Fig. 7-2(b) in the horizontal direction, we can obtain the splitting force P_{SP} applied by the wedge to the specimen as

$$P_{sp} = P_N \cos\Phi - \eta P_N \sin\Phi. \tag{5}$$

Therefore,

$$P_{sp} = \frac{1-\eta\tan\Phi}{2(\eta+\tan\Phi)} P_v, \tag{6}$$

where η (= 0.2) is the friction constant between the roller and the steel wedge; ϕ is a the angle of the steel wedge shown in Fig. 7-2(b).

Considering the moment equilibrium of the specimen about the right bottom corner of the half-specimen shown in Fig. 7-4, we have

$$t\int_0^h \sigma(w(\mathrm{y}))ydy = P_{sp}d_2 + \frac{1}{2}P_v d_1 + \frac{1}{2}mge, \tag{7}$$

where d_1 and d_2 are the lever arms of force P_v and P_{sp} as shown in Fig. 7-4, respectively; mg is the self-weight of the concrete block; and e is the distance of the center of gravity of the half specimen to the symmetric axis, as shown Fig. 7-4.

Considering Eq. (3), Eq. (7) can be rewritten as

$$\int_0^\delta \sigma(w)wdw = \frac{1}{t}\left(\frac{\delta}{h}\right)^2\left(P_{sp}d_2 + \frac{1}{2}P_v d_1 + \frac{1}{2}\,mge\right). \tag{8}$$

Taking derivatives on both sides of Eq. (8) with respect to δ yields

$$\sigma(\delta) = \frac{2}{h^2 t}\left(P_{sp}d_2 + \frac{1}{2}P_v d_1 + \frac{1}{2}mge\right) + \frac{\delta}{h^2 t}\left(d_2\frac{dP_{sp}}{d\delta} + \frac{d_1}{2}\frac{dP_v}{d\delta}\right). \tag{9}$$

Equation (9) directly gives the relationship between the separation δ and the traction (stress) σ of the epoxy-concrete interface. It requires neither a pre-assumed shape for the traction-separation curve, nor any complicated inverse analysis. By measuring the COD and the applied load, the traction-separation law for epoxy-concrete interface under mode-I can be directly calculated using Eq. (9). The total fracture energy of the epoxy-concrete interface under mode-I loading can then be calculated from the traction- separation law as

$$G_I = \int_0^\delta \sigma(\delta)d\delta. \tag{10}$$

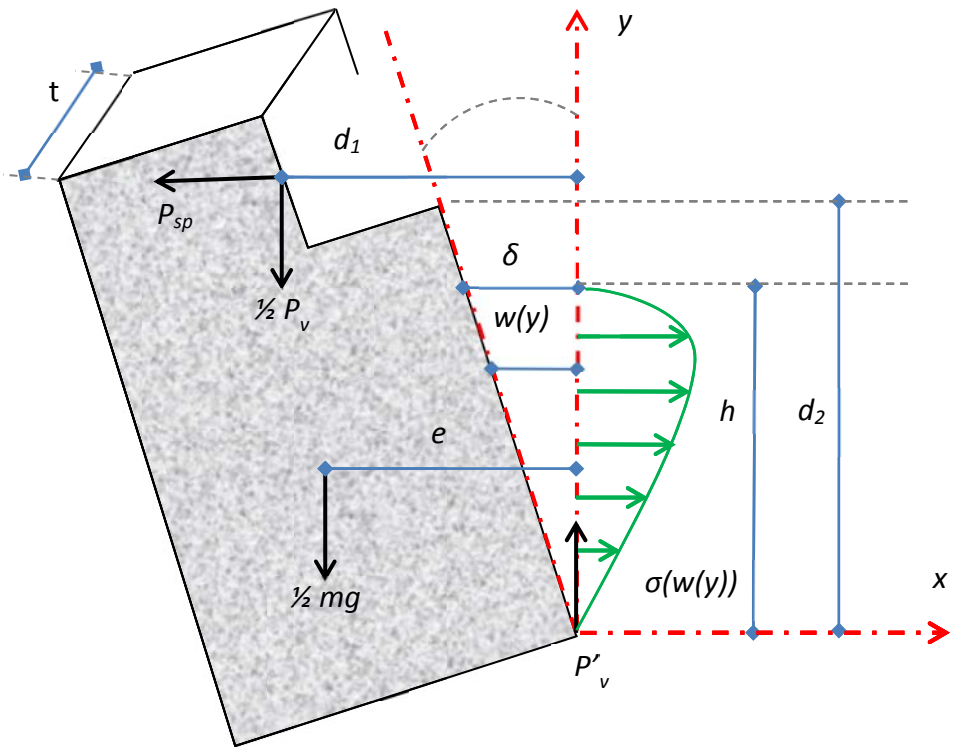

Fig. 7-4 Free-body diagram of the half specimen.

Wedge splitting testing was conducted with a MTS machine under displacement control at the rate of 0.13 mm/min to load specimens as shown in Fig. 7-2(a). The DIC system was used to take pictures of the specimens every 15 seconds. Images captured during the test were used to derive δ by simply reading the difference between displacements of two predetermined points at each half-specimen adjacent to the tip of the pre-crack.

Figure 7-5 shows a typical result of the measured splitting force P_{sp} versus COD δ for a WST specimen conditioned in water for 16 weeks. It can be seen that P_{sp} increases with COD initially. After reaching a peak value, it starts to drop with COD. In order to extract the traction-separation law, the measured P_{sp}-COD curve was first smoothened to make it possible to calculate the derivative of P_{sp} with respect to COD in Eq. (9), as shown by the red line in Fig. 7-5. Based on the smoothened P_{sp}-COD curve, the traction (σ)-separation (δ) law of the

concrete/epoxy interface under mode-I loading can be obtained using Eq. (9). A typical result of such traction-separation law is shown in Fig. 7-6 for a specimen conditioned in water for eight weeks. It can be seen that the traction within the interface appears to increase with the separation initially. After reaching its maximum, the traction starts to drop with the separation, as shown in Fig. 7-6. This traction-separation law can be approximated by a tri-linear traction-separation law shown in Figs. 7-6 and 7-7. This law consists of three segments: an linearly increasing segment before the traction reaches its maximum representing a linear behavior of the bond before debonding initiation, a rapid declining segment after the traction reaches its maximum representing a softening processing due to damage developing quickly in the concrete/epoxy interface, and a slow softening segment after the rapid one representing the residual strength of the interface induced by the mechanical interlock of the debonded interface.

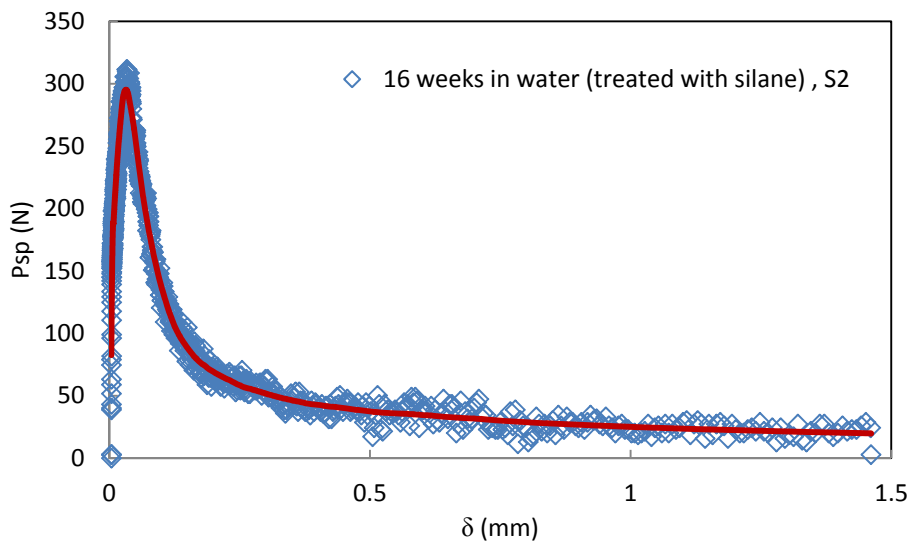

Fig. 7-5 Splitting load versus COD measured at the crack mouth (δ) for a specimen conditioned in water for 16 weeks.

The tri-linear traction-separation law can be described by

$$\sigma(\delta) = B_i - A_i\delta = \begin{cases} A_1\delta \\ B_2 - A_2\delta \\ B_3 - A_3\delta \end{cases} = ft * g(\delta), \tag{11}$$

where f_t is the maximum tensile strength (traction) applied perpendicular to the interface; A_i and B_i are coefficients of three lines used in this method. $g(\delta)$ is the softening function of the interface and can be written as

$$g(\delta) = \begin{cases} a_1\delta \\ b_2 - a_2\delta. \\ b_3 - a_3\delta \end{cases} \tag{12}$$

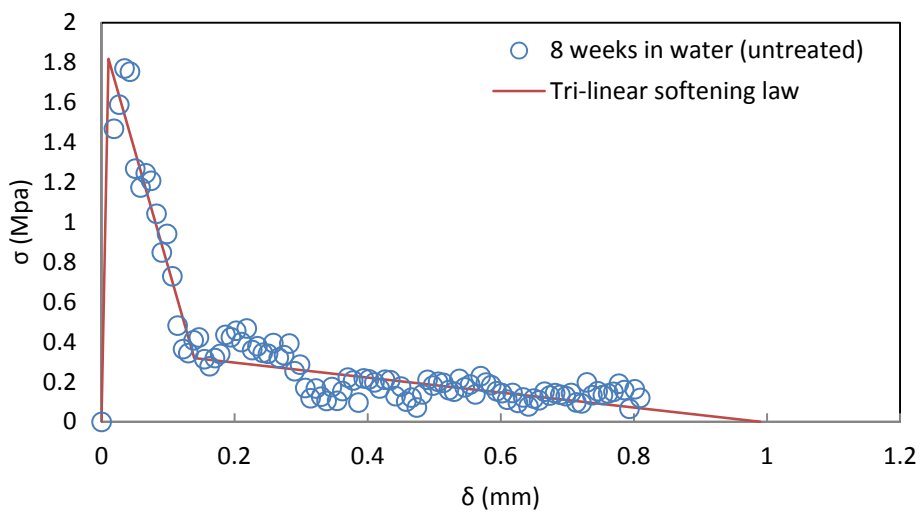

Fig. 7-6 Measured traction- separation law of the epoxy-concrete interface under mode-I for a specimen conditioned in water for 8 weeks.

The softening function and the coefficients used in its definition are shown in Fig. 7-7. The parameters used in this tri-linear law were obtained through fitting the measured traction-separation law and presented Table 7-1. All parameters are scaled in term of f_t. The resulted tri-linear traction-separation laws normalized by f_t are also shown in Fig. 7-8. As shown in Table 7-1 and Fig. 7-8, the control specimen exhibits much higher maximum tensile traction than the conditioned specimens, confirming that water ingress through the concrete/epoxy interface can

greatly reduce the strength of the interface. Silane coupling agent can improve the bond quality by forming a covalent bond of Si-O-Si between the epoxy and the concrete [36].

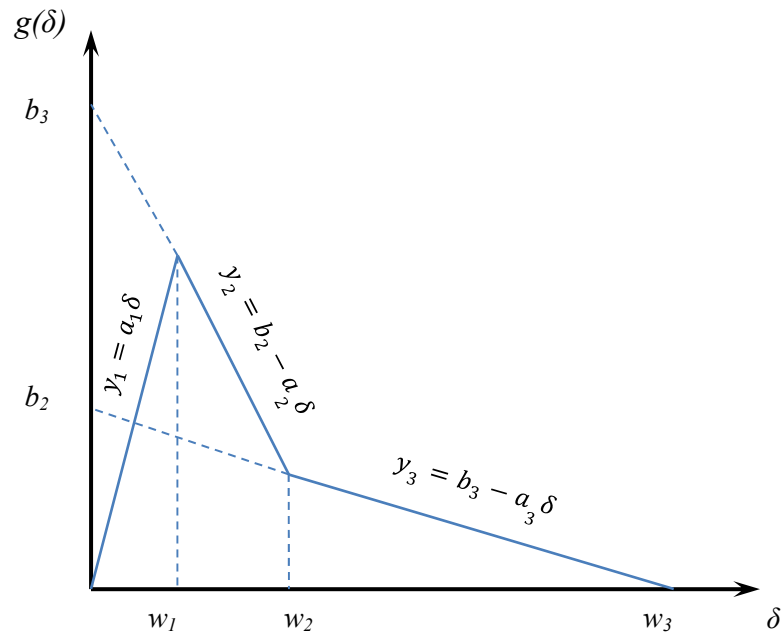

Fig. 7-7 Tri-linear traction-separation model for the concrete/epoxy interface under mode-I loading.

Table 7-1Tri-linear traction-separation law parameters.

Parameters	Control	4 week in water		8 week in water		16 week in water	
		untreated	treated with silane	untreated	treated with silane	untreated	treated with silane
f_t (Mpa)	7.71	1.99	2.69	1.88	3.05	1.85	2.96
a_1	233.76	60.27	125.70	51.11	65.41	56.82	39.04
a_2	17.25	9.18	24.71	6.31	14.45	14.25	12.31
b_2	1.07	1.15	1.62	1.12	1.22	1.25	1.32
a_3	0.32	0.76	0.69	0.29	0.25	0.51	0.44
b_3	0.22	0.35	0.44	0.23	0.23	0.27	0.27
w_1(mm)	0.004	0.017	0.011	0.020	0.015	0.018	0.026
w_2(mm)	0.050	0.095	0.049	0.148	0.070	0.071	0.088
w_3(mm)	0.684	0.464	0.633	0.787	0.923	0.534	0.620

As shown in Table 7-1 and Fig. 7-8(b), the f_t of the specimen treated by silane is up to 35% to 50% higher than that of the specimens without silane treatment after conditioned in water with the same duration. A comparison at the beginning segment of the traction-separation law shows that conditioning in water can significantly reduce the initial stiffness of the bond, making it remarkably softer in comparison with the control specimens, as shown in Fig. 7-8(c). This is exacerbated when longer conditioning duration is used. Silane coupling agent treatment can slightly improve the stiffness of the interface after short-term conditioning in water, as shown in Fig. 7-8(b).

Using Eq. Fig. 7-10, the mode-I fracture toughness for each group can be obtained and presented in Fig. 7-9. After conditioning in water for 4 weeks, the mode-I fracture toughness of all untreated specimens have been decreased remarkably compared to the control ones. It can be observed that no significant reduction in fracture toughness can be observed for 8 and 16 weeks conditioning, suggesting that four weeks conditioning is sufficient to introduce maximum deterioration to the interface by water. Figure 7-9 shows that silane coupling agent cannot prevent loss of the fracture toughness of the concrete/epoxy interface after conditioning in water. Nevertheless, silane does improve the durability of the interface as indicated by higher residual fracture toughness of the interface after conditioning in water achieved by the specimens treated with silane.

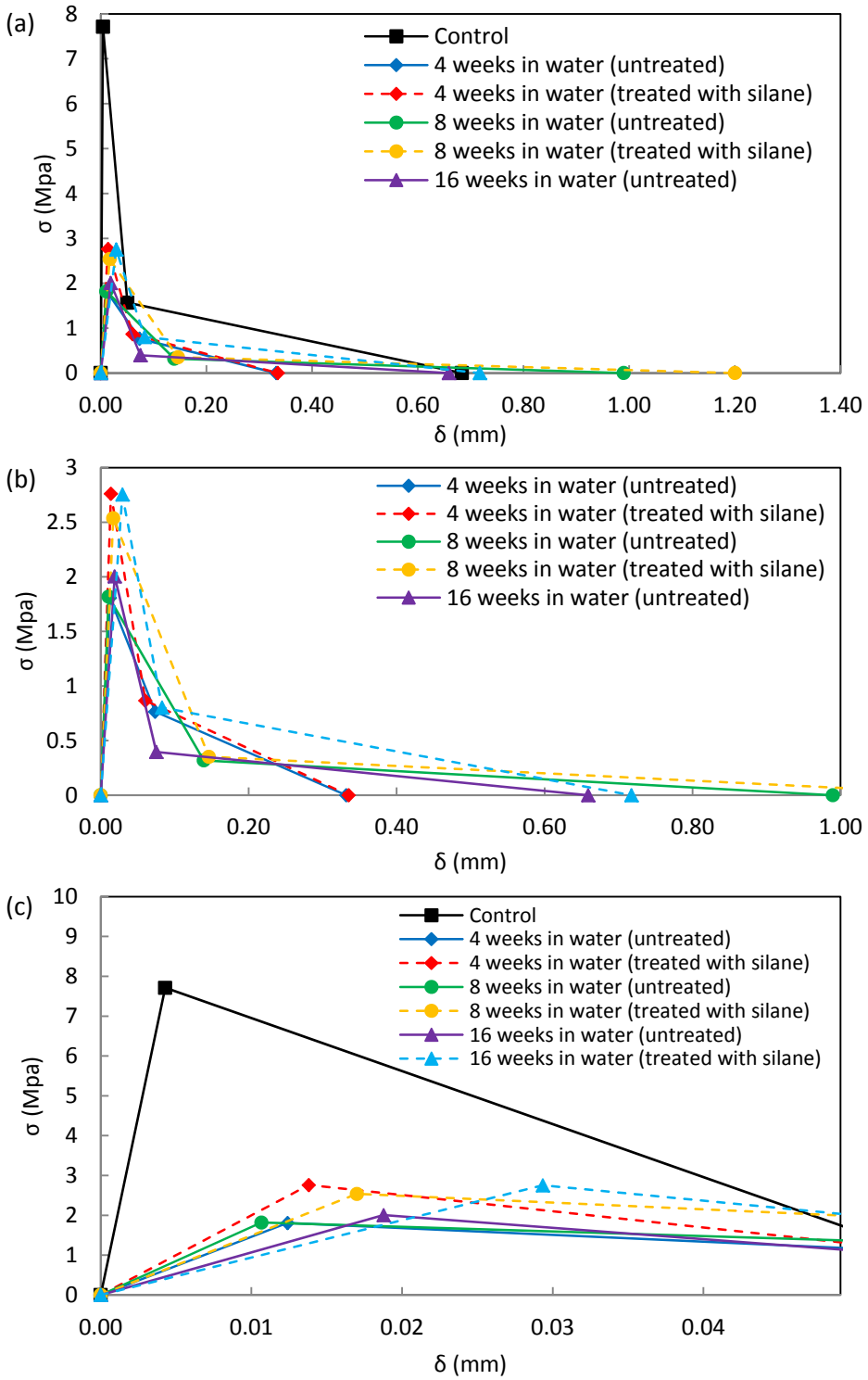

Fig. 7-8 Tri-linear traction-separation laws measured for concrete/epoxy interface after conditioning in water: (a) effect of conditioning in water on the traction-separation law, (b) effect of silane on the traction-separation law of the interface after conditioning in water, (c) effect of water conditioning on the stiffness of the concrete/epoxy interface .

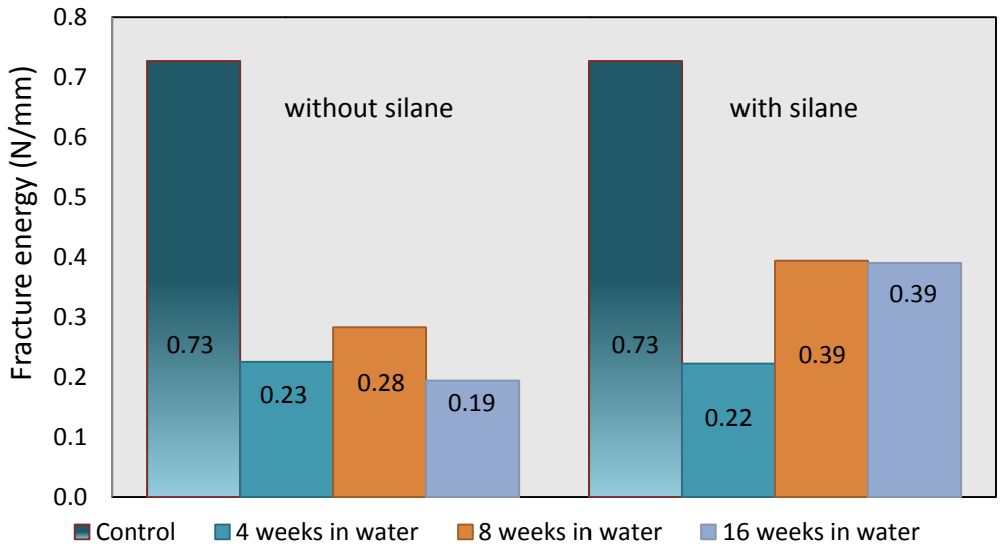

Fig. 7-9 Effect of duration of water conditioning on the fracture energy of the concrete/epoxy interface with and without silane coupling agent.

The effect of silane treatment can be further confirmed by studying the failure mode of the specimens shown in Fig. 7-10. In this figure, the epoxy sides of the split specimens are shown. Fig. 7-10(a) shows that the epoxy side of the control specimen is covered by a layer of concrete, suggesting the debonding is cohesive and occurred within the concrete layer. While the specimen conditioned in water for 4 weeks exhibits an almost adhesive failure, as shown in Fig. 7-10(b). By applying silane bonding agent, significant amount of concrete particles are attached to the epoxy surface, exhibiting a mixed adhesive/cohesive mode. Obviously, this difference in failure mode and fracture toughness is induced by silane coupling agent.

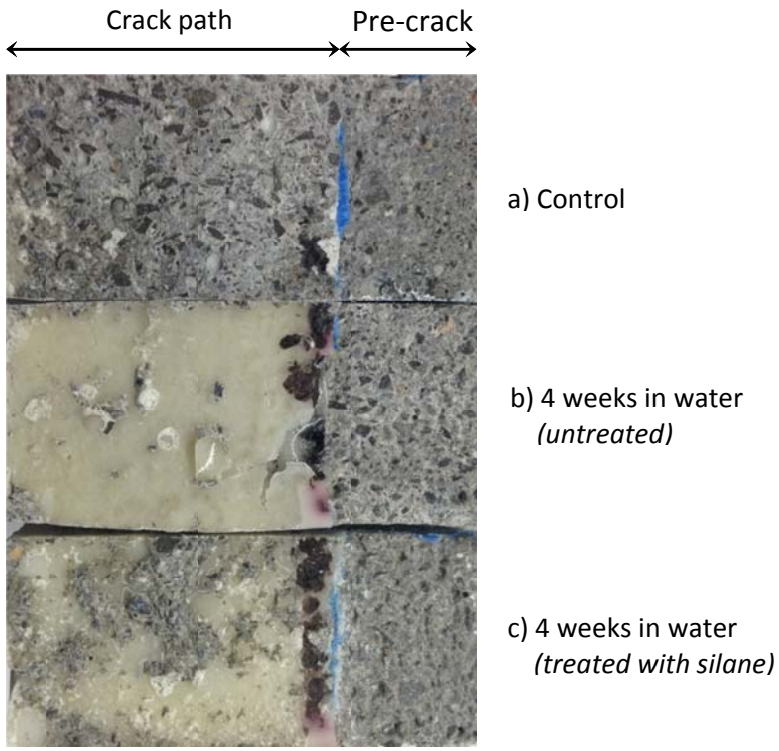

Fig. 7-10 Debonded epoxy sides of wedge splitting test specimens.

7.3. Conclusions

In this study, a novel testing method using WST specimen is proposed to directly measure the traction-separation law of the concrete/epoxy interface under mode-I loading. This new method is then used to evaluate the long-term durability of the concrete/epoxy interface subjected to moisture attack. Experimental study suggests that the traction-separation law of the concrete/epoxy interface under mode-I loading can be conveniently obtained using this new method. The traction-separation law of the concrete/epoxy interface under mode-I loading can be approximated by tri-linear laws. Conditioning the specimens in water can significantly reduce the tensile strength and fracture toughness of the interface. By applying saline coupling agent, the residual strength and fracture toughness of the concrete/epoxy interface after conditioning in water are higher than that of the specimens without silane treatment, suggesting that the silane

coupling agent is effective to improve the long-term durability of the concrete/epoxy interface subjected to moisture attack.

7.4. References

[1] Herrmann AW. ASCE 2013 Report Card for America's Infrastructure. IABSE Symp. Rep., vol. 99, International Association for Bridge and Structural Engineering; 2013, p. 9–10.

[2] Bakis CE, Ganjehlou A, Kachlakev DI, Schupack M, Balaguru PN, Gee DJ, et al. Guide for the design and construction of externally bonded FRP systems for strengthening concrete structures. Rep by ACI Comm 2002;440.

[3] Lu XZ, Teng JG, Ye LP, Jiang JJ. Bond-slip models for FRP sheet/plate-to-concrete interfaces. Proc. 2nd Int. Conf. Adv. Polym. Compos. Struct. Appl. Constr., Cambridge, England: Woodhead Publishing Limited; 2004, p. 152–61.

[4] Wan B, Sutton MA, Petrou MF, Harries KA, Li N. Investigation of bond between fiber reinforced polymer and concrete undergoing global mixed mode I/II loading. J Eng Mech 2004;130:1467–75.

[5] Au C, Büyüköztürk O. Peel and shear fracture characterization of debonding in FRP plated concrete affected by moisture. J Compos Constr 2006;10:35–47.

[6] Täljsten B. Strengthening of concrete prisms using the plate-bonding technique. Int J Fract 1996;82:253–66.

[7] TÄLJSTEN B. Strengthening of existing concrete structures with epoxy bonded plates of steel or fibre reinforced plastics. Lulea: Lulea University, 1994. 190p 1994.

[8] Täljsten B. Defining anchor lengths of steel and CFRP plates bonded to concrete. Int J Adhes Adhes 1997;17:319–27.

[9] Wu Z, Yuan H, Niu H. Stress transfer and fracture propagation in different kinds of adhesive joints. J Eng Mech 2002;128:562–73.

[10] Wang J. Cohesive zone model of intermediate crack-induced debonding of FRP-plated concrete beam. Int J Solids Struct 2006;43:6630–48.

[11] Wang J. Debonding of FRP-plated reinforced concrete beam, a bond-slip analysis. I. Theoretical formulation. Int J Solids Struct 2006;43:6649–64.

[12] Wang J. Cohesive zone model of FRP-concrete interface debonding under mixed-mode loading. Int J Solids Struct 2007;44:6551–68.

[13] Wang J. Cohesive-bridging zone model of FRP–concrete interface debonding. Eng Fract Mech 2007;74:2643–58.

[14] De Lorenzis L, Zavarise G. Cohesive zone modeling of interfacial stresses in plated beams. Int J Solids Struct 2009;46:4181–91.

[15] Rabinovitch O. Debonding analysis of fiber-reinforced-polymer strengthened beams: Cohesive zone modeling versus a linear elastic fracture mechanics approach. Eng Fract Mech 2008;75:2842–59.

[16] Xu R, Liu C. CZM-based debonding simulation of cracked beams strengthened by FRP sheets. J Eng Mech 2012.

[17] Cornetti P, Corrado M, De Lorenzis L, Carpinteri A. An analytical cohesive crack modeling approach to the edge debonding failure of FRP-plated beams. Int J Solids Struct 2015;53:92–106.

[18] Bizindavyi L, Neale KW. Transfer lengths and bond strengths for composites bonded to concrete. J Compos Constr 1999;3:153–60.

[19] Dugdale DS. Yielding of steel sheets containing slits. J Mech Phys Solids 1960;8:100–4.

[20] Barenblatt GI. The mathematical theory of equilibrium cracks in brittle fracture. Adv Appl Mech 1962;7:55–129.

[21] Yan A-M, Marechal E, Nguyen-Dang H. A finite-element model of mixed-mode delamination in laminated composites with an R-curve effect. Compos Sci Technol 2001;61:1413–27.

[22] Chandra N, Li H, Shet C, Ghonem H. Some issues in the application of cohesive zone models for metal–ceramic interfaces. Int J Solids Struct 2002;39:2827–55.

[23] Dai J, Ueda T, Sato Y. Development of the nonlinear bond stress–slip model of fiber reinforced plastics sheet–concrete interfaces with a simple method. J Compos Constr 2005;9:52–62.

[24] Bao G, Suo Z. Remarks on crack-bridging concepts. Appl Mech Rev 1992;45:355–66.

[25] Sørensen BF, Jacobsen TK. Determination of cohesive laws by the J integral approach. Eng Fract Mech 2003;70:1841–58.

[26] Achintha M, Burgoyne C. Fracture energy of the concrete–FRP interface in strengthened beams. Eng Fract Mech 2013;110:38–51.

[27] Qiao P, Xu Y. Evaluation of fracture energy of composite-concrete bonded interfaces using three-point bend tests. J Compos Constr 2004;8:352–9.

[28] Grace NF, Grace M. Effect of repeated loading and long term humidity exposure on flexural response of CFRP strengthened concrete beams. Proc. Int. Symp. Bond. Behav. FRP Struct. (BBFS 2005), Chen Teng, 2005, p. 539–46.

[29] Porter ML, Harries K. Future directions for research in FRP composites in concrete construction. J Compos Constr 2007;11:252–7.

[30] Davalos JF, Kodkani SS, Ray I, Lin C. Fracture evaluation of GFRP—concrete interfaces for freeze—thaw and wet-dry cycling. J Compos Mater 2008;42:1439–66.

[31] Ouyang Z, Wan B. Modeling of moisture diffusion in FRP strengthened concrete specimens. J Compos Constr 2008;12:425–34.

[32] Johnsen BB, Olafsen K, Stori A, Vinje K. Silanization of adhesively bonded aluminum alloy AA6060 with γ-glycidoxypropyltrimethoxysilane. II. Stability in degrading environments. J Adhes Sci Technol 2003;17:1283–98.

[33] Abel M-L, Allington RD, Digby RP, Porritt N, Shaw SJ, Watts JF. Understanding the relationship between silane application conditions, bond durability and locus of failure. Int J Adhes Adhes 2006;26:2–15.

[34] Kinloch AJ, Korenberg CF, Tan KT, Watts JF. Crack growth in structural adhesive joints in aqueous environments. J Mater Sci 2007;42:6353–70.

[35] Shokoohi S, Arefazar A, Khosrokhavar R. Silane coupling agents in polymer-based reinforced composites: a review. J Reinf Plast Compos 2008;27:473–85.

[36] Ye L, Friedrich K, Weimer C, Mai Y-W. Surface treatments and adhesion bonding between concrete and a CFRP composite. Adv Compos Mater 1998;7:47–61.

[37] Amidi S, Wang J. Subcritical debonding of FRP-to-concrete bonded interface under synergistic effect of load, moisture, and temperature. Mech Mater 2016;92:80–93.

[38] Linsbauer HN, Tschegg EK. Fracture energy determination of concrete with cube-shaped specimens. Zement Und Bet 1986;31:38–40.

[39] Brühwiler E, Wittmann FH. The wedge splitting test, a new method of performing stable fracture mechanics tests. Eng Fract Mech 1990;35:117–25.

[40] Denarie E, Saouma VE, Iocco A, Varelas D. Concrete fracture process zone characterization with fiber optics. J Eng Mech 2001;127:494–502.

[41] Skoček J, Stang H. Inverse analysis of the wedge-splitting test. Eng Fract Mech 2008;75:3173–88.

[42] Skoček J, Stang H. Application of optical deformation analysis system on wedge splitting test and its inverse analysis. Mater Struct 2010;43:63–72.

[43] ASTM C33/C33M, Standard Specification for Concrete Aggregates 2013. doi:10.1520/C0033-03R06.

[44] ASTM C 192/C192M, Standard Practice for Making and Curing Concrete Test Specimens in the Laboratory 2014. doi:10.1520/C0192_C0192M.

[45] ASTM:C39/C39M-15a, Standard Test Method for Compressive Strength of Cylindrical Concrete Specimens. ASTM Int 2015:1–7. doi:10.1520/C0039.

[46] Dastjerdi AK, Tan E, Barthelat F. Direct measurement of the Cohesive Law of adhesives using a rigid double cantilever beam technique. Exp Mech 2013;53:1763–72.

CHAPTER 8

INTRINSIC DEBONDING OF FRP-TO-CONCRETE INTERFACE

Abstract

Fiber reinforced polymers (FRPs) have been used to retrofit/rehabilitate old and aging concrete structures through external bonding for decades. The FRP-to-concrete interface plays a critical role in the effectiveness of this external bonding technique. This integrity of this interface in harsh environments is still an issue of major concern. This study proposes a new method to evaluate the long-term durability of the FRP-to-concrete interface in the presence of water. To this end, fracture specimens were first conditioned and then tested by wedge driving method to determine the residual fracture toughness of the interface. Unlike any existing studies in which the whole specimen is submerged in water for conditioning, the specimen is conditioned in this study by submerging only half of the specimen in water. In this way, the moisture distribution across the epoxy-concrete interface is more uniform than that in the case of full submerging. In this way, the effect of non-uniform distribution of moisture across the epoxy-concrete interface can be minimized. A relationship between the residual fracture toughness and the interface relative humidity was established based testing data, which can be used to predict the deterioration of the interface induced by water. This relationship is different from the one obtained through full submerging, confirming that existing testing method is extrinsic and specimen dependent. The effectiveness of silane on enhancing the long-term durability of the interface has also been confirmed in this study.

8.1. Introduction

For many years fiber reinforced polymer (FRP) composites have been considered as one of the most promising modern materials for construction. Both the advantages and disadvantages of FRP composites have been studied thoroughly and compared to the conventional construction materials such as steel, reinforced concrete, wood, etc. [1]–[4]. One popular application of these materials is retrofitting/rehabilitation reinforced concrete structures through external bonding. This technique has the minimal impact on the surrounding environment and is far easier and faster to be implemented compared to other enhancement techniques. The interface between the FRP and concrete plays a critical role in this technique through providing effective stress transfer from the existing structures to externally bonded FRP plates or sheets and keeping integrity and durability of the composite performance of the FRP–concrete structures. Debonding along the FRP-to–concrete interface can lead to premature failure of structures. Here, FRP–to-concrete interface refers to a thin layer of adhesive and the adjacent concrete within which the relative deformation between FRP and concrete mainly happens as revealed by experiment study [5]. Although extensive studies have been conducted on the short-term behavior and catastrophic failure of the FRP-to-concrete interface, much less attention has been paid to the long-term performance of this interface in presence of aggressive environments [6]–[8]. Experimental studies have shown that the most dangerous environmental threat to the FRP-to-concrete interface is moisture, specifically water ingress through the interface [6], [9]–[13]. It has also been experimentally proved that the water attack can also shift the failure locus of this interface from the concrete substrate (cohesive failure) to the epoxy-concrete interface (adhesive failure). In these experimental studies, testing specimens were first conditioned through fully immersing the specimens in water. The deterioration induced to the interface by water is then evaluated

through measuring the residual strength or fracture toughness of the interface. The major problem of this method is that testing results are specimen-dependent because the ingress of water within the FRP-to-concrete interface depends on geometries and material properties of the specimen. Experimental observations and numerical simulation suggest that the relative humidity across the interface in the width direction is not uniform in the specimens fully immersed in water because water diffusion from outside boundaries into the interface is mainly determined by its path. The longer the path, the lower relative humidity is at that location, and vice versa. It takes longer time for water to arrive at the interior zone of the epoxy-concrete interface than the exterior zone close the boundary. As a result, relative humidity is higher in the exterior zone and lower in the interior zone for the same conditioning duration. This non-uniform distribution of the relative humidity across the interface makes it difficult to correlate the residual fracture toughness to the interface relative humidity. In current practice, average relative humidity across the interface is noted as the interface relative humidity (I_{RH}). The major problem of using the average value to represent the moisture status of the whole interface in the width direction is obvious; the difference in real relative humidity distribution is ignored. We can obtain same average relative humidity across the epoxy-concrete interface by using different specimens and conditioning period. The real moisture distribution across the interface in these specimens, however, can be very different. As a result, relationships between the residual strength of the epoxy-concrete interface and the relative humidity established based on this average value in existing are dependent on the specimens because the real moisture distribution in those specimens are different. Clearly, these relationship based on the average relative humidity cannot represent the intrinsic effect of the moisture on the strength of the interface.

To overcome this issue in the existing studies, a new method is proposed to condition the specimen so that more even distribution of the relative humidity across the interface can be reached.

8.2. Specimen design

To overcome the problem in existing studies, a new conditioning method is proposed to create a relatively uniform distribution of moisture across the epoxy-concrete interface. This is done by partially submerging the specimen in water, rather than the whole one as used in existing studies. The working principle of this new conditioning method can be illustrated by simulating the water diffusion in the test specimen consisting of a 50.8 X 50.8 X 50.8 mm^3 (2 X 2 X 2 in^3) concrete block specimen, a layer of epoxy, and a carbon fiber reinforced polymer (CFRP) using finite element analysis (FEA) method in ABAQUS/CAE, (Fig. 8-1(a)). Same diffusivity coefficients as we experimentally obtained and used in our previous study are used here [13]. Different conditionings are considered in the simulation from submerging the whole specimen in water (100% in water) to only half of the concrete block in the depth direction from the bottom in water (50% in water). Relative humidity distributions across the epoxy-concrete interface in width direction corresponding to different conditioning method is then calculated and shown in Fig. 8-2. It can be seen that by submerging the whole specimen in water after one week, relative humidity across the interface reduces very fast from 100% at the side surface of the specimen to nearly zero at a distance about 15 mm from the surface (Fig. 8-2(a)). This non-uniform distribution can be alleviated by submerging only part of the concrete block of the specimen in water. As shown in Fig. 8-2(a), more uniform distribution of the relative humidity across the interface can be achieved by submerging less concrete block in water. An approximately uniform distribution of moisture distribution across the interface can be achieved

by submerging less than 70% of the concrete block in water after one week. However, the relative humidity is very low under such conditioning compared with full submerging the specimen in water because water has a longer diffusion path.

After conditioning in water for 16 weeks, much more water is present across the width of the interface, as shown in Fig. 8-2(b). It can be seen that submerging half of the concrete block in water induces a nearly uniform distribution of relative humidity across the interface. However, the relative humidity across the interface induced by this partial submerging is much lower than full submerging. It implies that much longer condition time is needed for partially-submerged specimen to reach similar relative humidity than that needed by fully-submerged specimens. To overcome this difficulty, we can reduce the thickness of the concrete block of the specimen by half (Fig. 8-1(b)) so that the diffusion path of water can be reduced accordingly.

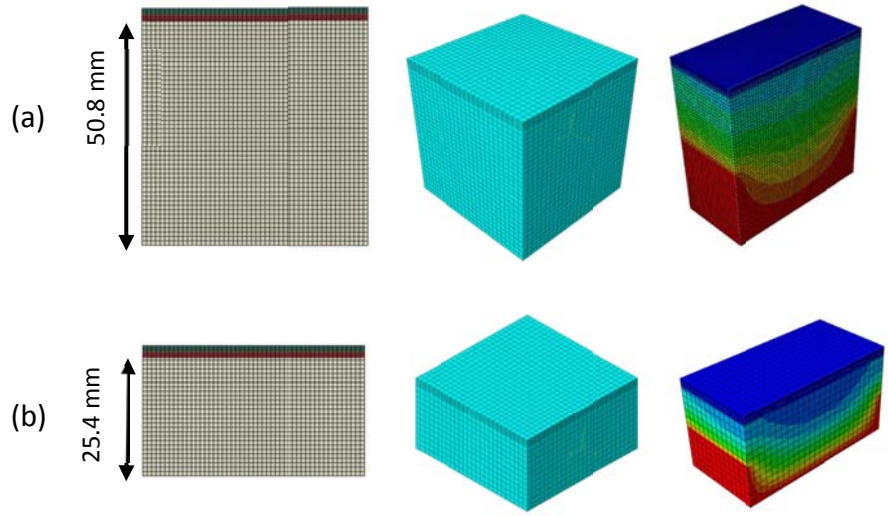

Fig. 8-1 FEA model (50.8 X 50.8 X 50.8 mm^3) for evaluation of water level on relative humidity along the epoxy-concrete interface: (a) Specimens size: 50.8 X 50.8 X 50.8 mm^3, (b) Specimens size 50.8 X 50.8 X 25.4 mm^3.

Fig. 8-3 shows the relative humidity across the epoxy-concrete interface for this specimen with half of concrete block submerged in water. It can be observed that after 16 weeks conditioning, relative humidity across the interface is improved from 23% to 60% by reducing the thickness of the concrete block by half.

Numerical simulations (Fig. 8-2 and Fig. 8-3) suggest that although it is not possible to create a uniform moisture distribution across the epoxy-concrete interface, we can minimize the non-uniformity of this distribution through partially submerging the concrete block of the specimen in water. Fig. 8-3 shows that by submerging half of the concrete block of this specimen with thickness of 25.4 mm can reach a relatively uniform distribution of relative humidity across the interface without needing extended conditioning time. This specimen and the conditioning method are therefore selected in this study to establish the relationship between the residual strength of the interface and the relative humidity of the interface. Since the variation of the relative humidity across the interface is much smaller than in the existing studies, the average relative humidity is more accurate to represent the real moisture distribution across the interface, we refer the obtained fracture toughness at different relative humidity using this specimen as intrinsic value of the interface. Accordingly, fracture toughness obtained through submerging the whole specimen in water as extrinsic one.

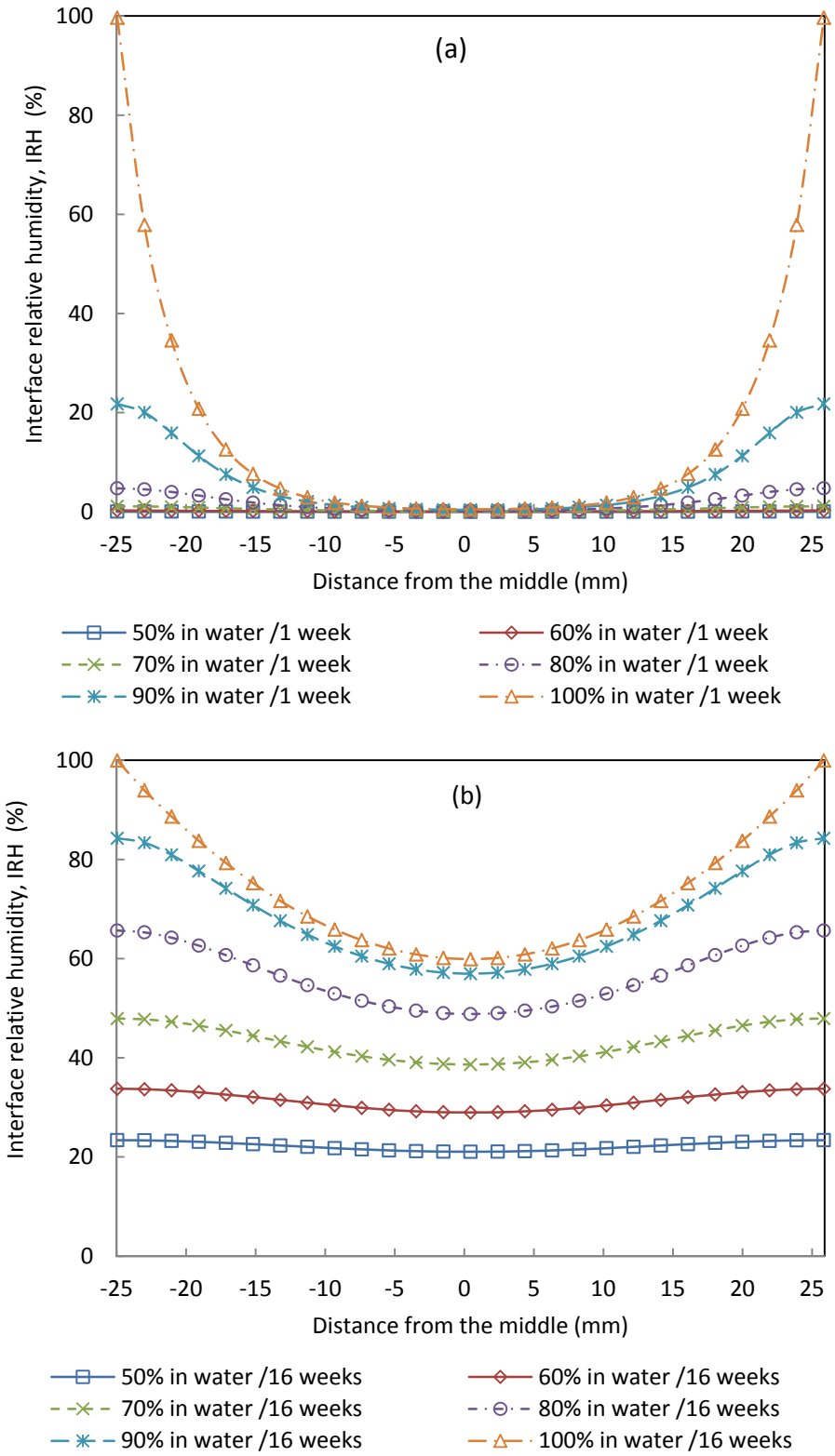

Fig. 8-2 Interface relative humidity along the epoxy-concrete interface exposed to different water levels: (a) after 1 week, (b) after 16 weeks.

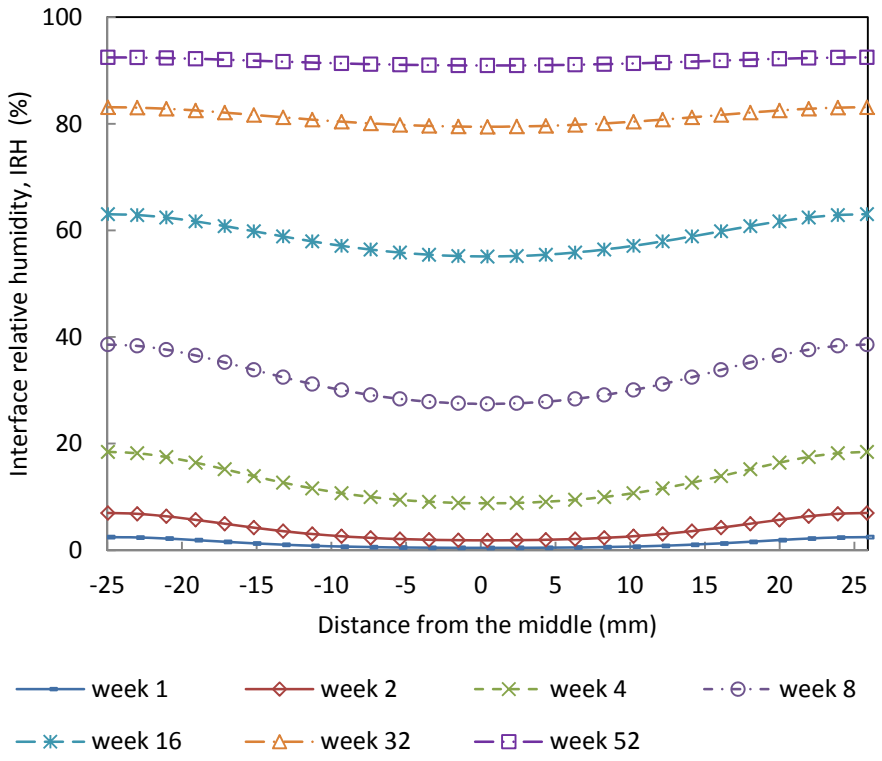

Fig. 8-3 Interface relative humidity along the epoxy-concrete interface of the specimen with 25.4 mm thickness concrete block and exposed to 50% water level.

8.3. Materials and testing method

The modified specimen used to measure the fracture toughness using wedge driving method is illustrated in Fig. 8-4, which consists a CFRP- procured plate, a layer of two-part epoxy, and a concrete block cured for 28 days and dried for two weeks at room temperature (23°C) following ASTM C33/C33M and ASTM C192,C192M [14], [15]. The width of the specimen is 50.8 mm (2 inch) in all layers. The mean 28-day compressive strength for the concrete specimens using 100 X 200 mm cylinders is about 30.9 MPa. A pre-crack using some Teflon tape is considered with length of 12.7 mm (1/2 inch) to ensure the crack propagation within the interface along the epoxy and concrete substrate. The top half-thickness of the concrete block in the specimen, 12.7 mm (1/2 inch), is covered with a thick layer of a commercial concrete sealer to guarantee no water ingress above the predefined 50% submerging level of this test. The regions adjacent to the

bond are grinded to eliminate any possibility of bridge formation due to sealer used alongside the interface. After removing from the conditioning tank, the specimen is tested using a steel wedge with thickness of *Δ*. During the test, the distance between the wedge contact point and the crack tip is read and recorded as the crack effective length *a*.

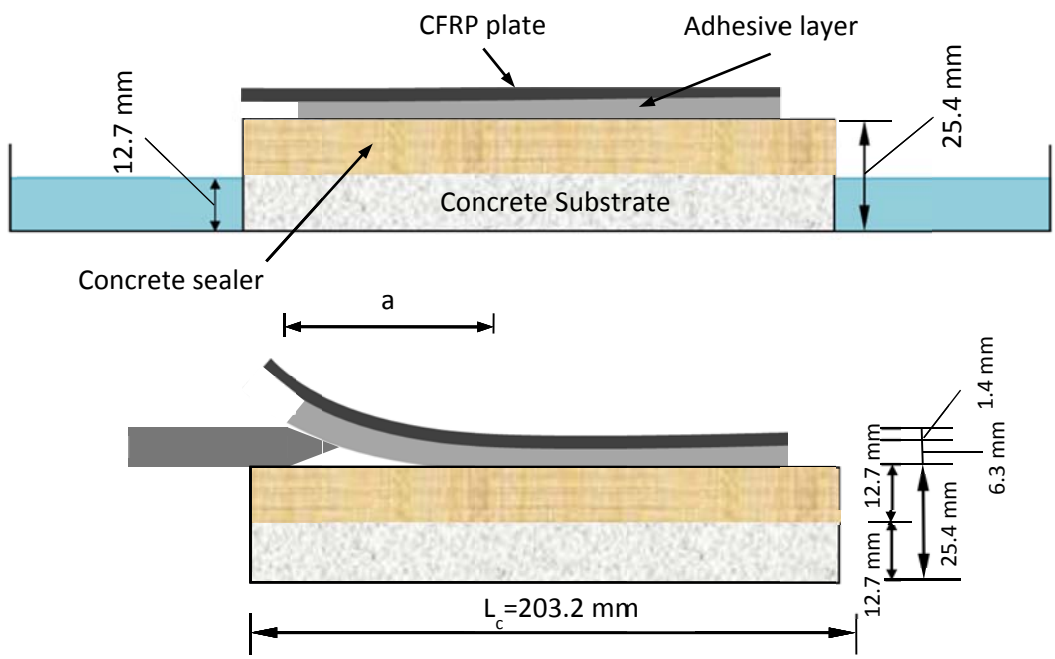

Fig. 8-4 Intrinsic debonding test specimen.

Mechanical properties and geometries of the CFRP plate and the two-part Tyfo TC epoxy are presented in Table 8-1 and Table 8-2, respectively. In this study a thicker epoxy layer than the one used in previous study to provide larger room for the insertion of the steel wedge with well vertical alignment. Manufacturing of this specimens follows a similar procedure to our previous study on the subcritical debonding of FRP-to-concrete bonded joints [16].

Table 8-1 Mechanical properties of CFRP.

Laminate Width	Laminate Thickness	Cross Sectional Area	Tensile Strength	Tensile Modulus of Elasticity	Ultimate Strain
50.8 mm	1.397 mm	71.10 mm^2	2413 MPa	131,000 MPa	0.0187 %

Table 8-2 Mechanical properties of the epoxy.

Compressive Strength	Epoxy layer Width	Epoxy layer Thickness	Cross Sectional Area	Tensile Strength	Tensile Modulus	Flexural Modulus	Flexural Strength
28.2 MPa	50.8 mm	6.30 mm	320 mm^2	22.7 MPa	1,200 MPa	1.23 GPa	45.8 MPa

A similar home-made fixture used in our previous tests is used here. A high-resolution camera is used to measure the crack length. The wedge is driven into the pre-crack by a hydraulic Testing Material System (MTS810) which can be controlled by a computer. All specimens are first conditioned in a water tank with half of their concrete block in water. It is a difficult task to maintain the water level in tank to exactly half of the height of the concrete block because of water evaporation and difference in size of the specimens. A flat, but shallow tank in which the level of water can be controlled by two minimum and maximum lines is used to condition the specimen. The minimum water line is used to ensure at least 50% of the concrete block is submerged in water. The maximal water line is used to control the highest water level of the water tank. By filling water in the tank to this line, water tank will have some extra water to compensate the loss of water due to evaporation. Once water level drops close to the minimum water line, new water shall be added to raise the water level close to the maximum line. In this way, water will never drop below the 50% line. To eliminate extra diffusion of water into the specimen when water level is above 50% line, the top half the concrete block is sealed with a thick layer of a commercial concrete sealer. The tank and specimens are kept in an

environmental chamber at 23.89°C (75°F) during the conditioning period. Water level is inspected on a daily basis and more water is added as needed. After conditioned in the tank for specific duration, the specimens are prepared for the teat by removing the surface moisture using a soft and dry cloth.

The wedge driving test, as shown in Fig. 8-5 and Fig. 8-6, measures the mode-I (peeling) fracture toughness test of the interface. Before placing the specimen in the loading fixture, a paper ruler is taped along the interface on the concrete side to make it easier to read the crack lengths from the captured images.

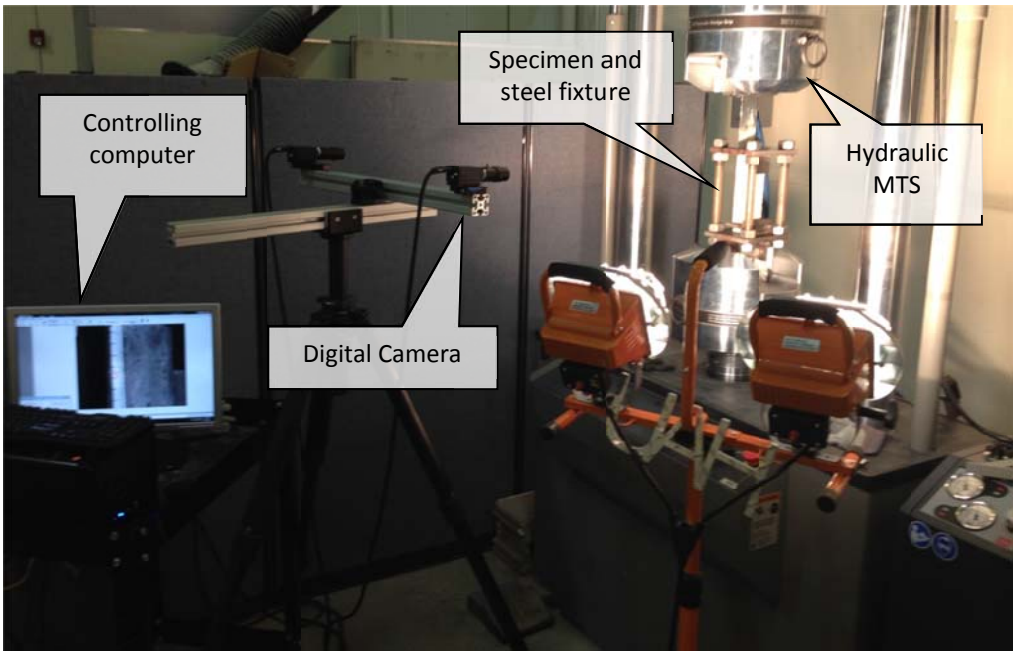

Fig. 8-5 Test set-up for intrinsic debonding tests.

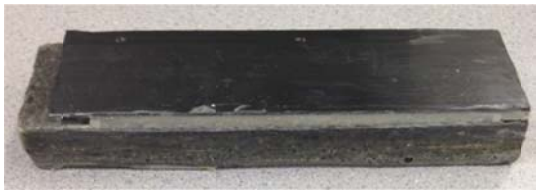

Fig. 8-6 Specimens for intrinsic debonding test.

A steel wedge designed and manufactured according to ASTM D3762-03 [17] (Δ=3.175 mm) is fixed to the upper grip of a MTS machine and gently driven into the pre-crack of the specimen close to tip of the pre-crack. Then the wedge is driven at a rate of 2.54 mm/minute (0.00167 inch/second) introduce the initiation and propagation of the interface crack along the interface. During the test, the applied load and the wedge vertical displacement are recorded using a computer. A picture is captured by the digital camera every 10 seconds from the crack tip to the contact point of the wedge. The captured picture is then used to determine the crack length a. The energy release rate at the crack tip of the interface can be obtained using Eq.(1)

$$G_{int} = \frac{9D\Delta^2}{2ba^4}, \tag{1}$$

where D is the bending stiffness of the CFRP-epoxy composite beam and b is the thickness of the bond, respectively.

Specimens were conditioned for four, eight and sixteen weeks. Two different sets of specimens were chosen for each conditioning period: untreated and treated with silane coupling agent. Silane coupling agents (SiH_4) are organic materials that can be used to improve the bond strength between an organic substrate such as epoxy and any inorganic substrate such as Aluminum [18]–[25]. Function of a cementitious material such as Portland cement concrete has been studied in last years and it has been shown that silane can improve the bond between concrete and epoxy [16], [26]. For the treated specimens, a 1% silane solution was brushed over the concrete surface before applying the CFRP plate and epoxy layer.

8.4. Testing results and discussion

8.4.1. Wedge driving test

Fig. 8-7 shows fracture toughness of CFRP-to-concrete specimens with half of the concrete block conditioned in water. The fracture toughnesses of the interface for both the

untreated and treated specimens reduce with the conditioning duration. Nevertheless, the silane treated specimen maintains higher fracture toughness for the same conditioning duration, suggesting that silane coupling agent can significantly improve the durability of the interface. For example, silane treatment improves the fracture toughness of the interface by 105% and 80% after 8 and 16 weeks conditioning in water, respectively. Compared with the specimen conditioned by full submerging in [13], the residual fracture toughness in this test are much higher for the same duration of conditioning because of different relative humidities within the interface are induced by different conditioning methods.

Residual strengths of the interface due to the intrinsic debonding are much lower in comparison to the re1ults obtained from the fully-submerged specimens that suggest that due to less water diffusion and, subsequently, less I_{RH}, intrinsic specimens experience far more moderate deterioration in a same time. As it was shown and discussed, for reaching the relative humidity above 90% for intrinsic test, for a period of one year conditioning is inevitable. As a result, in this study, residual strength at lower relative humidities are measured, and then, by finding a regression equation for each treated and untreated specimens, we can make a comparison to the fully-submerged results.

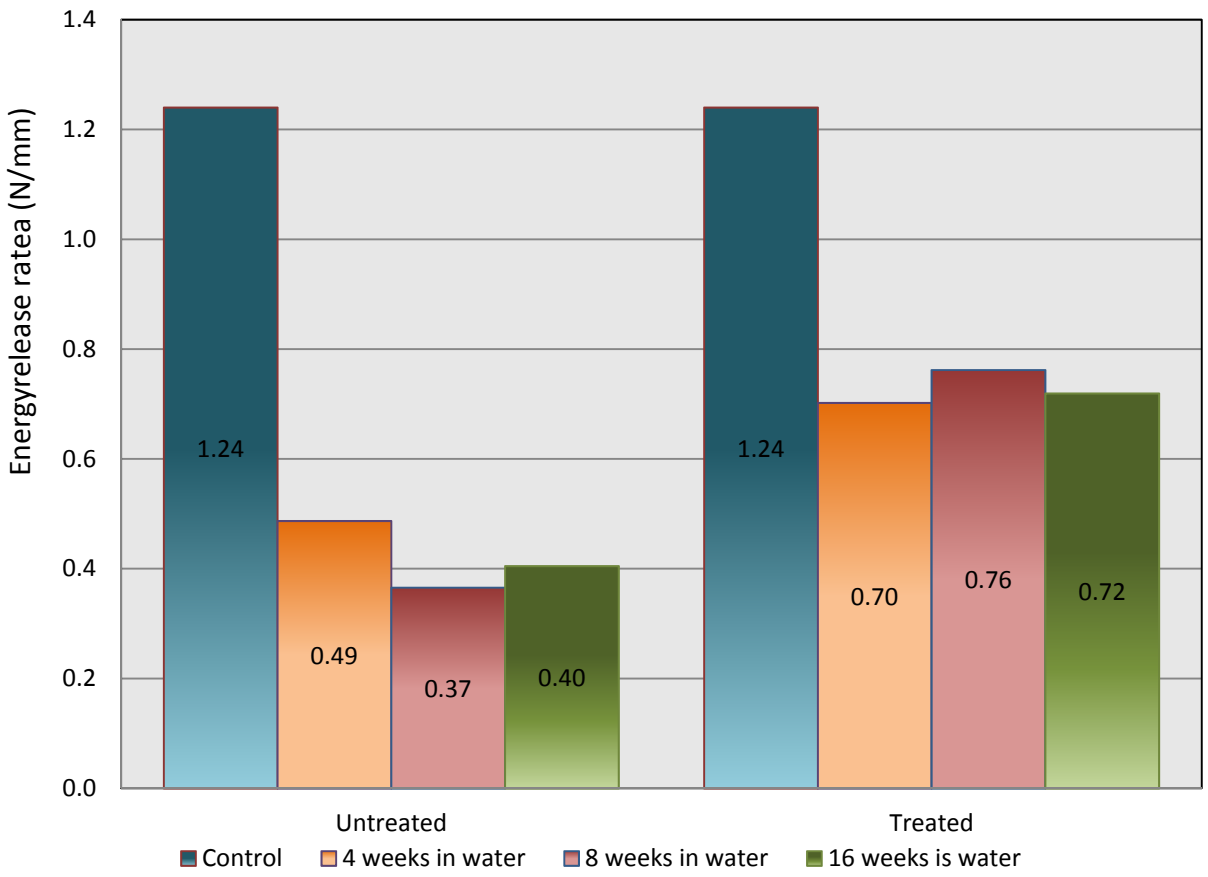

Fig. 8-7 Effect of water conditioning duration on intrinsic debonding fracture release rate for untreated or treated specimens with silane coupling agent.

Failure mechanisms of the specimens conditioned by submerging half concrete block in water are demonstrated in Fig. 8-8. After being conditioned for four weeks, a mixed debonding failure (cohesive and adhesive) can be identified on the epoxy side of the debonded interface as revealed by small amount of concrete particles scattered on the epoxy surface. As comparison, the control specimen without conditioning in water exhibits a cohesive failure mode since a layer of concrete is attached to the epoxy side. More concrete residue can be found on the epoxy side of the specimen treated by silane after four week conditioning, suggests that more cohesive debonding is occurred in this specimen. This is not unexpected since silane coupling agent can enhance the resistance of the bonds between the epoxy and concrete to water attack. As a result,

higher bond strength exists between the epoxy and the concrete than in the untreated specimen. If this strength is higher than the adjacent concrete, debonding will occur within concrete, rather than along the interface, leading to more cohesive failure and higher fracture toughness of the specimen. After eight and sixteen weeks conditioning, less concrete particles are attached to the debonded untreated interfaces. Specimens treated with silane also shows similar trend. Nevertheless, more concrete residue can be found on these specimens than on the one without surface treatment conditioned at the same duration, as shown in Fig. 8-7, verifying once gain the effectiveness of silane coupling agent on enhancing the durability of the FRP-to-concrete interface.

(a)

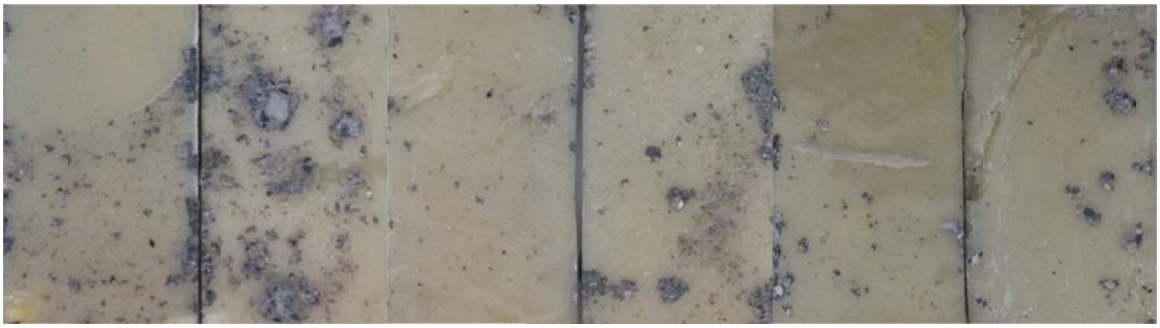

(b) (c) (d) (e) (f) (g)

Fig. 8-8 Debonded CFRP side of the intrinsic tested specimens: (a) control specimen, (b) 4 weeks in water (untreated), (c) 4 weeks in water (treated), (d) 8 weeks in water (untreated), (e) 8 weeks in water (treated), (f) 16 weeks in water (untreated), (g) 16 weeks in water (treated).

8.4.2. Interface relative humidity within the epoxy-concrete interface

Numerical simulation is used to determine the relative humidity within the epoxy-concrete interface [13]. A 3-dimensional model is constructed in ABAQUS/CAE to calculate the moisture distribution within the specimen as shown in Fig. 8-9. From the bottom to the top of the specimen, sizes of used 8-node linear DC3D8 elements gradually reduce from 5 to 1 mm and remain constant all along the interface (Fig. 8-9).

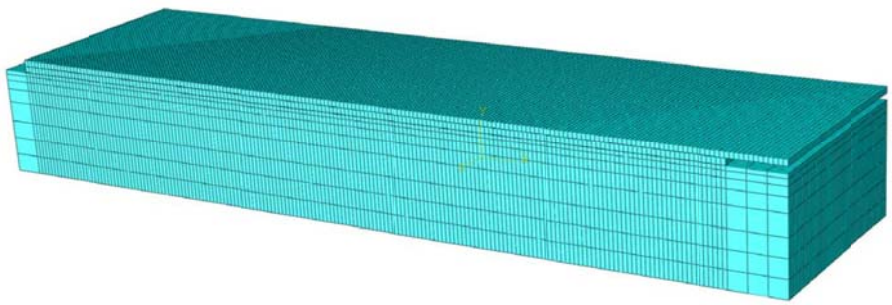

Fig. 8-9 FEA model used for moisture diffusion along the epoxy-concrete interface in an intrinsic debonding test.

A boundary condition of 100% relative humidity (i.e. water) is defined for half of the concrete block from the bottom. Initial relative humidity is 0% for the entire specimen including concrete block, epoxy layer and the CFRP plate. However, except the concrete, the rest of the specimen does not genuinely participate in the analysis because their diffusion coefficients are negligible compared with that of the concrete.

The relative humidity contour of a specimen with half of the concrete block submerged in water is presented in Fig. 8-10 and Fig. 8-11. Although the relative humidity adjacent to and along the interface in these specimens is much lower in comparison with those in fully submerged specimens. The moisture distribution is also relatively uniform across the interface, confirming the effectiveness of the proposed conditioning method in creating uniform relative humidity distribution across the interface.

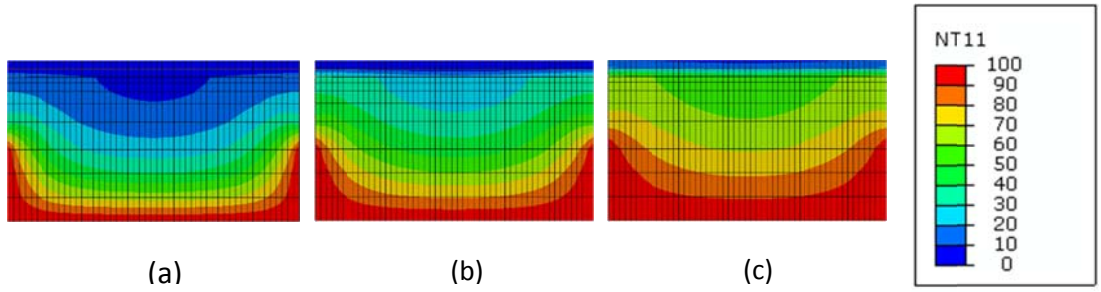

Fig. 8-10 Relative humidity contour versus immersion time in an intrinsic debonding test: (a) 4-week longitudinal section, (b) 8-week longitudinal section, (c) 16-week longitudinal section.

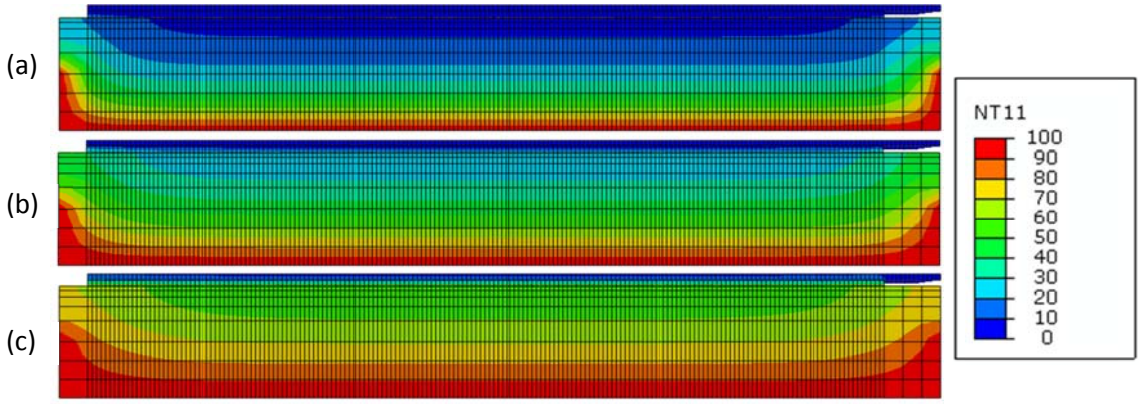

Fig. 8-11 Relative humidity contour versus immersion time in an intrinsic debonding test: (a) 4-week longitudinal section, (b) 8-week longitudinal section, (c) 16-week longitudinal section.

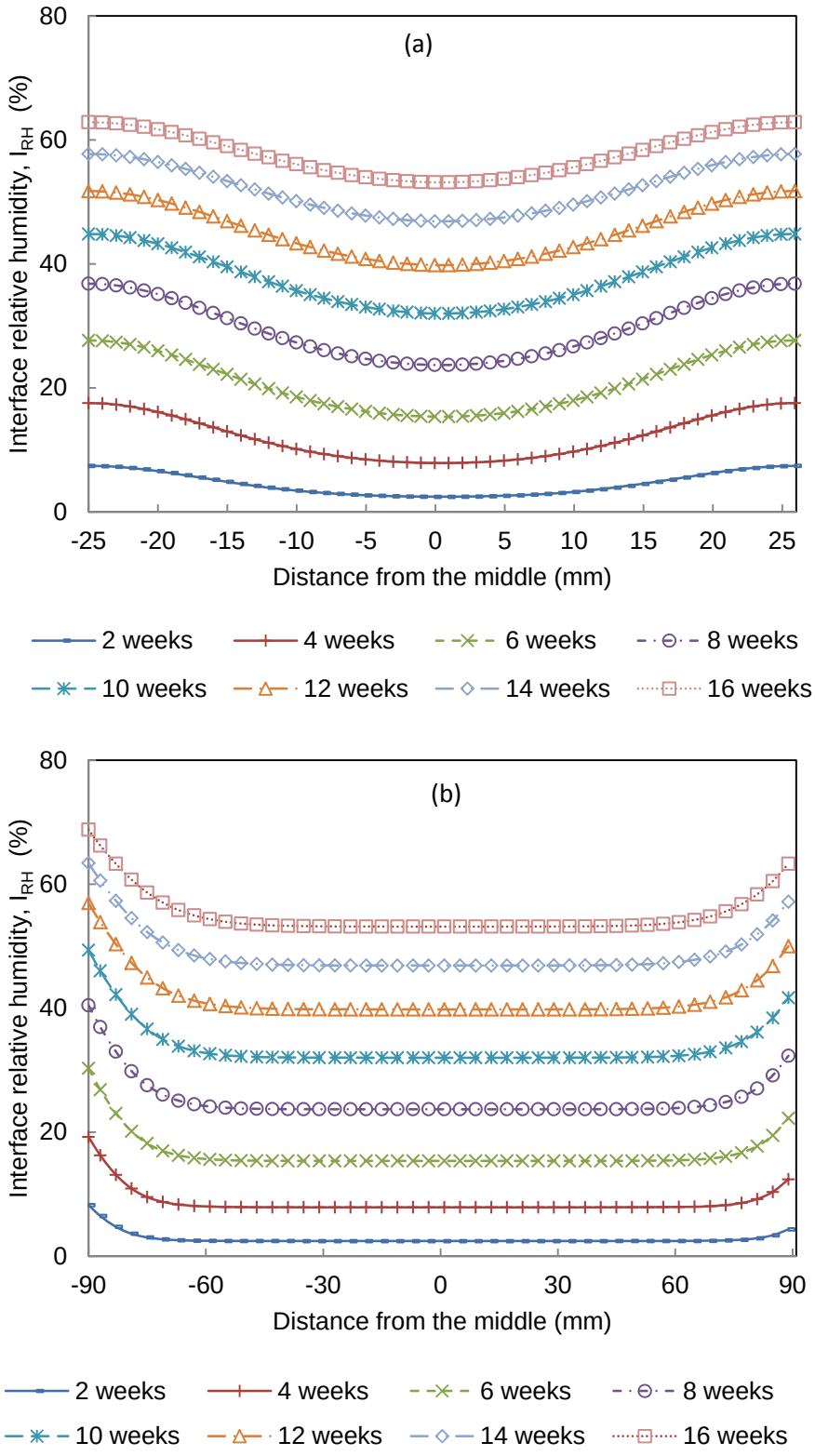

Fig. 8-12 Interface relative humidity along the epoxy-concrete interface for an intrinsic test: (a) Transverse section, (b) Longitudinal section 1.

The following equation can express the relationship between the average I_{RH} and the intrinsic fracture toughness energy (G_{int}) in an exponential regression model

$$G_{int} = \alpha . e^{(-\beta . I_{RH})}, \quad (2)$$

where α and β are constant values and can be determined after fitting experimental data to Eq. (2). Table 8-3 shows the fitting values of these parameters for each intrinsic test. As comparison, those constants for the specimens conditioned by full submerging (extrinsic ones in the table) are also presented. Fitted curves for both untreated and treated interface are presented in Fig. 8-13. Both curves can provide acceptable prediction of the fracture toughness of the interface reducing with relative humidity of the interface, particularly when relative humidity is not too low.

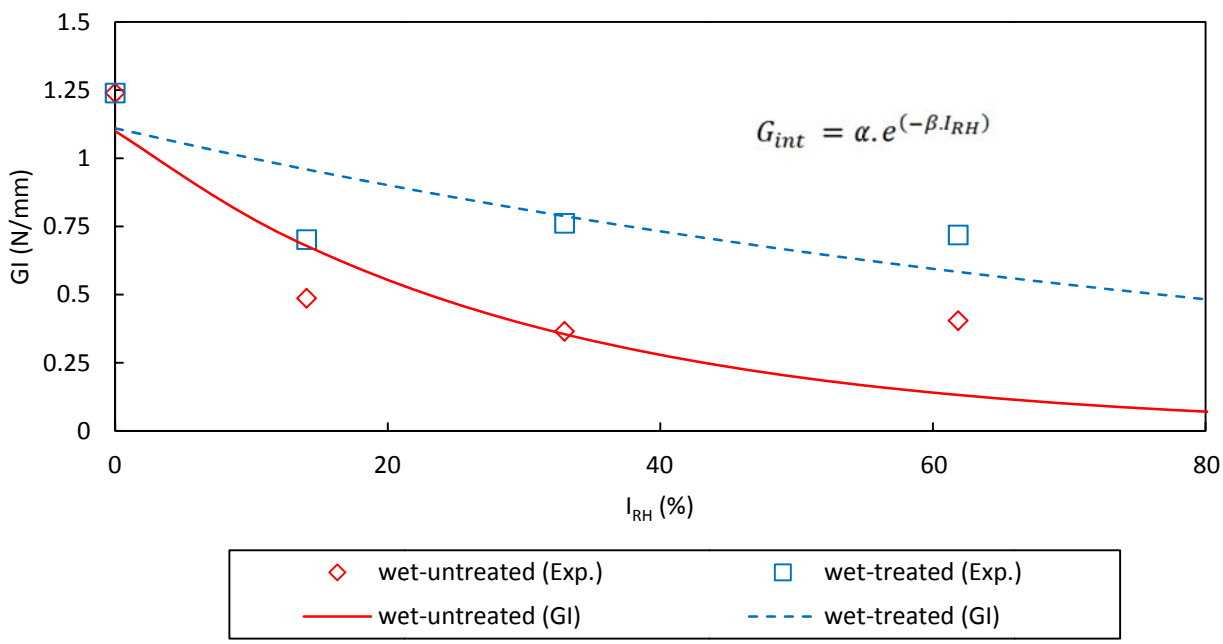

Fig. 8-13 The relationship between the fracture energy release rate and the average I_{RH} along the epoxy-concrete interface for an intrinsic debonding test 1.

Table 8-3 Parameters of the relationship between the fracture energy and the I_{RH}.

	Intrinsic mode-I Fracture		Extrinsic mode-I Fracture [13]	
Parameters	untreated	treated	untreated	treated
α	1.10	1.11	1.10	1.11
β	3.43	1.04	2.21	1.65

Fig. 8-14 compares the relationships between the fracture toughness and the I_{RH} obtained by full-submerging (extrinsic) and half-submerging (intrinsic) the specimens in water. As expected, two different relationships are obtained due to the difference in conditioning the specimen, confirming that the test results are specimen-dependent. At lower relative humidities (Fig. 8-14(b)), the intrinsic fracture toughness of the untreated specimens is lower than the extrinsic one for the same relative humidity. When relative humidity is high enough, this difference in intrinsic and extrinsic fracture toughness for the untreated specimen is small, as shown in Fig. 8-14(c). This phenomenon may be caused by the non-uniform moisture distribution in the specimens used to obtain the extrinsic fracture toughness. At lower relative humidity, relative humidity across the most area of the epoxy-concrete interface is still lower than the average value because of very high relative humidity in the area adjacent to the surface, while the relative humidity in most area across the interface in the intrinsic sample is close to the average value. This suggests although the same relative humidity is used to express the relative humidity in intrinsic and extrinsic results, the real relative humidity in intrinsic one is higher than that in extrinsic one at low relative humidity. As a result, fracture toughness of the extrinsic specimen provides a high value. After longer conditioning, relative humidities increase significantly and become more uniformly in both the intrinsic and extrinsic tests, leading to smaller difference in measured fracture toughness.

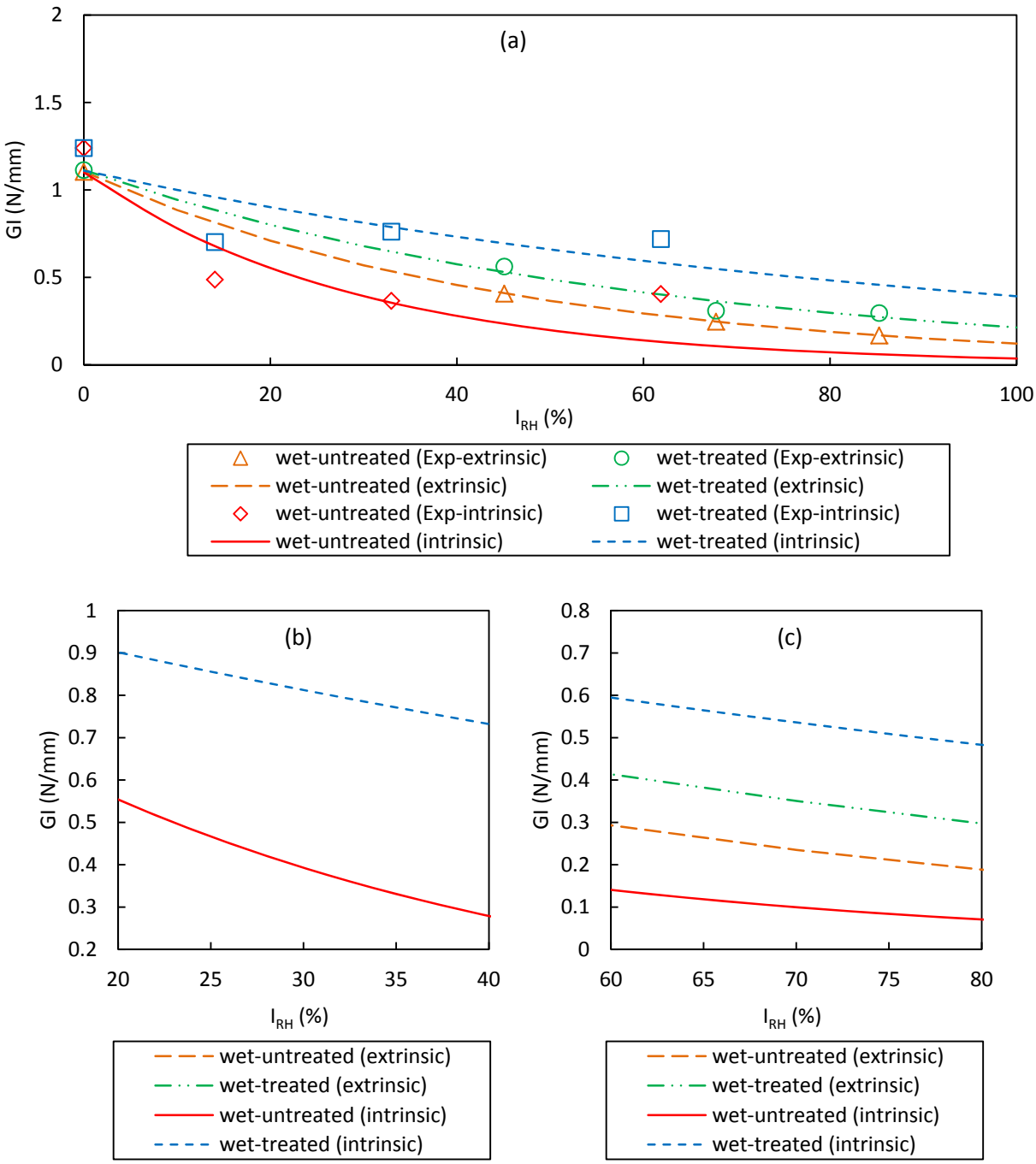

Fig. 8-14 Comparison between the intrinsic and extrinsic debonding fracture energy release rate versus I_{RH} along the epoxy-concrete interface: (a) at lower I_{RH}, (b) at higher I_{RH}.

In case of specimens treated with silane coupling agent, intrinsic fracture toughness is higher than the extrinsic one at both low and high relative humidities clearly because of silane. Silane coupling agent not only produces covalent bonds between the epoxy and concrete, but

also creates a thin hydrophobic concrete layer adjacent to the interface due to the penetration of the silane. As a result, water will have more difficulty to diffuse into the interface in intrinsic testing. While in extrinsic testing, water can still diffuse into the interface through the interface which usually has a much high diffusion coefficient than concrete. Therefore, the calculated relative humidity which does not account for the effect of silane application and faster water diffusion along the interface is lower than the real relative humidity in the extrinsic test and higher than that in the intrinsic test. In another word, the real relative humidity in an intrinsic sample is lower than an extrinsic one even though their simulated relative humidity is the same. As a result, the fracture toughness of the intrinsic test shows a high value than the extrinsic one.

8.5. Conclusions

This study proposes a new method to determine the residual fracture toughness of the FRP-to-concrete interface subjected to water attack. Unlike in the commonly used method in which the specimen is conditioned by submerging the whole specimen in water, the new method conditions the specimen through submerging half of the specimen in water. This advantage of new conditioning method is that more uniform moisture distribution across the interface can be achieved. While in existing studies in which the whole specimen in submerged in water, the moisture distribution is nonuniform. The relatively uniform distribution of the moisture across the interface makes it possible to establish a relationship between the residual fracture toughness and the interface relative humidity based testing data, which can be used to predict the deterioration of the interface induced by water. This relationship is different from the one obtained through full submerging, confirming that existing testing method is extrinsic and specimen dependent. The residual fracture toughness of the interface treated by silane coupling

agent is significantly higher than the one of the interface without silane treatment, confirming the effectiveness of silane on enhancing the long-term durability of the interface.

8.6. References

[1] B. Täljsten, "Defining anchor lengths of steel and CFRP plates bonded to concrete," *Int. J. Adhes. Adhes.*, vol. 17, no. 4, pp. 319–327, 1997.

[2] L. De Lorenzis and A. Nanni, "Characterization of FRP rods as near-surface mounted reinforcement," *J. Compos. Constr.*, vol. 5, no. 2, pp. 114–121, 2001.

[3] F. Seible, M. J. N. Priestley, G. A. Hegemier, and D. Innamorato, "Seismic retrofit of RC columns with continuous carbon fiber jackets," *J. Compos. Constr.*, vol. 1, no. 2, pp. 52–62, 1997.

[4] P. A. Ritchie, D. A. Thomas, L.-W. Lu, and G. M. Conelly, "External reinforcement of concrete beams using fiber reinforced plastics," *ACI Struct. J.*, vol. 88, no. 4, 1991.

[5] H. Yuan, J. G. Teng, R. Seracino, Z. S. Wu, and J. Yao, "Full-range behavior of FRP-to-concrete bonded joints," *Eng. Struct.*, vol. 26, no. 5, pp. 553–565, 2004.

[6] N. F. Grace and M. Grace, "Effect of repeated loading and long term humidity exposure on flexural response of CFRP strengthened concrete beams," in *Proceedings of the International Symposium on Bonded behavior of FRP in Structures (BBFS 2005), Chen and Teng (eds)*, 2005, pp. 539–546.

[7] M. L. Porter and K. Harries, "Future directions for research in FRP composites in concrete construction," *J. Compos. Constr.*, vol. 11, no. 3, pp. 252–257, 2007.

[8] V. M. Karbhari, Jw. Chin, D. Hunston, B. Benmokrane, T. Juska, R. Morgan, J. J. Lesko, U. Sorathia, and D. Reynaud, "Durability gap analysis for fiber-reinforced polymer composites in civil infrastructure," *J. Compos. Constr.*, vol. 7, no. 3, pp. 238–247, 2003.

[9] B. Wan, "The Effect of the Presence of Water on the Durability of Bond between CFRP and Concrete," *J. Reinf. Plast. Compos.*, vol. 25, no. 8, pp. 875–890, 2006.

[10] Z. Ouyang and B. Wan, "Experimental and Numerical Study of Moisture Effects on the Bond Fracture Energy of FRP/Concrete Joints," *J. Reinf. Plast. Compos.*, 2007.

[11] O. Büyüköztürk and T.-Y. Yu, "Understanding and assessment of debonding failures in FRP–concrete systems," in *17th International congress on advances in civil engineering, Yildiz Technical University, Istanbul, Turkey*, 2006.

[12] C. Au and O. Büyüköztürk, "Peel and shear fracture characterization of debonding in FRP plated concrete affected by moisture," *J. Compos. Constr.*, vol. 10, no. 1, pp. 35–47, 2006.

[13] S. Amidi and J. Wang, "Critical debonding of epoxy-to-concrete interface for FRP-to concrete bonded joints," *Draft Papaer*, 2015.

[14] "ASTM C33/C33M, Standard Specification for Concrete Aggregates." ASTM International, West Conshohocken, PA, 2013.

[15] "ASTM C 192/C192M, Standard Practice for Making and Curing Concrete Test Specimens in the Laboratory." ASTM International, West Conshohocken, PA, 2014.

[16] S. Amidi and J. Wang, "Subcritical Debonding of FRP-to-Concrete Bonded Interface under Synergistic Effect of Load, Moisture, and Temperature," 2015.

[17] "ASTM D3762-03, Standard Test Method for Adhesive-Bonded Surface Durability of Aluminum (Wedge Test)." ASTM International, West Conshohocken, PA, 2010.

[18] S. Shokoohi, A. Arefazar, and R. Khosrokhavar, "Silane coupling agents in polymer-based reinforced composites: a review," *J. Reinf. Plast. Compos.*, vol. 27, no. 5, pp. 473–485, 2008.

[19] C. F. Korenberg, A. J. Kinloch, and J. F. Watts, "Crack growth of structural adhesive joints in humid environments," *J. Adhes.*, vol. 80, no. 3, pp. 169–201, 2004.

[20] B. B. Johnsen, K. Olafsen, A. Stori, and K. Vinje, "Silanization of adhesively bonded aluminum alloy AA6060 with γ-glycidoxypropyltrimethoxysilane. II. Stability in degrading environments," *J. Adhes. Sci. Technol.*, vol. 17, no. 9, pp. 1283–1298, 2003.

[21] A. Rattana, M.-L. Abel, and J. F. Watts, "Degradation of interfacial chemistry of epoxy/silane/aluminium interfaces as a result of aqueous attack," *J. Adhes.*, vol. 81, no. 9, pp. 963–988, 2005.

[22] D. H. Berry and A. Namkanisorn, "Fracture toughness of a silane coupled polymer-metal interface: Silane concentration effects," *J. Adhes.*, vol. 81, no. 3–4, pp. 347–370, 2005.

[23] M.-L. Abel, R. D. Allington, R. P. Digby, N. Porritt, S. J. Shaw, and J. F. Watts, "Understanding the relationship between silane application conditions, bond durability and locus of failure," *Int. J. Adhes. Adhes.*, vol. 26, no. 1, pp. 2–15, 2006.

[24] M. Sautrot*, M.-L. Abel, J. F. Watts, and J. Powell, "Incorporation of an adhesion promoter in a structural adhesive: aspects of durability and interface chemistry," *J. Adhes.*, vol. 81, no. 2, pp. 163–187, 2005.

[25] A. J. Kinloch, C. F. Korenberg, K. T. Tan, and J. F. Watts, "Crack growth in structural adhesive joints in aqueous environments," *J. Mater. Sci.*, vol. 42, no. 15, pp. 6353–6370, 2007.

[26] L. Ye, K. Friedrich, C. Weimer, and Y.-W. Mai, "Surface treatments and adhesion bonding between concrete and a CFRP composite," *Adv. Compos. Mater.*, vol. 7, no. 1, pp. 47–61, 1998.

CHAPTER 9

SUMMARY, CONCLUSIONS AND FUTURE WORKS

9.1. Summary

A comprehensive program using both the analytical and experimental approach has been carried out in this study to examine the integrity and long-term durability of the FRP-to-concrete interface in presence of aggressive environments, which is critical to the success of FRP-strengthened concrete structures.

In analytical studies, three-parameter elastic/viscoelastic foundation models have been established for adhesively bonded joints. The superior features of the new analytical works include: 1) satisfying all boundary conditions, 2) predicting different peeling stresses along two interfaces between the adhesive and adherends, and 3) capturing stress redistribution in adhesively bonded joints. These analytical models have been verified by their excellent agreement with finite element analysis and experimental observations.

In experimental studies, a few new testing methods have been proposed and carried out, including: 1) novel environment-assisted subcritical debonding test to examine the synergistic effect of the mechanical loads and environmental conditions on the deterioration of the FRP-to-concrete interface using a wedge driving test; 2) wedge driving (the mode-I fracture) and pulling (the mode-II fracture) tests to evaluate the residual fracture toughnesses of the FRP-to-concrete interface after conditioning in water; 3) a novel wedge split test to directly determine the traction-separation law of the interface affected by conditioning in water, in addition to the

residual fracture toughness of the interface. A new technique to condition the FRP-to-concrete specimen has also been proposed which can introduce more evenly distributed moisture across the epoxy- concrete interface in the FRP-to-concrete specimens. By using this new conditioning method, the effect of the moisture content on the residual fracture toughness of the interface can be determined more reliably. Potential of using silane coupling agent to enhance the durability of the interface has also been evaluated.

The detailed findings of this dissertation study can be summarized as follows:

1. A three parameter elastic foundation model has been developed for double-lap joints. Based on this model, the following findings are obtained:
    a) Shear stress distribution within the adhesive layer reaches excellent agreement with the existing experimental data and numerical analysis, and satisfies zero-shear boundary condition at the free edges.
    b) Thinner adhesive layers lead to higher shear stress concentrations close to the ends, and vice versa.
    c) Peel stresses along two adhesive-adherend interfaces of the joint are different.
    d) The proposed model can successfully predict the location of the debonding initiation for double-lap joints, as verified by experimental observations.
2. A novel three-parameter viscoelastic foundation model has been established to predict the stress redistributions induced by the viscoelastic behavior of the adhesive in adhesively bonded joints. This model possesses the following features:
    a) It achieves excellent agreements with the FEA.
    b) It satisfies zero-shear boundary condition.

c) It successfully captures the shear and peel stress relaxations induced by the viscoelastic behavior of the adhesive layer.

3. Environment-assisted subcritical debonding test has been carried out to study the long-term durability of the FRP-to-concrete interface in aggressive environments. The following conclusions are obtained:

   a) The environment-assisted subcritical debonding test can capture the synergistic effects of mechanical loads and environmental conditions such as water, moisture and temperature on deterioration of the FRP-to-concrete interface.

   b) Applying silane coupling agent can improve the bond quality and slow the subcritical debonding. The hydrophobicity induced by silane and the swelling of the epoxy also can play important roles in the durability of the FRP-to-concrete interface.

   c) By fitting the relationship between the crack growth rate and the energy release rate to the empirical expression modified from Paris Law, the service-life of the interface can be predicted.

   d) Subcritical debondings in water and in air are significantly different. The debonding length and the crack growth rate are much larger in water than in air.

   e) While failure mode of specimens debonded in air is cohesive (within the concrete), the failure mode of specimens tested in water shifts to the adhesive failure.

4. Critical debonding of the FRP-to-concrete interface specimens conditioned in water was studied through wedge driving and pulling tests. Also the intrinsic debonding of the FRP-to-concrete interfaces subjected to water attack was studied through an innovative specimen design. This new design can create a relatively uniform distribution of the moisture content across the interface, making it possible to establish an intrinsic relationship between the

residual fracture toughness and the relative humidity of the interface based on testing data. The findings from this study are summarized as:

a) Specimens lose most of the mode-I and mode –II fracture toughness after being conditioned in water for one month.
b) Because the mechanical interlock plays more important role in fracture toughness of the interface under mode-II loading, the residual mode-II fracture toughness after conditioning in water is much higher than the one under mode-I loading.
c) After being conditioned in water for three months, no significant further reduction in residual fracture toughness of the interface can be observed.
d) Silane coupling agent is effective in improving the durability of the FRP-to-concrete interface subjected to attack of moisture. The relationships between the residual fracture toughness and the interface relative humidity can be approximated by exponential expressions.
e) The relationship between the residual fracture toughness and the relative humidity of the interface can be used to predict the deterioration of the interface induced by water. This intrinsic relationship is different from the one obtained using the existing method, in which the whole specimen is submerged in water. This difference suggests that the existing method is extrinsic and the testing results are specimen-dependent.

5. A novel wedge splitting test was carried to directly determine the traction-separation law of epoxy-concrete interface under mode-I loading. The traction-separation law of the epoxy-concrete interface has been successfully measured by this novel wedge splitting specimen. This law can be approximated by a tri-linear expression. The resulted traction-separation

laws show that conditioning the specimens in water significantly reduces the interface tensile strength compared to the control specimens (not conditioned).

9.2. Conclusions

This Ph.D. dissertation has developed both the analytical and the experimental tools to study the FRP-to-concrete interface, which is a key element in a new technology to repair/retrofit aged civil structures, external bonding of FRP to conventional construction materials such as reinforced concretes and steels. By using the three-parameter elastic and viscoelastic foundation models proposed in this study, engineers can correctly predict which interface will debond first in adhesively bonded joints. By knowing the failure location, effective measures can be taken to prevent the debonding initiation. It is important to differentiate the short-term interfacial stresses from the long-term stress distributions. The relationship between the crack growth rate and the energy release rate established through environment-assisted subcritical debonding testing provides a robust tool to predict the long-term durability of the FRP-to-concrete interfaces. Testing results have revealed that significant difference exists between the energy required to initiate debonding along the FRP-to-concrete interface in water and in air. Debonding of the interface in water can be started by a much smaller force and is faster compared to the one in air. Visual observations of the debonded FRP-to-concrete interface have confirmed this difference. Failure mode of specimens in air has been found to be cohesive and debonding locus is within the concrete regardless of the temperature and the relative humidity level; while it is adhesive when the specimen is conditioned in water. This difference may imply that existing studies on the long-term durability of the FRP-to-concrete interface overestimate the detrimental effect of moisture on the interface since all these testing results were obtained by submerging the whole specimen in water. In real application, the interface will not be fully submerged in water except

used in underwater environment. Therefore, its failure mode and debonding growth rate should be closer to the subcritical debonding in air rather than in water.

In order to enhance long-term durability of the interface, applying silane coupling agent to the surface of the concrete substrate can increase the residual fracture toughness of the epoxy-concrete interface in presence of water.

9.3. Public impacts

It is of great significance to develop new technologies to enhance the resilience and sustainability of aged and deteriorated civil infrastructures system. External bonding FRP to concrete has emerged as an exemplary new technology to enhance the performance and durability of existing structures. This new technique requires of using novel organic materials together with traditional construction materials such as concretes and steels which are inorganic. The combination of two different materials creates a new problem for structural and material engineers, the integrity and durability of this inorganic-organic interface. Many analytical and experimental methods have been developed to study the short and long-term performances of traditional in-organic materials and new organic materials such as FRP composites. However, the tools to either analyze or test the interface between the organic-organic are very limited.

In this dissertation a new research has been carried out to address this urgent research need by providing both analytical and experimental tools to study the FRP-to-concrete interfaces. This study not only sheds new lights on the long-term behavior and design of FRP-strengthened concrete structures, but also lays out the framework to analyze and test the organic-inorganic bi-material interface, on which our current knowledge is very limited.

9.4. Future works

A few problems exist in the present studies which need to be addressed in the future study,

1) The role of the swelling of epoxy: Very significant swelling of epoxy under certain environments has been observed in this study. However, their role in the debonding of the interface, which has never been addressed in existing studies, is not fully examined in this study. Future study should be carried out to gain fundamental understanding on the swelling of the adhesive on the durability of the FRP-to-concrete interface.

2) The role of epoxy creep: Similar to the swelling of the epoxy, the creep deformation of the adhesive layer is not excluded from the environment-assisted subcritical debonding test results. As a result, the estimated opening force applied by the wedge is higher than the real one. Consequently, the calculated energy release rate could be overestimated. In the future study, creep deformation of the adhesive layer should be excluded from the measured deformation of the cantilever beam so more accurate value of the energy release rate can be calculated.

3) Existence of critical moisture content: Studies on metal based adhesively bonded joints show that critical moisture content exists. Below this moisture content, the strength reduction of the interface is insignificant. However, when moisture along the interface surpasses this value, drastic reduction of the strength of interface can be observed. Some studies relate this sudden loss of the strength of the interface above the critical moisture content to the sudden change of the behavior of the epoxy when the moisture is above the critical value. Environment assisted subcritical debonding test results also shows the distinct difference between the slow debonding in water and in air with high humidity. The critical debonding test data also indicate that there exists a critical moisture content, above which no significant further reduction in strength can be observed. In addition, absorption test of the epoxy shows that the epoxy used in this study exhibits non-Fickian's behavior if the moisture content exceeding certain value, suggesting that epoxy may experience significant behavior change too. All these observations may imply such

REFERENCES

[1] A. W. Herrmann, "ASCE 2013 Report Card for America's Infrastructure," in *IABSE Symposium Report*, 2013, vol. 99, no. 33, pp. 9–10.

[2] U. S. DOT, "Transportation statistics annual report," *Washington, DC United States Dep. Transp.*, 2008.

[3] M. Arduini and A. Nanni, "Parametric study of beams with externally bonded FRP reinforcement," *ACI Struct. J.*, vol. 94, no. 5, pp. 493–501, 1997.

[4] Ce. Bakis, L. C. Bank, Vl. Brown, E. Cosenza, J. F. Davalos, J. J. Lesko, A. Machida, S. H. Rizkalla, and T. C. Triantafillou, "Fiber-reinforced polymer composites for construction-state-of-the-art review," *J. Compos. Constr.*, vol. 6, no. 2, pp. 73–87, 2002.

[5] A. Sharif, G. J. Al-Sulaimani, I. A. Basunbul, M. H. Baluch, and B. N. Ghaleb, "Strengthening of initially loaded reinforced concrete beams using FRP plates," *ACI Struct. J.*, vol. 91, no. 2, 1994.

[6] U. Meier and H. Kaiser, "Strengthening of structures with CFRP laminates," in *Advanced composites materials in civil engineering structures*, 1991, pp. 224–232.

[7] P. A. Ritchie, D. A. Thomas, L.-W. Lu, and G. M. Conelly, "External reinforcement of concrete beams using fiber reinforced plastics," *ACI Struct. J.*, vol. 88, no. 4, 1991.

[8] V. M. Karbhari, F. Seible, and G. A. Hegemier, "On the Use of Fiber Reinforced Composites for Infrastructure Renewal—A Systems Approach," in *Materials for the New Millennium*, 1996, pp. 1091–1100.

[9] C. E. Bakis, A. Ganjehlou, D. I. Kachlakev, M. Schupack, P. N. Balaguru, D. J. Gee, V. M. Karbhari, D. W. Scott, C. A. Ballinger, and T. R. Gentry, "Guide for the design and construction of externally bonded FRP systems for strengthening concrete structures," *Rep. by ACI Comm.*, vol. 440, no. 2002, 2002.

[10] E. Saadatmanseh and M. R. Ehsani, "Application of Fibre-Composites in Civil Engineering," in *Proceedings of the 7th ASCE Structures Congress*, 1989, pp. 526–535.

[11] J. Thomas, T. Kline, P. Emmons, and H. Kliger, "Externally bonded carbon fiber for strengthening concrete," in *Materials for the New Millennium*, 1996, pp. 924–931.

[12] L. C. Muszynski and R. L. Sierakowski, “Fatigue Fracture of Externally Reinforced Concrete Beams,” in *Materials for the New Millennium - Proceedings of the Fourth Materials Engineering Conference*, 1996, pp. 648–656.

[13] J. W. Tedesco, J. M. Stallings, M. El-Mihilmy, and M. W. McCauley, “Rehabilitation of a concrete bridge using FRP laminates,” in *Materials for the New Millennium*, 1996, pp. 631–637.

[14] D. V Reddy, G. B. Gervois, and L. A. Carlsson, “Laminate Bonding for Concrete Repair and Retrofit,” in *Materials for the New Millennium*, 1996, pp. 1579–1591.

[15] C. Zhang, “Mechanics and subcritical cracking of FRP-concrete interface.” The University of Alabama TUSCALOOSA, 2011.

[16] L. De Lorenzis and A. Nanni, “Characterization of FRP rods as near-surface mounted reinforcement,” *J. Compos. Constr.*, vol. 5, no. 2, pp. 114–121, 2001.

[17] J. G. Teng, L. De Lorenzis, B. Wang, R. Li, T. N. Wong, and L. Lam, “Debonding failures of RC beams strengthened with near surface mounted CFRP strips,” *J. Compos. Constr.*, vol. 10, no. 2, pp. 92–105, 2006.

[18] T. Hassan and S. Rizkalla, “Investigation of bond in concrete structures strengthened with near surface mounted carbon fiber reinforced polymer strips,” *J. Compos. Constr.*, 2003.

[19] L. De Lorenzis and A. Nanni, “Shear strengthening of reinforced concrete beams with near-surface mounted fiber-reinforced polymer rods,” *ACI Struct. J.*, vol. 98, no. 1, 2001.

[20] D. Novidis, S. J. Pantazopoulou, and E. Tentolouris, “Experimental study of bond of NSM-FRP reinforcement,” *Constr. Build. Mater.*, vol. 21, no. 8, pp. 1760–1770, 2007.

[21] R. Seracino, N. M. Jones, M. S. Ali, M. W. Page, and D. J. Oehlers, “Bond strength of near-surface mounted FRP strip-to-concrete joints,” *J. Compos. Constr.*, vol. 11, no. 4, pp. 401–409, 2007.

[22] G. Spadea, F. Bencardino, and R. N. Swamy, “Structural behavior of composite RC beams with externally bonded CFRP,” *J. Compos. Constr.*, vol. 2, no. 3, pp. 132–137, 1998.

[23] J. Yao, J. G. Teng, and J. F. Chen, “Experimental study on FRP-to-concrete bonded joints,” *Compos. Part B Eng.*, vol. 36, no. 2, pp. 99–113, 2005.

[24] B. Wan, “The Effect of the Presence of Water on the Durability of Bond between CFRP and Concrete,” *J. Reinf. Plast. Compos.*, vol. 25, no. 8, pp. 875–890, 2006.

[25] J. G. Dai, E. Kato, M. Iwanami, and H. Yokata, “Durability of carbon strand sheet to concrete bond interface under moisture condition,” in *Fourth Int. Conf. on FRP Composites in Civil Eingineering*, 2008.

[26] K. Harries, J. Aidoo, A. Zorn, and J. Quattlebaum, "Deterioration of FRP-to-concrete bond under failure loading," *Adv. Struct. Eng.*, vol. 9, no. 6, pp. 779–789, 2006.

[27] L. Bizindavyi, K. W. Neale, and M. A. Erki, "Experimental investigation of bonded fiber reinforced polymer-concrete joints under cyclic loading," *J. Compos. Constr.*, vol. 7, no. 2, pp. 127–134, 2003.

[28] R. Krishnaswamy and M. Lopez, "Time performance of concrete-CFRP bond under the effects of freeze-thaw cycles and sustained loading," in *Proceeding of 85th Annual Meeting. Transportation Research BoardNational Academies*, 2006.

[29] J. F. Davalos, S. S. Kodkani, I. Ray, and C. Lin, "Fracture evaluation of GFRP—concrete interfaces for freeze—thaw and wet-dry cycling," *J. Compos. Mater.*, vol. 42, no. 14, pp. 1439–1466, 2008.

[30] C. Au and O. Büyüköztürk, "Peel and shear fracture characterization of debonding in FRP plated concrete affected by moisture," *J. Compos. Constr.*, vol. 10, no. 1, pp. 35–47, 2006.

[31] N. F. Grace and M. Grace, "Effect of repeated loading and long term humidity exposure on flexural response of CFRP strengthened concrete beams," in *Proceedings of the International Symposium on Bonded behavior of FRP in Structures (BBFS 2005), Chen and Teng (eds)*, 2005, pp. 539–546.

[32] V. M. Karbhari, Jw. Chin, D. Hunston, B. Benmokrane, T. Juska, R. Morgan, J. J. Lesko, U. Sorathia, and D. Reynaud, "Durability gap analysis for fiber-reinforced polymer composites in civil infrastructure," *J. Compos. Constr.*, vol. 7, no. 3, pp. 238–247, 2003.

[33] M. L. Porter and K. Harries, "Future directions for research in FRP composites in concrete construction," *J. Compos. Constr.*, vol. 11, no. 3, pp. 252–257, 2007.

[34] C. Tuakta and O. Büyüköztürk, "Conceptual model for prediction of FRP-concrete bond strength under moisture cycles," *J. Compos. Constr.*, vol. 15, no. 5, pp. 743–756, 2011.

[35] J. G. Teng, S. T. Smith, J. Yao, and J. F. Chen, "Intermediate crack-induced debonding in RC beams and slabs," *Constr. Build. Mater.*, vol. 17, no. 6, pp. 447–462, 2003.

[36] L. Tong and C. Soutis, *Recent advances in structural joints and repairs for composite materials*. Springer Science & Business Media, 2013.

[37] O. Volkersen, "Die Nietkraftverteilung in zugbeanspruchten Nietverbindungen mit konstanten Laschenquerschnitten," *Luftfahrtforschung*, vol. 15, no. 1/2, pp. 41–47, 1938.

[38] M. Goland and E. Reissner, "The stresses in cemented joints," *J. Appl. Mech.*, vol. 11, no. 1, pp. A17–A27, 1944.

[39] S.-C. Her, “Stress analysis of adhesively-bonded lap joints,” *Compos. Struct.*, vol. 47, no. 1, pp. 673–678, 1999.

[40] Q. Luo and L. Tong, “Linear and higher order displacement theories for adhesively bonded lap joints,” *Int. J. Solids Struct.*, vol. 41, no. 22, pp. 6351–6381, 2004.

[41] D. W. Oplinger, “Effects of adherend deflections in single lap joints,” *Int. J. Solids Struct.*, vol. 31, no. 18, pp. 2565–2587, 1994.

[42] L. J. Hart-Smith, “Adhesive-bonded double-lap joints technical report, NASA CR-112235,” *Hampton, VA NASA Langley Res. Cent.*, 1973.

[43] L. J. Hart-Smith, *Adhesive-bonded single-lap joints*. Langley Research Center Hampton, VA, 1973.

[44] J. W. Renton and J. R. Vinson, “On the behavior of bonded joints in composite material structures,” *Eng. Fract. Mech.*, vol. 7, no. 1, pp. 41–60, 1975.

[45] W. J. Renton and J. R. Vinson, “The efficient design of adhesive bonded joints,” *J. Adhes.*, vol. 7, no. 3, pp. 175–193, 1975.

[46] U. Yuceoglu and D. P. Updike, “Bending and shear deformation effects in lap joints,” *J. Eng. Mech. Div.*, vol. 107, no. 1, pp. 55–76, 1981.

[47] O. T. Thomsen, “Elasto-static and elasto-plastic stress analysis of adhesive bonded tubular lap joints,” *Compos. Struct.*, vol. 21, no. 4, pp. 249–259, 1992.

[48] L. Tong, “Bond strength for adhesive-bonded single-lap joints,” *Acta Mech.*, vol. 117, no. 1–4, pp. 101–113, 1996.

[49] M. Y. Tsai, D. W. Oplinger, and J. Morton, “Improved theoretical solutions for adhesive lap joints,” *Int. J. Solids Struct.*, vol. 35, no. 12, pp. 1163–1185, 1998.

[50] F. Mortensen and O. T. Thomsen, “Analysis of adhesive bonded joints: a unified approach,” *Compos. Sci. Technol.*, vol. 62, no. 7, pp. 1011–1031, 2002.

[51] F. Delale, F. Erdogan, and M. N. Aydinoglu, “Stresses in adhesively bonded joints: a closed-form solution,” *J. Compos. Mater.*, vol. 15, no. 3, pp. 249–271, 1981.

[52] H. Yuan, J. G. Teng, R. Seracino, Z. S. Wu, and J. Yao, “Full-range behavior of FRP-to-concrete bonded joints,” *Eng. Struct.*, vol. 26, no. 5, pp. 553–565, 2004.

[53] Y. Frostig, “Behavior of delaminated sandwich beam with transversely flexible core—high order theory,” *Compos. Struct.*, vol. 20, no. 1, pp. 1–16, 1992.

[54] Y. Frostig, "On stress concentration in the bending of sandwich beams with transversely flexible core," *Compos. Struct.*, vol. 24, no. 2, pp. 161–169, 1993.

[55] Y. Frostig and M. Baruch, "Bending of sandwich beams with transversely flexible core," *AIAA J.*, vol. 28, no. 3, pp. 523–531, 1990.

[56] Y. Frostig and M. Baruch, "Localized load effects in high-order bending of sandwich panels with flexible core," *J. Eng. Mech.*, vol. 122, no. 11, pp. 1069–1076, 1996.

[57] Y. Frostig, O. T. Thomsen, and F. Mortensen, "Analysis of adhesive-bonded joints, square-end, and spew-fillet-high-order theory approach," *J. Eng. Mech.*, vol. 125, no. 11, pp. 1298–1307, 1999.

[58] D. Chen and S. Cheng, "An analysis of adhesive-bonded single-lap joints," *J. Appl. Mech.*, vol. 50, no. 1, pp. 109–115, 1983.

[59] D. Allman, "A theory for elastic stress in adhesively bonded lap joints," *Q. J. Mech. Appl. Math.*, no. 30, pp. 415–436, 1977.

[60] J. G. Teng, J. W. Zhang, and S. T. Smith, "Interfacial stresses in reinforced concrete beams bonded with a soffit plate: a finite element study," *Constr. Build. Mater.*, vol. 16, no. 1, pp. 1–14, 2002.

[61] J. Wang and C. Zhang, "Three-parameter, elastic foundation model for analysis of adhesively bonded joints," *Int. J. Adhes. Adhes.*, vol. 29, no. 5, pp. 495–502, 2009.

[62] R. D. Adams, R. W. Atkins, J. A. Harris, and A. J. Kinloch, "Stress analysis and failure properties of carbon-fibre-reinforced-plastic/steel double-lap joints," *J. Adhes.*, vol. 20, no. 1, pp. 29–53, 1986.

[63] L. J. Hart-Smith, "Further developments in the design and analysis of adhesive-bonded structural joints," *Join. Compos. Mater.*, pp. 3–31, 1981.

[64] R. D. Adams and V. Mallick, "A method for the stress analysis of lap joints," *J. Adhes.*, vol. 38, no. 3–4, pp. 199–217, 1992.

[65] A. E. Bogdanovich and I. Kizhakkethara, "Three-dimensional finite element analysis of double-lap composite adhesive bonded joint using submodeling approach," *Compos. Part B Eng.*, vol. 30, no. 6, pp. 537–551, 1999.

[66] R. D. Adams and N. A. Peppiatt, "Stress analysis of adhesive-bonded lap joints," *J. Strain Anal. Eng. Des.*, vol. 9, no. 3, pp. 185–196, 1974.

[67] E. Ferrier and P. Hamelin, "Influence of Time-Temperature-Loading on Carbon Epoxy Reinforcement for Concrete Structures," *ACI Spec. Publ.*, vol. 188, 1999.

[68] B. A. Mirman and S. Knecht, "Creep strains in an elongated bond layer," *Components, Hybrids, Manuf. Technol. IEEE Trans.*, vol. 13, no. 4, pp. 914–928, 1990.

[69] G. Dean, "Modelling non-linear creep behaviour of an epoxy adhesive," *Int. J. Adhes. Adhes.*, vol. 27, no. 8, pp. 636–646, 2007.

[70] H. F. Brinson, "The viscoelastic constitutive modelling of adhesives," *composites*, vol. 13, no. 4, pp. 377–382, 1982.

[71] G. Dean, L. Crocker, B. Read, and L. Wright, "Prediction of deformation and failure of rubber-toughened adhesive joints," *Int. J. Adhes. Adhes.*, vol. 24, no. 4, pp. 295–306, 2004.

[72] F. Delale and F. Erdogan, "Viscoelastic analysis of adhesively bonded joints," *J. Appl. Mech.*, vol. 48, no. 2, pp. 331–338, 1981.

[73] F. Ascione, V. P. Berardi, L. Feo, and A. Giordano, "An experimental study on the long-term behavior of CFRP pultruded laminates suitable to concrete structures rehabilitation," *Compos. Part B Eng.*, vol. 39, no. 7, pp. 1147–1150, 2008.

[74] K.-K. Choi, P. Meshgin, and M. M. R. Taha, "Shear creep of epoxy at the concrete–FRP interfaces," *Compos. Part B Eng.*, vol. 38, no. 5, pp. 772–780, 2007.

[75] H. Diab and Z. Wu, "Nonlinear constitutive model for time-dependent behavior of FRP-concrete interface," *Compos. Sci. Technol.*, vol. 67, no. 11, pp. 2323–2333, 2007.

[76] M. Savoia, B. Ferracuti, and C. Mazzotti, "Creep deformation of fiber reinforced plastics-plated reinforced concrete tensile members," *J. Compos. Constr.*, vol. 9, no. 1, pp. 63–72, 2005.

[77] K.-K. Choi, M. M. R. Taha, M. J. Masia, P. L. Shrive, and N. G. Shrive, "Numerical investigation of creep effects on FRP-strengthened RC beams," *J. Compos. Constr.*, vol. 14, no. 6, pp. 812–822, 2010.

[78] E. Ferrier, L. Michel, B. Jurkiewiez, and P. Hamelin, "Creep behavior of adhesives used for external FRP strengthening of RC structures," *Constr. Build. Mater.*, vol. 25, no. 2, pp. 461–467, 2011.

[79] P. Meshgin, K.-K. Choi, and M. M. R. Taha, "Experimental and analytical investigations of creep of epoxy adhesive at the concrete–FRP interfaces," *Int. J. Adhes. Adhes.*, vol. 29, no. 1, pp. 56–66, 2009.

[80] H. Ghoneim and Y. Chen, "A viscoelastic-viscoplastic constitutive equation and its finite element implementation," *Comput. Struct.*, vol. 17, no. 4, pp. 499–509, 1983.

[81] B. G. Schaffer and D. F. Adams, “Nonlinear viscoelastic analysis of a unidirectional composite material,” *J. Appl. Mech.*, vol. 48, no. 4, pp. 859–865, 1981.

[82] Y. Weitsman, “Interfacial stresses in viscoelastic adhesive-layers due to moisture sorption,” *Int. J. Solids Struct.*, vol. 15, no. 9, pp. 701–713, 1979.

[83] Y. Weitsman, “An Investigation of Non-Linear Viscoelastic Effects on Load Transfer in a Symmetric Double-Lap Joint,” *J. Adhes.*, vol. 11, no. 4, pp. 279–289, 1981.

[84] N. Houhou, K. Benzarti, M. Quiertant, S. Chataigner, A. Fléty, and C. Marty, “Analysis of the nonlinear creep behavior of concrete/FRP-bonded assemblies,” *J. Adhes. Sci. Technol.*, vol. 28, no. 14–15, pp. 1345–1366, 2014.

[85] W. G. Knauss and I. J. Emri, “Non-linear viscoelasticity based on free volume consideration,” *Comput. Struct.*, vol. 13, no. 1, pp. 123–128, 1981.

[86] C. Meaud, B. Jurkiewiez, and E. Ferrier, “Investigation of creep effects in strengthened RC structures through double lap shear testing,” *Compos. Part B Eng.*, vol. 42, no. 3, pp. 359–366, 2011.

[87] D. Peretz and Y. Weitsman, “The Nonlinear Thermoviscoelastic Characterizations of FM□73 Adhesives,” *J. Rheol.*, vol. 27, no. 2, pp. 97–114, 1983.

[88] A. K. Pickett and L. Hollaway, “The analysis of elastic-plastic adhesive stress in bonded lap joints in FRP structures,” *Compos. Struct.*, vol. 4, no. 2, pp. 135–160, 1985.

[89] M. Shishesaz and A. Reza, “The effect of viscoelasticity of polymeric adhesives on shear stress distribution in a single-lap joint,” *J. Adhes.*, vol. 89, no. 11, pp. 859–880, 2013.

[90] C. Sato, “Stress estimation of joints having adherends with different curvatures bonded with viscoelastic adhesives,” *Int. J. Adhes. Adhes.*, vol. 31, no. 5, pp. 315–321, 2011.

[91] R. A. Schapery, “A method of viscoelastic stress analysis using elastic solutions,” *J. Franklin Inst.*, vol. 279, no. 4, pp. 268–289, 1965.

[92] P. Qiao, J. Wang, and J. F. Davalos, “Analysis of tapered ENF specimen and characterization of bonded interface fracture under Mode-II loading,” *Int. J. Solids Struct.*, vol. 40, no. 8, pp. 1865–1884, 2003.

[93] A. A. Griffith, “The phenomena of rupture and flow in solids,” *Philos. Trans. R. Soc. london. Ser. A, Contain. Pap. a Math. or Phys. character*, pp. 163–198, 1921.

[94] M. F. Kaplan, “Crack propagation and the fracture of concrete,” in *ACI Journal proceedings*, 1961, vol. 58, no. 11.

[95] H. L. Groth, "A method to predict fracture in an adhesively bonded joint," *Int. J. Adhes. Adhes.*, vol. 5, no. 1, pp. 19–22, 1985.

[96] A. D. Crocombe, D. A. Bigwood, and G. Richardson, "Analysing joints for structural adhesive failure," *Int. J. Adhes. Adhes.*, vol. 10, no. 3, pp. 167–178, 1990.

[97] J. Wang and P. Qiao, "Fracture analysis of shear deformable bi-material interface," *J. Eng. Mech.*, vol. 132, no. 3, pp. 306–316, 2006.

[98] F. Ducept, P. Davies, and D. Gamby, "Mixed mode failure criteria for a glass/epoxy composite and an adhesively bonded composite/composite joint," *Int. J. Adhes. Adhes.*, vol. 20, no. 3, pp. 233–244, 2000.

[99] J. Wang and P. Qiao, "Novel beam analysis of end notched flexure specimen for mode-II fracture," *Eng. Fract. Mech.*, vol. 71, no. 2, pp. 219–231, 2004.

[100] Q. D. Yang, M. D. Thouless, and S. M. Ward, "Numerical simulations of adhesively-bonded beams failing with extensive plastic deformation," *J. Mech. Phys. Solids*, vol. 47, no. 6, pp. 1337–1353, 1999.

[101] G. Fernlund, M. Papini, D. McCammond, and J. K. Spelt, "Fracture load predictions for adhesive joints," *Compos. Sci. Technol.*, vol. 51, no. 4, pp. 587–600, 1994.

[102] D. B. Bogy, "Edge-bonded dissimilar orthogonal elastic wedges under normal and shear loading," *J. Appl. Mech.*, vol. 35, no. 3, pp. 460–466, 1968.

[103] Z. Suo and J. W. Hutchinson, "Steady-state cracking in brittle substrates beneath adherent films," *Int. J. Solids Struct.*, vol. 25, no. 11, pp. 1337–1353, 1989.

[104] Z. Suo and J. W. Hutchinson, "Interface crack between two elastic layers," *Int. J. Fract.*, vol. 43, no. 1, pp. 1–18, 1990.

[105] C. Au and O. Büyüköztürk, "Debonding of FRP plated concrete: a tri-layer fracture treatment," *Eng. Fract. Mech.*, vol. 73, no. 3, pp. 348–365, 2006.

[106] P. Qiao and J. Wang, "Novel joint deformation models and their application to delamination fracture analysis," *Compos. Sci. Technol.*, vol. 65, no. 11, pp. 1826–1839, 2005.

[107] A. J. Kin Loch and S. J. Shaw, "The fracture resistance of a toughened epoxy adhesive," *J. Adhes.*, vol. 12, no. 1, pp. 59–77, 1981.

[108] P. G. De Gennes, "Soft adhesives," *Langmuir*, vol. 12, no. 19, pp. 4497–4500, 1996.

[109] F. Dubois, C. Chazal, and C. Petit, "Viscoelastic crack growth process in wood timbers: An approach by the finite element method for mode I fracture," *Int. J. Fract.*, vol. 113, no. 4, pp. 367–388, 2002.

[110] R. Frassine, M. Rink, and A. Pavan, "Viscoelastic effects on the interlaminar fracture behaviour of thermoplastic matrix composites: II. Rate and temperature dependence in unidirectional PEEK/carbon-fibre laminates," *Compos. Sci. Technol.*, vol. 56, no. 11, pp. 1253–1260, 1996.

[111] S. H. Song, G. H. Paulino, and W. G. Buttlar, "A bilinear cohesive zone model tailored for fracture of asphalt concrete considering viscoelastic bulk material," *Eng. Fract. Mech.*, vol. 73, no. 18, pp. 2829–2848, 2006.

[112] R. A. Schapery, "Correspondence principles and a generalizedJ integral for large deformation and fracture analysis of viscoelastic media," *Int. J. Fract.*, vol. 25, no. 3, pp. 195–223, 1984.

[113] C. Hui, D. Xu, and E. J. Kramer, "A fracture model for a weak interface in a viscoelastic material (small scale yielding analysis)," *J. Appl. Phys.*, vol. 72, no. 8, pp. 3294–3304, 1992.

[114] D. Xu, C. Hui, and E. J. Kramer, "Interface fracture and viscoelastic deformation in finite size specimens," *J. Appl. Phys.*, vol. 72, no. 8, pp. 3305–3316, 1992.

[115] P. Rahulkumar, A. Jagota, S. J. Bennison, and S. Saigal, "Cohesive element modeling of viscoelastic fracture: application to peel testing of polymers," *Int. J. Solids Struct.*, vol. 37, no. 13, pp. 1873–1897, 2000.

[116] O. Buyukozturk and B. Hearing, "Failure behavior of precracked concrete beams retrofitted with FRP," *J. Compos. Constr.*, vol. 2, no. 3, pp. 138–144, 1998.

[117] O. Büyüköztürk and T.-Y. Yu, "Understanding and assessment of debonding failures in FRP–concrete systems," in *17th International congress on advances in civil engineering, Yildiz Technical University, Istanbul, Turkey*, 2006.

[118] M. F. Green, L. A. Bisby, Y. Beaudoin, and P. Labossière, "Effect of freeze-thaw cycles on the bond durability between fibre reinforced polymer plate reinforcement and concrete," *Can. J. Civ. Eng.*, vol. 27, no. 5, pp. 949–959, 2000.

[119] J. Jia, T. E. Boothby, C. E. Bakis, and T. L. Brown, "Durability evaluation of glass fiber reinforced-polymer-concrete bonded interfaces," *J. Compos. Constr.*, vol. 9, no. 4, pp. 348–359, 2005.

[120] Z. Ouyang and B. Wan, "Experimental and Numerical Study of Moisture Effects on the Bond Fracture Energy of FRP/Concrete Joints," *J. Reinf. Plast. Compos.*, 2007.

[121] "FRP-concrete bond in structural strengthening and rehabilitation. RILEM." Technical Committee FRP, 2003.

[122] S. M. Wiederhorn, "Moisture assisted crack growth in ceramics," *Int. J. Fract. Mech.*, vol. 4, no. 2, pp. 171–177, 1968.

[123] D. Maugis, "Subcritical crack growth, surface energy, fracture toughness, stick-slip and embrittlement," *J. Mater. Sci.*, vol. 20, no. 9, pp. 3041–3073, 1985.

[124] J. E. Ritter and K. Conley, "Moisture-assisted crack propagation at polymer/glass interfaces," *Int. J. Adhes. Adhes.*, vol. 12, no. 4, pp. 245–250, 1992.

[125] R. H. Dauskardt, M. Lane, Q. Ma, and N. Krishna, "Adhesion and debonding of multi-layer thin film structures," *Eng. Fract. Mech.*, vol. 61, no. 1, pp. 141–162, 1998.

[126] C. K. Gurumurthy, E. J. Kramer, and C.-Y. Hui, "Water-assisted sub-critical crack growth along an interface between polyimide passivation and epoxy underfill," *Int. J. Fract.*, vol. 109, no. 1, pp. 1–28, 2001.

[127] E. P. O'Brien, S. L. Case, and T. C. Ward, "Critical and subcritical adhesion measurements of a model epoxy coating exposed to moisture using the shaft-loaded blister test," *J. Adhes.*, vol. 81, no. 1, pp. 41–58, 2005.

[128] H. K. Singh, K.-T. Wan, J. G. Dillard, D. A. Dillard, P. Reboa, J. Smith, E. Chappell, and A. Sharan, "Subcritical delamination in epoxy bonds to silicon and glass adherends: Effect of temperature and preconditioning," *J. Adhes.*, vol. 84, no. 7, pp. 619–637, 2008.

[129] E. J. Ripling, S. Mostovoy, and C. Bersch, "Stress corrosion cracking of adhesive joints," *J. Adhes.*, vol. 3, no. 2, pp. 145–163, 1971.

[130] S. Mostovoy and E. J. Ripling, "The fracture toughness and stress corrosion cracking characteristics of an anhydride hardened epoxy adhesive," *J. Appl. Polym. Sci.*, vol. 15, no. 3, pp. 641–659, 1971.

[131] S. Mostovoy and E. J. Ripling, "Effect of temperature on the fracture toughness and stress corrosion cracking of adhesives," in *Applied Polymer Symposium*, 1972, pp. 395–408.

[132] A. J. Kinloch, "Interfacial fracture mechanical aspects of adhesive bonded joints—a review," 1979.

[133] A. J. Kinloch, C. F. Korenberg, K. T. Tan, and J. F. Watts, "Crack growth in structural adhesive joints in aqueous environments," *J. Mater. Sci.*, vol. 42, no. 15, pp. 6353–6370, 2007.

[134] C. F. Korenberg, A. J. Kinloch, and J. F. Watts, "Crack growth of structural adhesive joints in humid environments," *J. Adhes.*, vol. 80, no. 3, pp. 169–201, 2004.

[135] E. B. Becker, M. E. Mear, and K. Ravi-Chandar, “Durability of adhesive joints between concrete and FRP reinforcement in aggressive environments,” 2004.

[136] J. G. Dai and T. Ueda, “Local bond stress slip relations for FRP sheets-concrete interfaces,” in *Proc of the Sixth International Symposium on FRP Reinforcement for Concrete Structures (FRPRCS-6) Singapore*, 2003, pp. 8–10.

[137] S. Shimizu, T. Yanagimoto, and M. Sakai, “Pyramidal indentation load–depth curve of viscoelastic materials,” *J. Mater. Res.*, vol. 14, no. 10, pp. 4075–4086, 1999.

[138] C. Zhang, J. Wang, and K. J. Fridley, “Environment-Assisted Subcritical Debonding of Epoxy-Concrete Interface,” *J. Compos. Constr.*, vol. 16, no. 5, pp. 563–571, 2012.

[139] O. Buyukozturk, C. Au, A. Reyes, V. Barzov, and I. Jacobi, “Failure Behavior of FRP Bonded Concrete Affected by Interface Fracture. Part 2. Moisture Degradation in FRP Bonded Concrete Systems: An Interface Fracture Approach,” 2004.

[140] A. Namkanisorn, A. Ghatak, M. K. Chaudhury, and D. H. Berry, “A kinetic approach to study the hydrolytic stability of polymer–metal adhesion,” *J. Adhes. Sci. Technol.*, vol. 15, no. 14, pp. 1725–1745, 2001.

[141] M.-L. Abel, R. D. Allington, R. P. Digby, N. Porritt, S. J. Shaw, and J. F. Watts, “Understanding the relationship between silane application conditions, bond durability and locus of failure,” *Int. J. Adhes. Adhes.*, vol. 26, no. 1, pp. 2–15, 2006.

[142] D. H. Berry and A. Namkanisorn, “Fracture toughness of a silane coupled polymer-metal interface: Silane concentration effects,” *J. Adhes.*, vol. 81, no. 3–4, pp. 347–370, 2005.

[143] A. Rattana, M.-L. Abel, and J. F. Watts, “Degradation of interfacial chemistry of epoxy/silane/aluminium interfaces as a result of aqueous attack,” *J. Adhes.*, vol. 81, no. 9, pp. 963–988, 2005.

[144] M. Sautrot*, M.-L. Abel, J. F. Watts, and J. Powell, “Incorporation of an adhesion promoter in a structural adhesive: aspects of durability and interface chemistry,” *J. Adhes.*, vol. 81, no. 2, pp. 163–187, 2005.

[145] S. Shokoohi, A. Arefazar, and R. Khosrokhavar, “Silane coupling agents in polymer-based reinforced composites: a review,” *J. Reinf. Plast. Compos.*, vol. 27, no. 5, pp. 473–485, 2008.

[146] B. B. Johnsen, K. Olafsen, A. Stori, and K. Vinje, “Silanization of adhesively bonded aluminum alloy AA6060 with γ-glycidoxypropyltrimethoxysilane. II. Stability in degrading environments,” *J. Adhes. Sci. Technol.*, vol. 17, no. 9, pp. 1283–1298, 2003.

[147] L. Ye, K. Friedrich, C. Weimer, and Y.-W. Mai, "Surface treatments and adhesion bonding between concrete and a CFRP composite," *Adv. Compos. Mater.*, vol. 7, no. 1, pp. 47–61, 1998.

[148] S. U. Al-Dulaijan, M. M. Al-Zahrani, A. Nanni, and T. E. Boothby, "Effect of environmental pre-conditioning on bond of FRP reinforcement to concrete," *J. Reinf. Plast. Compos.*, vol. 20, no. 10, pp. 881–900, 2001.

[149] J. Lyons, D. Laub, V. Giurgiutiu, M. Petrou, and H. Salem, "Effect of hygrothermal aging on the fracture of composite overlays on concrete," *J. Reinf. Plast. Compos.*, vol. 21, no. 4, pp. 293–309, 2002.

[150] V. M. Karbhari and M. Engineer, "Effect of environmental exposure on the external strengthening of concrete with composites-short term bond durability," *J. Reinf. Plast. Compos.*, vol. 15, no. 12, pp. 1194–1216, 1996.

[151] K. V Subramaniam, M. Ali-Ahmad, and M. Ghosn, "Freeze–thaw degradation of FRP–concrete interface: impact on cohesive fracture response," *Eng. Fract. Mech.*, vol. 75, no. 13, pp. 3924–3940, 2008.

[152] P. Mukhopadhyaya, R. N. Swamy, and C. J. Lynsdale, "Influence of aggressive exposure conditions on the behaviour of adhesive bonded concrete–GFRP joints," *Constr. Build. Mater.*, vol. 12, no. 8, pp. 427–446, 1998.

[153] D. Lau and O. Büyüköztürk, "Fracture characterization of concrete/epoxy interface affected by moisture," *Mech. Mater.*, vol. 42, no. 12, pp. 1031–1042, 2010.

[154] Z. Ouyang and B. Wan, "Modeling of moisture diffusion in FRP strengthened concrete specimens," *J. Compos. Constr.*, vol. 12, no. 4, pp. 425–434, 2008.